

# Study of the Electronic Properties of Three- and Two-Dimensional Transition Metal Dichalcogenides

Thesis submitted for the degree of

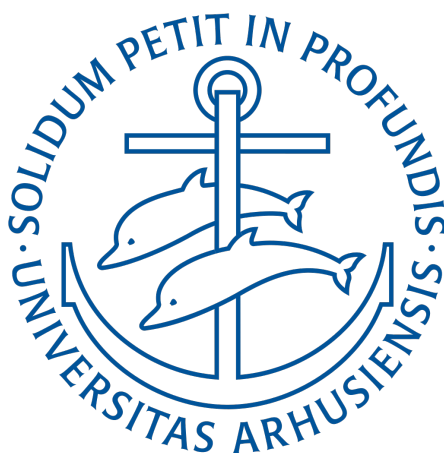
Doctor of Philosophy (Science)

in

Physics

by

**Arlette Sohanfo Ngankeu**



Aarhus University, Denmark

November, 2017



---

# Abstract

---

Transition metal dichalcogenides (TMDCs) are a class of materials that have been studied for decades due to the rich nature of their d-orbitals, which have granted researchers the power to design new materials with unique and novel properties. Metallic TMDCs such as 1T-TaS<sub>2</sub> develop series of charge density waves (CDW) and superconductivity below some onset temperatures. Such materials are interesting for device applications, especially if a way could be found for electrically controlling the transition between each CDW phase. Although these TMDC materials have been studied for a long time, recent advances studies of these materials have offered various attractive features for use in the next generation electronic and optoelectronic devices. Thus, this opens up new opportunities for carefully investigating different TMDCs from bulk to their corresponding single layer (SL). Interest in the SL derives from new properties resulting from the reduction of symmetry in the SL as well as the strict electronic confinement in the SL; for example, MoS<sub>2</sub> is characterized by a bandgap that changes from indirect in the bulk to direct in single layer. Thus, SL TMDCs provide an ideal platform to pursue new fundamental research and achieve technological innovations. However, it is still very challenging to grow high quality SL TMDCs with very big domain size.

The epitaxial growth procedures developed in our group to make high-quality and large area SL TMDCs are presented in this thesis. We describe the synthesis of single to few layers of TaS<sub>2</sub> on Au(111). The electronic structures of these samples are studied with angle resolved photoemission spectroscopy (ARPES). The experimental results of SL TaS<sub>2</sub>/Au(111) from ARPES are then compared with density-functional theory (DFT) calculations, for both a free-standing layer and when the metallic substrate is taken into account. The morphology and crystal structure of SL TaS<sub>2</sub>/Au(111) are characterized by scanning tunneling microscopy (STM) and low-energy electron diffraction (LEED). The suppression of the CDW in SL TaS<sub>2</sub>/Au(111) is revealed by the low-temperature STM/STS studies. The absence

of CDW in this system is assigned to substantial doping that originates from the Au(111) substrate. Recently, some theoretical calculations have proposed that the doping observed in SL TaS<sub>2</sub>/Au(111) might be caused by band hybridization instead of charge transfer through the interface.

We also investigated bilayer (BL) TaS<sub>2</sub>/Au(111) prepared by a similar procedure. A ( $\sqrt{3} \times \sqrt{3}$ )R30° reconstruction of TaS<sub>2</sub> is observed on the STM and LEED scans from the BL TaS<sub>2</sub>/Au(111).

The lifting of the spin degeneracy of the upper valence band of single layer WS<sub>2</sub>, MoS<sub>2</sub> and 1H-TaS<sub>2</sub> is caused by the lack of inversion symmetry. The study of the electron-phonon coupling in the spin-split valence band of single layers WS<sub>2</sub>, MoS<sub>2</sub> and 1H-TaS<sub>2</sub> is presented in this thesis. The electron-phonon coupling strength of the three types of single layers are found using ARPES spectra. The values of the coupling strength  $\lambda$  of the two spin-split branches at K in SL WS<sub>2</sub> are compared with the values from the first principles calculations, Einstein and Debye models. The theoretical results are in good agreement with the experimental results. The values of the electron-phonon coupling strength for the SL MoS<sub>2</sub> and SL 1H-TaS<sub>2</sub> are extracted from ARPES spectra and are then compared with those obtained from the Einstein and Debye models. The coupling strength is found to be highly different for the two spin-split branches in single layer WS<sub>2</sub>, MoS<sub>2</sub> and 1H-TaS<sub>2</sub>.

The metallic 1T-TaS<sub>2</sub> is among the famous bulk TMDCs due to its multiple CDW phases observed at different temperatures, each of which is accompanied with a lattice distortion. However, its electronic structure is not fully studied experimentally within each series of CDWs, or even in/above the normal phase. Therefore, in this thesis we present the study of the three-dimensional (3D) 1T-TaS<sub>2</sub> by means of ARPES within each CDW series. Furthermore, recent theoretical calculations have predicted the coexistence of the CDW phase in the commensurate CDW with a nearly one-dimensional metallic dispersion perpendicular to the crystal planes. We demonstrate that this one-dimensional metallic state in fact exists. However, we also show that the metallic dispersion not only exists in the commensurate CDW, it exists also in the nearly-commensurate CDW phase. We also study the effect of the presence/absence of CDW on the tantalum 4f peaks at different phases by means of X-ray photoelectron spectroscopy (XPS).

---

# Dansk Resumé

---

*Transition metal dichalcogenides* (TMDC'er) er en type af materialer, som er blevet forsket i årtier på grund af den rige natur af deres d-orbitaler, hvilket har givet forskerne evnen til at udvikle nye materialer med unikke og nye egenskaber. Metallisk TMDC'er såsom 1T-TaS<sub>2</sub> udviste en række *charge density waves* (CDW) og superledningsevner under nogle start temperaturer. Disse materialer er interessante for apparat anvendelser, specielt hvis man kunne finde en metode til at kontrollere overgangen mellem hver CDW fase elektrisk. Selv om disse TMDC materialer er blevet forsket i et stykke tid, er der, fra det nyeste forskning af disse materialer, udbudt adskillige attraktive områder til brug i den næste generation af elektroniske og *opto*-elektroniske apparater. Dette åbner op for nye muligheder for nøje undersøgelser af forskellige TMDC'er fra volumestof til deres korresponderende *single layer* (SL). Interessen i SL stammer fra nye egenskaber, der er resulteret fra redueringen af symmetri i SL såvel som den strikte *electronic confinement* i SL. For eksempel, MoS<sub>2</sub> er karakteriseret ved et båndgab, der ændrer sig fra indirekte i stoffet til direkte i SL. Derfor, giver SL TMDC'er en ideal platform til at forfølge nye fundamentale forskning and opnå teknologiske innovationer. Det er imidlertid meget vanskelig at fremstille SL TMDC'er af høj kvalitet, som har store domæner.

Metoderne af *epitaxial growth*, som blev udviklet af vores gruppe, for at fremstille SL TMDC'er af høj kvalitet og store domæner, er beskrevet i denne afhandling. Vi beskriver syntesen af enkelt til få lag af TaS<sub>2</sub> på Au(111). De elektroniske strukturer af disse materialer er blevet undersøgt med *angle resolved photoemission spectroscopy* (ARPES). De eksperimentelle resultater af SL TaS<sub>2</sub>/Au(111) fra ARPES er blevet sammenlignet med *density-functional theory* (DFT) beregninger, både for et frit-stående lag og når det metalliske substrat er medtaget. Morfoligien og krystal strukturen af SL TaS<sub>2</sub>/Au(111) er karakteriseret ved *scanning tunneling microscopy* (STM) og ved *low-energy electron diffraction* (LEED). Dæmpningen af CDW'en i SL TaS<sub>2</sub>/Au(111) er vist med lav-temperatur STM/STS. Ude-

blivelsen af CDW i dette system er tilskrevet til den omfattende doping, der udsprang fra Au(111) substraten. For nylig, har teoretiske udregninger foreslået, at doping observeret i SL TaS<sub>2</sub>/Au(111) kan skyldes af båndhybridisering i stedet for ladning overførsel gennem grænsefladen.

Vi undersøgte også *bilayer* (BL) TaS<sub>2</sub>/Au(111), som er udarbejdet med en tilsvarende procedure. En ( $\sqrt{3} \times \sqrt{3}$ )R30° rekonstruktion af TaS<sub>2</sub> er observeret ved STM og LEED fra BL TaS<sub>2</sub>/Au(111).

Hævningen af spin degeneration af den øvre valensbånd af SL WS<sub>2</sub>, MoS<sub>2</sub> og 1H-TaS<sub>2</sub> er forårsaget af manglen på inversion symmetri. Undersøgelsen af elektron-fonon koblingen i den spin-delte valensbånd af SL'er af WS<sub>2</sub>, MoS<sub>2</sub> og 1H-TaS<sub>2</sub> er fremlagt i denne afhandling. Styrken af elektron-fonon koblingen af disse tre typer af SL'er er fundet ved at benytte ARPES spektre. Værdierne for koblingstyrken ( $\lambda$ ) af de to spin-delte grene ved K i SL WS<sub>2</sub> er sammenlignet med værdierne fra *the first principles calculations*, Einsteins og Debyes modeller. De teoretiske værdier er i god overensstemmelse med de eksperimentelle resultater. Værdierne af elektron-fonon koblingstyrken for SL MoS<sub>2</sub>'en og SL 1H-TaS<sub>2</sub>'en er fundet ud fra ARPES spektre, og er efterfølgende sammenlignet med dem fundet fra Einsteins og Debye modeller. Koblingstyrken er fundet til at være meget forskelligt for de to spin-delte grene i SL WS<sub>2</sub>, MoS<sub>2</sub> og 1H-TaS<sub>2</sub>.

Den metalliske 1T-TaS<sub>2</sub> er blandt de populære *bulk* TMDC'er på grund af deres multiple CDW faser, der er observeret ved forskellige temperaturer, hvor hver af dem er ledsaget med en gitter forvrængning. Dog, er dens elektroniske strukture ikke helt fuld ud blevet forsket i eksperimentelt inden for hver serie af CDW'er, eller hverken i/over normalfasen. Derfor præsenterer vi undersøgelsen af den tre-dimensionelle (3D) 1T-TaS<sub>2</sub> ved hjælp af ARPES inden for hver serie i denne afhandling. Endvidere, har nye teoretiske beregninger forudsagt den koeksistense af CDW fasen i den *commensurate* CDW med en næsten en-dimensionel metallisk dispersion vinkelret på krystalplanerne. Vi demonstrerer, at denne en-dimensionelle metallisk tilstand faktisk eksisterer. Vi viser også, at den metalliske dispersion ikke kun eksisterer i den *commensurate* CDW, men at den også eksisterer i den næsten-*commensurate* CDW fase. Vi undersøger også effekten af den tilstedeværende/ikke tilstedeværende af CDW på t antal 4f toppene ved forskellige faser ved hjælp af *X-ray photoelectron spectroscopy* (XPS).

---

# Preface

---

The research work presented in this dissertation was carried out from December 2014 to November 2017. The work was done under the supervision of Professor Philip Hofmann, at the Department of Physics and Astronomy, Interdisciplinary Nanoscience Centre, Aarhus University, 8000 Aarhus C, Denmark.

The thesis was submitted to the Graduate School of Science and Technology at Aarhus University in order to fulfill the requirements to obtain a Philosophiae Doctor (Ph.D) degree in Physics. The majority of the work has been carried out at the SGM3 beamline for angle-resolved photoemission on ASTRID2 at the Institute for Storage Ring Facilities in Aarhus (ISA). The projects presented in this thesis were done in collaboration with groups from the Department of Chemistry, Aarhus University, the University of Kiel, Radboud University and finally from the SuperESCA beamline located at Elettra Sincrotrone. A list of my own publications, including those not directly relevant to the material presented in this thesis, is given below. In the outlook, some ongoing projects are also described.

---

# Acknowledgements

---

The work presented in this thesis has been carried out from December 2014 to November 2017, under the supervision of Prof. Philip Hofmann. All the work presented here would not have been possible without the help of talented and kind people in my research group, from whom I have benefited greatly. I will be forever grateful.

I am much indebted to the excellent group of people that I have luckily come into contact with and benefited from in the course of this thesis work.

First of all my greatest thanks go to my advisor, Prof. Philip Hofmann, for allowing me into his research group. I was very lucky to have such an inspiring and considerate advisor, who has made my PhD enjoyable and fruitful. Besides the encouragement, training and support that he gave me in science, I also deeply appreciate his willingness to care about students' life beyond the work. The past 3 years working with him have been a fortune for me. His endless enthusiasms for science, his wisdom and his open mindedness to balance work and life have set him as a role model for me. I could not ask for better advisor than him.

A very special thanks goes to Dr. Charlotte Sanders for being a great mentor regarding all growth procedures, UHV, STM, ARPES, LEED experiments... , in fact for everything because the list is very long. Furthermore, I would like to thank you again for your support, patience with various beamtimes, for proofreading this thesis, for being a very good driver from Aarhus to Nijmegen for low temperature STM measurements and for many friendly and useful discussions.

Another special thanks goes to Prof. Jill Miwa for teaching me how to cool down the Aarhus STM and for always caring about people.

Further special thanks goes to Dr. Marco Bianchi for introducing me to UHV systems, ARPES measurements and Igor procedures; for valuable discussions about various topics; and also for proofreading parts of this thesis.

Further special thanks goes to Dr. Sanjoy Mahatha for his great help during the preparation and measurements of different samples for different beamtimes, for valuable discussions about various topics during the data analysis, and for proofreading parts of my thesis.

Another special thanks goes to Dr. Antonija Grubišić Čabo for being always willing to help me at anytime, for being also a great roommate on beamtimes, for the very useful scientific discussions, and for your great help during the teaching.

Another special thanks goes to Dr. Maciej Dendzik for being always willing to help me and for teaching me how to write Igor procedures.

Another special thanks goes to Prof. Kai Rossnagel, for providing me with the first 1T-TaS<sub>2</sub> samples for measuring, and also to Prof. Martin Bremholm and Christina Breth Nielsen for growing nice 1T-TaS<sub>2</sub> samples. Without all of you, I would never have had chapter 3 of my thesis.

Another special thanks to Fabian Arnold for helping me multiple times during teaching, experiments and much more; and to Dr. Matteo Michiardi for organizing the road trips and for helping me get an accommodation here in Aarhus.

The collaboration with many theorists has been quite pleasant and beneficial. Dr. Albert Bruix and Dr. Nicki Frank Hinsche, are our primary theoretical collaborators on projects presented in this thesis. Their deep knowledge of Physics and enthusiasm for finding solutions are very inspiring to me. It has been a great pleasure to work with them. I am grateful to all the people involved in the 2D TaS<sub>2</sub> project, especially to Dr. Andreas Eich and Umut Kamber from Radboud University for performing low-temperature STM. A special thanks goes to Prof. Alexander A. Khajetoorians and Prof. Silvano Lizzit for allowing me to work in their laboratories.

I would also like to thank Raluca-Maria Stan for her multiples jokes that always make me laugh and for being a great roommate during the DPG conference; Klara Volckaert for the nice pub quiz during the Sandbjerg outing activities; Henriette Elisabeth Lund for her multiples jokes also and for always being willing to help me during various experiments; to Dr. Kevin Guillo, Dr. Davide Curcio, Ann Julie Holt and Prof. Søren Ulstrup for their good company.

Finally, another special thanks go to my biological and Christ families, especially to my parents, sisters and brothers for all their support, encouragements and love that have been the constant fuel of my life as a graduate student.

Arlette Sohanfo Ngankeu

30.11.2017

Aarhus, Denmark

---

# List of Publications

---

## Publications relevant for this thesis

1. Charlotte E. Sanders, Maciej Dendzik, Arlette S. Ngankeu, Andreas Eich, Albert Bruix, Marco Bianchi, Jill A. Miwa, Bjørk Hammer, Alexander A. Khajetoorians, and Philip Hofmann: “*Crystalline and Electronic Structure of Single-layer TaS<sub>2</sub>*”, Phys. Rev. B **94**, 081404(R), 2016.
2. Nicki Frank Hinsche, Arlette S. Ngankeu, Kevin Guilloy, Sanjoy K. Mahatha, Antonija Grubišić Čabo, Marco Bianchi, Maciej Dendzik, Charlotte E. Sanders, Jill A. Miwa, Harsh Bana, Elisabetta Travaglia, Paolo Lacovig, Luca Bignardi, Rosanna Larciprete, Alessandro Baraldi, Silvano Lizzit, Kristian Sommer Thygesen and Philip Hofmann: “*Electron-phonon Coupling in the Spin-split Valence Band of Single Layer WS<sub>2</sub>*”, Phys. Rev. B **96**, 121402(R), 2017.
3. Arlette S. Ngankeu, Sanjoy K. Mahatha, Kevin Guilloy, Marco Bianchi, Charlotte E. Sanders, Kerstin Hanff, Kai Rossnagel, Jill A. Miwa, Christina Breth Nielsen, Martin Bremholm, and Philip Hofmann: “*Quasi-One-dimensional Metallic Band Dispersion in the Commensurate Charge Density Wave of 1T-TaS<sub>2</sub>*”, Phys. Rev. B **96**, 195147, 2017.

## Other Publications

1. M. Vališka, J. Warmuth, M. Michiardi, M. Vondráček, A. S. Ngankeu, V. Holý, V. Sechovský, G. Springholz, M. Bianchi, J. Wiebe, P. Hofmann, and J. Honolka: “*Topological Insulator Homojunctions Including Magnetic Layers: The Example of n-p type*

*(n-QLs Bi<sub>2</sub>Se<sub>3</sub>/Mn-Bi<sub>2</sub>Se<sub>3</sub>) Heterostructures*”, Appl. Phys. Lett. **108**, 108, 2016.

2. Maciej Dendzik, Albert Bruix, Matteo Michiardi, Arlette S. Ngankeu, Marco Bianchi, Jill A. Miwa, Bjørk Hammer, Philip Hofmann, Charlotte E. Sanders: “*Contact-Induced Semiconductor-to-Metal Transition in Single-Layer WS<sub>2</sub>*”, arXiv:1708.02799, Phys. Rev. B, in press.

---

# List of Abbreviations and Acronyms

---

<b>2D, 3D</b>	Two-, Three-Dimensional
<b>TMDC</b>	Transitional Metal Dichalcogenide
<b>TMDCs</b>	Transitional Metal Dichalcogenides
<b>SL</b>	Single-Layer
<b>CDW</b>	Charge Density Wave
<b>C-CDW</b>	Commensurate Charge Density Wave
<b>NC-CDW</b>	Nearly Commensurate Charge Density Wave
<b>IC-CDW</b>	Incommensurate Charge Density Wave
<b>ARPES</b>	Angle Resolved Photoemission Spectroscopy
<b>LEED</b>	Low Energy Electron Diffraction
<b>STM</b>	Scanning Tunneling Microscopy
<b>STS</b>	Scanning Tunnelling Spectroscopy
<b>VB</b>	Valence Band
<b>VBM</b>	Valence Band Maxima
<b>RT</b>	Room Temperature
<b>SC</b>	Superconducting
<b>BL</b>	Bilayer
<b>BZ</b>	Brillouin Zone
<b>CVD</b>	Chemical Vapour Deposition

<b>EDC</b>	Energy Distribution Curve
<b>MDC</b>	Momentum Distribution Curve
<b>MBE</b>	Molecular Beam Epitaxy
<b>FL</b>	Fermi Level
<b>FS</b>	Fermi Surface
<b>MBE</b>	Molecular Beam Epitaxy
<b>IMFP</b>	Inelastic Mean Free Path
<b>ML</b>	Monolayer
<b>e-ph</b>	Electron-Phonon
<b>UHV</b>	Ultrahigh Vacuum
<b>DOS</b>	Density of States
<b>LDOS</b>	Local Density of States
<b>SS</b>	Surface State
<b>Au</b>	Gold
<b>LDA</b>	Local Density Approximation
<b>WS<sub>2</sub></b>	Tungsten Disulfide
<b>MoS<sub>2</sub></b>	Molybdenum Disulfide
<b>TaS<sub>2</sub></b>	Tantalum Disulfide
<b>LT</b>	Low Temperature
<b>DFT</b>	Density Functional Theory
<b>MCP</b>	Multi Channel Plate
<b>PES</b>	Photoemission Spectroscopy
<b>XPS</b>	X-ray Photoemission Spectroscopy
<b>trPES</b>	time-resolved Photoelectron Spectroscopy

---

# Contents

---

<b>Abstract</b>	<b>i</b>
<b>Dansk Resumé</b>	<b>iii</b>
<b>Preface</b>	<b>v</b>
<b>Acknowledgements</b>	<b>vi</b>
<b>List of Publications</b>	<b>ix</b>
<b>List of Abbreviations and Acronyms</b>	<b>xi</b>
<b>1 Introduction</b>	<b>1</b>
1.1 Bulk Transition Metal Dichalcogenides . . . . .	1
1.2 2D Transition Metal Dichalcogenides . . . . .	5
1.3 Molybdenum (MoS <sub>2</sub> ) and Tungsten (WS <sub>2</sub> ) Disulfide . . . . .	6
1.4 Tantalum Disulfide TaS <sub>2</sub> . . . . .	8
1.4.1 Crystal Structure and Charge Density Waves in Tantalum Disulfide TaS <sub>2</sub> . . . . .	9
1.4.2 Electronic Structure of Tantalum Disulfide TaS <sub>2</sub> . . . . .	12
1.5 Thesis Structure . . . . .	13

<b>2</b>	<b>Experimental Techniques</b>	<b>15</b>
2.1	Introduction . . . . .	15
2.2	Low Energy Electron Diffraction . . . . .	16
2.3	Scanning Tunneling Microscopy . . . . .	18
2.4	Angle Resolved Photoemission Spectroscopy . . . . .	22
2.4.1	Photoemission Spectroscopy . . . . .	22
2.4.2	Single Particle Spectral Function . . . . .	27
2.4.3	Energy Distribution Curves (EDCs) and Momentum Distribution Curves (MDCs) . . . . .	30
2.4.4	Core Level Photoemission Spectroscopy . . . . .	32
2.4.5	ARPES Spectral Acquisition and Analysis . . . . .	33
2.4.6	The SGM3 Beamline and ASTRID2 . . . . .	37
2.4.7	The Setup of the SGM3 Endstation . . . . .	39
<b>3</b>	<b>Study of the 3D Band Dispersion of Bulk 1T-TaS<sub>2</sub> at Different Temperatures</b>	<b>42</b>
3.1	Introduction . . . . .	42
3.2	ARPES Study on 1T-TaS <sub>2</sub> in the C-CDW Phase . . . . .	47
3.3	ARPES Study on 1T-TaS <sub>2</sub> in the NC-CDW Phase . . . . .	54
3.4	ARPES Study on 1T-TaS <sub>2</sub> in the IC-CDW Phase . . . . .	58
3.5	ARPES Study on 1T-TaS <sub>2</sub> in the Normal Phase . . . . .	61
3.6	ARPES Study on 1T-TaS <sub>2</sub> above the Normal Phase . . . . .	66
3.7	Temperature Dependence Maps from 1T-TaS <sub>2</sub> . . . . .	67
<b>4</b>	<b>Growth and Electronic Structure of the Single- and Bi-layer TaS<sub>2</sub></b>	<b>71</b>
4.1	General Growth Procedure of TaS <sub>2</sub> . . . . .	73
4.2	SL of TaS <sub>2</sub> on Au(111) . . . . .	76

4.2.1	ARPES Study of SL TaS <sub>2</sub> on Au(111) . . . . .	78
4.2.2	Absence of CDW in SL TaS <sub>2</sub> on Au(111) . . . . .	79
4.3	ARPES Study on BL of TaS <sub>2</sub> on Au(111) . . . . .	85
<b>5</b>	<b>Electron-Phonon Coupling in Single-Layer TMDCs</b>	<b>89</b>
5.1	Electron-phonon Coupling . . . . .	90
5.1.1	Determination of the e-ph Coupling Strength . . . . .	91
5.2	Analysis of temperature-dependent EDCs/MDCs . . . . .	96
5.3	Tungsten and Molybdenum Dichalcogenides . . . . .	97
5.3.1	Extraction of $\lambda$ from the Spin-Split Valence Bands of SL WS <sub>2</sub> /Au(111)	99
5.3.2	Extraction of $\lambda$ from the Spin-Split Valence Band of SL MoS <sub>2</sub> /Au(111) . . . . .	106
5.4	Extraction of $\lambda$ from SL 1H-TaS <sub>2</sub> /Au(111) . . . . .	108
<b>6</b>	<b>Conclusion and Outlook</b>	<b>111</b>
6.1	Conclusion . . . . .	111
6.2	Outlook . . . . .	113
<b>A</b>	<b>Free-Electron Final States</b>	<b>115</b>
<b>B</b>	<b>Origin of Kinks in the Measured Band Dispersion</b>	<b>117</b>
B.1	Additional Information about the Sample Growth . . . . .	119
	<b>References</b>	<b>134</b>

---

# Introduction

---

The aim of this chapter is to give a general description of the structure and some properties of the compounds studied in this thesis, as well as of the class of materials to which they all belong. First, a review of the 3D (bulk) and 2D transition metal dichalcogenides (TMDCs) are presented in sections 1.1 and 1.2, respectively. Sections 1.3 and 1.4 are devoted to introducing molybdenum ( $\text{MoS}_2$ ), tungsten ( $\text{WS}_2$ ) and tantalum ( $\text{TaS}_2$ ) disulfide. Finally, section 1.5 gives the structure of this thesis.

## 1.1 Bulk Transition Metal Dichalcogenides

Transition metal dichalcogenides (TMDCs) constitute a very large class of materials with the common chemical formula  $\text{MX}_2$ , where M represents a transition metal within the groups 4 to 10 of the periodic table (cf. highlighted elements in purple on the periodic table shown in Figure 1.1(a)). X stands for chalcogen elements from group 16 of the periodic table (see Figure 1.1(a)). Sulfur (S), selenium (Se) and tellurium (Te) are chalcogens in layered TMDCs (elements highlighted in pink on the periodic table shown in Figure 1.1(a)). TMDCs exhibit a wide range of physical and electronic properties due to the layered crystal structure that these materials adopt [1, 2].

There are at least 60 known TMDCs and approximately two thirds have hexagonal and layered structures. These layered structures are constituted of hexagonal-packed transition metal atoms sandwiched between two layers of chalcogens (see Figure 1.1(b)). Between

the metal (M) and the chalcogens (X), there is a strong intralayer covalent bonding, and the possible coordinations adopted by the transition metal (M) inside the TMDCs is either trigonal prismatic (H) or octahedral (T) as shown in Figures 1.1(c) and 1.1(d), respectively.

In bulk TMDCs, there exist different stacking orders, or polytypes (2H, 1T, 3R etc.), but the basic crystal structure is generally limited to one of the two types just described, or to slight modifications of these. For instance, the most common stable polytype, the so-called 2H<sup>1</sup> phase, is formed when two opposed layers of trigonal prismatic MX<sub>2</sub> units cell are stacked on each other. Aside from the common AB stacking sequence existing in the 2H phase, another common phase can be realized in the ABC stacking, consisting of 3 trigonal prismatic layers, and this phase is known as the 3R phase. Some TMDCs can also be crystallized in metastable phases. In these phases, the coordination of the X atoms is different from trigonal prismatic: for example, these phases can include both the distorted (1T') and non-distorted octahedral (1T, AA stacking) phases. Figures 1.1(c) and 1.1(d) show the most common coordination of the basic unit cell of the crystal structures studied in this thesis.

In all bulk layered TMDCs, the X-M-X layers are weakly bound by van der Waals forces [7]. This weak interlayer bonding allow for easy cleavage of the bulk TMDCs along the layer surface, leading to few layer or single layer samples [8]. The weak interlayer bonds lead to easy intercalation of metals atoms or organic molecules between the layers [9, 10]. This intercalation can introduce important changes in the physical properties of the host compound.

The existence of various TMDCs with different polytypes results in a wide range of possible electronic properties. Thus, one can engineer the band structure of TMDCs in a certain way with a substitution of a transition metal in TMDCs. These bulk TMDCs have been extensively studied and their electronic properties range from insulating (e.g., HfS<sub>2</sub> [11]) to semiconducting (TMDCs in the 2H phase from groups 4, 6, 7, 9, 10 such as MoS<sub>2</sub>) to semimetallic (TiSe<sub>2</sub>, MoTe<sub>2</sub> and WTe<sub>2</sub>) materials. These semimetals are interesting and have been predicted to contain examples of type II Weyl semimetals [12, 13]. Metals (group 5) such as TaS<sub>2</sub> and TaSe<sub>2</sub> host CDW states [14, 15]. At low temperature, superconductivity can be observed in niobium and tantalum based structures. TMDC materials have many applications and can be used as solid lubricants [16], photoactive materials [17], energy storage media [11] and hydrodesulfurization catalysts [18].

---

<sup>1</sup>It should be noted that in 2H, the number 2 stands for the two basic units cell, while H represents the hexagonal symmetry.

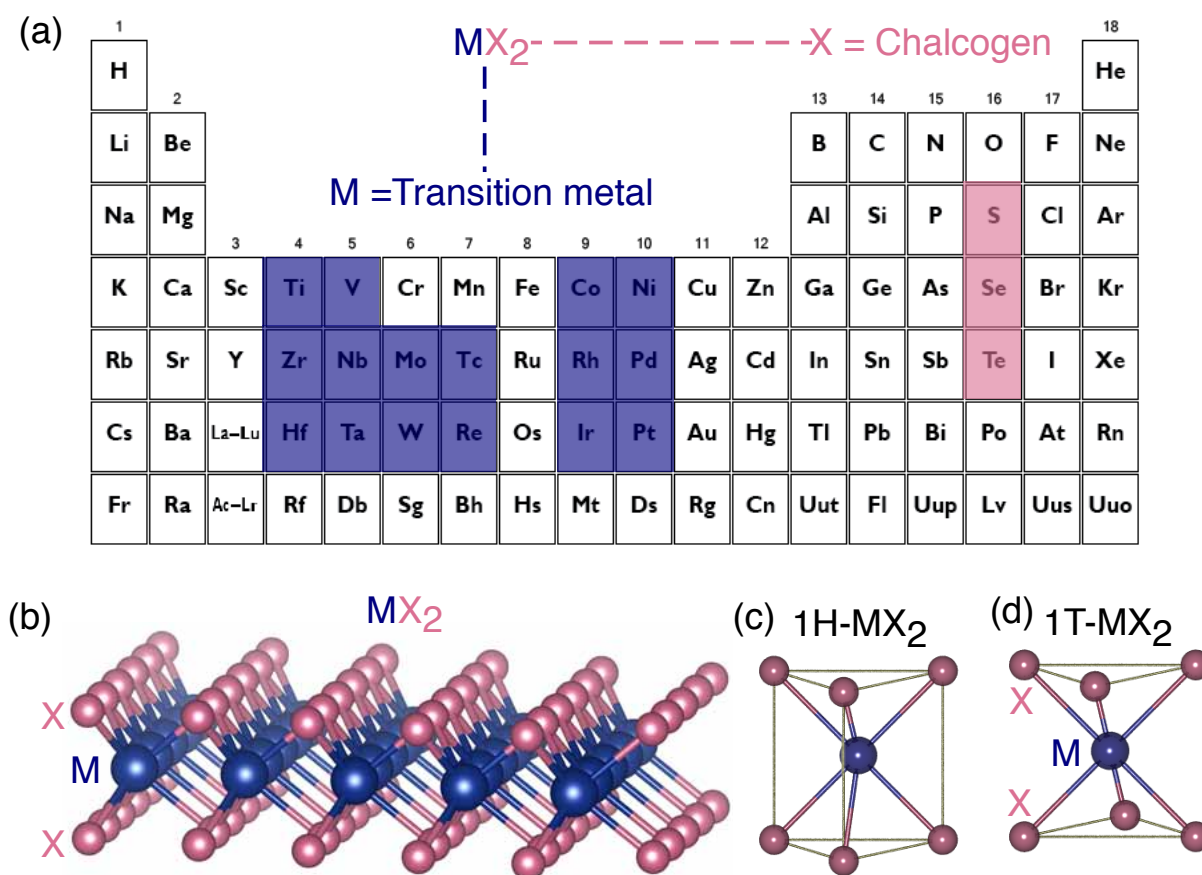


**Figure 1.1:** (a) Periodic table of elements presenting the possible combinations of elements forming layered TMDCs  $\text{MX}_2$ . Purple color indicates the transition metals (M), while chalcogens (X) are indicated by the pink color. This figure was taken from Ref. [3] and modified. Schematics of the two most common structural polymorphs of TMDCs, where M atom is shown in purple and X atoms is shown in pink. (b) Drawing of an hexagonal structure TMDC exhibiting an octahedral coordination unit forming the X-M-X sandwiches. The figure was generated with VESTA software [4, 5]. (c) This figure shows an hexagonal (H) symmetry with trigonal prismatic coordination around the metal M sites, while, the trigonal (T) symmetry with approximately octahedral coordination around the metal M sites is presented in (d). Figures (c) and (d) were created with POV-Ray software [6].

Molybdenum and tungsten disulfides have industrial applications such as high-temperature dry lubrication, and catalysis. These materials are metallic in the metastable 1T phase. Nevertheless, the 2H phase of bulk  $\text{MoS}_2$  is an indirect band gap semiconductors with a gap of approximately 1.3 eV.

For the sake of understanding the origin of the richness of the electronic properties observed in the large family of TMDCs, Figure 1.2 exhibits the d-orbital filling and electronic character of different TMDCs. The various electronic structures exhibited by the TMDC family depend greatly on the number of valence electrons associated with the transition metal and on its

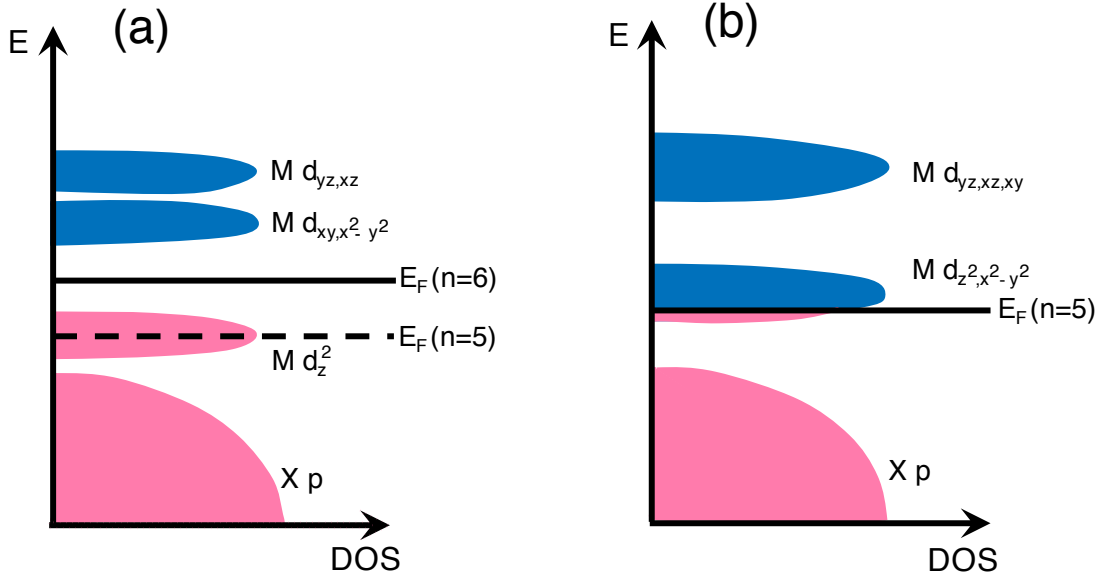


**Figure 1.2:** Schematic diagram of the comparison of the d band density of states for 2H-MX<sub>2</sub> (a) and 1T-MX<sub>2</sub> (b). This figure presents how the electronic structure of TMDCs depends on the coordination environment and the number of valence electrons. The occupied and empty states of MX<sub>2</sub> are indicated by the pink and blue areas, respectively. (a) This sketch presents a group n=6 TMDCs with a trigonal prismatic coordination, such as 2H-MoS<sub>2</sub>, for instance. The lowest d band (d<sub>z<sup>2</sup></sub>) is filled, making 2H-MoS<sub>2</sub> a semiconductor. The Fermi level of a TMDCs with group n=5 metal atom, such as 2H-TaS<sub>2</sub> for example, is indicated by the black dashed line. In this case, the lowest band (d<sub>z<sup>2</sup></sub>) would be half filled and this makes 2H-TaS<sub>2</sub> a metal. (b) This sketch represents a group n=5 metallic TMDCs with octahedral coordination, such as 1T-TaSe<sub>2</sub>, for instance. Since the lowest d subband is partially filled, this makes 1T-TaSe<sub>2</sub> a metal.

coordination environment [11]. Based on the atomic energy levels, the valence d-orbitals from the metal M are higher in energy than the valence p-orbitals in the chalcogen X. In the MX<sub>2</sub> crystal, there are 6 p bands per unit cell due to the presence of two X atoms. These bands are occupied by 8 electrons from X atoms and by 4 other electrons from M metal, leaving n-4 electrons to occupy the d bands. It should be noted that n here stands for the group number of metal M [1]. The d bands are split by the crystal field according to their coordination environment. When the transition metal atoms M are octahedrally coordinated, the d band is divided into d<sub>z<sup>2</sup>,x<sup>2</sup>-y<sup>2</sup></sub> and d<sub>yz,xz,xy</sub> subbands [1] (see Figure 1.2(b)). By contrast, with trigonal prismatic coordination, the d bands is divided into 3 subbands d<sub>z<sup>2</sup></sub>, d<sub>x<sup>2</sup>-y<sup>2</sup>,xy</sub> and d<sub>xz,yz</sub> [1] (see Figure 1.2(a)). Based on these arguments, for instance, 1T-TaSe<sub>2</sub> (n=5) is predicted to have one electron occupying the d bands and then be metallic as illustrated in Figure 1.2(b). On the other hand, 2H-MoS<sub>2</sub> (n=6) is expected to have one filled d band and then a gap before the next set of d bands, making this compound a semiconductor, as

illustrated in Figure 1.2(a). It should be noted that there are no pure p nor d bands in a real compound, due to the hybridization between different atomic orbitals. Furthermore, in some real compounds, some bands have further splittings and overlap in energy, which make the picture even more complicated [1]. Nonetheless, Figure 1.2 presents a good way to understand trends in the electronic structure within the  $\text{MX}_2$  class of materials. For the studies presented in this thesis, the two semiconducting systems  $\text{MoS}_2$  and  $\text{WS}_2$  together with the metallic system  $\text{TaS}_2$  have been chosen. The theoretical predictions describing these materials in the single layer limit are presented below.

## 1.2 2D Transition Metal Dichalcogenides

The properties of 2D TMDCs are inherited from their 3D parents to a large extent. This class of materials has experienced a rebirth after the discovery of graphene—single layer carbon sheets characterized by a hexagonal honeycomb lattice—by A. Geim and coworkers [19], who were awarded the Nobel prize in 2010. It was realized after the first exfoliation of graphene that other layered materials (TMDCs, black phosphorous and more) can be isolated in the single layer limit in a similar way to graphene; among the first materials,  $\text{NbSe}_2$  and  $\text{MoS}_2$  can be named [11].

With the observation of an indirect-direct band gap transition that takes place when the  $\text{MoS}_2$  crystal is reduced to a SL limit due to quantum confinement, the scientific interest for studying the 2D TMDCs was also born in the 2010s [20, 21].

The most studied TMDC is molybdenum disulfide and it presents many electronic applications such as photoemitting devices [22], diodes [23], solar cells [24], memristors [25] and transistors [26, 27]. Much stronger spin orbit coupling occurs in tungsten disulfide than in the case of molybdenum disulfide, and all the properties just enumerated above for the case of  $\text{MoS}_2$  should be more stable at room temperature for the case of tungsten disulfide [28, 29, 30].

Recently, the metallic TMDCs have received an extensive attention due to the presence of both superconductivity (SC) and charge density wave (CDW) in SL  $\text{NbSe}_2$  [31]. There exist many potential applications of the 2D TMDCs, as well as different type of approaches to characterizing their electronic properties. A large area and high quality TMDCs crystal is required in order to study them. Therefore, this thesis introduces some methods for the

epitaxial growth of 2D TaS<sub>2</sub>/Au(111) down to its SL form. The structure of the TMDCs is characterized by the means of low energy electron diffraction (LEED), scanning tunneling microscopy (STM) and angle resolved photoemission spectroscopy (ARPES).

In summary, one should note that generally, due to the absence of the neighboring layers, thinning down layered materials reduces the screening compared to the bulk. Therefore, this can lead to a strong coulomb interactions and a large exciton binding energy [32]. Several TMDCs have various symmetry in their single and few layer forms. The lack of inversion symmetry in some 2D TMDCs give rise to new properties. A thin layer (SL) of materials is more sensitive to its environment than its bulk counterpart. The SL materials are also very sensitive to their substrates, which makes it possible to improve the desirable properties or to suppress the undesirable by using the appropriate substrate.

### 1.3 Molybdenum (MoS<sub>2</sub>) and Tungsten (WS<sub>2</sub>) Disulfide

Bulk MoS<sub>2</sub> can crystallise in either 2H (with space group P6<sub>3</sub>/mmc (D<sub>6h</sub><sup>4</sup>)) or 3R [33] polymorph structures. These two structures are identical in the SL structures and they only differ in stacking. The crystal structure of MoS<sub>2</sub> has trigonal prismatic coordination (see section 1.1). Its in-plane unit cell parameter is approximately 3.15 Å and its thickness is approximately 6.5 Å [34]. Although the interaction between the blocks X-M-X in the bulk TMDCs is quite weak, their electronic structure can be influenced by interlayer coupling. This can be seen in the electronic band structure calculations for bulk 2H-MoS<sub>2</sub> presented in Figure 1.3(c).

In the case of SL MoS<sub>2</sub>, the conduction band minimum (CBM) and valence band maximum (VBM) are located at the  $\bar{K}$  points of the hexagonal surface Brillouin zone (BZ) (see Figure 1.3(a)). Thus, SL MoS<sub>2</sub> is a semiconductor with direct band gap. The optical band gap size measured with photoluminescence (PL) measurements is equal to 1.9 eV [20, 36]. By contrast, in the case of bilayer MoS<sub>2</sub>, the extended nature of d<sub>z<sup>2</sup></sub> orbitals of molybdenum (Mo) results in a splitting of the bands at the  $\bar{\Gamma}$  point (see Figure 1.3(b)). Therefore, the VBM shifts to  $\bar{\Gamma}$  point, which makes bilayer MoS<sub>2</sub> an indirect band gap semiconductor (see Figure 1.3(b)). In the case of multiple layer MoS<sub>2</sub>, the CBM shifts into the middle point of the  $\Gamma$ - $K$  line. This is due to the interactions of S p<sub>z</sub> and Mo d<sub>z<sup>2</sup></sub> orbitals. In the bulk case, the band gap is indirect and its size is 1.3 eV [20, 33]. The spin orbit splitting of the VB at the  $\bar{K}$  point is observed in all cases (see Figure 1.3). In the SL materials, the splitting is totally

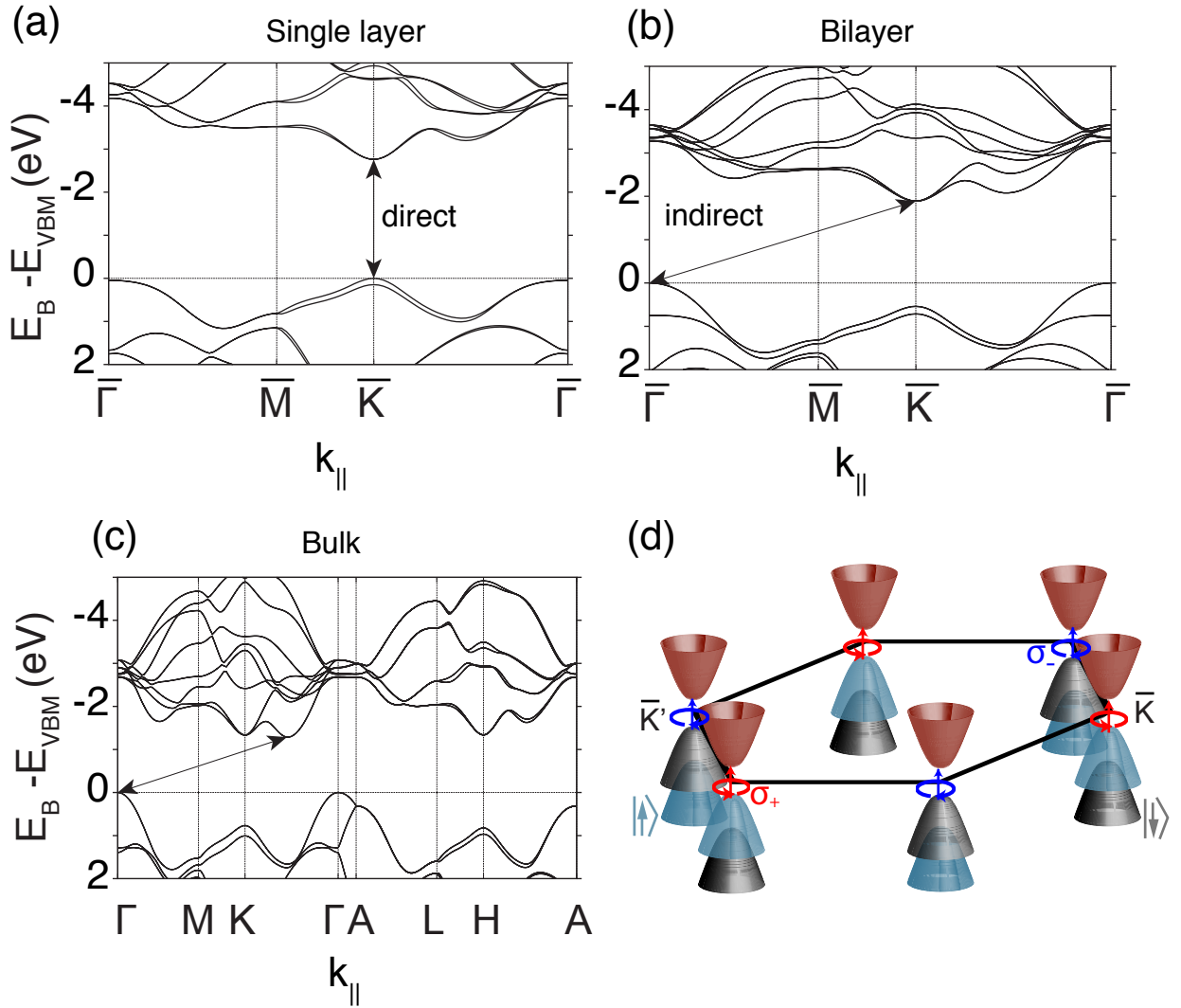


**Figure 1.3:** Electronic band structure of single layer (a), bilayer (b) and bulk (c) MoS<sub>2</sub> at high symmetry points ( $\Gamma$ ,  $M$ ,  $K$ ,  $A$ ,  $L$ ,  $H$ ), from DFT calculations. The valence band maximum is set at 0 eV. The arrow in each figure indicates the direct and indirect band gap. The direct band gap occurs at the  $K$  point for the single layer, unlike in the other cases. (d) schematic drawing showing the valleys and the optical selection rules for the SL MoS<sub>2</sub>. After Ref. [35].

due to the lack of inversion symmetry and to spin-orbit coupling (SOC) [35]. On the other hand, in the inversion symmetric bulk material, the splitting is due to the combination of the layer interactions and the SOC, and does not remove the spin degeneracy. A huge effect on the photoluminescence in the single layer limit has been noticed due to the change of the band gap character. Thus, the quantum yield of single layer MoS<sub>2</sub> photoluminescence was observed to be two (four) orders of magnitude greater for a single layer than for a double layer (bulk) [20]. There are two degenerate  $\bar{K}$  points—i.e.,  $\bar{K}$  and  $\bar{K}'$ —located at the edges of the BZ of SL MoS<sub>2</sub> (see Figure 1.3(d)). The conduction band is presented with the maroon

cones and it is almost spin degenerate, whereas, the valence band is spin split degenerate and turquoise (black) cones indicate bands with spin up (spin down). By using the different helicities of circularly polarised light [37], it is feasible to excite electrons into a precise valley (either the  $\bar{K}$  or  $\bar{K}'$  points) with a certain spin, due to the lifting of the spin degeneracy in the VB. Figure 1.3(d) schematically illustrates a selective excitation of electrons with spin down (up) by right-(left-) circularly polarized light with blue (red) arrows.

Since the dispersion of electrons, near the Fermi level carries important implications for the electronic and transport properties, it is useful to study their bands dispersion around the VBM. It should be noted that the fundamental physics for WS<sub>2</sub> is similar to that of the MoS<sub>2</sub>, both in the bulk and SL form. The band dispersions of SL MoS<sub>2</sub> and SL WS<sub>2</sub> for the valence band very close to the Fermi level are quantitatively similar (see the blue band dispersion in Figures 1.4(a) and 1.4(b) from density functional theory (DFT) calculations). The important difference between the two compounds is the spin orbit coupling, which leads to the different splitting of the spin split bands, as emphasized by the red rectangles in Figure 1.4. As a result of the larger SOC, the spin split energy difference of the VBM at the K point is approximately 145 meV for MoS<sub>2</sub> in comparison to 430 meV for WS<sub>2</sub>, and this can be seen in Figures 1.4(c) and 1.4(d) [35].

One can also expect that the strong spin orbit splitting of the bands leads to an increased band curvature near the top of the valence band, and thus to the reduced effective mass. For this reason, WS<sub>2</sub> should be the best candidate among all TMDCs for a field effect transistor, due to its low effective hole mass [38]. In addition, WS<sub>2</sub> with its large spin splitting can be a potential candidate in future spintronics applications [28].

## 1.4 Tantalum Disulfide TaS<sub>2</sub>

Tantalum disulfide (TaS<sub>2</sub>) belongs to the TMDCs of group 5. This group of materials presents a metallic character at high temperature due to the existence of an unpaired electron in the d-orbitals. Their crystal structure in the bulk has been determined with X-ray [39] and neutron [40] diffraction experiments. The metallic TMDC materials with group 5 (V, Nb, Ta) metals are usually rich in CDW phases [41]. A CDW can be defined as a periodic distortion of charge density in a periodic solid, which lowers the total energy of the system and possesses a spatial period characterized by the CDW wave vector [42]. The CDW appears below some onset temperature, and the periodic distortion of charge density occurs with the distortion

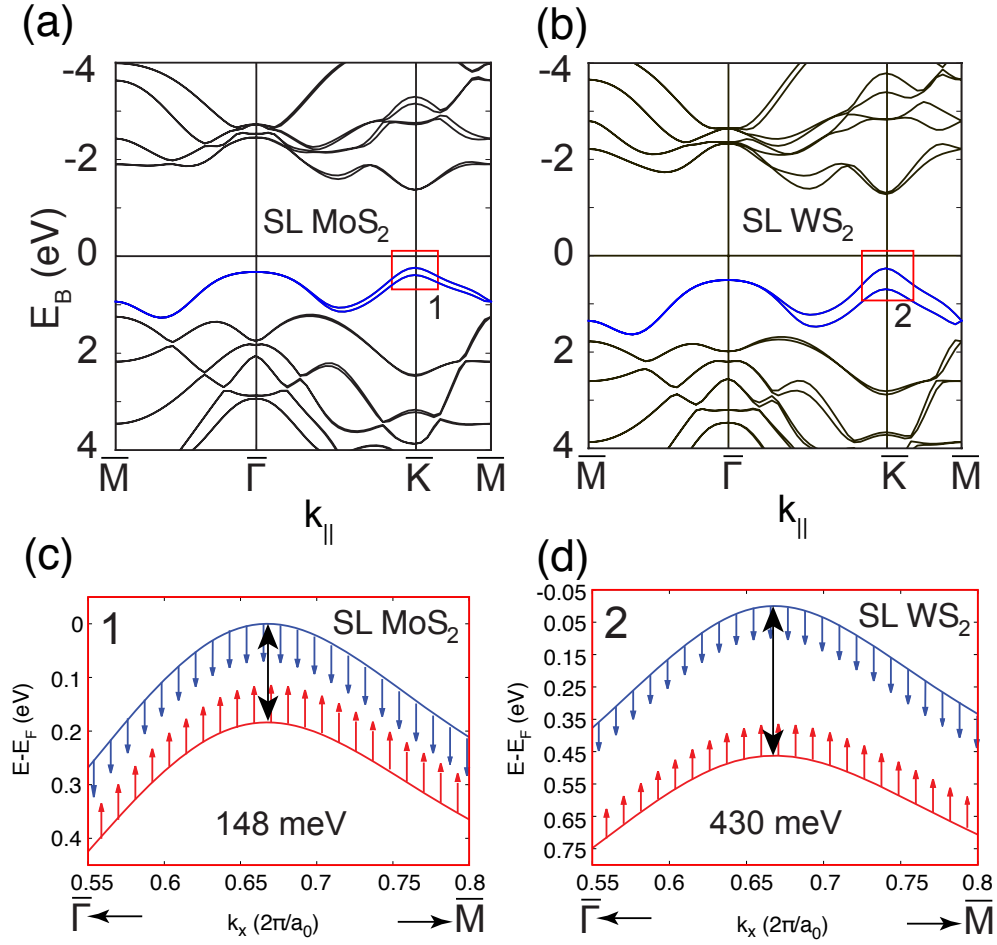


**Figure 1.4:** Electronic band structures of (a) SL MoS<sub>2</sub>, and (b) WS<sub>2</sub>, from DFT calculations. Details of the spin directions (see red and blue arrows) and the dispersion around VBM in the vicinity of the K point from DFT calculations for MoS<sub>2</sub> and WS<sub>2</sub>, respectively. The vertical black line with arrow on both ends shows the position of the K point. Figure based on Ref. [38]

of the crystal lattice.

### 1.4.1 Crystal Structure and Charge Density Waves in Tantalum Disulfide TaS<sub>2</sub>

TaS<sub>2</sub> crystallizes in either the 2H or the 1T polymorph structures (see Figures 1.1(c), 1.1(d)), like its neighbors the MoS<sub>2</sub> and WS<sub>2</sub> compounds. The unit cell parameter of 1H-TaS<sub>2</sub> is approximately 3.315 Å and its thickness is approximately 6.04 Å [43], while the unit cell parameter of 1T-TaS<sub>2</sub> is approximately 3.36 Å and its thickness is approximately 5.9 Å [43]. In the bulk form and at low temperatures, both 2H- and 1T- TaS<sub>2</sub> are subject

to electron instabilities, leading to metal-insulator transition with the appearance of CDW states, detectable by measurements of electronic transport [43, 44]. Bulk 1T-TaS<sub>2</sub> has been a typical system for CDW studies because of the presence of multiple CDW phases at different temperature ranges that even surpass room temperature. At temperatures greater than 543 K, the 1T-TaS<sub>2</sub> crystal is metallic and undistorted. Upon cooling, the first CDW phase to appear in the 1T-TaS<sub>2</sub> is incommensurate (IC) with a distorted bulk lattice [45], and this phase persists down to 347 K. Upon further cooling, the second CDW phase is nearly commensurate (NC) with respect to the underlying lattice and characterized by hexagonally ordered domains [46]. The NC phase persists from the onset temperature of 347 K down to 183 K, and is accompanied by an abrupt increase in resistivity. The commensurate (C) phase appear at temperatures lower than 183 K [47]. In this phase, 1T-TaS<sub>2</sub> is supposed to simultaneously undergo CCDW and Mott transitions [48, 49, 50]. A transition of a material from a metal to an insulator is known as Mott transition. An additional triclinic (T) phase (temperature above 223 K) occurs in the 1T-TaS<sub>2</sub> system after heating the sample from the commensurate phase, and the entire phase diagram presents an hysteresis with respect to the temperature [47]. The CCDW phase is characterized by a  $(\sqrt{13} \times \sqrt{13})R13.9^\circ$  superlattice (see Figure 1.5(a)). In this phase, the metal atoms form 13-atom clusters—the so-called star of David—in which sets of 12 atoms move inward toward a central 13th atom, driven by polaronic effects [47] (see orange arrows in Figure 1.5(a)). Other CDW phases have star of David reconstructions rearrange in different ways and more information about this will be given in chapter 3 together with detailed information on the occurrence of these phases.

On the other hand, the 2H-TaS<sub>2</sub> polymorph only develops one type of CDW phase, at temperatures lower than 75 K [44, 51]. Based on electron diffraction experiments, the CDW superstructure for the bulk 2H-TaS<sub>2</sub> is generally believed to be a  $3 \times 3$  distortion [44], where seven atom clusters are formed as shown in Figure 1.5(b). It was proposed by S. Sugai et al., based on Raman spectroscopy, that this distortion is incommensurate with the primitive lattice [52, 53, 54, 55]. Based on neutron diffraction, Moncton et al., proposed that the atomic displacement pattern in the 2H-TaS<sub>2</sub> CDW phase is similar to that shown by green arrows in Figure 1.5(b) [40].

Even though these materials have been intensively studied for the last five decades, the driving mechanism behind the formation of the CDW observed in these systems is still not fully understood. Many explanations of these mechanisms have been proposed, such as the simple one dimensional model of the Peierls transition [56], Fermi surface nesting [45], electron-phonon coupling [57, 58], and van Hove singularities (vHs) in the electronic

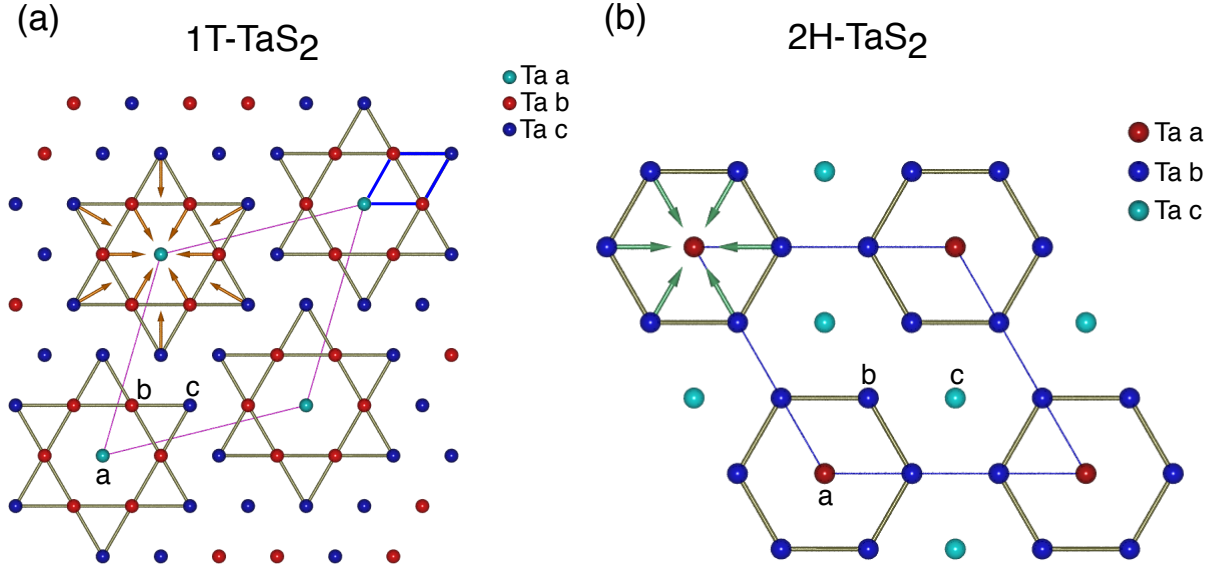


**Figure 1.5:** (a)  $(\sqrt{13} \times \sqrt{13})R13.9^\circ$  CDW superlattice of 1T-TaS<sub>2</sub>. The blue rhombus in the upper right corner indicates the unit cell of the Ta plane without the CDW. The formation of the Star of David cluster takes place with the presence of the CDW. The displacement of the Ta atoms is shown by the orange arrows. The pink solid line connecting the stars exhibits the new unit cell. (b)  $3 \times 3$  supercell of the CDW phase in 2H-TaS<sub>2</sub>. The direction of the displacement of Ta atoms is indicated by the green arrows. The blue diamond indicates the unit cell of the Ta plane with the CDW. Different colors in the illustrations of Ta atoms sites (a,b,c) in panel (a) and (b), were used to distinguish different inequivalent Ta sites in the supercell. These figures were created with Pov-Ray software [6].

structure, but the conclusive answer has still not been reached.

It is interesting to note that a competition of the CDW with low temperature superconductivity ( $<1$  K) was found in the 2H-TaS<sub>2</sub> compound [14]. Meanwhile, in 1T-TaS<sub>2</sub>, the CDW seems to coexist with superconductivity [59] at  $T_C = 1.5$  K [59] in the commensurate CDW phase. Little is known about how these interesting phenomena are affected by crystal dimensionality down to the 2D limit. Recently, it has been shown that the metallic 2H-NbSe<sub>2</sub>, undergoes a CDW instability in both its bulk and single layer form [31]. Moreover, the superconductivity also persists in the 2D limit but with the suppression of the  $T_C$  from  $T_C$  (bulk) = 7.2 K [60] to  $T_C = 1.9$  K in its SL form. Therefore, the very small amount of research done on SL metallic TMDC, was one of the main motivations to synthesize and study TaS<sub>2</sub> in its SL limit in this thesis [31].

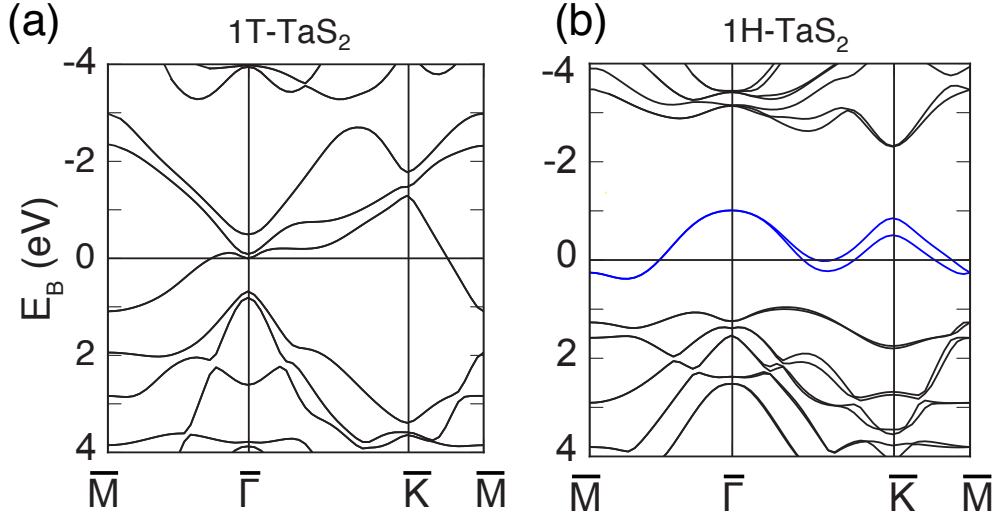


**Figure 1.6:** Electronic band structure of (a) 1T-TaS<sub>2</sub> and (b) 1H-TaS<sub>2</sub>, respectively from DFT calculations.

### 1.4.2 Electronic Structure of Tantalum Disulfide TaS<sub>2</sub>

Figures 1.6(a) and 1.6(b) present the theoretical band structures of SL 1T-TaS<sub>2</sub> and 1H-TaS<sub>2</sub>, respectively, using DFT calculations. These DFT calculations of the theoretical bands were performed by Albert Bruix Fusté in Aarhus University. The topmost valence band with the blue color in Figure 1.6(b) looks very similar in shape to those presented in Figures 1.4(a) and 1.4(b). The main differences are the splitting size (0.348 eV [61]) of the bands around the  $\bar{K}$  point and also the binding energy of the bands. Furthermore, the band dispersion of SL 1H-TaS<sub>2</sub> is strongly similar to the dispersion of heavily p-doped SL WS<sub>2</sub>. Figure 1.6 will be later used in chapter 4 to compare our measured band structure of TaS<sub>2</sub> obtained after the synthesis and measurement with ARPES.

In the literature, there are many calculated band structures of bulk 1T-TaS<sub>2</sub> from DFT, especially in the C-CDW and normal phases [62, 63, 64, 65]. For the C-CDW phase, there is a good agreement between the DFT calculations and ARPES band structure results along the covalently bonded crystal planes. This is especially true for the presence of gaps located at  $\Gamma$  and between the high symmetry points  $M$  and  $K$ , which are the Mott gap and CDW gap, respectively [63, 64]. For the normal phase, we present in chapter 3 the first ARPES study along the covalently bonded crystal planes, which is in perfect agreement also with the theory presented in Ref. [62, 65].

In addition, less is known from DFT band calculations of bulk 1T-TaS<sub>2</sub> in the NC-CDW

and IC-CDW phases. Therefore, the study of the band structure of bulk 1T-TaS<sub>2</sub> along the crystal plane acquired in the NC-CDW and IC-CDW phases is also presented in chapter 3. We will then compare our results with the existing experimental band structures not taken at the same temperature but in the range of NC-CDW and IC-CDW phases.

Furthermore, many calculations predict the formation of a one dimensional metallic band along the high symmetry direction  $\Gamma$ - $A$  of the BZ in the ground state CDW of 1T-TaS<sub>2</sub> [63, 66]. Nevertheless, no experiment has investigated the three-dimensional (3D) character of the band structure of bulk 1T-TaS<sub>2</sub>. In this thesis, we also present in chapter 3, a study of the 3D character of bulk 1T-TaS<sub>2</sub> in four different phases i.e., at the commensurate, nearly-commensurate, incommensurate and normal phase. This was done using high-quality crystals by determining the band structure along the direction perpendicular to the crystal planes of 1T-TaS<sub>2</sub>, with the main focus on the possible metallicity of the compound in the perpendicular direction.

## 1.5 Thesis Structure

The remainder of this thesis is organized as follows.

**Chapter 2** is devoted to the experimental techniques: scanning tunneling microscopy (STM), low energy electron diffraction (LEED), angle resolved photoemission spectroscopy (ARPES) and x-ray photoelectron spectroscopy (XPS). These techniques were used to acquire the majority of data presented in this thesis. The emphasis is placed on the physics underlying the ARPES technique. A brief discussion of the basic physics behind the LEED and STM techniques is presented. A very brief discussion of XPS is also included in this chapter. The setup of the SGM3 beamline and endstation is also presented, as well as a brief presentation of ASTRID2.

**Chapter 3** presents the study and the comparison of the electronic structure of the 3D dispersion of bulk 1T-TaS<sub>2</sub> at different temperatures. The recent band structure calculations of bulk 1T-TaS<sub>2</sub> have predicted the coexistence of the CDW with a nearly one-dimensional metallic dispersion perpendicular to the crystal planes. We have shown by mean of synchrotron radiation based ARPES that this metallic band indeed exists.

**Chapter 4** describes the methods used to synthesis the SL- and few-layer TaS<sub>2</sub>. This chapter also explores the electronic structures of these types of samples. The electronic structure of

---

SL TaS<sub>2</sub>/Au(111) is compared to the DFT calculations. The suppression of the CDW in SL TaS<sub>2</sub>/Au(111), as revealed by low temperature STM/STS, is also presented and discussed. These samples were characterized using ARPES, STM and LEED techniques.

**Chapter 5** presents the study of the electron-phonon coupling in 2D TMDCs such as MoS<sub>2</sub>/Au(111), WS<sub>2</sub>/Au(111) and TaS<sub>2</sub>/Au(111). This chapter also demonstrates that the large difference of the electron-phonon coupling in the two spin-split branches observed at the high symmetry point  $\bar{K}$  of the SL WS<sub>2</sub>/Au(111), as well as on SL MoS<sub>2</sub>/Au(111) and 1H-TaS<sub>2</sub>/Au(111), even remains in the presence of a strongly interacting substrate.

**Chapter 6** gives the conclusion of our study and suggestions for future work.

---

# Experimental Techniques

---

## 2.1 Introduction

While various types of measurements have made relevant contributions to the understanding of the 2D and 3D TMDCs, the angle resolved photoemission spectroscopy (ARPES) technique gives the most direct measurements of the momentum-resolved electronic band structure of solids. Low energy electron diffraction (LEED) measurements give information on the overall surface quality and order, and also allow quantitative surface determination. The scanning tunneling microscopy (STM) technique offers local and real space information of the sample surface at the atomic level, and is, therefore, a perfect complement to the LEED technique.

It is not our aim in this chapter to give a full review of these three techniques; we will rather give a broad overview of these techniques. The physics underlying the LEED technique is given in section 2.2. Section 2.3 presents the STM technique, followed by a description of the ARPES technique in section 2.4. This section will also present the description of the setup used in order to acquire the ARPES data presented in this thesis.

## 2.2 Low Energy Electron Diffraction

The pertinent information presented in this section is mainly taken from reference [67]. One of the most common techniques for surface characterization is LEED. This technique is used to study the surface structures of crystalline materials, as well as to make quantitative structure determination [67]. LEED is based on elastic diffraction of low energy electrons from the surface. This technique probes only the region close to the surface due to the low energy range ( $\sim 20\text{-}500$  eV) and the corresponding short inelastic mean free path [68] ( $\sim 5\text{-}10$  Å) of the electrons used (see Figure 2.1(a)). Thus, this technique is highly surface sensitive. The inelastic mean free path (IMFP) denotes the average distance traveled by an electron between inelastic collisions. The IMFP of the electrons in a solid does not depend strongly on the chemical identity of the solid, but rather on the kinetic energy of the electrons. For this reason, the curve of the IMFP versus the kinetic energy possesses an universal behavior since the graph of the IMFP versus electron kinetic energy from the calculations (red dashed curves) and measurements (dots) follow the same trend (see Figure 2.1(a)). This means that these curves have a broad minimum kinetic energy around  $\sim 70$  eV and IMFP of  $\sim 5$  to  $10$  Å (see the light red shaded area in Figure 2.1(a)).

Figure 2.1(b) shows a typical LEED optics. This setup consists of two essential components: namely, an electron gun and a detector. The electron gun generates a beam of low energy monochromatic electrons which is incident on the crystal surface probed. It is possible to control the angle between the crystal surface and the electron beam. A detector system detects scattered electrons and it is constituted of four metal grids at different voltages, and a fluorescent screen. The first grid (the closest to the sample) is generally at ground potential to ensure a field free region around the sample, which is also grounded. The two middle grids are set to the retarding voltage ( $E_r$ ). The value of this voltage is a little bit lower than the kinetic energy of the electrons produced by the electron gun. This is so just to let pass only elastically scattered electrons, because almost all inelastically scattered electrons are repelled by these grids. The elastically scattered electrons finally pass through the next grid which is fixed to the ground potential and are then accelerated toward the fluorescent screen at a high positive voltage ( $E_s$ ) [67]. Once the elastically scattered electrons hit the screen, they give rise to a pattern of intense spots that creates an image that can be seen by naked eye. In front of the screen, a viewport in the vacuum system allows LEED patterns to be observed by eye and recorded with a camera. It is essential to know that the whole LEED system is enclosed inside a ultrahigh vacuum (UHV) chamber.

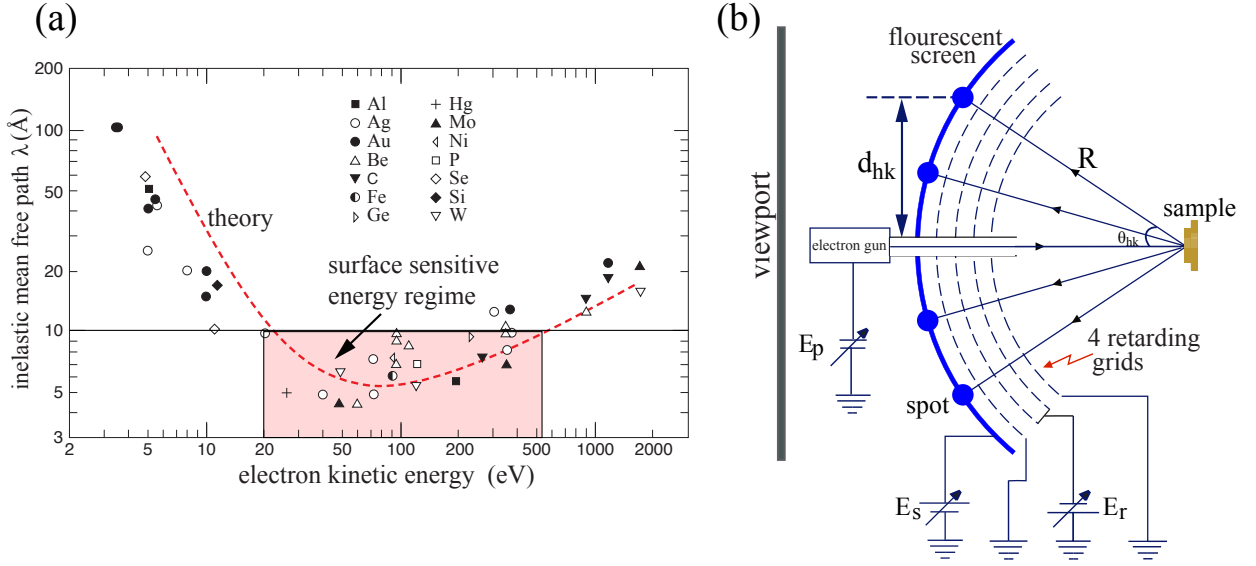


**Figure 2.1:** (a) The universal curve of electron mean free path for the inelastic scattering of electrons in a solid as a function of electron kinetic energy. The red dashed curve and the dots are calculations and measurements, respectively. (b) Schematic of a conventional LEED system. The two figures were reproduced from Ref. [67].

This technique is based on the electron diffraction phenomenon. The diffraction conditions for a 2D lattice, for electrons coming to the sample surface at a normal incidence, i.e.,  $k_i^{\parallel} = 0$ , are given by the Laue conditions as follows:

$$\Delta \mathbf{k}_{\parallel} = \mathbf{k}_s^{\parallel} - \mathbf{k}_i^{\parallel} = \mathbf{k}_s^{\parallel} = h\mathbf{b}_1 + k\mathbf{b}_2,$$

where  $h, k$  are integers,  $\mathbf{b}_1$  and  $\mathbf{b}_2$  are 2D reciprocal lattice vectors, and  $\mathbf{k}_i^{\parallel}$  and  $\mathbf{k}_s^{\parallel}$  are incident and scattered electrons wave vectors parallel to the surface, respectively.  $\mathbf{k}_i^{\parallel} = 0$  in the case of LEED, since incident electrons are coming to the surface at normal incidence.

Knowing  $\theta_{hk}$ , which is the angle between the sample normal vector and the scattering vector to one of the spots in the diffraction pattern, together with the magnitude of the scattering electrons  $|\mathbf{k}_s|$  (see Figure 2.1(b)), it is possible to express the emission angle  $\theta_{hk}$  to the surface reciprocal lattice vector  $h\mathbf{b}_1 + k\mathbf{b}_2$ :  $\sin \theta_{hk} = |h\mathbf{b}_1 + k\mathbf{b}_2|/|\mathbf{k}_s|$ . The position of the diffraction maxima on the viewport ( $d_{hk}$ ), from Figure 2.1(b) is given by:

$$d_{hk} = R \sin \theta_{hk} = R \frac{|h\mathbf{b}_1 + k\mathbf{b}_2|}{|\mathbf{k}_s|} = R \frac{\hbar}{\sqrt{2m_e}} \frac{1}{\sqrt{E}} |h\mathbf{b}_1 + k\mathbf{b}_2|, \quad (2.1)$$

where  $R$  is the distance between the sample and the screen (see Figure 2.1(b)), and  $|\mathbf{k}_s|$  can be obtained from the expression of the kinetic energy  $E$  ( $E = \frac{\hbar^2 |\mathbf{k}_s|^2}{2m_e}$ ) of a free electron.

From equation 2.1, it is easy to see that by increasing the kinetic energy of electrons ( $E$ ), the visible spots will move closer to the center of the viewport. Thus, the spots that are invisible at lower kinetic energies, on account of having large scattering angles  $\theta_{hk}$ , will move onto the screen's edge when the kinetic energy is increased. Furthermore, it is possible to calculate the reciprocal lattice vectors  $\mathbf{b}_1$  and  $\mathbf{b}_2$  associated with the sample from the measured LEED pattern and equation 2.1. In case the surface is covered by adsorbates or has many defects, the LEED spots become diffuse or yet fully extinguished [69]. On the other hand, adsorbates form periodic structures from which extra LEED spots will be observed. One can determine from the position and shape of the LEED, the orientation of the adlayer with respect to the substrate and get information about superstructures, like moiré patterns. The information about the existence of different domains of the sample crystal can also be obtained from the LEED technique. In case of multiple rotational domains on the surface of the sample, one will observe multiple reciprocal lattice rotated with respect to each other, or a ring or elongated LEED spots if the sample is rotationally disordered.

The LEED is a powerful technique for characterisation of 2D and 3D materials because it enables a very fast qualitative determination of orientation, coverage, quality, periodicities, symmetry and the presence of superstructures of the sample crystal. Detailed quantitative analysis is also possible. For example, the intensity of different diffracted beams as a function of incident electron kinetic energy can be measured in order to generate I-V curves. Thus, one can compare these curves with sophisticated multiple-scattering calculations for a model system [67]. One then needs to change the model parameters until there is a good accord between the I-V curves and the modeling curves.

LEED data presented in this thesis were mainly used for qualitative analysis of the surface structure, and were mostly acquired using rear-view LEED optics, with a flange-sample distance of 254 mm and 4 retarding grids.

## 2.3 Scanning Tunneling Microscopy

The scanning tunneling microscopy (STM) technique is capable of real-space imaging of surfaces at resolution up to the atomic level. This technique is based on the quantum mechanical tunneling phenomenon. From the STM data or STM images, information about the surface topography of the sample can be obtained, as well as the information about the position-dependent local density of states of the sample close to the Fermi energy. Many

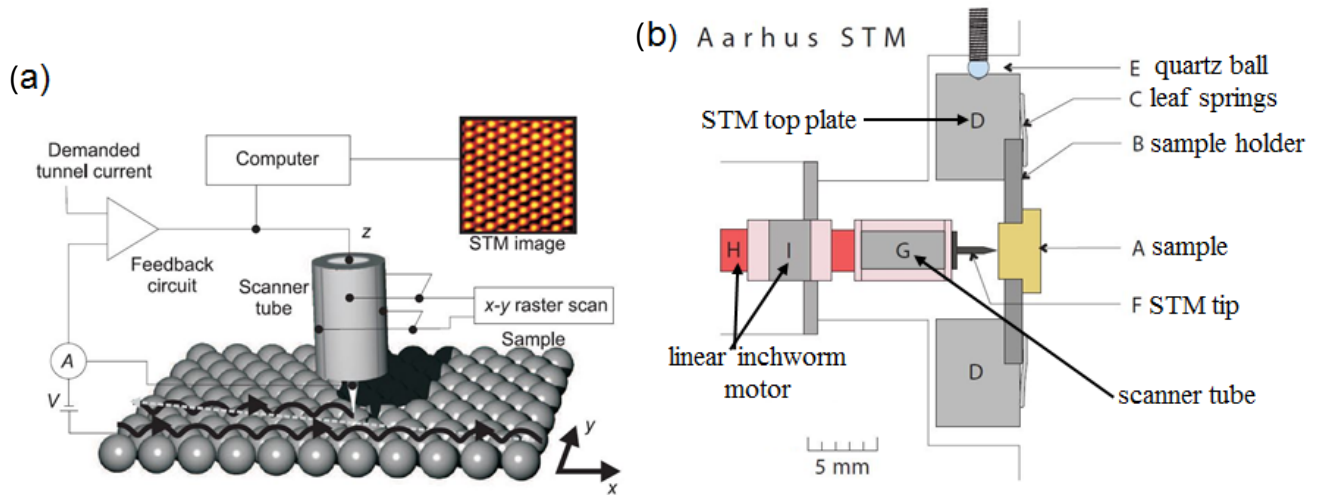


**Figure 2.2:** Schematic of the working principle of STM technique. a) The tip is raster-scanned over the  $xy$  surface of the sample with a scanner tube. During a scan in constant current mode, the tunneling current between the tip and the surface is kept constant by a feedback loop that applies voltage to a piezo that controls the  $z$  position (height) of the tip above the surface. An STM image is recorded as  $xy$ -position-dependent changes in the extension of the  $z$  piezo. b) The design of Aarhus-type STM. Figures (a) and (b) were taken from Ref. [72].

topics can be studied by this technique, ranging from the surface topography and electronic properties to film growth (by tracking adsorption process and observing chemical reactions at surfaces) to molecular manipulation [70]. STM was developed by Binnig and Rohrer [71], who in 1986 received the Nobel prize for their work.

A common STM is composed of a very sharp tip, which can be brought to the vicinity ( $\sim 5$  Å) of the surface as shown in Figure 2.2(a). This small distance allows the wave functions of the tip and the sample to overlap, to allow the electrons to quantum mechanically tunnel through the vacuum gap between the tip and the surface. By applying a small bias voltage ( $V_t$ ) between the STM tip and the sample, the electrons from the filled states in the tip will tunnel to the empty states in the sample or vice versa, resulting in the measurable tunneling current  $I_t$ . This tunnelling current is a function of the tip-surface separation  $d$ ,

$$I_t \propto V_t \cdot \exp\left(-\frac{\sqrt{8m_e\Phi}}{\hbar}d\right); \quad (2.2)$$

where  $V_t$  is the tunnelling voltage,  $m_e$  is the mass of the electron,  $\Phi$  is the average work function of the tip and sample,  $d$  is the tip-surface separation [73, 74].

For typical values of metallic work functions between 4 and 5 eV, the expression of the tunneling current  $I_t$  given by equation 2.2 decays approximately one order of magnitude when the tip-surface separation  $d$  is increased by 1 Å. Thus, electrons effectively tunnel only

through the apex atom of the tip, enabling atomic resolution during the scan of the surface of the sample.

The working principle of the STM technique is shown in Figure 2.2(a). It should be noted that there are two common STM operating modes, the so-called constant height and constant current modes, but we will focus more on the constant current mode since it is the most commonly used mode. Generally in experiments, the tip is raster-scanned over the surface in the  $xy$  plane by the action of piezoelectric transducer motors in the scanner tube. The movement of the tip is proportional to the applied voltage. In the constant current mode, the tip moves up and down (in the  $z$  direction) by means of a feedback loop in order to maintain a constant tunneling current while the tip is scanning across the surface. Thus, an image is obtained by recording the  $z$  positions of the tip. The resulting image reflects the topography of the surface atoms, as well as the local density of states (LDOS) of the sample convoluted with the LDOS of the tip is measured. By reversing the sign of the applied tunnelling voltage  $V_t$ , one can probe with STM both the occupied and the unoccupied states of the sample. It is important to vibrationally isolate the STM due to the necessity of sub-Ångstrom stability to achieve atomic resolution. This can be done for example by lowering the transmission of the environmental vibration by using suspension springs and a damping mechanism [75, 76]. It is more difficult to achieve atomic resolution with STM on metals than on semiconductor surfaces. This is due to the higher degree of corrugation on the semiconductors caused by the presence of directional bonds. This directional bonding makes the interpretation of STM images from the semiconductor surfaces as a pure atomic structure more difficult than on metal surfaces. Thus, one has to be prudent when interpreting the images from STM. In the case of a small tunneling voltage in the constant current mode, the STM image can exhibit the LDOS at the Fermi energy to an even greater degree than the true topography. In case where there are adsorbates on the surface, their appearance will rely on how the LDOS at the Fermi energy is varied. If the adsorbates decrease the LDOS, they will appear as holes, while if the adsorbates increase the LDOS, they will appear as protrusions. It will not be possible to observe the adsorbates in case they do not affect the LDOS.

Detailed local information about the electronic LDOS is provided by scanning tunneling spectroscopy (STS). In STS measurements,  $dI_t/dV_t$  curves are recorded by sweeping the applied voltage and keeping the tip-sample distance (i.e.,  $z$  position) and tip lateral position constant an accurate calibration and a careful analysis of the results is required. This measurement, performed at various locations on the sample surface, provides the spatially resolved LDOS of the sample as a function of voltage, thus giving information about the

electronic structure of the sample. Both the unoccupied and occupied states can be probed by varying the sign of applied voltage. From STS measurement, one can also get the information about the band gap value for semiconducting samples [77].

STM experiments can be performed in different atmospheres, but they are most generally performed in UHV. The operating temperature for STM technique can range, depending on the design of the STM system, from close to absolute zero to hundreds of Kelvin [75, 76]. It should be noted that the chemical composition of the tip and its interactions with the sample can influence the tunneling process. The chemical forces have a deep effect on the tunneling current even for very small tip-sample distances.

The STM data presented in this thesis were obtained by using an Aarhus-type STM [78, 79, 80, 81] setup mounted in a UHV chamber. Figure 2.2(b) shows the design, with labels showing some principal parts of a typical Aarhus-type STM. Aarhus-type STM is a very compact design mounted to the vacuum chamber directly on a flange. This setup is not suitable for very low temperatures, but cooling is however possible with liquid nitrogen. All the STM data obtained from this setup and presented in this thesis were obtained at room temperature. The rough approach of the tip (F) to the surface of the sample, in preparation for scanning, is realized by a linear inchworm motor (H,I) constituted of a piezoelectric tube with the three segments of electrodes clamped on a SiC rod. The tip is mounted at the end of the piezoelectric scanner tube (G). The tip used in order to acquire the data presented in this thesis is made up of pulled tungsten wire. The proper biasing of segments of the motor ensures the clamp/unclamp motion of the outermost segments, whereas the middle section expands/contracts the rod during the approach. The precise motion of the tip during the scanning is realized by the piezoelectric tube. A set of three quartz spheres (E) ensure both electrical and thermal insulation of the top plate. The sample (A) is maintained in a sample holder (B) that is fixed in place by springs (C) that hold the sample firmly to the STM body (D). During the measurement, the entire STM is floating on light springs in order to highly decrease the mechanical noise. For more information about the Aarhus-type STM, the reader can consult Ref. [82].

It should be noted that the Aarhus-type STM setup used for this project is mounted at the SGM3 end station, which will be described in more details in section 2.4, in the proximity of the synchrotron ASTRID2. Therefore, this neighboring synchrotron generates some electrical noise problems that cannot be easily resolved.

Where noted, additional STM measurements at low temperature by the collaborating group

of Prof. Alexander Khajetoorians (Radboud University) [83] were performed. For the characteristics of their machine, the sample is cooled to liquid He temperature (4.7 K) with a static bath cryostat and a home-built STM head based on an Omicron design.

## 2.4 Angle Resolved Photoemission Spectroscopy

ARPES is an extensively used experimental technique for measuring the electronic structure of materials in a direct way. With recent developments of the photoemission spectroscopy technique, ARPES allows extremely high precision measurements of the energy and angular distribution of photoelectrons. This technique provides detailed information on the shape and size of the Fermi surfaces and electronic band structures of materials. Moreover, ARPES has afforded great insight into high-temperature superconductors [85], correlated materials including Mott insulators [86, 87, 88], and many-body interactions that govern the occupied electronic states in a crystal such as electronic correlations and electron-phonon coupling. Furthermore, the spectrum measured by ARPES provides the one-electron spectral function of the material, giving a true mixture of information on the single-particle excitations.

This section presents in detail the underlying physics of ARPES relevant for understanding results presented in subsequent chapters of this thesis. The discussion of many-body effects such as electron-phonon coupling that are relevant to the interpretation of the data presented in Chapter 4 will be also given. The description of the experimental setup used to acquire the electronic structure of all samples studies in this thesis is presented in section 2.4.6.

### 2.4.1 Photoemission Spectroscopy

The basic physical principle behind all the myriad photoemission (photoelectron) spectroscopy techniques is the photoelectric effect. The photoelectric effect is the process where electrons from the surface of a material are ejected to energy levels above the vacuum energy level after they have been excited by incoming photons of sufficient energy (see Figures 2.3(a) and 2.3(b)). This effect was initially discovered in 1887 by Hertz [89], and later explained by Einstein [90] who, in 1921, was awarded a Nobel prize for his work.

The photoemission process is frequently described by a simplified, three-step model, which is schematically presented in Figure 2.3(b). In the first step, electrons are excited from the initial to the final state due to an interaction with a photon. The kinetic energy of

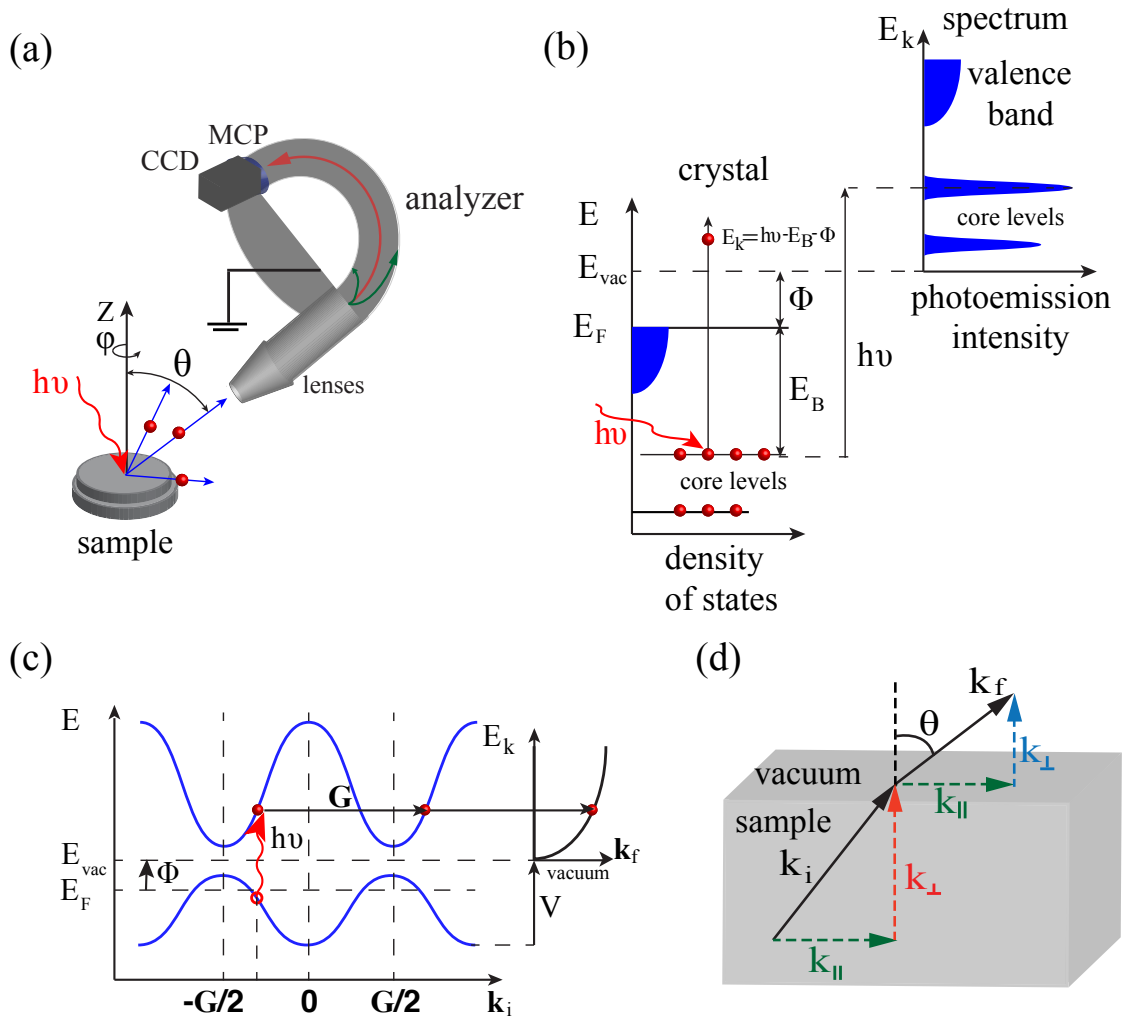


**Figure 2.3:** (a) Schematic of a typical experimental realization of ARPES: the emission direction of the photoelectrons is described by the azimuthal ( $\varphi$ ) and polar ( $\theta$ ) angles, respectively. These photoelectrons are then focused by electrostatic lenses onto the entrance slit of the hemispherical analyzer. Applying an electric field between the two hemispheres changes the electron's trajectory depending on its incoming kinetic energy until it reaches the detector. Afterwards, the photoelectrons are captured by the multichannel plates (MCP) that multiply the number of filtered electrons. Finally, the electrons strike a fluorescence phosphorous screen mounted behind the MCP. A CCD camera captures the image on the phosphorous screen. (b) The energy diagram for the photoemission process [84]. An electron in a solid (red sphere) is excited by a photon energy  $h\nu$ . The kinetic energy of the photoelectron is given as a function of the excitation energy ( $h\nu$ ), the binding energy ( $E_B$ ) and the work function of the material ( $\Phi$ ). (c) The kinematic scheme of the photoemission process in the dispersing valence band region within the three step model [84]. An electron from the valence band in a solid is excited with a direct optical transition. The momentum provided by the lattice makes it possible to associate the wave function with a free electron final state in the vacuum. The potential step  $V$  models the surface. (d) Schematic showing the initial and final momentum vectors of the photoemission process inside the solid and outside the solid (i.e., in vacuum). The component perpendicular to the surface is not maintained, while the parallel component is maintained.

the photoemitted electrons is obtained from the energy conservation law and satisfies the expression

$$E_k = h\nu - E_B - \Phi, \quad (2.3)$$

where  $h\nu$  is the photon energy and  $\Phi$  is the work function of the material (and its value is usually between 4 and 5.5 eV).  $E_B$  is the electron binding energy inside the solid. Equation 2.3 shows that the photon energy needs to be greater than the work function  $\Phi$  for photoemission to occur.

In the second step, the excited electron travels to the surface, and may get scattered. The background in the observed spectrum results from the contribution of the inelastically scattered electrons. UV light ranging from 5 to 100 eV is generally used for ARPES measurements. In this energy range ( $E_k \propto h\nu$ ), the IMFP (see Figure 2.1(a)) has values of only a couple of Ångstroms (5 - 30 Å). Therefore, only electrons close to the surface are effectively probed and this is the reason for the surface sensitivity of this technique. By tuning the photon energy, it is possible to reduce or enhance the bulk (surface) sensitivity. The use of the light in the X-ray regime (usually ranging from 0.1 to 2 keV) makes it possible to excite the electrons of the non-dispersing core levels of an atom. Thus, XPS gives important information on the chemical composition and atomic environments found in the material under study.

In the third step, the photoelectrons are transmitted into vacuum through the surface potential barrier. The wave function of the final state must match a free-electron state in the vacuum. The crystal potential gives to the electron the additional momentum it requires to reach the excited state, so that this momentum comes in multiples of the reciprocal vectors  $\mathbf{G}$ . The vertical transitions in the reduced-zone scheme ( $\mathbf{k}_f = \mathbf{k}_i$ ) are described by optical transitions in a crystal. It is helpful to describe the photoemission process in the extended-zone scheme ( $\mathbf{k}_f = \mathbf{k}_i + \mathbf{G}$ ), as exhibited in Figure 2.3(c). In addition, the surface gives a boundary condition that breaks the translational symmetry of the emitted electrons only in the perpendicular direction to the surface ( $\mathbf{k}_\perp$ ) and  $\mathbf{k}_\perp$  is not a good quantum number for the system near to the surface because of the destroyed periodicity. Therefore, only the parallel component ( $\mathbf{k}_\parallel$ ) is conserved during this step (see Figure 2.3(d)).

One can measure the out-coming polar ( $\theta$ ) and azimuthal ( $\varphi$ ) distributions angles and the kinetic energy  $E_k$  of the photoelectrons from ARPES in order to extract information about the crystal momentum of the electrons. By neglecting the momentum of a photon and assuming the free-electron dispersion in vacuum for the final state, one can derive from the

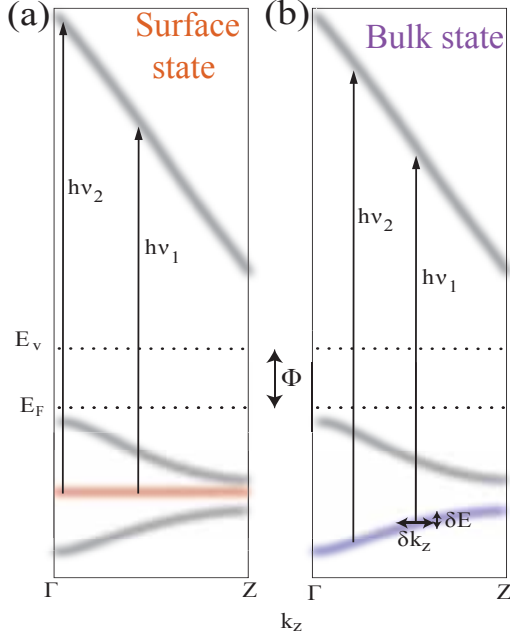


**Figure 2.4:** Schematics of the photoemission process: (a) for a surface state and (b) for a bulk state.  $E_V$  is the vacuum level,  $E_F$  is the Fermi level, and  $\Phi$  is the work function. The dispersion of these two different states as a function of wave vector  $\mathbf{k}_z$  perpendicular to the surface is exhibited in these two panels. The binding energy for the surface state (distance from  $E_F$ ) does not depend on the photon energy  $h\nu$  due to the fact that the dispersion of the surface state does not depend on  $\mathbf{k}_z$ . The position of bulk states measured with different photon energies appears at different binding energies in the spectrum, because the bulk state shows the dispersion with different photon energy  $h\nu$ . The broadening of  $\delta k_z$  is due to a not well defined  $\mathbf{k}_z$ , which is then reflected in an expansion of energy  $\delta E$  of the observed peaks. Figure adapted from Ref. [91].

simple geometrical consideration, the parallel ( $\mathbf{k}_{\parallel}$ ) and perpendicular ( $\mathbf{k}_{\perp}$ ) momentum vector components as follows:

$$\mathbf{k}_{\parallel,i} = \mathbf{k}_{\parallel,f} = \frac{1}{\hbar} \sqrt{2m_e E_k} \sin \theta (\hat{\mathbf{x}} \cos \varphi + \hat{\mathbf{y}} \sin \varphi), \quad \mathbf{k}_z = \mathbf{k}_{\perp}^f = \frac{1}{\hbar} \sqrt{2m_e E_k} (\hat{\mathbf{z}} \cos \theta); \quad (2.4)$$

where  $E_k$  is the kinetic energy of the photoemitted electron.  $\theta$  is the polar angle, i.e., the angle between the surface normal and the trajectory of the photoemitted electron.  $\varphi$  is the azimuthal angle (see Figure 2.3(a)). For 2D systems, the electronic structure is approximately determined by  $\mathbf{k}_{\parallel}$ , and thus the uncertainty in  $\mathbf{k}_{\perp} = \mathbf{k}_z$  is less relevant. But for the 3D systems, this is not the case. The information regarding the  $\mathbf{k}_z$  dispersion can be obtained by collecting the photoemission intensity in normal emission (i.e., at  $\mathbf{k}_{\parallel} = 0$ ) as a function of binding energy ( $E_B$ ) and photon energy ( $h\nu$ ) [84] and then convert the photon energy axis to  $\mathbf{k}_z$ . The expression of  $\mathbf{k}_z$  will be derive further below. Nevertheless, for the 2D SL TMDCs presented in this work, equations 2.3 and 2.4 constitute a good recipe for the transformation  $I(\theta, \varphi, E_k)$  to  $I(\mathbf{k}_{\parallel}, E_{bin})$  which can be regarded in the first approximation as the measured electronic band structure.

When taking a measurement at the normal emission, where the spectrometer looks along

the sample surface normal (i.e., at  $\theta = 0$ ),  $\mathbf{k}_{\parallel} = 0$  and  $\mathbf{k}_{\perp} \neq 0$ . It is also straightforward to see from equation 2.4 that changing the photon energy and hence the kinetic energy does not modify  $\mathbf{k}_{\parallel}$ . On the other hand, the measured perpendicular vector of the momentum  $\mathbf{k}_{\perp}$  depends on the kinetic energy and the photon energy used. Therefore, these two relations (see equation 2.4) provides a good way to distinguish the two dimensional (2D) states from the three dimensional states (3D). Figure 2.4(a) presents the dispersion of a bulk initial state, a surface state and a final state as a function of  $\mathbf{k}_z$ . The surface state energy does not depend on  $\mathbf{k}_z$ , due to its two dimensionality, while the two other states disperse in  $\mathbf{k}_z$ . In the photoemission process, the permissible value of  $\mathbf{k}_z$  for the transition from the initial state to the final state is determined by the photon energy during the excitation of the electrons from occupied initial states into the unoccupied final states. For the surface state, the measured binding energy of the photoemitted electron with respect to the Fermi energy level does not depend on the photon energy, while the kinetic energy of the photoemitted electron does. The absence of dispersion as a function of photon energy is a necessary condition for the identification of a state as a surface state. Thus, using different photon energies to probe the 2D band always results in the same binding energy.

On the other hand, in the 3D bulk state, photons with different energies probe the states at different  $\mathbf{k}_{\perp}$  and the observed binding energy alters. Figure 2.4(b) illustrates the photoemission from the bulk at different photon energies. As already mentioned above, the perpendicular component of the momentum is not conserved across the sample surface due to the sudden change of potential along the  $z$  direction (i.e.,  $\mathbf{k}_{\perp}$  is a good quantum number only in the depth of the solid), which means that the expression of  $\mathbf{k}_{\perp}$  given in equation 2.4 is not valid in this case. It should be noted that equation 2.4 is valid when one views it as the expression of  $\mathbf{k}_{\perp}$  of the electron outside the surface. Moreover, the momentum vector  $\mathbf{k}_{\perp}$  in this case carries an uncertainty that is reflected as a spectral function broadening of the band, which makes the bulk bands generally broader than the surface states. This broadening can be observed in both energy and momentum directions. An energy broadening  $\delta E$  is observed in the dispersion due to the fact that the bulk state disperses in the  $\mathbf{k}_z$  direction. Furthermore, both a  $\mathbf{k}_z$  broadening  $\delta k_z$  as well as an energy broadening  $\delta E$  are due to the finite escape depth of the photoelectron [91] (see Figure 2.4(b)). It should be noted that even if this is a convenient way to distinguish surface to bulk states, one must remember that sometimes bulk states have zero or small  $\mathbf{k}_{\perp}$  dispersion, particularly in layered materials, and can be misinterpreted as surface states.

As mentioned above, for the 3D bulk states, the final  $\mathbf{k}_{\perp}^f$  is known from equation 2.4, but this

does not correspond to the  $\mathbf{k}_\perp^i$  inside the solid. To determine the perpendicular component  $\mathbf{k}_\perp$  before the transmission through the surface, one needs to make some assumption about the dispersion of the electron final states  $E_f(\mathbf{k})$  inside the solid. In particular, this assumption can either use the results of band structure calculations, or can adopt of a nearly free-electron description for the final bulk states, i.e., a parabolic dispersion [84]. In this case the electron dispersion can be written as:

$$E_f(\mathbf{k}) = \frac{\hbar^2 \mathbf{k}^2}{2m_e} - |E_0| = \frac{\hbar^2 (\mathbf{k}_\parallel^2 + \mathbf{k}_\perp^2)}{2m_e} - |E_0| = E_k + \Phi, \quad (2.5)$$

where  $E_0$  is the energy of the bottom of the valence band and is referenced to the Fermi energy  $E_F$ . By inserting the expression of  $\mathbf{k}_\parallel$  from equation 2.4 into equation 2.5 and by doing some rearrangement, one obtains:

$$\mathbf{k}_\perp = \frac{1}{\hbar} \sqrt{2m_e (E_k \cos^2 \theta + V_0)}, \quad (2.6)$$

with  $V_0 = |E_0| + \Phi$  defined as the inner potential. The only unknown parameter in equation 2.6 is the inner potential  $V_0$ . Many methods can be used in order to find the correct value of  $V_0$ . One way to find the right value of  $V_0$ , is to choose  $V_0$  such as it reproduces the right  $\mathbf{k}_z$  periodicity in the spectroscopic features [92]. This approach is generally used and enables for the good identification of the  $\mathbf{k}_\perp$  dispersion, even in the case where the assumption on the final state is not necessarily correct. The equation 2.6 was used in order to transform the intensity  $I(\theta, \varphi, E_k)$  to  $I(\mathbf{k}_z, E_{bin})$  of the  $\mathbf{k}_z$  dispersion of the observed states presented in the bulk 1T-TaS<sub>2</sub> presented in chapter 3.

## 2.4.2 Single Particle Spectral Function

It is possible from the photoemission spectrum to get not only the information about the band structure of the material, but also to get insight into the many body effects inside the solid. Thus, this opens the gate to the large world of solid state quasiparticles. Every time that electrons are ejected, photohole/photoelectron pairs are produced and the system left behind is in a perturbed state. The many body system will try to fill the empty state through interactions between electrons and lattice. This will have some consequences on the observed line shape in ARPES. To understand how to quantify many body interactions in the system, one needs to look at the expression of the photoemission intensity. To extract quantitative

information about the many body interactions, it is possible to model the remaining (N-1)-body system as a quasiparticle and then perform the perturbation calculation.

The N-electron wave function before and after the photoemission  $\psi_{i,f}^N$  can be written as the product of the single particle wave function of the photoelectron  $\psi_{i,f}^{\mathbf{k}}$  and the remaining photohole (N-1)-body system  $\psi_{i,f}^{N-1}$  as follows:

$$\psi_{i,f}^N = \hat{A}\psi_{i,f}^{\mathbf{k}}\psi_{i,f}^{N-1};$$

where  $\hat{A}$  is an antisymmetric operator that correctly antisymmetrizes the N-electron wave function in such a way that the Pauli principle is satisfied. This hypothesis is valid under the assumption that the photoelectron escapes from the system without interaction with the rest of the electrons; this approximation is called the *sudden approximation* [84]. For the photoemission process, the light-matter interaction is described by the Hamiltonian  $H_{int}$  where the photon is considered as a perturbation:

$$H_{int} = -\frac{e}{2mc}(\mathbf{A} \cdot \hat{\mathbf{p}} + \hat{\mathbf{p}} \cdot \mathbf{A});$$

where  $\mathbf{A}$  stands for the electromagnetic vector potential and  $\hat{\mathbf{p}}$  is defined as the electronic momentum operator. By applying Fermi's golden rule, the transition probability for an optical excitation between the N-electron ground state  $\psi_i^N$ , and one of the possible final states  $\psi_f^N$  can be expressed as follows:

$$\begin{aligned} W_{i,f} &= \frac{2\pi}{\hbar} |\langle \psi_f^N | H_{int} | \psi_i^N \rangle|^2 \delta(E_f^N - E_i^N - h\nu) \\ &= \frac{2\pi}{\hbar} |M_{i,f}^{\mathbf{k}}|^2 |\langle \psi_m^{N-1} | \psi_i^{N-1} \rangle|^2 \delta(E_k + E_m^{N-1} - E_i^N - h\nu); \end{aligned}$$

where  $|\langle \psi_m^{N-1} | \psi_i^{N-1} \rangle|^2$  is the density probability that the photohole is left in the excited state  $m$ ,  $E_i^N = E_i^{N-1} - E_B^{\mathbf{k}}$  and  $E_f^N = E_f^{N-1} + E_k$  are respectively the initial and final energies state of the N-particle system.  $E_B^{\mathbf{k}}$  is the binding energy of a photoelectron in the ground state with kinetic energy  $E_k$  and momentum  $\mathbf{k}$ .  $M_{i,f}^{\mathbf{k}}$  is the single particle matrix element containing the information about the electron-photon interaction.

The overall photoemission intensity observed in ARPES is then given by the sum over all possible transitions  $W_{i,f}$  from the occupied states which, after the multiplication with the Fermi Dirac distribution function  $f_{FD}$ , is given by the expression

$$I(\mathbf{k}, E_k) \propto f_{FD}(E_k) \sum_{i,f} |M_{i,f}^{\mathbf{k}}|^2 \mathcal{A}(\mathbf{k}, E_k), \quad (2.7)$$

where  $\mathcal{A}(\mathbf{k}, E_k)$  is defined as the photohole spectral function and it is expressed as:

$$\mathcal{A}(\mathbf{k}, E_k) = \sum_m |\langle \psi_m^{N-1} | \psi_i^{N-1} \rangle|^2 \delta(E_k + E_m^{N-1} - E_i^N - h\nu).$$

From equation 2.7, one can see that the ARPES intensity provides directly the information about the photohole spectral function of the material, as well as the information associated with the matrix elements. Moreover, the intensity of the spectra can be modulated by the matrix elements, which can even cause the complete suppression of the ARPES signal, depending on the polarization and the energy of the incoming light, as well as the optical selection rules between the initial and the final states of the single particle wave functions [85, 93].

If the many-body wave function is treated within the Green's function formalism, then the one electron spectral function that describes theoretically the energy and momentum of an electron in a material is given in terms of the self-energy  $\Sigma(\mathbf{k}, \omega) = Re \Sigma(\mathbf{k}, \omega) + i Im \Sigma(\mathbf{k}, \omega)$  and can be rewritten as:

$$\mathcal{A}(\mathbf{k}, \omega) = -\frac{1}{\pi} \frac{Im \Sigma(\mathbf{k}, \omega)}{[\hbar\omega - \varepsilon_{\mathbf{k}} - Re \Sigma(\mathbf{k}, \omega)]^2 + [Im \Sigma(\mathbf{k}, \omega)]^2}, \quad (2.8)$$

where  $\hbar\omega$  is the binding energy of the electron,  $\varepsilon_{\mathbf{k}}$  is the single-particle dispersion or bare band structure, and  $Im \Sigma(\mathbf{k}, \omega)$  and  $Re \Sigma(\mathbf{k}, \omega)$  are imaginary and real parts of the electronic self-energy, respectively. The real part of the self-energy  $Re \Sigma(\mathbf{k}, \omega)$  gives the information on how the single particle bands renormalise: i.e., how the binding energy of the particle shifts. The imaginary part of the self energy  $Im \Sigma(\mathbf{k}, \omega)$  carries the information about different scattering processes contributing to the finite quasiparticle lifetime ( $\tau$ ) of the particle state due to the many body effects. Equation 2.8 shows that the constant energy cuts through the spectral function, generally referred to as momentum distribution curves (MDCs), are Lorentzians. By assuming the simplest case of the 1D linear dispersion  $\varepsilon_k = \hbar vk$ , the Lorentzian peaks have a maximum centered around  $k_0 = w/v - Re \Sigma/(\hbar v)$  and a full width half maximum (FWHM) of  $FWHM = |2Im \Sigma/(\hbar v)|$ . The Lorentzian profiles of MDC curves are valid under the hypothesis that there is no dependence on  $k$  in the self energy.

From the preceding, we see that from the ARPES intensity we can have many types of information: for example, the renormalization of the band and the quasiparticle lifetime (that is proportional to the inverse FWHM) to mention just two. The complex self-energy possesses all information about the contributions from many-body effects like electron-defect, electron-electron and electron-phonon interactions. Thus, the self energy can also be expressed as

follows:

$$\Sigma(\mathbf{k}, E) = \Sigma^{el-df}(\mathbf{k}, E) + \Sigma^{el-el}(\mathbf{k}, E) + \Sigma^{el-ph}(\mathbf{k}, E) + \dots, \quad (2.9)$$

where  $\Sigma^{el-df}(\mathbf{k}, E)$  is the contribution from electron-defect interactions,  $\Sigma^{el-el}(\mathbf{k}, E)$  from electron-electron interactions,  $\Sigma^{el-ph}(\mathbf{k}, E)$  from electron-phonon interactions. The energy dependence of the  $\Sigma^{el-df}(\mathbf{k}, E)$  interaction is negligible, since it typically appears as a constant offset. We will make use of this information in the study of the electron-phonon interaction in TMDCs presented in chapter 5.

### 2.4.3 Energy Distribution Curves (EDCs) and Momentum Distribution Curves (MDCs)

An EDC is defined as the photoemission intensity taken at a fixed values of momentum ( $\mathbf{k}$ ) as a function of binding energy  $E_B$  (or  $E_k$ ) (see Figure 2.5). To the contrary, the MDC is the photoelectron intensity plotted at a fixed binding energy  $E_B$  ( $E_k$ ) as a function of  $\mathbf{k}$ . Thus, the EDCs and MDCs constitute the two standard types of curves that are generally used in order to analyze the 2D image extracted from ARPES data.

The expression of the intensity of the photoemission from the ARPES spectra given in equation 2.7 can also be written as [94]:

$$I(\mathbf{k}, \omega) \propto |M_{i,f}^{\mathbf{k}}|^2 f_{FD}(\omega) \mathcal{A}(\mathbf{k}, \omega). \quad (2.10)$$

From equation 2.10, the EDC function can be expressed as [94]:

$$I_{EDC}(\omega) \propto |M_{i,f}^{\mathbf{k}_{const}}|^2 f_{FD}(\omega) \mathcal{A}(\mathbf{k}, \omega), \quad (2.11)$$

where  $|M_{i,f}^{\mathbf{k}_{const}}|^2$  is the magnitude of the matrix element at a constant electron momentum  $\mathbf{k}$  and polarization of the incoming photon [94].  $\omega$  denotes the energy. From equation 2.11, one can see that the EDC function has a constant matrix element for a constant momentum, which is the advantage of using EDCs in the data analysis process. However, the EDC function presented by equation 2.11 has a non-trivial  $\omega$ -dependence i.e.,: The EDC function contains the Fermi function term, which can make the EDC function asymmetric.

The MDC function can be given in the form [94]:

$$I_{MDC}(\mathbf{k}) \propto |M_{i,f}^{\mathbf{k}}|^2 f_{FD}(\omega_0) \mathcal{A}(\mathbf{k}, \omega). \quad (2.12)$$

The MDC function has a simpler lineshape than the EDC function, since the MDC is obtained at constant energies (see equation 2.12): the inelastic background and the Fermi function depend strongly on the energy and a little on the momentum. Thus, the MDC analysis presents some advantages, as for example: In the vicinity of the Fermi energy, the MDC lineshape is a Lorentzian and it is not affected by the Fermi function. Thus, this makes the MDC analysis very helpful to follow the band dispersion around the Fermi level and to extract the imaginary part of the self-energy function  $Im \Sigma(\mathbf{k}, \omega)$ . It is not straightforward to extract the real part of the self-energy  $Re \Sigma(\mathbf{k}, \omega)$  from the MDC analysis, since the knowledge of the non-interacting (bare band dispersion) velocity is required and it is not measured experimentally [95]. However, when one considers the bare dispersion as a linear line, the extracting of the band dispersion from an MDC analysis is generally not difficult. Thus, the resulting dispersion  $\omega(\mathbf{k})$  can be compared to a non-interacting bare band  $\epsilon(\mathbf{k})$  to extract the real part of the self-energy  $Re \Sigma(\mathbf{k}, \omega)$  as well as the lifetime information.

Figure 2.5 shows the model of a linear band dispersion in three different cases with various values of the real and imaginary part of the self energy. This figure allows the understanding of the role of the self energy on the spectral features. For a non-interacting system the contribution of both the real and imaginary part of the self energy become zero (see Figure 2.5(a)) and the band resembles a simple line. The inset of Figure 2.5(a) shows the EDC intensity curve taken along the cut presented with a red line. This EDC profile has the shape of the simple delta function. The spectral feature is broadened when the imaginary part of the self energy ( $Im \Sigma(\mathbf{k}, \omega)$ ) has a finite value (see Figure 2.5(b)). In this case, the EDC profile has a Lorentzian shape centered around the bare energy  $\epsilon(\mathbf{k})$ . When a fixed real part of the self energy having an arbitrary Lorentzian profile in energy is added to the system, the dispersion (together with the curvature, the band velocity,  $\dots$ ) changes with respect to the bare energy (see Figure 2.5(c)).  $Re \Sigma(\mathbf{k}, \omega)$  renormalizes the energy dispersion with an offset in the peak position of the dispersion of the quasiparticle. Thus, this generally translates into kinks in the dispersion as seen in high temperature superconductors and many others compounds [96, 97, 98, 99]. The real and imaginary part of the self energy are related to each other through the Kramers-Kronig relation, so they are not actually independent.

A standard method to investigate many-body interactions in detail is the use of EDCs and MDCs analysis [101]. The use of the EDCs and MDCs curves for the analysis of the ARPES spectra, enables the extraction of the dispersion and scattering rate of quasiparticles and the observation of the phonon effects in the electronic structure of diverse materials. In addition, the EDCs and MDCs analysis allow to study various features of bands crossing the

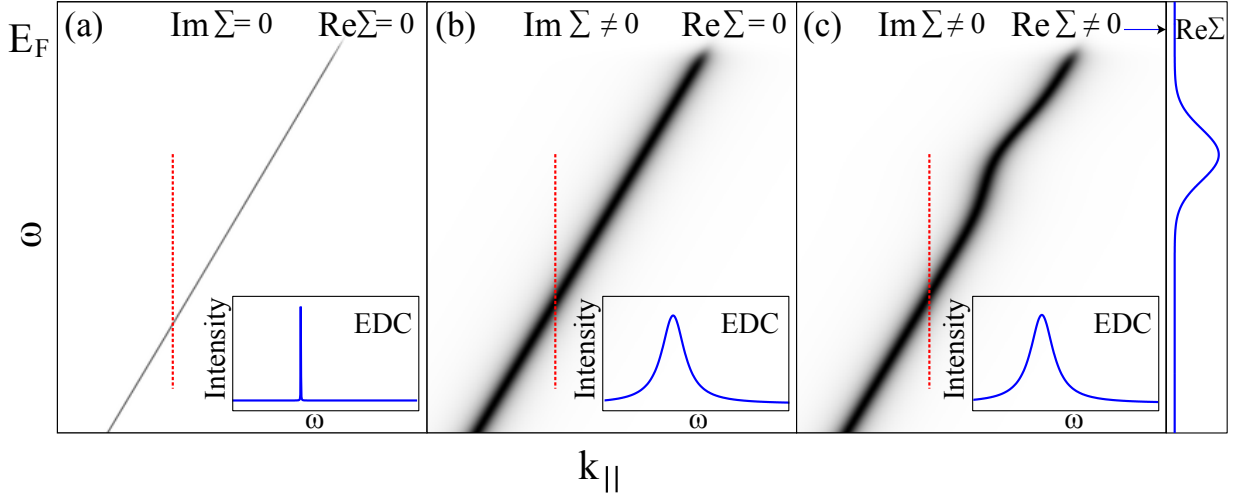


**Figure 2.5:** The effect of self-energy on the spectral function of a linear dispersion band. (a) A model of the spectral function showing that the dispersion is just a single line when the self energy tends to zero ( $Im \Sigma(\mathbf{k}, \omega) = 0$ ,  $Re \Sigma(\mathbf{k}, \omega) = 0$ ). The EDC curve presented in the inset is taken along the red dashed line. The curve has the shape of a Dirac function around the value of the bare energy  $\epsilon(\mathbf{k})$ . (b) Here, the imaginary part of the self energy ( $Im \Sigma(\mathbf{k}, \omega)$ ) is set to a fixed value, whereas the real part of the self energy ( $Re \Sigma(\mathbf{k}, \omega)$ ) is fixed to zero. The dispersion is still in this case equal to the bare energy but the spectral feature is widened by  $Im \Sigma(\mathbf{k}, \omega)$ . The EDC profile shown in the inset is supposed to have a Lorentzian shape with a peak centered around  $\epsilon(\mathbf{k})$ . (c) In this case, the real and imaginary part of the self energy possess fixed values and  $Re \Sigma(\mathbf{k}, \omega)$  possess an arbitrary Lorentzian shape shown on panel c. The real part of the self energy causes the renormalisation of the energy dispersion with an offset equal to  $Re \Sigma(\mathbf{k}, \omega)$ . It should be noted that this is a simple example with arbitrary values.  $Re \Sigma(\mathbf{k}, \omega)$  and  $Im \Sigma(\mathbf{k}, \omega)$  are in fact related via Kramers-Kronig transformations and the real and imaginary part of the self energy depends on  $\omega$ . This figure was taken from [100].

Fermi level and the renormalized bands that exhibit kink behavior in the electronic band dispersion. From this discussion, one can see that the quantities derived from EDCs and MDCs are in some way different. For more details about the EDCs and MDCs analysis from different ARPES spectra, the reader can consult Ref. [102]. The EDCs and MDCs analysis are used in chapter 5 in order to extract the electron-phonon strength  $\lambda$  from the 2D TMDCs MoS<sub>2</sub>, WS<sub>2</sub> and TaS<sub>2</sub>.

#### 2.4.4 Core Level Photoemission Spectroscopy

Even though XPS is based on the photoelectric effects, the photoemission from the core level necessitates an additional discussion. The XPS spectral lines are identified by the shell from which the electron was ejected. The difference between ARPES and XPS signals is

the absence of the momentum dispersion in the XPS signals. The XPS technique is widely used to investigate oxidation states, and the chemical compositions of surfaces. The binding energies of observed peaks can be used to identify the elemental composition of a sample. A rigorous analysis of the obtained XPS spectral lines allows one to obtain a detailed chemical composition of the material, and is so sensitive that it can detect even a very small amounts of contamination. This technique can also be used to study the structural phase transitions (for example in 1T-TaS<sub>2</sub> compounds) or changes in the electronic structure due to the interactions with nearby atoms (intercalants, adsorbants or substrate). A splitting of main components can show the existence of non-equivalent atomic positions in a material (for example, due to a surface reconstruction). The CDW phases can also be identified and studied based on XPS spectral lines [103].

The entire description of all the processes occurring with the photoemission from the core-levels is quite complex. Besides the photoelectron peaks observed from the XPS spectral lines, Auger peaks are also present in the XPS spectrum. Auger peaks can easily be identified since the observed kinetic energies of Auger electrons are independent of the photon energy. Electrons with enough kinetic energy can excite collective oscillations of an electron gas (surface plasmon or bulk). For more information about these collective oscillations and to further study of the XPS spectral lines, references [104, 105, 106, 107, 108] can be consulted. The XPS technique was used in the present study only to study the temperature-dependence of the CDW phases in the bulk 1T-TaS<sub>2</sub> compound (see chapter 3).

### 2.4.5 ARPES Spectral Acquisition and Analysis

To perform ARPES experiments, many conditions need to be met. First, the experiment needs to be performed in UHV in order to keep the surface of the sample clean and also to reduce the scattering of the photoelectrons. Moreover,  $\mu$ -metal shielding can be used in order to screen any residual magnetic field; even the small contribution from the Earth's and other external magnetic fields can influence the obtained results for example the measured dispersion of the electrons. The simultaneous detection of the kinetic energy and the emission angle of the photoelectrons is realized by the hemispherical electron energy analyzer that is made up of hemispherical capacitor, cylindrical electrostatic lenses and a 2D detector, to mention just few components. The analyzer will be discussed in detail below. The study of the CDW and SC materials usually necessitates low temperature measurement, meaning that a sample manipulator with sample cooling capability is necessary.

One can only study a limited range of materials with the ARPES technique. The sample must be somehow conductive, in order to prevent charge accumulation. The area that is probed depends on the size of the light spot, which can place some restrictions on the size and homogeneity of a sample. For example, mechanically exfoliated layered crystals are generally not well suited for the ARPES technique due to their lack of uniformity.

Precise control over the energy of light is required for good energy resolution. Optimally, one would like to use a highly monochromatic and highly brilliant light source, with a wide tunability of the photon energy, and a high energy resolution. This can be achieved by using synchrotron radiation.

Figure 2.3(a) exhibits a schematic of the typical ARPES experimental setup. Recently, with the improvement of the experimental aspects of ARPES, the data sets are nowadays collected with a 2D detector, which enables the detection of a large angular range at once. The use of this 2D detector, allows simultaneous measurements of the kinetic energy and the incoming angle of photoelectrons. One can map the dispersion in the entire surface Brillouin zone (BZ) by rotating a sample and stacking together the obtained images. The selection of the kinetic energy of the electron is performed by a hemispherical analyzer. In the work presented here, all the results obtained from ARPES, were acquired using the SPECS Phoibos 150 hemispherical analyzer. Thus, the following discussion is based on this kind of instrument.

The application of the electric field between the two hemispheres alters the trajectories of the electrons depending on their incoming kinetic energy. Thus, this is realized in the mirror plane of the analyser, which is also called the “dispersive plane” (see Figure 2.6(a)). Electrons that pass the electrostatic lenses and go through the hemispherical part of the analyser are retarded to the energy called the pass energy  $E_p$ . Only the electrons within the small energy range  $E_p \pm \Delta E$  can reach the 2D detector because the two concentric hemispheres with the electrostatic field between them act as a band-pass filter. Since  $\Delta E \propto E_p$ , the size of the energy window can be controlled by changing the value of the pass energy during the experiment, while the detected energy range can be controlled by the parameter called the retarding ratio  $r = E_k/E_p$ . The energy resolution of the analyser  $\Delta E_A$  is proportional to the pass energy  $E_p$  and its expression is given by the following formula:

$$\Delta E_A = \frac{E_p(S_1 + S_2)}{4R},$$

where  $S_1$  and  $S_2$  denote the entrance and exit slit widths, respectively, and  $R$  stands for the mean radius of the analyser. The best resolution is achieved by choosing a low value of  $E_p$

together with a narrow slit. However, this lowers the number of observed electrons on the detector and limits the energy range of the acquisition.

The discrimination of the electrons by their emission angle  $\varphi$  occurs in the non-dispersive plane of the hemispherical analyser (see Figure 2.6(b)). The acceptance angular range  $\pm\beta$  can be selected based on the chosen lens system operation mode (applied voltage on the lenses). Thus, only electrons emitted in this range ( $\pm\beta$ ) will be capable of reaching the 2D detector. By modifying the polar ( $\theta$ ) and tilt ( $\alpha$ ) angles, an arbitrary cut through the entire emission hemisphere can be chosen, allowing the band mapping in the entire BZ. The transformation of the angles defined in Figure 2.6 into  $k$ -space is obtained by using the following expressions of  $k_x$  and  $k_y$ :

$$\mathbf{k}_x = \frac{1}{\hbar} \sqrt{2m_e E_k} (\cos \alpha \sin \varphi - \sin \alpha \cos \theta \cos \varphi),$$

and

$$\mathbf{k}_y = \frac{1}{\hbar} \sqrt{2m_e E_k} \sin \theta \cos \varphi.$$

From the first order approximation, the angular resolution can be converted to  $k$ -resolution  $\Delta k_{\parallel}$  as follows:

$$\Delta k_{\parallel} = \frac{1}{\hbar} \sqrt{2m_e E_k} \cos \varphi \Delta \varphi, \quad (2.13)$$

where  $\Delta\varphi$  is the angular resolution, which depends on the chosen lens mode. The best angular resolution that one can reach is generally  $0.1^\circ$ . From equation 2.13, one can see that the  $k$ -resolution is a function of the kinetic energy  $E_k$ , the angular resolution  $\Delta\varphi$  and the electron emission angle  $\varphi$ . This shows that the  $k$ -resolution can be increased by increasing the emission angle and by using low energy light source or by measuring the dispersion in the higher order BZ (i.e., with large  $\varphi$ ). The best  $k$ -resolution that one can achieved is smaller than  $0.01 \text{ \AA}^{-1}$  [109]. Besides the angle resolved mode, one can exchange the lens settings to the spatially resolved mode, where the electrons originating from within a small emission angular range are focused on the same place on the 2D detector. This operation mode is useful for XPS experiments and light source alignment.

From so-called polar scans, one can obtain the full map of the photoemission intensity throughout the BZ. During this scan, the sample is rotated in front of the analyser around the axis orthogonal to the dispersive plane and acquires a spectrum for each value of the polar angle  $\theta$ . By contrast, acquiring a scan at normal emission angle, while varying the

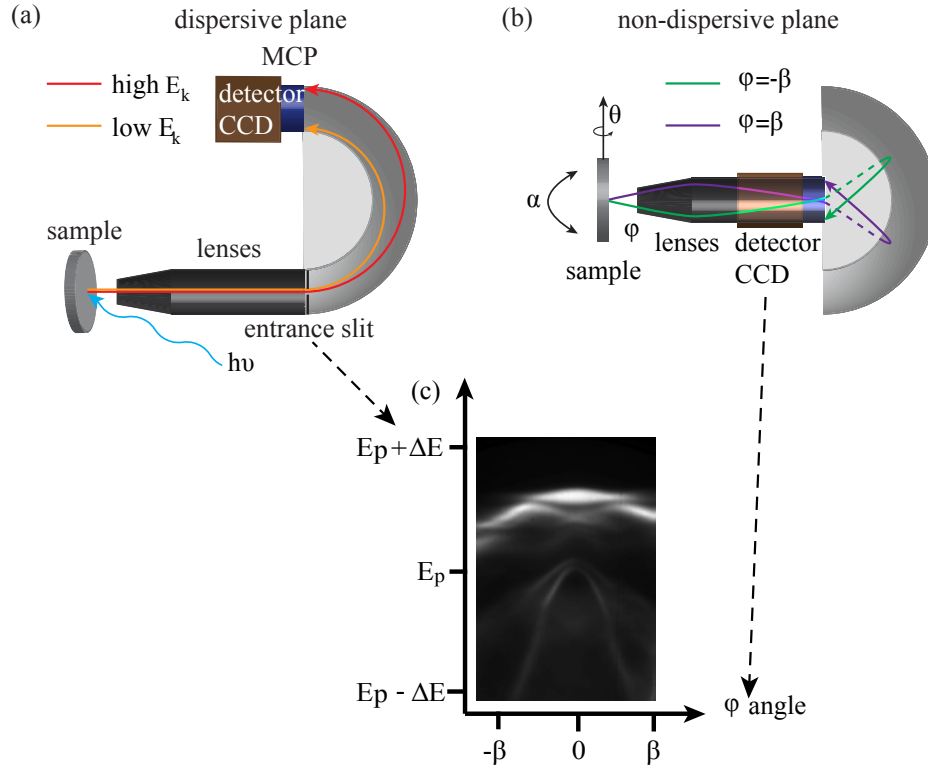


**Figure 2.6:** Schematic depicting the hemispherical analyser and its associated geometry. (a) Cross sectional and illustration of the dispersive plane of the hemispherical analyser. In this plane, electrons are discriminated by their kinetic energy. (b) Cross sectional illustration of the non-dispersive plane. Here, the electrons within the acceptance angle range  $\pm\beta$  are measured. (c) An example of the photoemission spectra of 1T-TaS<sub>2</sub> from the 2D detector of ARPES as a function of energy and angle at the entrance slit of the analyser is presented. Some parts of the figure are from Ref. [110].

photon energy values, generates so-called energy scans. In this type of scan the dispersion along the  $\mathbf{k}_\perp$  component of the sample can be obtained.

A micro channel plate (MCP) detector is typically used in order to enhance the signal to noise ratio. After traveling through the two hemispheres of the analyser, the photoelectrons impinge on the regular array of electron multipliers that is kept at high voltage. The avalanche of electrons produced by the MCP is imaged on the phosphorous screen. A CCD camera is used to capture the image. An example of such image is shown in Figure 2.6(c).

It should be kept in mind that some image artifacts such as spherical and chromatic aberrations are produced by the analyser. The spherical aberration, lead electrons with the same kinetic energy to appear dispersing with the emission angle and this is due to the hemispherical geometry of the analyser. This can be compensated by using a curved entrance slit.

The chromatic aberration, lead instead electrons with different kinetic energies emitted in the same direction are detected at different emission angles, causing the energy dispersion lines to be curved. The correction of this type of aberrations can be made after an image is acquired.

The quantitative analysis of ARPES spectra requires that one take into account several effects that are extrinsic to the photoemission process, such as the Gaussian broadening  $G(\Delta\omega, k_{\parallel})$  related to a fixed energy and momentum resolution, together with the secondary electrons constituting the observed background  $I_b(\omega)$ . By implementing this in equation 2.10, the experimental photoemission intensity is given by:

$$I(\omega, \mathbf{k}_{\parallel}) = [\mathcal{A}(\mathbf{k}_{\parallel}, \omega)M(\omega, \mathbf{k}_{\parallel})f_{FD}(\omega)] * G(\Delta\omega, k_{\parallel}) + I_b(\omega),$$

where the term  $\Delta\omega$  is defined as the total energy resolution, combining both the analyser and light source contributions. Through a convolution with Gaussian function  $G$ , the measured product of the spectral function, the matrix element and the FD function can be modified by the finite energy and momentum resolutions  $\Delta E$  and  $\Delta k$ . Furthermore, the measured intensity will have a contribution from a background  $I_b$ , which is coming from inelastically scattered secondary electrons. MDC and EDC curves from ARPES spectra are generally fitted using the Lorentzian or Voigt profiles on top of a polynomial background. The measured kinetic energy is converted into the binding energy by finding the position of the Fermi edge and using equation 2.3.

### 2.4.6 The SGM3 Beamline and ASTRID2

All ARPES, LEED, XPS, and some part of the STM measurements presented in this thesis, as well as the growth of TaS<sub>2</sub> on Au(111), were performed at the SGM3 endstation (ASTRID2 storage ring, Institute for Storage Ring Facilities, Aarhus University). Some STM results were obtained as a part of collaboration with the group of Prof. Alexander Khajetoorians (Radboud University) [83].

ASTRID stands for Aarhus STorage RIng in Denmark. ASTRID2 is a small electron storage ring located in the basement of the Department of Physics and Astronomy of Aarhus University. It has a circumference of 45.7 m and it is operating with an energy of 580 MeV, with an almost constant current of 200 mA. The old synchrotron ASTRID is used as a booster

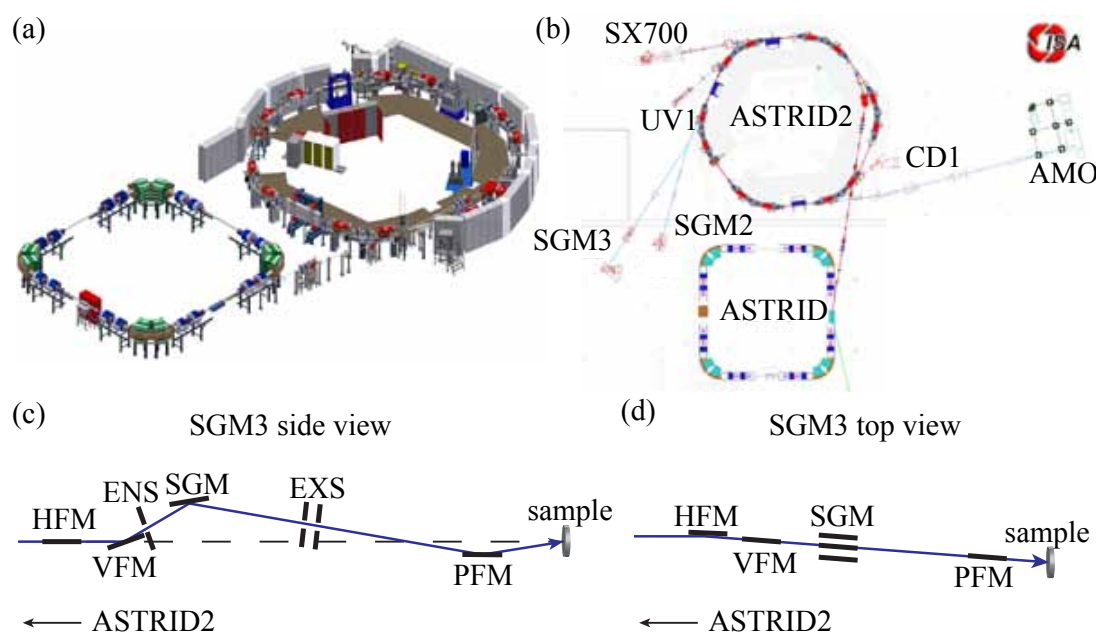


**Figure 2.7:** (a) and (b) Design of ASTRID and ASTRID2 synchrotrons. (b) The beamline arrangement in the ISA facility. (c) and (d) Schematic outline of the SGM3 beamline (c) Side view. (d) Top view. For more detailed description about these figures, please see the text. This figure was taken from Ref. [111].

ring for ASTRID2. This allows ASTRID2 to run in the top-up mode. In addition, the upgrade of ASTRID to ASTRID2 reduced the horizontal emittance from 140 nm to 12 nm, resulting in a much tinier beam spot on a sample. ASTRID2 is designed with combined-function magnets such as dipole, quadrupole and sextupole fields in the same magnet. It has a hexagonal structure with 4 straight sections for magnetic insertion devices. There are currently 6 beamlines operating at ASTRID2 with application varying from atomic and molecular physics to surface science. An overview of the Institute for Storage Ring Facilities in Aarhus (ISA) is presented in Figure 2.7. More information about ASTRID and ASTRID2 can be found in Refs. [111, 112]

The acronym SGM stands for Spherical Grating Monochromator. The SGM3 beamline receives light from an undulator installed on ASTRID2 [113]. An undulator is a type of insertion device consisting of a movable array of magnets with alternating polarities, which forces the electrons inside their region to wiggle [114, 115]. This curved trajectory of the electron inside the undulator stimulates the emission of highly-collimated and polarized synchrotron radiation. The emitted radiation is linearly polarized due to the confinement to the plane of the undulator [111, 115]. By changing the gap between the magnets inside

the undulator, the photon energy can be changed continuously over a large energy range, ranging in our case from 10 eV to 150 eV. This beamline is designed to operate in this photon energy range, which is covered by three spherical gratings and exploiting from the first to the fifth harmonics of the undulator. Two spherical mirrors—namely, a spherical horizontal focusing mirror (HFM) and a spherical vertical focusing mirror (VFM)—focus the beam of light to enter the beamline through the entrance slit (ENS) (see Figures 2.7(a) and 2.7(b)). The selection of the light energy (ranging from 10 to 150 eV) requires three interchangeable spherical grating mirrors (SGM) as well as the exit slit (EXS). By adjusting the toroidal post focusing mirror (PFM), the final alignment of the light beam can then be performed in order to focus the light spot on the sample in the measurement position. The spot size on the sample is roughly ( $\sim$ )  $200 \mu\text{m} \times 50 \mu\text{m}$ . The total energy resolution of the beamline depends on the size of the exit slit (EXS), but generally, its value is better than 10 meV, but not at the high energies in the  $h\nu$ -scans. The reader can consult Ref. [111] for more information about the SGM3 beamline.

### 2.4.7 The Setup of the SGM3 Endstation

Figure 2.8 presents a schematic of the SGM3 endstation. The endstation is composed of four chambers isolated from each other by valves. The load-lock (LL) chamber, with a base pressure of low  $10^{-8}$  mbar is used to introduce the sample into the UHV system without venting the other chambers. The sample is generally mounted on a rectangular Aarhus-type sample holder which is made up of a Mo or Ta plate. The LL is also used as an additional pumping system for the rotational feedthrough of the MC manipulator. The reading of the temperature of the sample in all chambers except the LL chamber is performed with a K-type thermocouple attached to the back of the sample holder.

The preparation chamber (PC) has a base pressure of  $2 \times 10^{-10}$  mbar and it is used for surface treatments, such as ion  $\text{Ne}^+$  sputtering and annealing. The sample socket in the PC can be water or nitrogen cooled and can allow the sample's heating to go up to  $1300^\circ\text{C}$  with electron bombardment, using a tungsten filament mounted on the socket. This chamber is also used for sample storage of up to 10 samples at once and it hosts an Aarhus-type STM instrument that allows surface characterization.

There are two sample manipulators available for use in the MC. The older of these is a 5-axis manipulator and the most recent manipulator has six axes of motion that can be

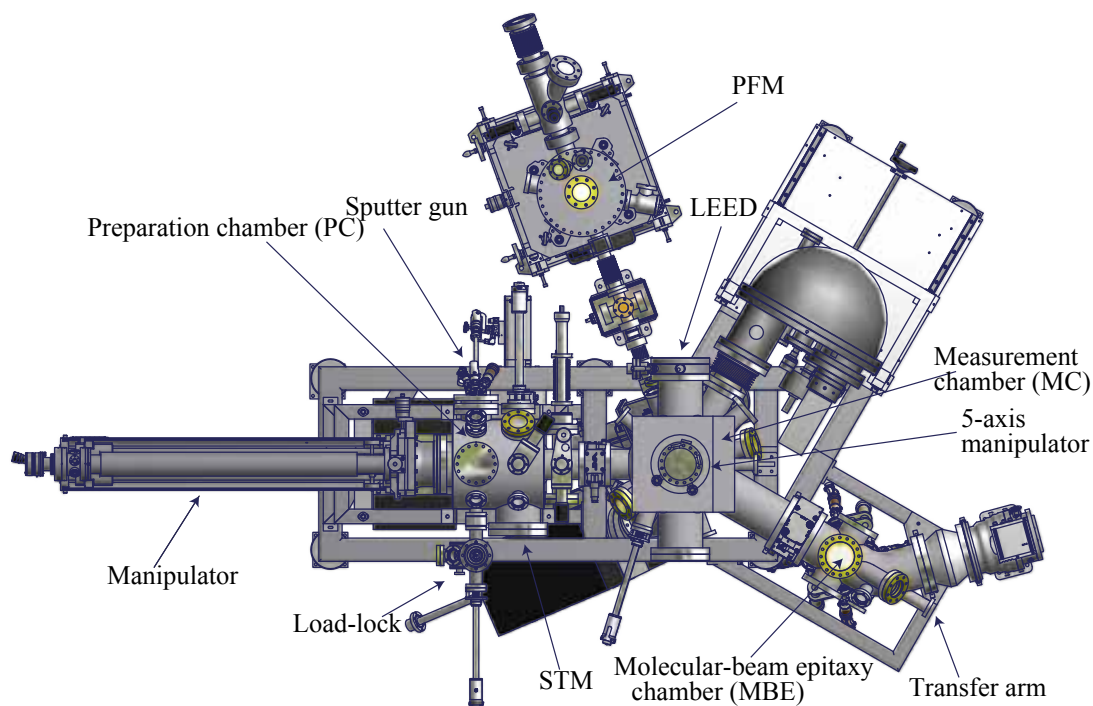


**Figure 2.8:** A schematic of the SGM3 endstation equipped with UHV chambers. The load lock chamber (LL) is used to introduce samples into the system and to cleave them if necessary. The preparation chamber (PC) is used to prepare the surface of samples and for STM measurements. The measurement chamber (MC) holds the LEED unit, the hemispherical analyzer and the 5-axis manipulator. The molecular beam epitaxy (MBE) chamber is used to synthesize 2D materials. The endstation is connected to the beamline through the post focusing mirror (PFM) chamber. The transfer of a sample is executed by motorized transfer manipulator and magnetic transfer arms.

motorized. The MC has a base pressure of  $7 \times 10^{-11}$  mbar and it is equipped with a hemispherical analyser (Phoibos 150, SPECS GmbH) used for ARPES measurements and a LEED instrument for surface characterization. The sample stage is connected to a closed-cycle Helium (He) cryostat, which enables the sample to be cooled down to a temperature of approximately 70 K (for the older manipulator) and approximately 30 K (for the new manipulator). With the recent manipulator, the sample stage is cooled down with a more powerful He cryostat which allows a temperature of approximately 30 K on the sample. A filament is mounted on the head of the MC socket, which can be used to anneal the sample in order to perform temperature-dependence ARPES. The communication of the system with the synchrotron, data analysis, the rotation of the MC manipulator and the data acquisition to only mention a few, are done by a dedicated software written in Igor Pro by our group. Thus, this allows measurements to be automatized to a large extent.

---

The molecular beam epitaxy (MBE) chamber has a base pressure of  $2 \times 10^{-10}$  mbar. The growth of samples is done inside this chamber, which contains an electron beam evaporator (EBE-4, SPECS) with high purity source materials from Goodfellow or high-purity hand-wound filaments as alternative sources for evaporation, and a custom built H<sub>2</sub>S doser. The MBE chamber can also host, as needed, a reflection high-energy electron diffraction (RHEED) unit. A home built suitcase can be directly attached to the MBE chamber, for transportation of synthesized samples to other laboratories for more measurements. Battery-powered ion pumping systems together with the non-evaporable getter make the suitcase convenient to use and handy to carry. Moreover, the suitcase is compatible with different sample holders, such as those used by SPECS and Omicron systems and has been use to bring the samples to Nijmegen.

---

# Study of the 3D Band Dispersion of Bulk 1T-TaS<sub>2</sub> at Different Temperatures

---

## 3.1 Introduction

Bulk 1T-TaS<sub>2</sub> is a layered material composed of planes of tantalum (Ta) atoms octahedrally coordinated by sulphur (S) atoms. A unit layer of 1T-TaS<sub>2</sub> consists of one Ta layer sandwiched between two layers of chalcogens S layers. This bulk material has an in-plane lattice constant of  $a = 3.365 \text{ \AA}$  and an out-of-plane lattice constant of  $c = 5.897 \text{ \AA}$  [39]. Several reports on peculiarities in the electronic and physical properties of 1T-TaS<sub>2</sub> have drawn considerable interests over the past and recent years. These researches have led to the discovery of a rich repertoire of correlated phenomena in this system. Among them, we can mention: the Mott-insulating behavior, the superconductivity, its rich electronic phase diagram that includes multiple charge density waves (CDW) transitions that vary remarkably in their electronic properties, to mention just a few.

Before rushing into the results, I shall present the particularity of each CDW phase transition, as well as the temperature ranges in which each phase occurs. Thus, this will allow us to understand in some degree the temperature dependence electronic structure of 1T-TaS<sub>2</sub> near the Fermi level, determined by means of ARPES presented in the subsequent sections.

At low temperature and below 180 K, the single crystal is in a commensurate (C)-CDW state

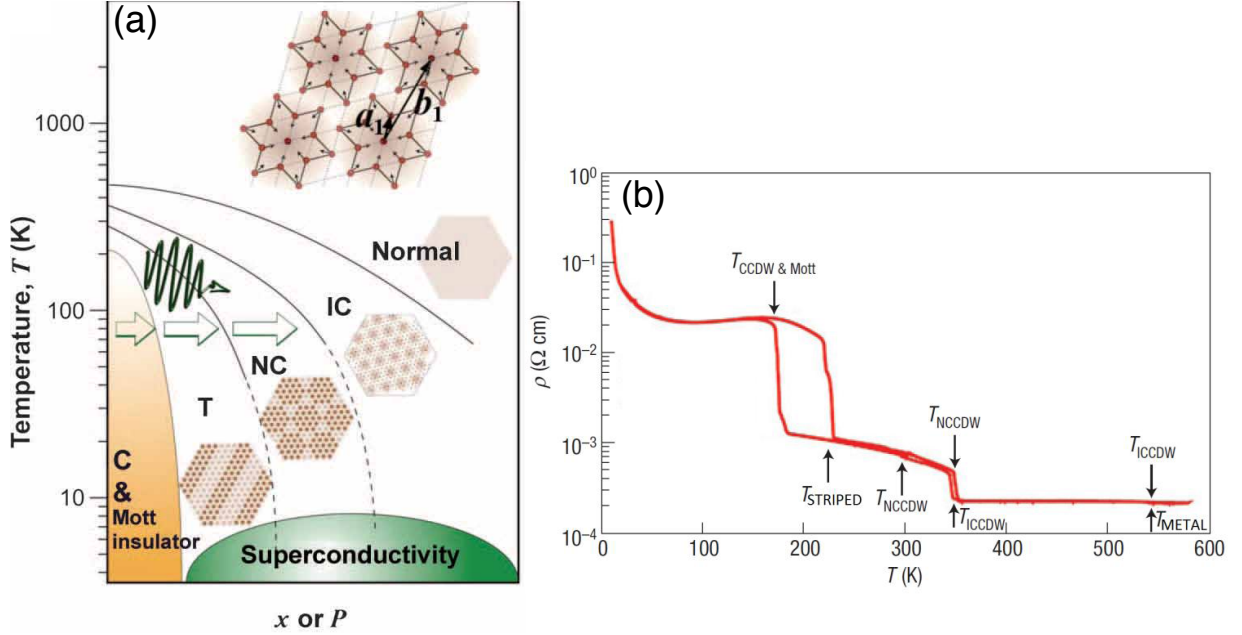


**Figure 3.1:** (a) Sketch of the general phase diagram of 1T-TaS<sub>2</sub> under several physical domains (doping  $x$ , or pressure, temperature). The evolution of the CDW phase can be described by the strong charge density redistribution coupled with the lattice distortion within each star. In this figure the angle ( $13.9^\circ$ ) between the lattice vector  $\mathbf{a}_1$  and the C-CDW vector  $\mathbf{b}_1$  is shown. This figure has been taken from Ref. [47]. (b) Temperature-dependent resistivity for the single crystal 1T-TaS<sub>2</sub>. This picture has been taken from Ref. [59]. Arrows below the resistivity curves point out the starting temperature for each CDW phase transitions upon heating. From CCDW/Mott phase, the striped phase appears at 220 K, NC-CDW phase occurs at 290 K, while ICCDW phase appears at the temperature close to 350 K and the metal phase appears above 550 K. Arrows above the resistivity curves indicate the starting temperature for each CDW phase transitions upon cooling the sample. From metal phase, the ICCDW phase appears at 550 K. NCCDW phase occurs at 350 K and CCDW/Mott phase at temperature below 180 K.

where the lattice structure is periodically distorted and makes a  $(\sqrt{13} \times \sqrt{13})$  superlattice that is rotated by  $13.9^\circ$  against the lattice. In this phase, the Ta atoms displace to make “David Star” clusters, in which the set of 12 atoms within each star move inward toward the atom at the center [116, 117] (see the inset in Figure 3.1(a)). The presence of the periodic lattice distortion in this system creates energy gaps in its band structure, leaving exactly one conduction electron per David Star clusters (i.e., the single electron localized at the center atom of David Star cluster) [116, 117]. These conduction electrons are further localized by the on-site Coulomb repulsion and produce a Mott insulator state in the system that has been confirmed by many experiments [48, 49, 50]. Bulk 1T-TaS<sub>2</sub> is an insulator in the C phase [43, 59, 118]. Upon heating the system to 225 K, it experiences a sequence of first order phase transition to triclinic (T)-CDW that becomes stable at up to 280 K [47]. The

T-CDW phase is constituted of elongated C-CDW domains with triclinic symmetry (or of striped triclinic C-CDW domains structure [47]) see Figure 3.1(a). After further heating, the nearly commensurate (NC)-CDW phase appears and becomes stable at up to 355 K [47]. This new NC-CDW phase is constituted of Mott insulating C-CDW domains arranged hexagonally and separated by metallic incommensurate (IC)-CDW domain walls [47]. In other words, the arrangement of Ta atoms in the new NC-CDW phase may be visualized as roughly hexagonal C-CDW domains suspended in an interdomain phase [47, 59, 119] (see Figure 3.1(a)). Scanning tunneling microscopy study of 1T-TaS<sub>2</sub> has determined that the domain walls observed in this phase are discommensurate regions that completely shrink and dissolve above the temperature  $T \sim 350$  K, and a new domain free state occurs with incommensurate (IC)-CDW order [47], while the system is transformed to incommensurate (IC)-CDW state [119] (see Figure 3.1(a)). The standard metallic phase of 1T structure that appears at high temperatures i.e., above 535 K is known as Normal phase [45, 59] (see Figure 3.1(a)).

In summary, at each transition temperature, the lattice structure is distorted (see Figure 3.1(a)), thus creating energy gaps in band structure of 1T-TaS<sub>2</sub> in each transition phase [116, 117]. Moreover, the angle between the CDW vector and lattice vector is different and this can be seen in Table 3.1. Table 3.1 also summarizes the temperature ranges where each phase of CDW occurs upon cooling and heating the 1T-TaS<sub>2</sub> single crystal. The electrical resistivity increases abruptly at each phase transition as shown the temperature dependent resistivity on the multitude phase transition observed in 1T-TaS<sub>2</sub> (see Figure 3.1(b)). The most prominent features in this figure are the first order phase transitions and a large hysteresis observed around 200 K.

One of the reasons why the bulk 1T-TaS<sub>2</sub> crystal is so important is because it exhibits abrupt and reversible changes in resistivity. This type of material is attractive for device applications, specially when the transition can be controlled electrically. A fast and reversible electrical switching between insulating and metallic states in 1T-TaS<sub>2</sub> flakes of thickness 10 nm or more has been demonstrated by Hollander et al., [120]. The NC-C transition in 1T-TaS<sub>2</sub> samples as thin as 4 nm was electrically controlled by Tsen and et., and they identified the current flow as a mechanism that drives transitions between metastable and thermodynamically stable states [121]. Theoretical works indicate that in the C phase of few-layer 1T-TaS<sub>2</sub> crystals, the absence or existence of a band gap depends on the c-axis orbital texture and suggest an alternate approach to tune the electronic properties of this material [63]. Due to the reduced screening and higher electric field penetration in SL or

**Table 3.1:** Different CDW phases observed in 1T-TaS<sub>2</sub> with their corresponding CDW orientation angles  $\phi$  ( $\phi$  is defined as an angle between the CDW unit cell and that of the unreconstructed atomic lattice). This table was taken from Ref. [47].

Phases	T on cooling (K)	T on heating (K)	$\phi$ on cooling ( $^\circ$ )	$\phi$ on heating ( $^\circ$ )
C-CDW	<183	< 223	13.9	13.9
T-CDW	-	223 < T < 280	-	13.0 - 12.3
NC-CDW	183 < T < 347	280 < T < 357	10.9 - 12.3	12.3 - 11.5
IC-CDW	347 < T < 543	357 < T < 543	0	0
Normal	> 543	> 543	-	-

Note: The acronyms C, T, NC and IC denotes commensurate, triclinic, nearly commensurate and incommensurate, respectively.

few-layers, this samples might exhibit easier switching than bulk crystals. Advances on the study of the 2D exfoliation and growth TMDCs have allowed to know how dimensionality and interlayer interactions may affect the phase diagram of 1T-TaS<sub>2</sub>. For instance, some research groups have reported that thinner samples (lower than 10 nm) lack the jump in resistivity which signals the transition to the C-CDW phase [122].

Even though the bulk 1T-TaS<sub>2</sub> phase diagram has been widely studied [39, 43, 46, 59, 118], the exact origin of the electronic and lattice instabilities observed in this system remain unclear. Interlayer interactions, electron-electron interactions, disorder as well as electron-phonon coupling might all play a role on the presence of the electronic and lattice instabilities observed in the ground state of bulk 1T-TaS<sub>2</sub>. Fazekas et al., [123] have assumed that a Mott-Hubbard gap observed in the C phase is opened by electron correlations. It has been also suggested that these CDW transitions observed in 1T-TaS<sub>2</sub> have driven by strong electronic correlations and electron-phonon interaction [62, 116]. But recent theoretical work have suggested that the insulating behavior of the C phase might come instead from the disorder in orbital stacking [63, 66].

Despite the fact that the bulk 1T-TaS<sub>2</sub> have been studied for more than 50 years, the rebirth of studying this material has been driven by the possibility to clarify transitions between different CDW states using ultrafast techniques [124, 125] and to access experimentally the metallic SL TMDCs [31, 61]. Most recently, Law and his coworker [126] have suggested that the bulk 1T-TaS<sub>2</sub> should be considered as a quantum spin liquid based on the existing experimental evidence on this material.

Although this compound has been widely studied both theoretically and experimentally in some extent, clearly there are still many remaining open questions to be answered. For example, recent reports have challenged the classical Fermi nesting picture as the origin of the CDW observed in 1T-TaS<sub>2</sub>. Many calculations have predicted the formation of a one-dimensional metallic band along the  $\Gamma$ -A direction of the Brillouin zone (i.e., the perpendicular direction to the planes) in the ground state CDW of bulk 1T-TaS<sub>2</sub>. This result was found by the DFT calculations [63, 65, 127, 128], but when electronic correlations are taken into account, the results becomes disputable [65, 66]. Recently, Ritschel and coworkers have shown that the dispersion along the  $\Gamma$ -A direction depend on the stacking order of the CDW unit cell between adjacent planes [63].

Several ARPES studies have been performed on bulk 1T-TaS<sub>2</sub> [62], but very little attention has been paid to the possibly three-dimensional character of its band structure at different temperature. Therefore, in this chapter we report a systematic determination of the band dispersion along and out-of 1T-TaS<sub>2</sub> planes from very high quality crystals in the commensurate, nearly commensurate, incommensurate CDW phase. A special focus will be on the possible metallicity of the compound in direction perpendicular to 1T-TaS<sub>2</sub> crystal plane in all phases. Furthermore, we will present the first experimental study on the 3D band structure of 1T-TaS<sub>2</sub> in the normal phase, which is in perfect agreement with the theory.

This project was done in collaboration with groups from Aarhus and Kiel Universities. The sample A was grown by the research group AG Electronic Structure/Synchrotron Radiation from the Institute of Experimental and Applied Physics, University of Kiel led by Prof. Kai Rossnagel. The sample B was grown by Christina Breth Nielsen from the Department of Chemistry of Aarhus University led by Prof. Martin Bremholm. Regarding my role in this project, I prepared and measured the samples for LEED, XPS and ARPES measurements, and analyzed the data. Sanjoy K. Mahatha was also helping with samples preparation, measurements and verification of the analyzed results.

Article of relevance for this chapter:

Arlette S. Ngankeu, Sanjoy K. Mahatha, Kevin Guilloy, Marco Bianchi, Charlotte E. Sanders, Kerstin Hanff, Kai Rossnagel, Jill A. Miwa, Christina Breth Nielsen, Martin Bremholm, and Philip Hofmann: *Quasi-one-dimensional metallic band dispersion in the commensurate charge density wave of 1T-TaS<sub>2</sub>*, Phys. Rev. B **96**, 195147, 2017.

In this study, we used two sets of bulk 1T-TaS<sub>2</sub> samples (sample A and sample B) grown by two different groups as mentioned above. Both single crystal of 1T-TaS<sub>2</sub> were synthesised

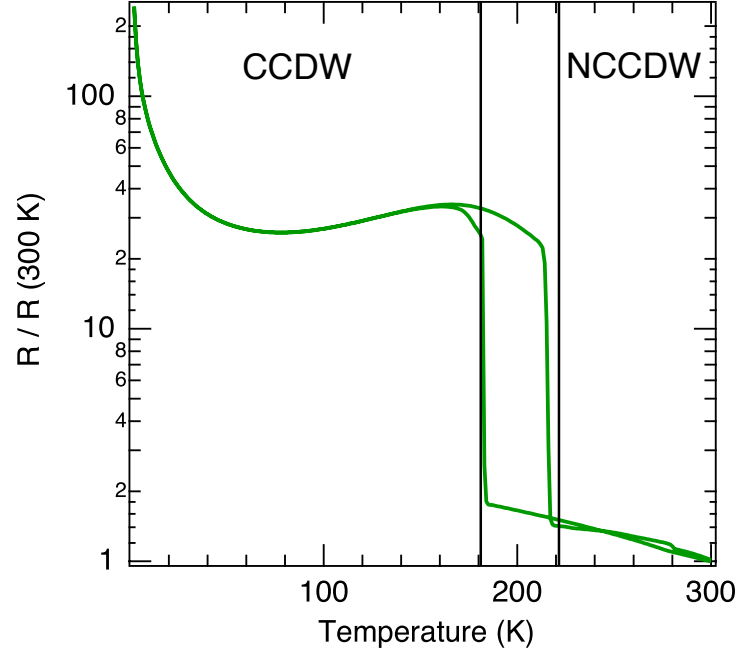


**Figure 3.2:** In-plane temperature (T) dependence of the resistivity (R/R) for bulk 1T-TaS<sub>2</sub> single crystal (sample A). The bulk sample showed the NCCDW-CCDW transition at 200 K.

from high purity elements by chemical vapor transport using iodine as a transport agent [129]. Figure 3.2 shows the in-plane transport measurements as a result of further characterization of sample A. Moreover, Figure 3.2 is in perfect agreement with other temperature dependent in-plane resistivity of bulk 1T-TaS<sub>2</sub> reports for high quality crystals in the literature [59]. Furthermore, this figure is also in perfect accord with the crystals used to study the in-plane/out-of-plane transport anisotropy by Ref. [130].

The crystals were cleaved at  $\approx 30$  K in ultra high vacuum of about  $3 \cdot 10^{-10}$  mbar in the measurement chamber. ARPES data were collected on the SGM3 end station at ASTRID2 [113]. The energy resolution altered from  $\approx 50$  to  $\approx 130$  meV for the lowest and highest photon energies, respectively. The angular resolution was better than  $0.2^\circ$ . The Fermi level (at zero binding energy) was calibrated using the Fermi edge from the polycrystalline gold.

## 3.2 ARPES Study on 1T-TaS<sub>2</sub> in the C-CDW Phase

The temperature during the ARPES measurements in the C-CDW phase was  $\approx 30$  K. By assuming free-electron final states model and by using a procedure described in appendix

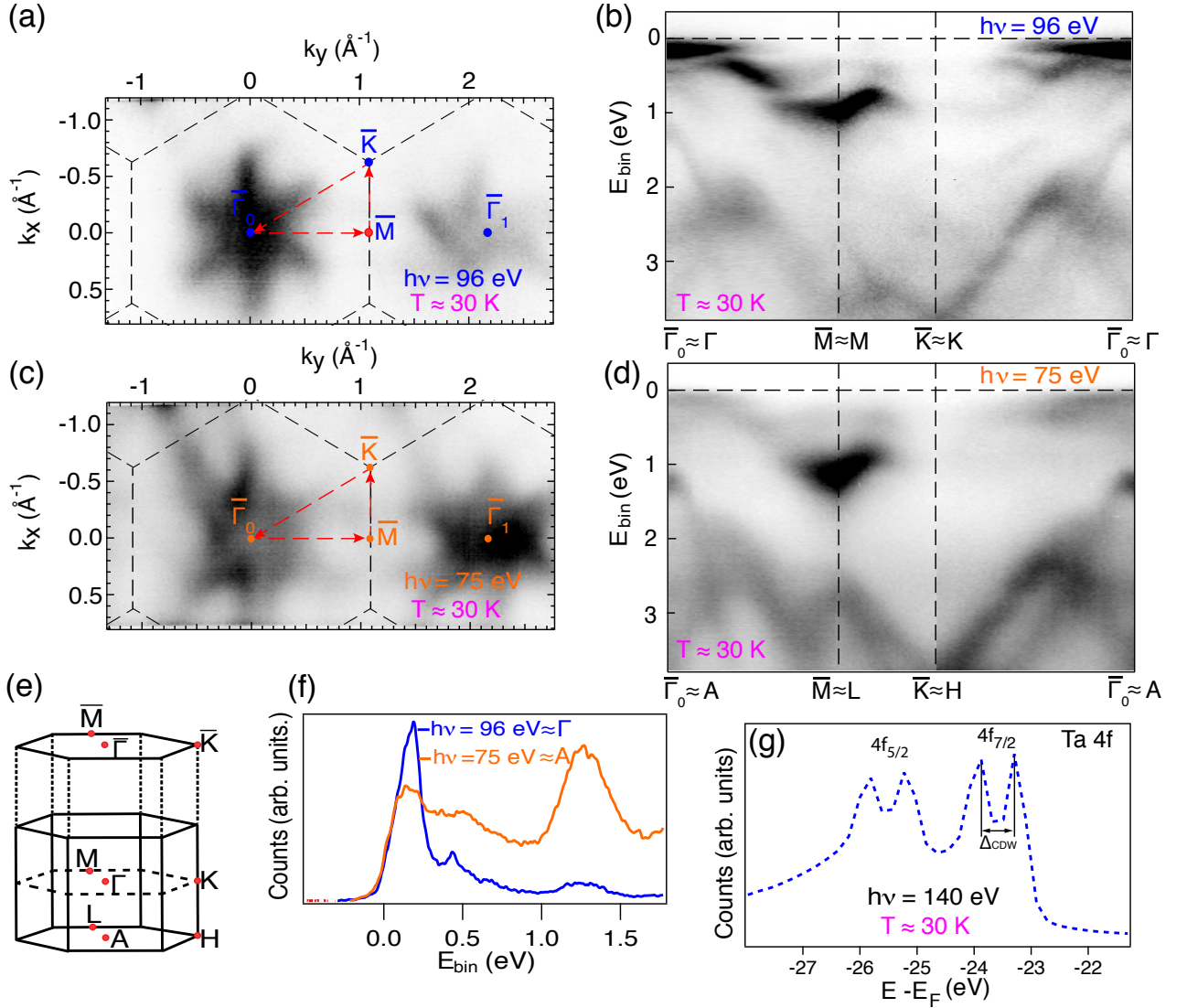


**Figure 3.3:** Constant binding energy cuts acquired with photon energies of 96 (a) and 75 eV (c), respectively. The photoemission intensity map was taken at 90 meV below the Fermi energy.  $\bar{\Gamma}_0$  represents the normal emission and the bulk  $\Gamma$  and  $A$  points in (a) and (c), respectively. ARPES bands dispersion of 1T-TaS<sub>2</sub> along the high symmetry directions of the surface Brillouin zone (presented by red dashed arrows in Figures a and c) for photon energies of 96 (b) and 75 eV (d), respectively. The dark and white colors correspond to high and low photoemission intensity, respectively. The bulk high symmetry points are reached approximately while the high symmetry points in the surface Brillouin zone are exactly reached (note the bar over the letter and see text for more detailed). (e) Drawing of the first Brillouin zone of 1T-TaS<sub>2</sub> and its projection on the (0001) surface. (f) Energy dispersion curves extracted from  $\bar{\Gamma}_0$  point in figures (b) and (d) for photon energies of 96 (blue) and 75 eV (orange). These curves correspond to the bulk  $\Gamma$  and  $A$  points, respectively. These data were reprinted from [131]. (g) Ta 4f core level spectrum of 1T-TaS<sub>2</sub> measured with the photon energy of 140 eV. Both the Ta 4f<sub>5/2</sub> and Ta 4f<sub>7/2</sub> levels are split into two peaks and these two peaks are associated with lattice sites b and c shown in Figure 1.5(a). The peak splitting is indicated by  $\Delta_{\text{CDW}}$ . These data are from sample A and were acquired  $\approx$  at 30 K.

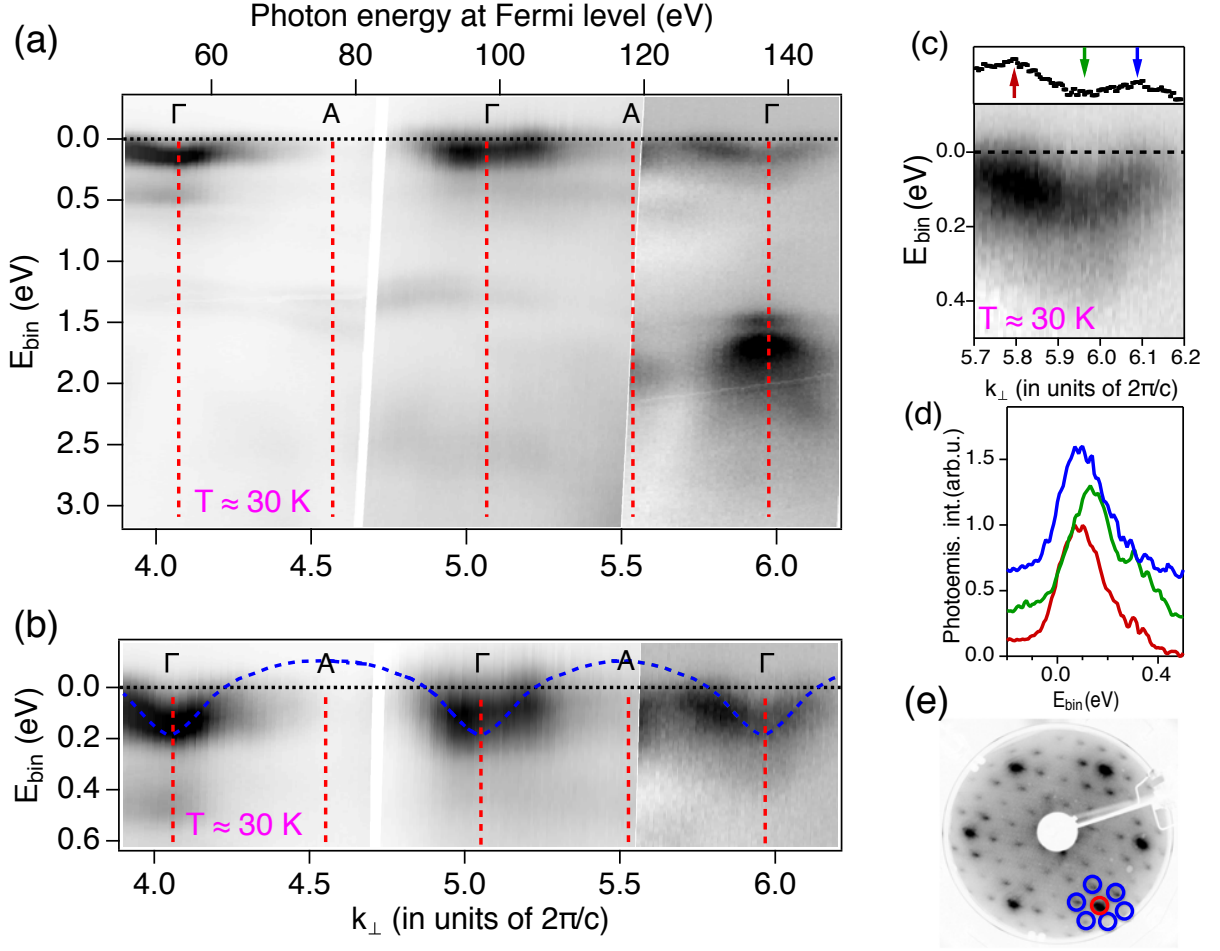
A, the two photon energies (i.e., 96 and 75 eV) used to collect the angular scan data have been choosing such that data are collected approximately in the  $\Gamma MK$  (96 eV) and  $ALH$  (75 eV) planes of the bulk Brillouin zone, respectively. The position of the high symmetry points are indicated on the sketch of the first Brillouin zone shown in Figure 3.3(e). From chapter 2 we know that in the photoemission process, only the parallel component of the crystal momentum  $\mathbf{k}_{\parallel}$  is conserved. Therefore, the high symmetry points of the surface Brillouin zone can be reached exactly. However, the high symmetry points  $\Gamma$  and  $A$  in the bulk Brillouin zone are also reached quite precisely. While the high symmetries points  $M$ ,  $K$ ,  $L$ ,  $H$  are approximately reached at finite  $\mathbf{k}_{\parallel}$ . Figures 3.3(a) and 3.3(c) show the constant energy maps taken at a binding energy of 90 meV below the Fermi level at photon energies of 96 eV and 75 eV, respectively. We can notice the difference on states close to the Fermi level, in particular on the intensity of the visible states around the  $\bar{\Gamma}_0$  and  $\bar{\Gamma}_1$  points. The photoemission intensities along the high symmetry directions  $\Gamma$ - $M$ - $K$ - $\Gamma$  and  $A$ - $L$ - $H$ - $A$  in the surface Brillouin zone for two different photon energy, 96 and 75 eV are shown in Figure 3.3(b) and 3.3(d), respectively. The two dispersions seem to look very similar to each other and are in perfect agreement with the previous ARPES results presented in the literature [50, 63, 132, 133, 134, 135, 136]. From these figures, we can notice the broad states close to the Fermi level  $E_F$ . The broadness of this states is due to the strongly correlated character of the material, with a lack of any clear Fermi surface crossings. By looking more closer these two figures, some differences can be seen. The deeper states derived from sulfur 2p [137, 138] should be less two-dimensional and indeed present a different dispersion, for instance around  $\bar{M}$  point. On the other hand, the states near the  $E_F$  are mostly differ in their intensity. This can be seen in the flat band located immediately below  $E_F$  near the  $\Gamma$  point in Figure 3.3(b) which is well defined, while it is weak at  $A$  point (see Figure 3.3(d)). The difference can also be well seen in a direct comparison of energy distribution curves passing through  $\Gamma$  and  $A$  points, as shown in Figure 3.3(f). The photoemission intensity reaches a maximum at normal emission ( $\bar{\Gamma}_0$ ) in Figure 3.3(b), while it shows a local minimum in Figure 3.3(d). Thus, this difference on intensity is an indication of a clear dependence of the electronic structure on the perpendicular crystal momentum  $k_{\perp}$ .

Figure 3.3(g) shows the Ta 4f core level spectrum measured at a photon energy of 140 eV. The tantalum  $4f_{5/2}$  and  $4f_{7/2}$  levels are split due to the spin-orbit coupling, which are both further split due to the existence of three inequivalent Ta sites (see a, b, c sites in Figure 1.5(a)) in the CDW phase [139]. It should be noted that the 4f levels on Ta a and b sites are close in energy and combine into a single peak [139]. Figure 3.3(g) is in good agreement

with such spectrum found in the literature [140, 141]. The peak splitting is indicated by  $\Delta_{CDW}$ . The value of the splitting  $\Delta_{CDW}$  is found to be in the range of 620-690 meV below the temperatures of 180 K [142]. In our case we cannot give any value for  $\Delta_{CDW}$  since the data for the core level is not good enough because we have few points and we cannot really fit the core level spectra in order to extract the value of  $\Delta_{CDW}$ .

The study of the possible existence of the quasi one-dimensional band dispersion predicted along the high symmetry direction  $\Gamma$ - $A$ , can be done by collecting the photoemission intensity in normal emission as a function of binding ( $E_{bin}$ ) and photon ( $h\nu$ ) energies, respectively. Figure 3.4(a) shows the result of such type of photoemission intensity scan. The photon energy axis (see the top axis of 3.4(a)) of the scan presented in Figure 3.4(a) was converted to  $k_{\perp}$  (see the bottom axis of 3.4(a)) using the assumption of the free-electron final states presents in appendix A. The small electron pockets appearing close to the Fermi energy around the  $\Gamma$  points (i.e., at integer multiples of  $k_{\perp} = 2\pi/c$ ) is the most important feature in the data. For the sake of clarity, the intensity near the Fermi level is magnified and shown in Figure 3.4(b). Figure 3.4(c) presents a high resolution scan of the electron pocket close to  $k_{\perp} = 12\pi/c$  (a magnification of Figure 3.4(b) around  $k_{\perp} = 12\pi/c$ ), with a momentum distribution curve (MDC) at the Fermi level on top of the figure. The central result from this photon energy scan is the experimental observation of the predicted metallic band in the  $k_{\perp}$  direction of the 1T-TaS<sub>2</sub>. Energy distribution curves taken at the position indicated by red, green and blue arrows in Figure 3.4(c) near the Fermi level crossings and at the maximum binding energy of the band are presented in Figure 3.4(d). These curves were normalized and displaced vertically. Figure 3.4(e) shows the LEED pattern of the ( $\sqrt{13} \times \sqrt{13}$ ) superstructure acquired with the kinetic energy of  $E_{kin} = 65.9$  eV at  $\approx 30$  K in the pristine 1T-TaS<sub>2</sub>. The blue circles on the LEED image indicate the ( $\sqrt{13} \times \sqrt{13}$ )R13.9° CDW superlattice and one of the Bragg spots is indicated by the red circle. This picture is in excellent agreement with those present in the literature [132, 143].

To recover an approximate initial states  $k_{\perp}$  using free-electron final states model, it is required to choose an appropriate inner potential  $V_0$  and work function  $\Phi$  of the solid [144]. Here we used  $V_0 = 20$  eV and  $\Phi = 4.5$  eV in order to place electron pockets that appear periodically close to each  $\Gamma$  point of the Brillouin zone. It should be noted that the value of the inner potential that we used is different from those used in the very early studies [138]. Therefore, we underline that the exact choice of this parameter is not crucial. In fact, due to the symmetry of the band dispersion of the electron pocket, it can only be put at the symmetry point  $\Gamma$  or  $A$ . Moreover, the choice of the inner potential below 40 eV would not lead the



**Figure 3.4:** (a) Photon energy dependent ARPES measurements, presenting the dispersion and intensity variation of the electronic states around  $\Gamma$  for the bulk 1T-TaS<sub>2</sub>. Here, the free-electron final states were used to convert the photon energy to  $k_{\perp}$  and these values are presented in units of the reciprocal lattice vector  $2\pi/c$ . The photon energy values given at the top axis of this figure, are assigned to the photon energy for the states at the Fermi energy. The maximum binding energy of the small electron pocket near  $\Gamma$  together with the  $k_{\perp}$  located in the middle of the two  $\Gamma$  points are marked by the dashed red lines. (b) Scale up view of the intensity in the surroundings of the Fermi energy. The intensity was normalized by an exponential function of the photon energy. The dashed blue lines are the result of the calculation from Ref. [66]. (c) High resolution ARPES scan of the electron pocket close to the Fermi level and  $k_{\perp} = 12\pi/c$  from (b). The black curve on top of this figure is a momentum distribution curve taken at the Fermi level. The data in this image were normalized by dividing each energy distribution curve (EDC) with its integrated intensity. (d) EDCs taken at the maximum binding energy and close to the Fermi level crossings of the band as indicated by green, red and blue arrows in (c). These data were reprinted from [131]. (e) Low energy electron diffraction (LEED) patterns for 1T-TaS<sub>2</sub> measured with the kinetic energy  $E_{\text{kin}} = 65.9$  eV. The blue circles on the LEED image denote the  $(\sqrt{13} \times \sqrt{13})R13.9^{\circ}$  CDW superlattice. One of the Bragg spots is indicated by the red circle. These data are from sample B and were acquired at  $\approx 30$  K.

electron pocket to be found at  $A$  point. The symmetry of the deeper p-bands of sulphur that show a binding energy minimum at  $\Gamma$  also confirms the choice of the inner potential [137]. This minimum is well pointed out at a binding energy of  $\approx 0.17$  eV for  $k_{\perp} = 12\pi/c$ . Figure 3.4(b) presents the perfect agreement between the calculated band structure (dashed blue lines) from Ref. [66] and the data. Very similar calculated band dispersions were calculated in references [63, 127, 128, 145]. Furthermore, a real space periodicity of only one unit cell is suggested by the observed  $k_{\perp}$  periodicity of  $2\pi/c$  and thus, the  $\tau_c$  stacking i.e., a stacking in which the central atoms of the stars of David are put directly on top of each other in adjacent layers.

On the other hand, a regular  $\tau_c$  stacking is not in agreement with a large amount of information on the stacking structure of bulk 1T-TaS<sub>2</sub> along the  $c$ -axis available in the literature on the commensurate CDW phase [146, 147]. Disorder in the  $c$  direction of the bulk 1T-TaS<sub>2</sub> structure was revealed by data from different techniques, which is accompanied by different stacking orders. A direct probe of the  $c$ -axis order by electron microscopy has proposed a quasi-periodic ordering with  $\tau_c$  stacking alternating with stacking which involves an in-plane translation [147]. The diffraction pattern derived from this looks similar like that for a doubled periodicity in the  $c$  direction. Nevertheless, the ARPES observations are not directly contradicted by these structural results. It should be noted that disorder simply increases the background intensity while, only periodic contributions to the stacking produce any regular band structure. Furthermore, the quasi-periodic stacking with a  $2c$  real space periodicity [147] would be compatible with the dispersion seen along the  $k_{\perp}$  direction in our data if the Fourier components for the expected replica bands around  $A$  were very weak.

Another way to see the  $2\pi/c$  periodicity of the band structure presented in Figures 3.4(a) and 3.4(b) is that, even in the presence of a CDW, this would be expected for every band in the 1T polymorph. Furthermore, an accurate calculation on the band structure of the distorted 1T structure (where the significant spin-orbit coupling was taking into account [148]) have shown a very similar metallic dispersion along the  $\Gamma$ - $A$  direction, despite that the in-plane dispersion is completely different from the CDW case [66].

The distinct differences in the constant energy maps in Figures 3.3(a) and 3.3(c) (the band is occupied at  $\Gamma$  and empty at  $A$ ) can also be explained by the observed electron pocket around  $\Gamma$ . Ritschel and coworkers have disputed the common opinion that this band is the lower Hubbard band of the Mott insulating state because it can be reproduced by a calculation that does not include correlations [63]. Nevertheless, the situation seems to be more complicated

than we think, because the metallic band structure appears to coexist with a portion of the spectral weight at the original peak position of the lower Hubbard band, as shown the energy distribution curves in Figure 3.3(f). Indeed, the peak usually assigned to the lower Hubbard band significantly changes its intensity but never completely disappears, not even at point A of the Brillouin zone (corresponding to  $h\nu = 75$  eV) where the highly dispersive metal band is predicted to be well above the Fermi level. Given the partly disordered character of the CDW along  $c$  [146, 147], such a complex behavior is not unexpected, and it restricts the formation of a well-defined band structure in this direction.

The transport measurements done in this material are partially compatible with the observation of a metallic band in this system. A metallic temperature dependence of the resistivity is observed in the temperature range below the transition to the commensurate CDW ( $\approx 50$ – $80$  K), which is consistent with the remaining metallic band [149], but, the resistivity increases strongly at very low temperature [149] and this is consistent with transport data shows in Figure 3.2 from the samples used in this work.

One would expect the resistivity  $\rho_c$  in the  $c$  direction to be lower than the resistivity  $\rho_a$  in the plane because of the one-dimensional metallic dispersion along this direction. But this is not the case, because a direct measurement of  $\rho_c/\rho_a$  done by Hambourger and his colleague gives a value of  $\approx 500$  [130], even in the metallic conductance's temperature range. This seems to contradict our results, but the lack of metallic conduction could be due to a gap opening in the one-dimensional dispersion close to the Fermi level  $E_F$ . But this is not what we see in the dispersion presented in Figure 3.4(c), which clearly shows a Fermi level crossings. However, the broad features presents in Figure 3.4(c) do not allow us to give a definite conclusion about the formation of a small gap around the Fermi level. It should be noted that this broadening is an intrinsic limitation of  $k_\perp$  bands dispersion measured by ARPES because  $k_\perp$  is not conserved in photoemission process due to the broken translational symmetry at the crystal surface. Furthermore, the measured  $k_\perp$  experienced an intrinsic uncertainty that comes from the short inelastic mean free path of electrons in solids [144]. The presence of the lower Hubbard band and the dispersive band in the  $k_\perp$  direction throughout the bulk Brillouin zone rise the difficulty to identify a clear gap opening.

In conclusion, in our study we have indeed observed the theoretically predicted one-dimensional metallic band in the direction perpendicular to the planes. This has recently been predicted by many calculations but so far has never been observed. Furthermore, the occupied band width and the periodicity observed in the dispersion are in agreement with a simple  $\tau_c$  stack-

ing order of the CDW. This experimental result strongly shows that one cannot view the TMDCs CDW materials as quasi two-dimensional. Due to the rich physics presented by the bulk TaS<sub>2</sub>, one can also expect to have some more interesting physics in its monolayer form. Due to the absence of interaction between neighboring planes in the crystal and also because its electronic properties can be affected by substituting these planes with other materials of choice. Chapter 4 will present some studies done on TaS<sub>2</sub> in its single and bilayer form.

### 3.3 ARPES Study on 1T-TaS<sub>2</sub> in the NC-CDW Phase

The similar study on the bulk 1T-TaS<sub>2</sub> presented in section 3.2 is done in this section. The only difference is the temperature at which we acquired the data. The temperature during the ARPES measurements in the NC-CDW phase was  $\approx 340$  K. There are very few ARPES studies on 1T-TaS<sub>2</sub> in the NC-CDW phase, but we will compare our results with the existing data in Refs. [138, 150, 151] and data presented in the previous section. It should be noted that the data present in this section were obtained upon heating the 1T-TaS<sub>2</sub> single crystal. The data are from sample B.

Figures 3.5(a) and 3.5(c) present constant energy scans acquired at photon energy of 96 and 75 eV, respectively. In these two figures, we can notice from the photoemission maps that the band is occupied at  $\Gamma$  and empty at  $A$ . The well defined flat band found immediately below the Fermi level  $E_F$  close to  $\Gamma$  point is shown in Figure 3.5(b), whereas it appears to be weak at  $A$  point (see Figure 3.5(d)). This can be seen further in Figure 3.5(f) that compares directly the energy distribution curves passing through  $\Gamma$  and  $A$  points. Figure 3.5(e) shows the surface and Brillouin zone of 1T-TaS<sub>2</sub> and the notations of high symmetry points. Even at  $\approx 340$  K a CDW splitting of the Ta 4f lines is clearly resolved (see Figure 3.5(g)). Zwick and coworkers [49] have also studied the temperature dependence on the 4f spectra and their results on Ta 4f lines taken at the NC-CDW phase (300 K) show the splitting of the Ta 4f lines which is in agreement with our result.

Figure 3.6 shows ARPES data within the  $k_x k_y$ -plane at different binding energies and two photon energies 96 (left) and 75 (right) eV. The intensity distribution of ARPES spectra for both photon energies shows a pronounced sixfold symmetry up to few meV below the Fermi level, while the threefold symmetry is pronounced at the higher binding energy for instance at 0.91 eV. Thus, this variation of the photoemission intensity might be assigned to the matrix elements effects. The same observation was made on the data acquired on bulk

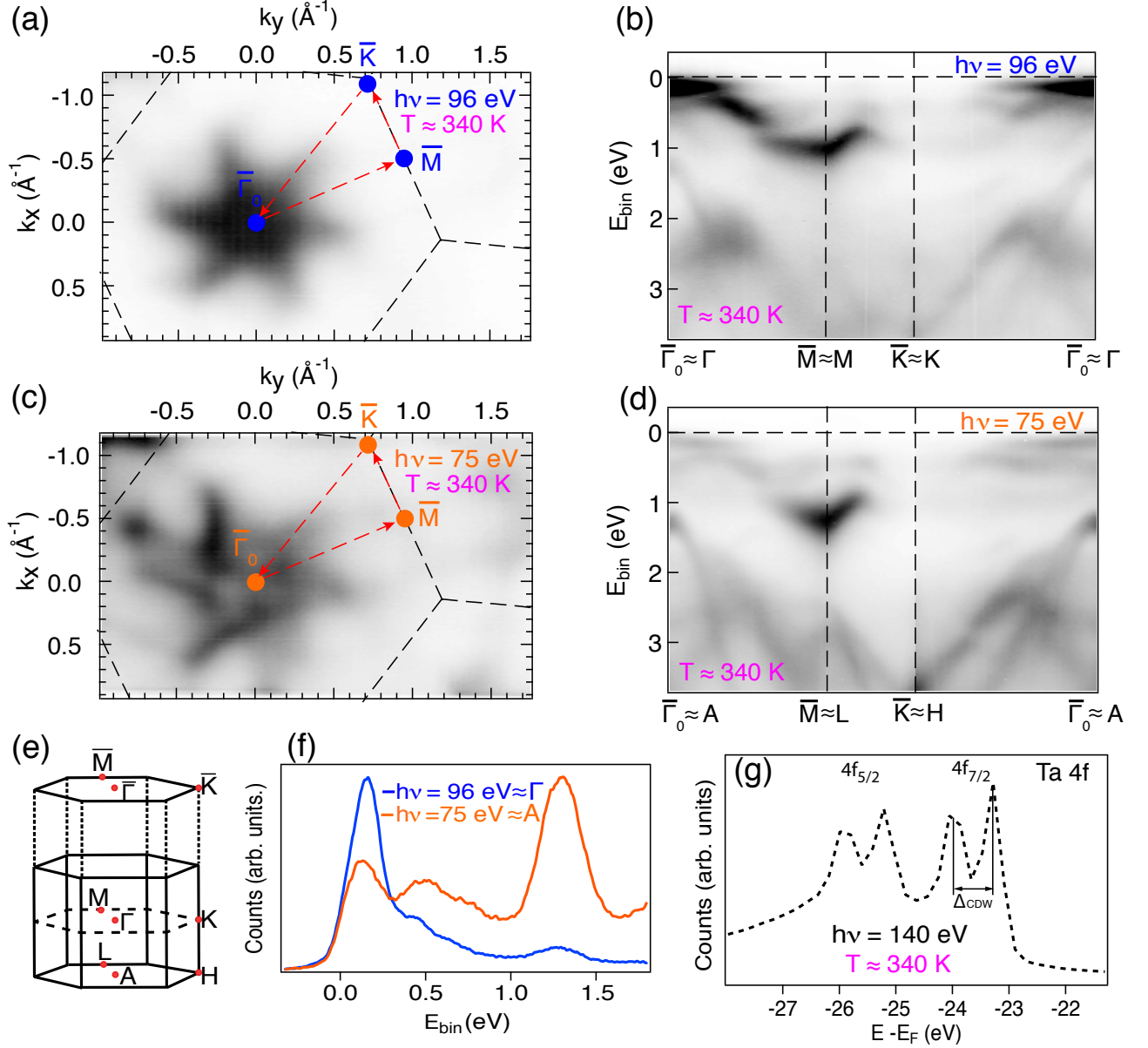


**Figure 3.5:** In-plane electronic structure of bulk 1T-TaS<sub>2</sub> acquired at  $\approx 340$  K. Constant binding energy maps taken at 90 meV below the Fermi energy level for photon energies of 96 (a) and 75 eV (c), respectively. The normal emission here is represented by  $\bar{\Gamma}_0$ . The Brillouin zone boundaries (dashed black lines) were plotted on top of the two maps. The high symmetry points are also indicated. The red dashed lines shows the cuts direction presented in (b) and (d). Photoemission intensity along high symmetry directions of the surface Brillouin zone for photon energies of 96 (b) and 75 eV (d), respectively. (e) Surface and bulk Brillouin zones of the single crystal 1T-TaS<sub>2</sub>. (f) Energy dispersion curves taken at  $\bar{\Gamma}_0$  point from figures (b) blue and (d) orange. (g) Tantalum Ta 4f core level line of 1T-TaS<sub>2</sub> measured at 140 eV. The splitting of the  $4f_{5/2}$  and  $4f_{7/2}$  is observed on this spectrum and the distance between the peak splitting ( $\Delta_{\text{CDW}}$ ) is also indicated.

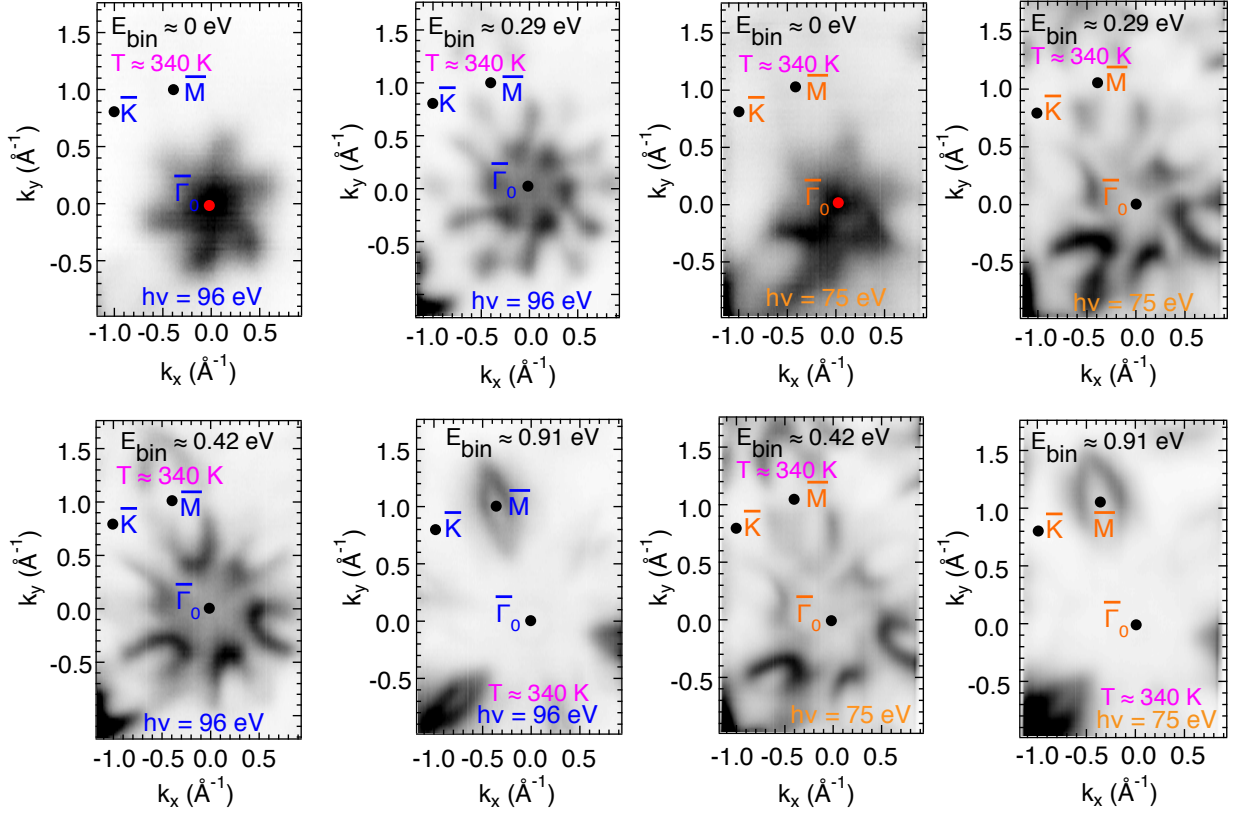


**Figure 3.6:** Constant energy contours through the first Brillouin zone of bulk 1T-TaS<sub>2</sub>, showing how the distribution of the photoemission intensity is sixfold symmetry few meV below the Fermi energy, and becomes threefold at a very high binding energy for example at 0.91 eV.

1T-TaS<sub>2</sub> at different temperatures ( $\approx 30$ ,  $\approx 340$ ,  $\approx 450$ , and  $\approx 600$  K) but we did not show the scans in this thesis.

Figure 3.7(a) exhibits a photon energy dependent ARPES measurements of 1T-TaS<sub>2</sub> acquired at  $\approx 340$  K. Here the conversion of the top axis ( $h\nu$  axis) into the bottom ( $k_{\perp}$  axis) was done using the free-electron final states as shown in appendix A. The relevant result here is the small electron pockets observed in the dispersion around  $\Gamma$  point and close to the Fermi level. This feature at  $\Gamma$  point is enlarged and presented in Figure 3.7(b) in order to highlight those parabolas. The blue dashed curves plotted on top of 3.7(b) are the calculated band structure from Ref. [66], which is in good accord with the data. A high resolution scan of the electron pocket near to  $k_{\perp} = 12\pi/c$  presents in Figure 3.7(c) is simply the enlargement of Figure 3.7(b) around  $k_{\perp} = 12\pi/c$ . This figure also present MDC (black curve) extracted from the Fermi level. The red, green and blue arrows indicate the position where the different EDCs present in Figure 3.7(d) were taken. The EDCs were normalized and displaced vertically.

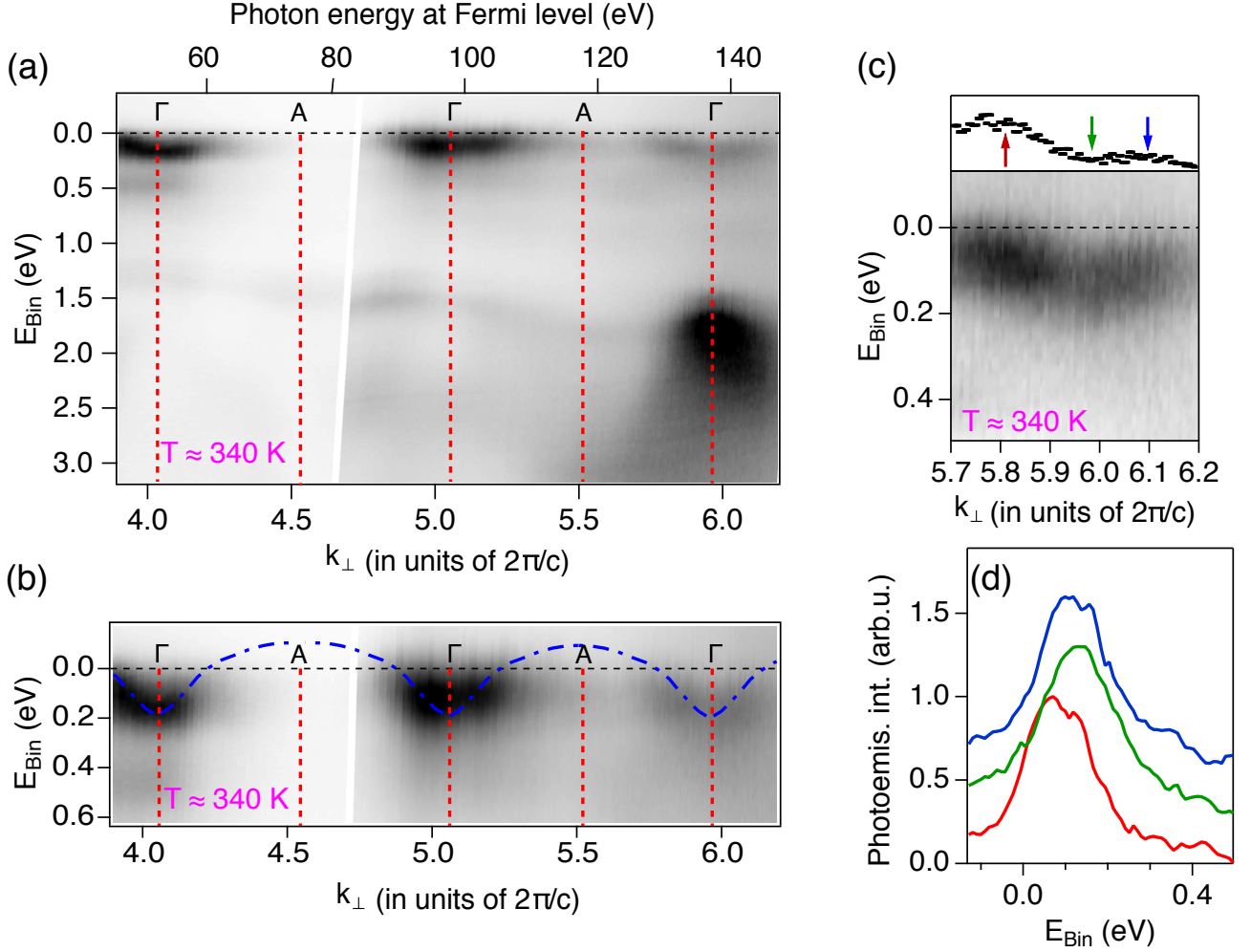


**Figure 3.7:** (a) Photoemission intensity measured in normal emission as a function of photon energy  $h\nu$  (top axis) from the single crystal 1T-TaS<sub>2</sub>. This scan shows the intensity variation and the dispersion of the electronic states around  $\Gamma$  point. Here the photon energy axis was converted to  $k_{\perp}$  (bottom axis) using free electron final states, and  $k_{\perp}$  is given in units of the reciprocal lattice vector  $2\pi/c$ . The maximum binding energy of the small electron pocket close to  $\Gamma$  point and the  $k_{\perp}$  values located in the middle of two  $\Gamma$  points are indicated by red dashed lines. Here, the intensity was normalized by an exponential function of the photon energy. (b) Enlargement of the photoemission intensity showing in (a) in the proximity of the Fermi energy, in order to show the well resolved parabola shape of the electron pocket around  $\Gamma$  points. The dashed blue curves are the theoretical result of the calculation from Ref. [66]. (c) Band dispersion showing a high resolution scan of the electron pocket close to  $k_{\perp} = 12\pi/c$ . A momentum distribution curve (MDC) taken at the Fermi energy is presented by the black curve plotted on top of this figure. The data presented in this image was normalized by dividing each energy distribution curve (EDC) by its integrated intensity. (d) Different EDCs taken at the positions showing by red, green and blue arrows in (c) i.e., close to the Fermi level crossings and at maximum binding energy of the band. The curves were normalized and displaced vertically. The Data are from sample B.

In summary, the overall results on the ARPES study of bulk 1T-TaS<sub>2</sub> presented in this section are very similar to those presented in section 3.2 since the electronic structure of 1T-TaS<sub>2</sub> in this phase is still influenced by the CDW states. As mentioned at the beginning of this chapter, the only difference between the two set of studies is that the NC-CDW phase contains distorted kagome lattice domains [39] or in other words, CDW hexagonal domains separated by metallic incommensurate (IC)-CDW domain walls (see Figure 3.1(a)). Therefore, we can just draw the same conclusion made in the CDW phase i.e., in the NC-CDW phase the one-dimensional metallic band dispersion along the  $k_{\perp}$  is also observed.

### 3.4 ARPES Study on 1T-TaS<sub>2</sub> in the IC-CDW Phase

The exact same study on the bulk 1T-TaS<sub>2</sub> presented in sections 3.2 and 3.3 has been performed in this section, but the only difference is the temperature at which we took the data. The temperature during the ARPES measurements in the IC-CDW phase was  $\approx 450$  K. We have performed this ARPES experiment on 1T-TaS<sub>2</sub> in the IC-CDW phase in order to reveal the electronic structure of this system in this phase. There is a very little study on the electronic structure of 1T-TaS<sub>2</sub> in the IC-CDW phase. We will compare our data with the existing electronic structure of this system taken at 370 K by Ref. [134]. It should be noted that the data presented in this section were obtained upon cooling down the sample (1T-TaS<sub>2</sub> single crystal) from elevated temperature. The data are from sample B.

Figures 3.8(a) and 3.8(c) shows the ARPES photoemission intensity map along  $k_y k_x$  plane taken at photon energy of 96 (a) and 75 eV (c), respectively. From these figures we can again see that the band around  $A$  seems to be absent, while the one around  $\Gamma$  is occupied. The band structure along the high symmetry direction indicated by red dashed lines is presented in Figures 3.8(b) and 3.8(d). The states close to  $E_F$  differ also in their intensity. This can be seen on the well defined band located below  $E_F$  close to  $\Gamma$  point in Figure 3.8(b), while it is weak at  $A$  (see Figure 3.8(d)). This can be clearly seen in the EDCs spectra presented in Figure 3.8(f). It should be noted that these EDCs spectra are taken from the normal emission ( $\bar{\Gamma}_0$ ) from Figures 3.8(b) and 3.8(d). Figure 3.8(e) just exhibits the bulk and surface Brillouin zone of 1T-TaS<sub>2</sub>, with the high symmetry point notations. The band dispersion along the  $\Gamma$ - $M$  direction presents by Ref. [134] is in perfect agreement with our result obtained in the same direction. The influence of the CDW on the electronic structure of 1T-TaS<sub>2</sub> on this phase is still visible in the proximity of the Fermi level  $E_F$

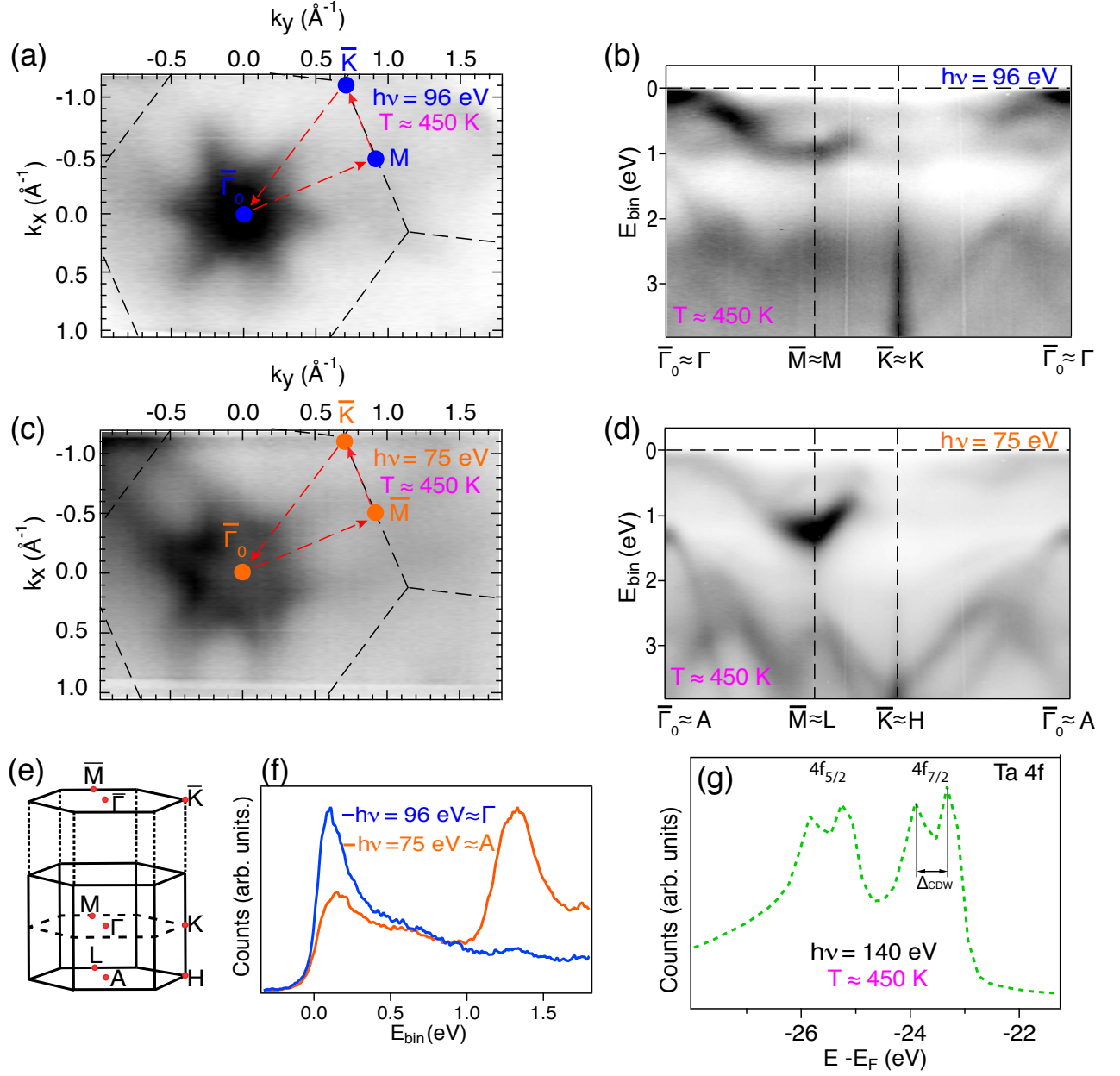


**Figure 3.8:** (a) In- plane electronic structure of bulk 1T-TaS<sub>2</sub> acquired at  $\approx 450$  K. ARPES constant energy maps obtained at 90 meV below the Fermi energy from two photon energies 96 (a) and 75 eV (c), respectively.  $\bar{\Gamma}_0$  denotes the normal emission. The surface Brillouin zone (dashed black lines) is superimposed with the two maps. The high symmetry directions  $\bar{\Gamma}_0$ - $\bar{M}$ - $\bar{K}$ - $\bar{\Gamma}_0$  (red lines) is also indicated. ARPES bands dispersion taken along the high symmetry directions of the Brillouin zone for photon energies of 96 (b) and 75 eV (d), respectively. (e) Surface and bulk Brillouin zone of 1T-TaS<sub>2</sub>. (f) Energy dispersion curves extracted at  $\bar{\Gamma}_0$  point from figures (b) blue and (d) orange. (g) Ta 4f core level spectrum of 1T-TaS<sub>2</sub> measured at 140 eV. The splitting of the  $4f_{5/2}$  and  $4f_{7/2}$  is still visible at  $\approx 450$  K. The distance between the peak splitting is given by  $\Delta_{\text{CDW}}$ .

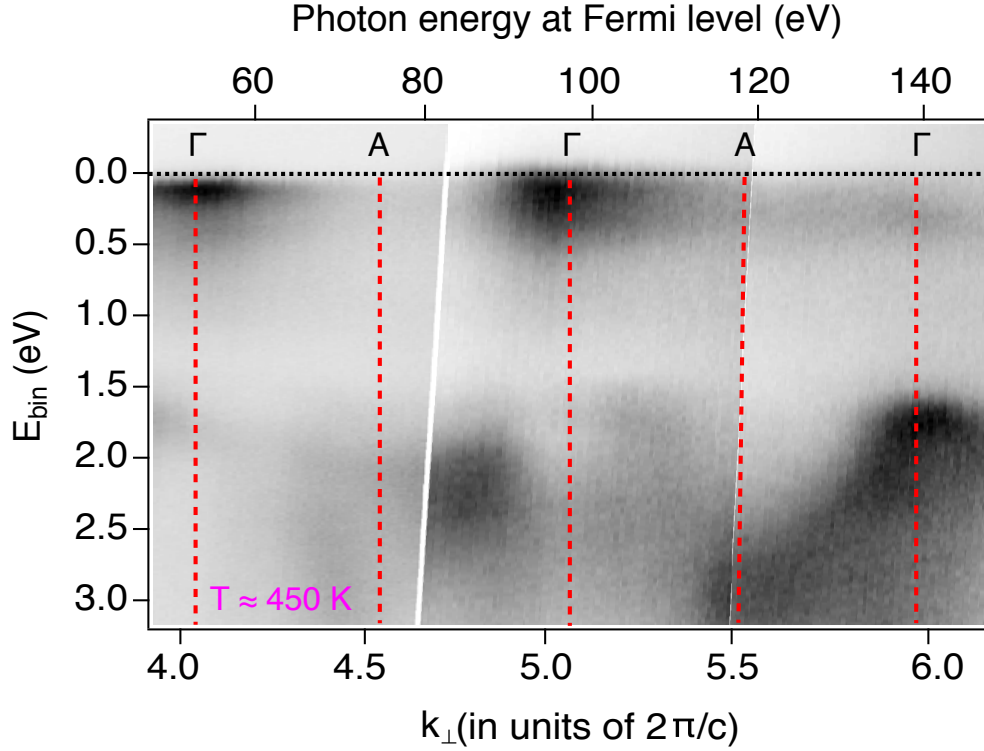


**Figure 3.9:** Out of plane electronic structure of bulk 1T-TaS<sub>2</sub> acquired at  $\approx 450$  K. Photon energy  $h\nu$  ( $k_{\perp}$ ) dependence measurements of the bulk 1T-TaS<sub>2</sub>. The photon energy  $h\nu$  (top axis) was converted to  $k_{\perp}$  (bottom axis) by using the free electron final states model. The values of  $k_{\perp}$  are presented in units of the reciprocal lattice vector  $2\pi/c$ . The dashed red lines indicated the maximum binding energy of the small electron pocket located in the proximity of  $\Gamma$  point and the values of the  $k_{\perp}$  located between those two electron pockets. The intensity was normalized by an exponential function of the photon energy. The Data are from sample B.

Figure 3.8(g) shows that even at  $\approx 450$  K a CDW splitting of the Ta 4f lines is still resolved, indicating the presence of the CDW domains in this state. One should note the decreasing splitting on the Ta 4f lines observed in Figure 3.8(g) is due to the reduction of the CDW domains size in the IC-CDW phase (see Figure 3.1(a)). There are many studies on the Ta 4f in the literature [140, 152] in the IC-CDW which do not agree with our result. For example, Ishizaka et al., [152] have studied the temperature dependent core level of the 1T-TaS<sub>2</sub> using time resolved photoelectron spectroscopy with 60 eV laser source. In their results they found that at 373 K, where the CDW is supposed to be incommensurate, the Ta 4f spectrum shows rather a broad peak feature, which is in contradiction with our result. We rather obtained a broad peak features on the core level of 1T-TaS<sub>2</sub> acquiring at  $\approx 600$  K that we believe to be the temperature for the normal state.

Figure 3.9 exhibits the photon energy scan acquired at  $\approx 450$  K. The photon energy axis (top

axis) has been converted to  $k_{\perp}$  (bottom axis) by using again the free-electron final states model presented in appendix A. As one can notice there is no parabola dispersion around  $\Gamma$  point even though the system still present some lattice distortions in this phase. We can still see the strong intensity modulation with the band being more intense at  $\Gamma$  point. One reason for seen this strong intensity modulation with the band being most intense at  $\Gamma$  point in Figures 3.9 might be due to the fact that the entire dispersion shows in Figures 3.4(a) or 3.4(b) is lifted above the Fermi level and we are just observing a tail of it below the Fermi level. We have already mentioned in section 3.2 that the metallic band structure appears to coexist with a portion of the spectral weight at the original peak position of the lower Hubbard band (located around 0.2 eV below the Fermi energy [135]). Thus, this band around  $\Gamma$  point is the signature of the lower Hubbard band. This is supported by Ref. [153] which states that at high temperature there are still some strong fluctuation of David stars with no long range order. Thus, we can still have some character of the CDW at high temperature in the crystal and this can still be observed from the photoemission intensity from ARPES, since this technique averages everything.

### 3.5 ARPES Study on 1T-TaS<sub>2</sub> in the Normal Phase

For the normal undistorted phase of 1T-TaS<sub>2</sub>, there exist many band structure calculations [66, 154, 155, 156] but there is no experimental band structures of this system acquired in this phase. In this section we will present the first ARPES photoemission study of 1T-TaS<sub>2</sub> at the normal phase. The temperature during the ARPES measurements at the normal phase was  $\approx 600$  K. It should be noted that the data present in this section were obtained upon heating the 1T-TaS<sub>2</sub> single crystal. The data are from sample B.

The Fermi surface of 1T-TaS<sub>2</sub> in the normal phase consists of electron pockets centered around  $M$  points as shown Figures 3.10(a) (96 eV) and 3.10(c) (75 eV), respectively. The band dispersion taken along the high symmetry direction indicated by red lines in Figures 3.10(a) and 3.10(c) is presented in Figures 3.10(b) and 3.10(d), respectively. We can still notice from Figures 3.10(a) and 3.10(c) that the state around  $\Gamma$  point is occupied, while it is empty at  $A$  point. This can be well seen in Figure 3.10(f), which present the MDCs curves taken at the normal emission ( $\bar{\Gamma}_0$ ) from (b) blue and (d) orange. The bulk and surface Brillouin zone of the TMDC 1T-TaS<sub>2</sub> is presented by Figure 3.10(e). Furthermore, the influence of the CDW is not seen in the band located in the proximity of the Fermi

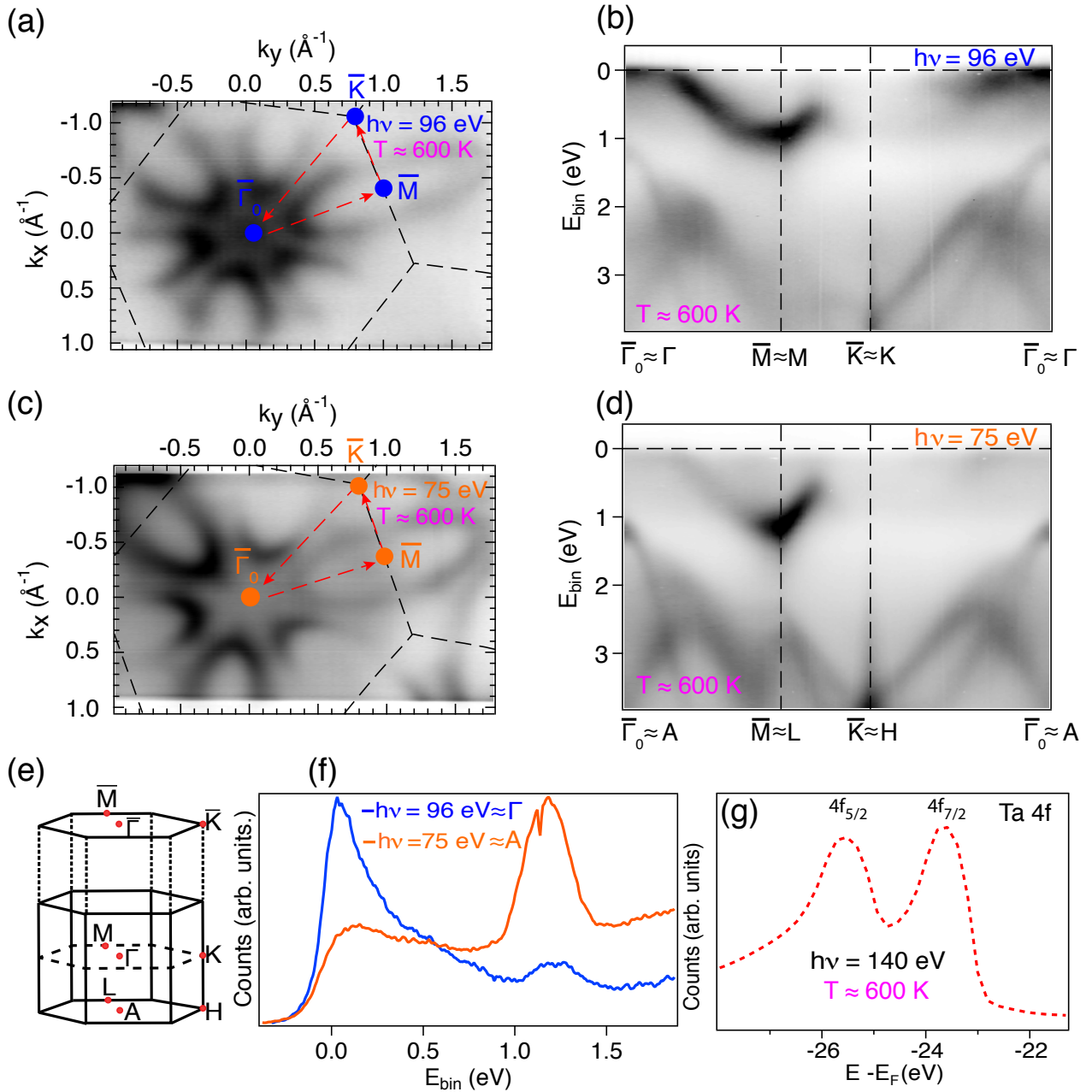


**Figure 3.10:** ARPES data measured at  $\approx 600 \text{ K}$  obtained with two photon energies. Photoemission intensity near the Fermi energy showing the topology of the equi-energy contours for the transition metal d derived states in the normal phase acquired at photon energy of 96 (a) and 75 eV (c), respectively. The normal emission is indicated by  $\bar{\Gamma}_0$ . The Brillouin zone boundaries (dashed black lines) are overlaid on the data. Band dispersion maps as a function of binding energy and momentum along the high symmetry directions of the first Brillouin zone for photon energy of 96 (b) and 75 eV (d) are presented. (e) Bulk and surface Brillouin zone of 1T-TaS<sub>2</sub> and notations of high symmetry points. (f) Energy distribution curve extracted at  $\bar{\Gamma}_0$  point from figures (b) blue and (d) orange. (g) Tantalum Ta 4f core level line of 1T-TaS<sub>2</sub> measured at 140 eV. There is no splitting on the  $4f_{5/2}$  and  $4f_{7/2}$  peaks. The Data are from sample B.

energy. Our results agree very well with the theory [66, 154, 155, 156]. Figure 3.11 show a comparison of the Fermi surface of the bulk 1T-TaS<sub>2</sub> acquired at 96 eV (a) and 75 eV (b) with its calculated Fermi contours (c) from Ref. [62]. The black hexagon in (c) and the dashed lines in (a) and (b) are Brillouin zone boundaries.

Figure 3.10(g) shows that at  $\approx 600$  K no splitting is resolved in the Ta 4f peaks, the two peaks are rather broad without any shoulders associated to them. Refs. [103, 140, 152] obtained the same type of peaks. In particular, Ishizaka et al., [152] observed the same broadening Ta 4f peaks in the high temperature phase where the lattice crystal of bulk 1T-TaS<sub>2</sub> do not present any lattice distortion.

In addition to the study of the in-plane electronic band structure of 1T-TaS<sub>2</sub> in the normal phase, we also study the band dispersion along the  $k_z$  direction (i.e., out-of-plane or perpendicular to the crystal plane) of this system in this phase. The photon energy scan acquired at  $\approx 600$  K is presented in Figure 3.12. No parabolic dispersion is observed around  $\Gamma$  point in this figure, we rather see again the strong intensity modulation with the band being most intense at the  $\Gamma$  point as seen in section 3.4. Since Figures 3.12 and 3.10 are similar, we can just draw the same conclusion mentioned at the end of section 3.4 i.e., the strong intensity modulation with the band being most intense at  $\Gamma$  point below the Fermi level in Figure 3.12 might be due to the fact that the entire dispersion shows in Figures 3.4(a) or 3.4(b) is also lifted above the Fermi level and we are just observing a tail of it below the Fermi level. Furthermore, this band around  $\Gamma$  point is a signature of the lower Hubbard band. This is supported by Ref. [153] that explains that at high temperature there are still some fluctuation of David stars with no long range order. Since, the photoemission technique averages everything, we can still observed some character of the CDW at high temperature on the photoemission scans.

For the sake of checking whether the data obtained on the electronic structure of the 1T-TaS<sub>2</sub> compound taken at the temperature of  $\approx 600$  K are consistent with the expected electron filling, we have calculated the number of electron per unit cell using the method and similar formula (see equation 3.1) given in section 4.2.2 from chapter 4. In order to calculate the area of the six electron pockets centered around M point, we have calculated the area of the full ellipse shows by the stars in cyan color in Figures 3.11(d) or 3.11(e) and then divided the answer by 2 since only half of the pocket is contained inside the Brillouin zone boundary, and finally we multiplied the answer by 6 since we have six electron pockets centered around M point. The areas of one electron pocket centered around M point (see the stars in cyan

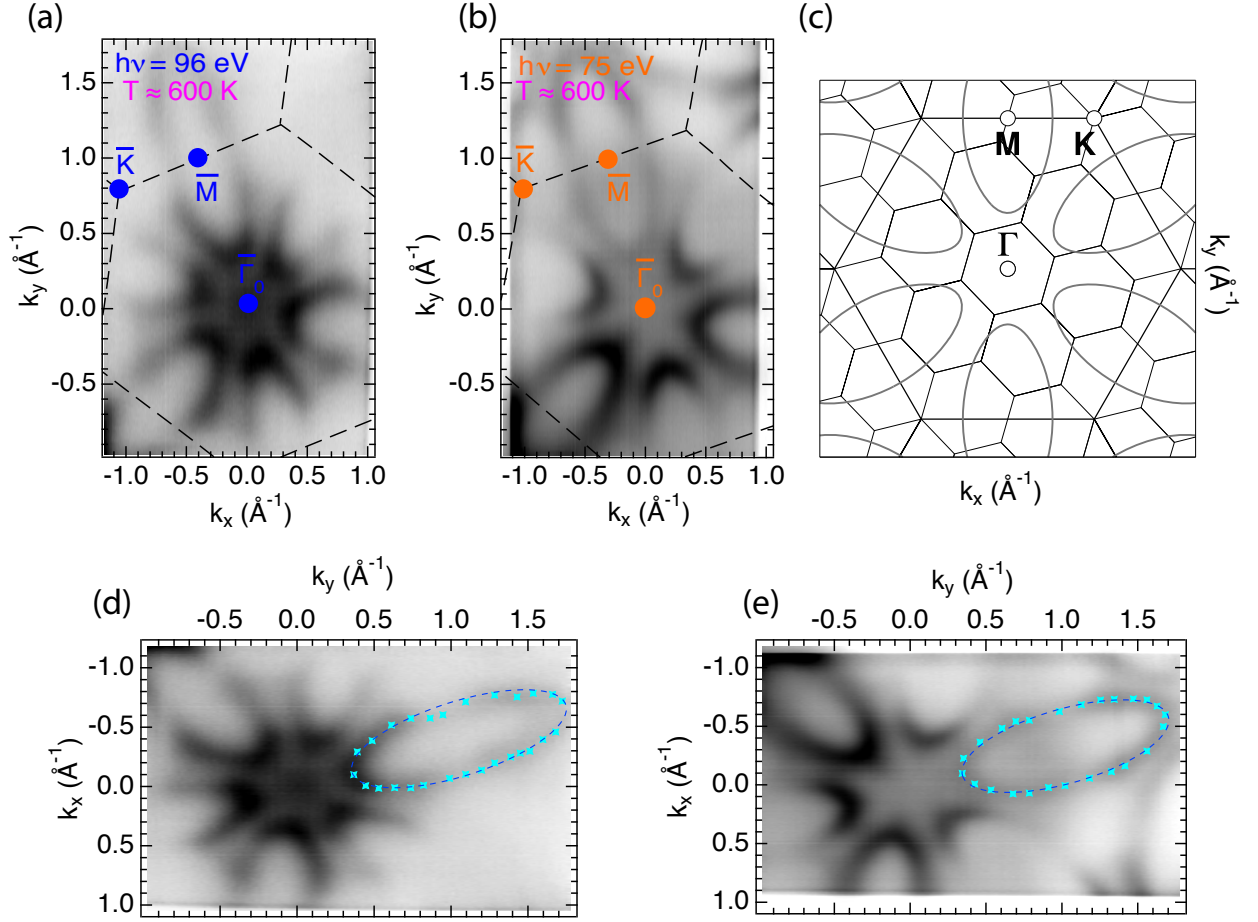


**Figure 3.11:** Comparison of photoemission intensity maps within the  $k_x k_y$ -plane near the Fermi energy of the bulk 1T-TaS<sub>2</sub> acquired at  $\approx 600$  K in the normal state at the photon energy of 96 (a) and 75 eV. (b) with the theoretical maps (c) from Ref. [62]. (d, e) Fermi surface of 1T-TaS<sub>2</sub> presented in (a) and (b) showing the extrapolated Fermi level crossings indicated by stars in cyan color. The method used in order to obtain these Fermi level crossings is explained in section 4.2.2 in chapter 4. The blue ellipses are guide to the eye to follow one electron pocket centered around M points. The ARPES data presented here were acquired with sample B.

color in Figures 3.11(d) or 3.11(e)) were calculated with the formula from a regular ellipse together with some built-in functions in Igor pro software (for example polygonarea). The values for the calculated areas from these methods were similar. The areas for the whole six electron pockets centered around M point from the photoemission scans taken at 96 (Figure 3.11(a)) and 75 eV (Figures 3.11(b)) are  $1.96 \text{ \AA}^{-2}$  and  $2.06 \text{ \AA}^{-2}$ , respectively. The area of the hexagonal Brillouin zone boundary was calculated as well by using the in-plane lattice parameter  $a=3.365 \text{ \AA}$  and its value was found to be  $4.03 \text{ \AA}^{-2}$ . By now using the equation

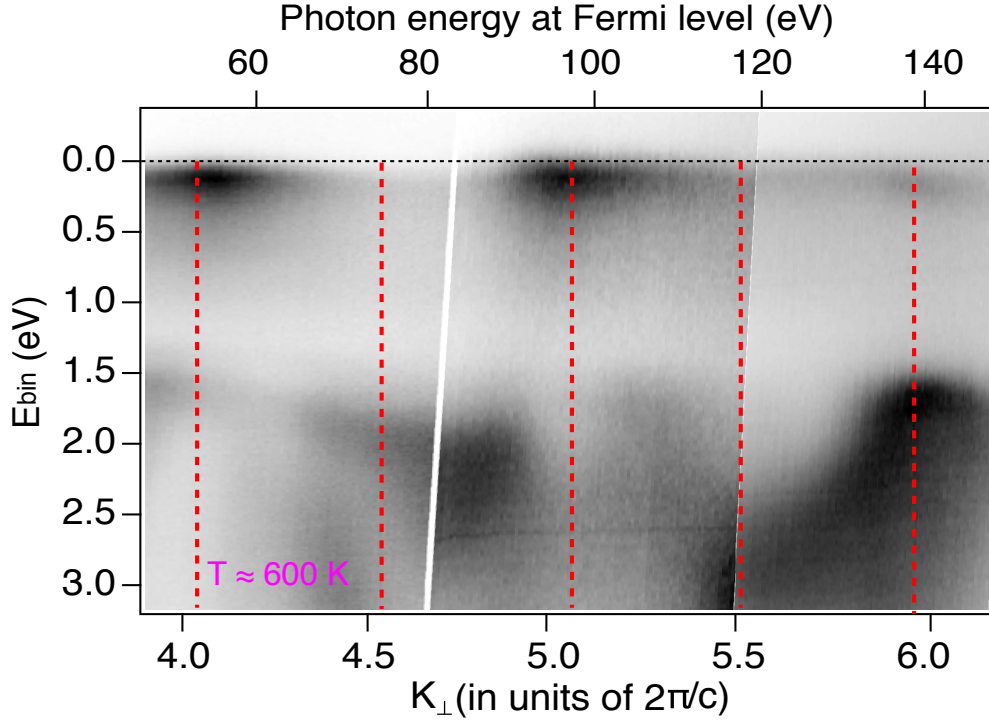


**Figure 3.12:** Bulk electronic states of 1T-TaS<sub>2</sub> probed by photon energy dependent ARPES measurements acquired at  $\approx 600$  K. The photon energy  $h\nu$  (top axis) was converted to  $k_{\perp}$  (bottom axis) by utilizing the free electron final states.  $k_{\perp}$  are expressed in units of the reciprocal lattice vector  $2\pi/c$ . The maximum binding energy of the small electron pocket located in the proximity of  $\Gamma$  point and  $k_{\perp}$  values between those two electron pockets, are indicated by the dashed red lines. The photoemission intensity was normalized by an exponential function of the photon energy. The Data are from sample B.

3.1 that was derived in the similar way like equation 4.1 i.e.,

$$\text{number of electron per unit cell} = 2 - \frac{2 \times (6 \times A_e)}{\text{Area of BZ}}; \quad (3.1)$$

where  $A_e$  denotes the area of half ellipse. The number of electron per unit cell was found to be  $1.03 \pm 0.03$  ( $\approx 1$ ) and  $0.98 \pm 0.04$  ( $\approx 1$ ) for the scans taken at 96 (Figure 3.11(a)) and 75 eV (Figure 3.11(b)), respectively. These two values turn out to be pretty close to 1 electron per unit cell as expected. This result shows that the 1T-TaS<sub>2</sub> crystal measured in this phase was not doped since normally we would expect a half-filled band i.e., 1 electron per unit cell for the 1T-TaS<sub>2</sub> in this state. This result is consistent with the bands located at  $\Gamma$  point in Figure 3.12 which are pushed above the Fermi level  $E_F$ ; because with one electron per unit cell, we should not expect any metallic band in the  $k_z$  direction. Furthermore, we also see that the photon energy does not have a strong influence on the sizes of the six electron pockets ( $6 \times A_e$ ) presents in the Fermi surface of 1T-TaS<sub>2</sub> acquired in the normal phase at a

photon energy of 96 eV (Figure 3.11(a)) and 75 eV (Figure 3.11(b)) ( $6 \times A_e = 1.96 \text{ \AA}^{-2}$  for the scan acquired at 96 eV and  $6 \times A_e = 2.06 \text{ \AA}^{-2}$  for the scan acquired 75 eV).

### 3.6 ARPES Study on 1T-TaS<sub>2</sub> above the Normal Phase

It should be noted that the data present in this section were obtained upon heating the 1T-TaS<sub>2</sub> single crystal above 600 K. The data are from sample B. The temperature during the ARPES measurements in this phase was  $\approx 30$  K. At the very high temperature it is very likely for the 1T-TaS<sub>2</sub> to convert into the metallic 2H-TaS<sub>2</sub> phase [157], and the temperature range between the normal phase and this to happen is very narrow. We will present in this section the data from the metallic 2H-TaS<sub>2</sub> resulting of the conversion of the bulk 1T-TaS<sub>2</sub> upon heating it above the normal state temperature.

Figures 3.13(a) and 3.13(c) show the topography of the Fermi surface of the sample (after heating above 600 K) acquired at  $\approx 30$  K with photon energy of 96 (a) and 75 eV (b), respectively. The reason for acquiring these data at  $\approx 30$  K was to see narrow bands. These figures are in accordance with recent studies on the similar material 2H-TaSe<sub>2</sub> [62, 158, 159]. The FS consists of holelike pockets centered around the  $\Gamma$  and  $K$  points and electronlike “dogbones” centered around  $M$  point [62, 158, 159].

The electronic structure of the metallic 2H-TaS<sub>2</sub> seems to be well resolved at 96 eV. The Fermi surface maps of a similar system i.e., 2H-TaSe<sub>2</sub> crystal presented in the literature and taken at the temperature above and below the CDW transition temperature ( $< 75$  K [44, 51]) present different features around  $M$  point. These maps are not presented here because is beyond the scope of this thesis and the reader can consult Refs. [62, 158]. Figures 3.13(b) and 3.13(d) present the band dispersion of 2H-TaS<sub>2</sub> along the high symmetry direction  $\bar{\Gamma}-\bar{M}-\bar{K}-\bar{\Gamma}$ , the two maps seems to be very similar at the first view, but the band located around 1 eV below the Fermi level for example in Figure 3.13(b) is not visible in Figure 3.13(d). These maps are in accordance with those present in the literature in the similar system 2H-TaSe<sub>2</sub> [62, 158, 159, 160]. The 4f core level spectrum of the single crystal 2H-TaS<sub>2</sub> are clearly asymmetric, with apparent shoulders on the high binding energy side as shown in Figure 3.13(e). This is in good agreement with the Ta 4f spectrum of 2H-TaS<sub>2</sub> presented in the literature [161].

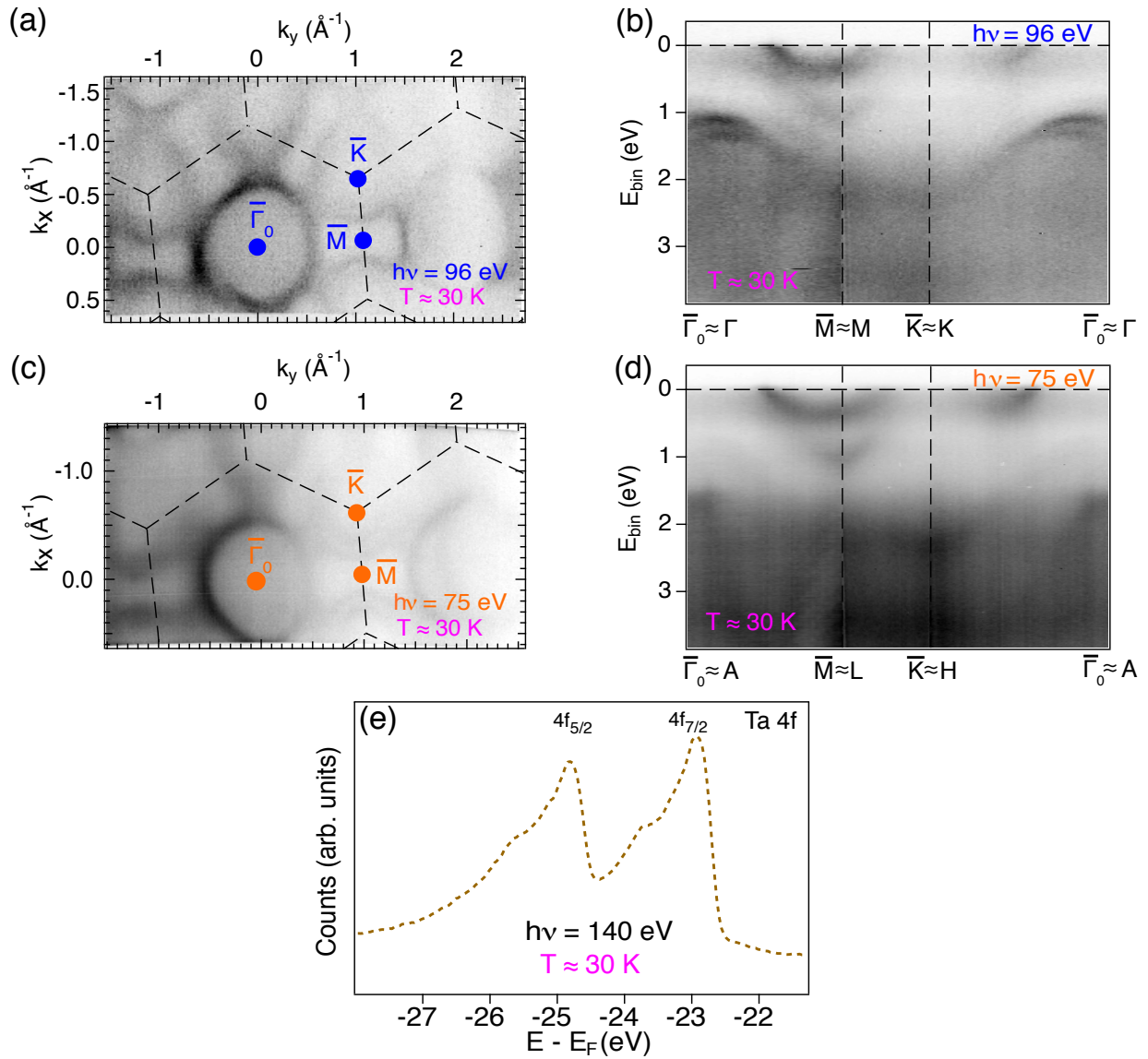


**Figure 3.13:** ARPES intensity maps of 2H-TaS<sub>2</sub> measured with the photon energy of 96 (a) and 75 eV (c), respectively. The black dashed hexagons are the Brillouin-zone schemes for the metallic 2H-TaS<sub>2</sub>. Electronic band structure of 2H-TaS<sub>2</sub> acquired at two different photon energies 96 (b) and 75 eV (d). The dark color indicates the high photoemission intensity. (e) Tantalum 4f core level spectrum of the single crystal 2H-TaS<sub>2</sub> measured at 140 eV.

### 3.7 Temperature Dependence on the Photoemission Intensity Maps from 1T-TaS<sub>2</sub>

This section summarizes the way the overall data presented in this chapter were taken. The scans presented in Figures 3.14(a) and 3.15(a) are from sample A, while the remaining scans

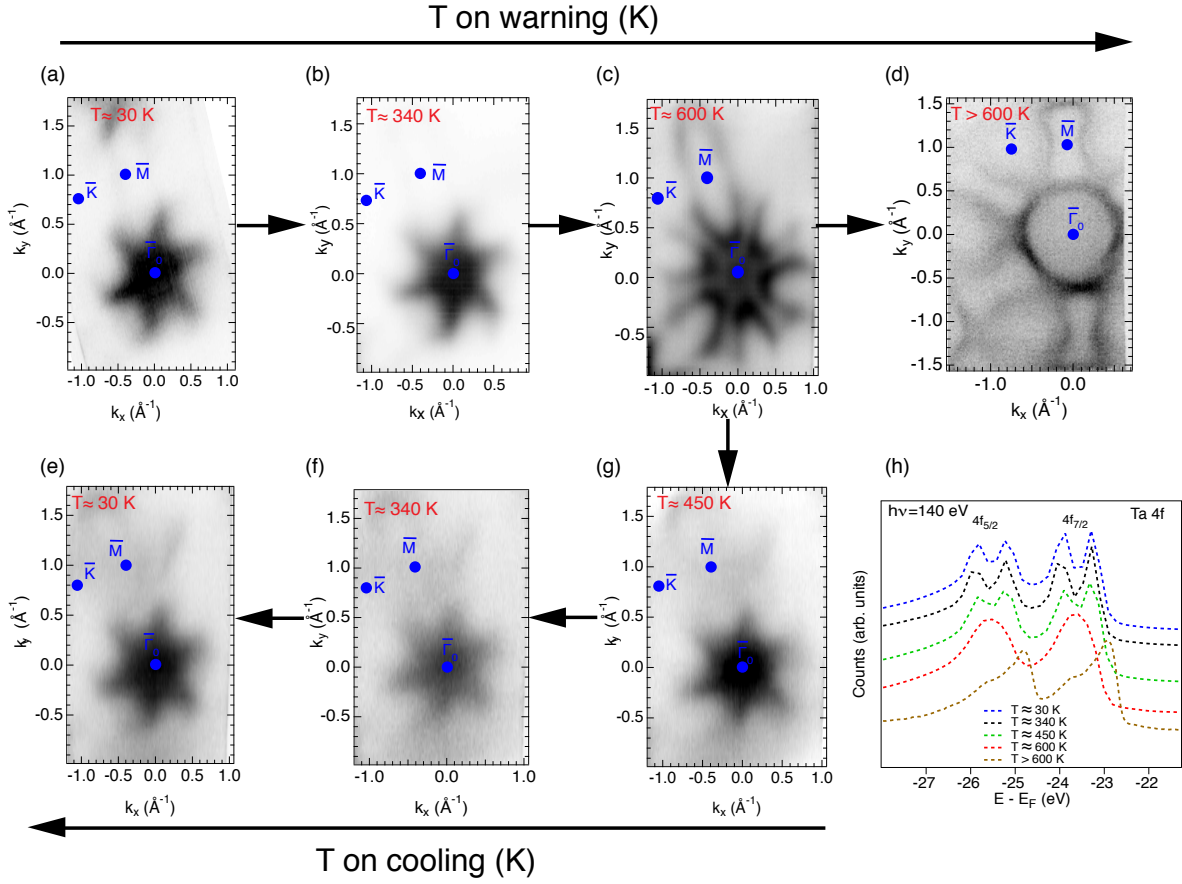


**Figure 3.14:** Photoemission study on 1T-(2H) TaS<sub>2</sub>: (a)-(g) Comparison of the photoemission intensity maps acquired at 90 meV below the Fermi level at different temperatures with photon energy 96 eV. (h) Comparison of core level spectra taken at 140 eV at different temperatures. The photoemission scan presented in (a) is from sample A, while the rest of data are from sample B.

presented in Figures 3.15 and 3.14 are from sample B, this can be noticed with the rotation of Figures 3.14(a) and 3.15(a) of  $\approx 18^\circ$  in order to be similar to the orientation of the remaining scans in Figures 3.14 and 3.15.

During the first experiment, the data were acquired on sample A at lower temperature (Figures 3.14(a) and 3.15(a)). During the second experiment, the scans show in Figures 3.14(b) and 3.15(b) were acquired upon heating the sample to  $\approx 340$  K. Afterwards, upon further heating the sample to  $\approx 600$  K, we obtained the scans presented in Figures 3.14(c) and 3.15(c). The new data set of sample showing in Figures 3.14(g) and 3.15(g) were acquired upon cooling the sample to  $\approx 450$  K. After cooling the sample to  $\approx 340$  K we took the scans (Figures 3.14(f) and 3.15(f)) in order to compare with those acquired upon heating the sample (Figures 3.14(b) and 3.15(b)). Figures 3.14(e) and 3.15(e) were also taken in order to compare with the scans acquired at  $\approx 30$  K. The reason why we heat the sample

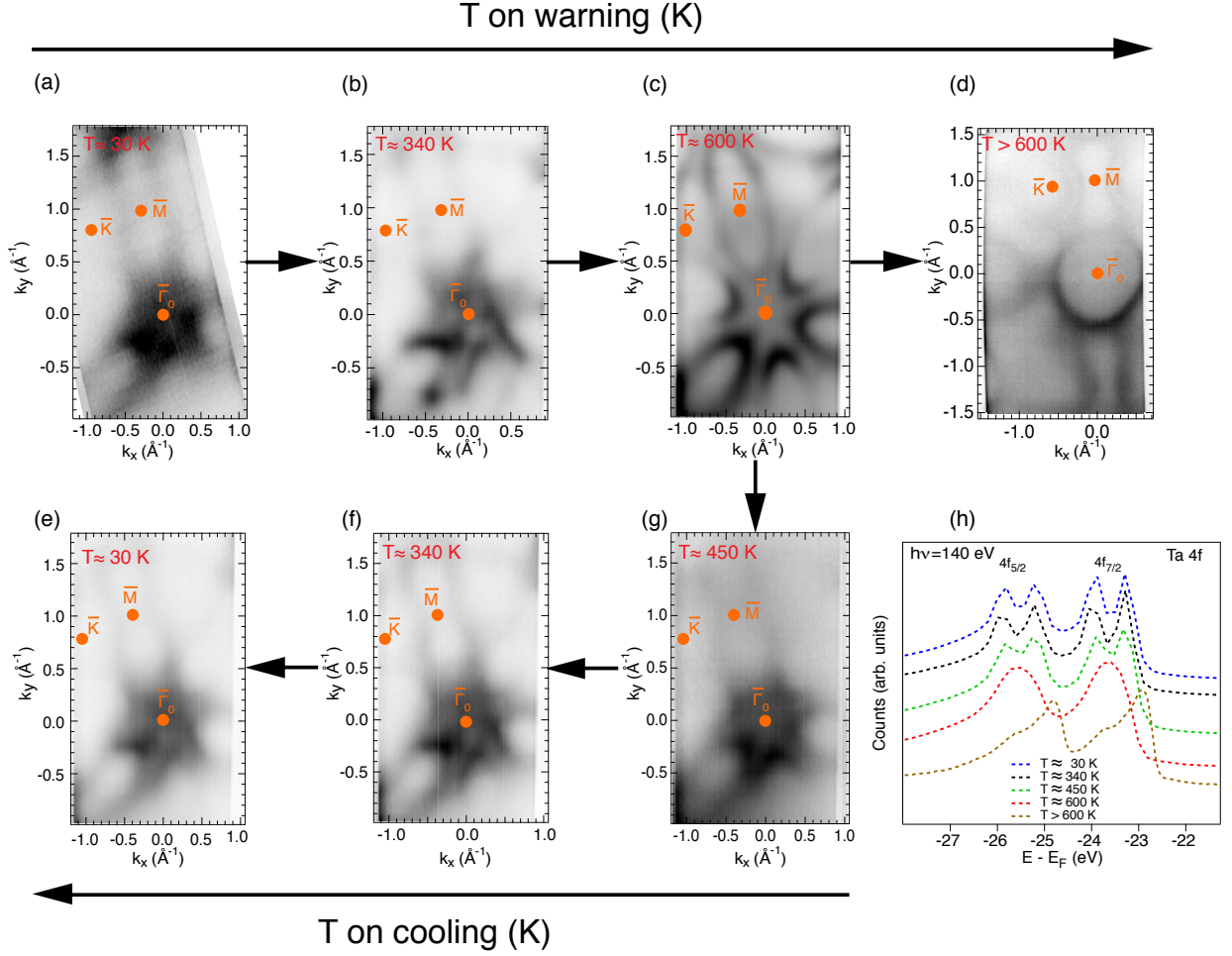


**Figure 3.15:** (a)-(g) Comparison of the ARPES intensity maps of 1T-(2H) TaS<sub>2</sub> within the  $k_x k_y$ -plane acquired at 90 meV below the Fermi level at different temperatures with photon energy 75 eV. (h) Temperature dependence of core level lines of 1T-(2H) TaS<sub>2</sub> taken at 140 eV. The scan in (a) is from sample A, while the rest of data are from sample B.

to  $\approx 600$  K and then cooling it down again to  $\approx 30$  K was to check if the crystal had not converted into its 2H form. By comparing the scans taken upon heating and cooling at the same temperature, we see an agreement and no sign of an additional band coming from the 2H-TaS<sub>2</sub>. Thus, this results tell us that the sample was still in the 1T form.

During the third attempt of the experiment, the measurements in the normal undistorted phase above 543 K were extremely difficult due to two reasons: first because this phase exists only in a narrow temperature range, and second, the reading of our thermocouple was not accurate. Therefore, due to the inaccuracy of the thermocouple we reached a high temperature region and the bulk 1T-TaS<sub>2</sub> slowly transforms into the bulk 2H-TaS<sub>2</sub> (see

Figures 3.14(d) and 3.15(d)) as predicted by Ref. [157].

We summarize in this section XPS measurements on the tantalum Ta 4f core lines for 1T-TaS<sub>2</sub> at temperatures between  $\approx 30$  K and above 600 K as seen in Figures 3.14(h) and 3.15(h). From these figures we can notice how the splitting decrease when the CDW domains sizes also decrease in the crystal. Furthermore, the peaks at the normal state is broad without shoulder, while the one obtained from 2H-TaS<sub>2</sub> possess two sharp peaks associated to their corresponding shoulders located at the higher binding energy.

In summary, we have presented in this chapter the photoemission intensity of bulk 1T-TaS<sub>2</sub> acquired at different temperatures within the CDW, NC-CDW, IC-CDW, normal phase and above the normal phase, by mean of ARPES and XPS techniques. All the band dispersion located below  $E_{\text{bin}} \approx 1.1$  eV in all these phases are identical, while the band dispersion located above 1.1 eV are affected by the distortions of the lattice. We also observed the predicted one-dimensional metallic band along the  $k_{\perp}$  direction in the CDW and NC-CDW phases. The first experiment data on the band dispersion of 1T-TaS<sub>2</sub> acquired at the normal phase were presented as well. Our results on other CDW phases reveal the experimental bands dispersion on this compound with a better resolution. It should be noted that for the XPS data we just compared the behaviors of the Ta 4f peaks in particular on the presence of new features like CDW peaks.

---

# Growth and Electronic Structure of the Single- and Bi-layer TaS<sub>2</sub>

---

Early research based on the study of 2D TMDCs was performed on mechanically exfoliated samples [20, 21, 162, 163]. However, using this approach results in small flakes with size of  $\approx 10 \mu\text{m}$  with different numbers of layers and random orientations. These types of samples are appropriate for local techniques such as optical measurements and electronic transport. Moreover, these kind of samples are typically not suitable for ARPES measurements because traditional ARPES generally probes a wide area defined by a light spot size larger than the  $10 \mu\text{m}$  flake size; in the setup used for the experiments described here, the spot size is of the order of  $\approx 200 \mu\text{m}$  is probed. Recently, it was shown by Dumcenco and coworkers [164] that large area epitaxial samples can be grown on a sapphire substrate using a CVD method. However, an insulator substrate prevents one from taking measurements with the ARPES technique due to charging problems.

Many recent studies have been performed on bulk metallic TaS<sub>2</sub> since it hosts a large range of symmetry breaking electronic instabilities such as superconductivity, Mott states [165, 166] and charge density waves, as seen in chapter 3. However, there is still an open question about how these properties would change in the single layer (SL) limit. This question has been theoretically explored in similar systems by Refs. [33, 62] and, very recently, some studies have presented the evidence for the realization of 2D CDW phase without Fermi surface nesting in SL titanium diselenide (1T-TiSe<sub>2</sub>) [167, 168] and SL niobium diselenide (NbSe<sub>2</sub>)

[31, 169]. On the contrary, our study on STM/STS measurements of SL TaS<sub>2</sub> on Au(111) reveals the suppression of CDW in this system. Therefore, this effect will be elucidated in this chapter. The study of the absence of the CDW in SL TaS<sub>2</sub> on Au(111) was done by means of STM/STS, LEED and ARPES techniques. The biggest challenge in this study consisted in finding a suitable way to synthesize high quality SL to few layer TaS<sub>2</sub> with large domain size. It is noteworthy that the thinnest crystals of TaS<sub>2</sub> reported in the literature previously, which were obtained by exfoliating TaS<sub>2</sub> bulk crystals, has actually thicknesses of a few monolayers, with a small flake size.

This chapter focuses on the synthesis of single- and bi-layer 1H- and 2H-TaS<sub>2</sub> epitaxially grown on Au(111), together with the study of their geometries and electronic structures by ARPES. Furthermore, ARPES results on SL 1H-TaS<sub>2</sub>/Au(111) are compared with DFT calculations. Low temperature STM/STS data indicating the absence of the CDW in SL TaS<sub>2</sub>/Au(111) are also presented. A ( $\sqrt{3} \times \sqrt{3}$ )R30° reconstruction of the TaS<sub>2</sub> seen from the room temperature LEED image and low temperature STM observed on the so-called “bilayer 2H-TaS<sub>2</sub>” is also presented.

This project was done in collaboration with groups from Aarhus and Radboud Universities. The samples were synthesized at the SGM3 endstation of the ASTRID2 synchrotron radiation facility, where ARPES and LEED measurements were performed *in situ*. The low temperature STM/STS measurements were done in the Scanning Probe Microscopy group in Raboud University led by Prof. Alexander A. Khajetoorians. The DFT calculations were performed by Albert Bruix from the group of Prof. Bjørk Hammer in Aarhus University. The low temperature STM/STS measurements on SL TaS<sub>2</sub>/Au(111) were done by Charlotte Sanders and Andreas Eich. The low temperature STM measurements on BL TaS<sub>2</sub>/Au(111) were done by Umut Kamber from Radboud University. Concerning my role in this project, I have participated in the sample growth, ARPES and LEED measurements on SL TaS<sub>2</sub>/Au(111) in collaboration with Charlotte Sanders and Maciej Dendzik, together with the data analysis. I have analyzed the electron-filling based on the size of the Fermi surface presented in section 4.2.2. I have performed ARPES, room temperature LEED, and room temperature STM measurements on the SL-, BL- TaS<sub>2</sub>/Au(111).

Article of relevance for this chapter:

Charlotte E. Sanders, Maciej Dendzik, Arlette S. Ngankeu, Andreas Eich, Albert Bruix, Marco Bianchi, Jill A. Miwa, Bjørk Hammer, Alexander A. Khajetoorians and Philip Hofmann, *Crystalline and electronic structure of single-layer TaS<sub>2</sub>*, Phys. Rev. B **94**, 081404(R)

(2016) [61].

## 4.1 General Growth Procedure of TaS<sub>2</sub>

Before the synthesis of TaS<sub>2</sub> on Au(111), the single crystal Au(111) substrates (99.999%, MaTecK GmbH) were thoroughly cleaned. The cleaning procedure consisted in the repetition of several cycles of sputtering (Ne<sup>+</sup>, energy = 1.5 keV, Pressure =  $3.5 \cdot 10^{-6}$  mbar, time = 30 minutes) and annealing (650° C, time = 30 minutes) in UHV conditions. The sample's surface cleanliness was assessed either by means of STM, LEED, ARPES or XPS measurements (see Figure 4.1). A clean surface of Au(111) exhibits a regular herringbone reconstruction [170]. The presence of herringbone is a clear indication of the Au cleanliness since it can be lifted by a small amount of adsorbates. During the growth, herringbone elbows (see Figure 4.1(a)) can act as nucleation sites for metallic clusters. Figure 4.1(b) shows the LEED image of a clean Au(111). The herringbone reconstruction is also visible in this LEED image and is manifested in the satellites around the main spots. The spin splitting of the Au(111) surface state [171], shown in Figure 4.1(c), is also a clear indication of a clean Au surface, as is the presence of the surface component on the Au 4f core level spectrum (see Figure 4.1(d)).

All synthesized samples that are presented in this chapter were grown inside the MBE chamber connected to the MC and the PC (see Figure 2.8), which facilitates the transfer of the sample into the MC under UHV conditions. The growth method that we used is based on one that was originally developed for the growth of MoS<sub>2</sub> nanoislands [172]. Modifications of this method allowed us to grow high quality samples with coverage of a large area of the substrate.

One approach to the TaS<sub>2</sub> synthesis begins with deposition of Ta (99.95% purity from a commercial e-beam evaporator) under a H<sub>2</sub>S pressure in the range of  $2 \times 10^{-5}$ - $5 \times 10^{-6}$  mbar. During the growth, the H<sub>2</sub>S gas was introduced inside the chamber through a homemade nozzle situated approximately 1 cm away from the surface of the Au(111) substrate. The proximity of the nozzle to the sample surface enabled there to be a local H<sub>2</sub>S gas pressure directly at the surface that was presumably higher than that in the chamber as a whole. After the deposition of the Ta, the sample was annealed up to 400 – 700° C for 30-60 minutes in a H<sub>2</sub>S atmosphere. The desired coverage was achieved after repeating several cycles of deposition and annealing; the coverage was checked by STM in-between the cycles. This growth method is hereafter referred to the “evaporator method”.

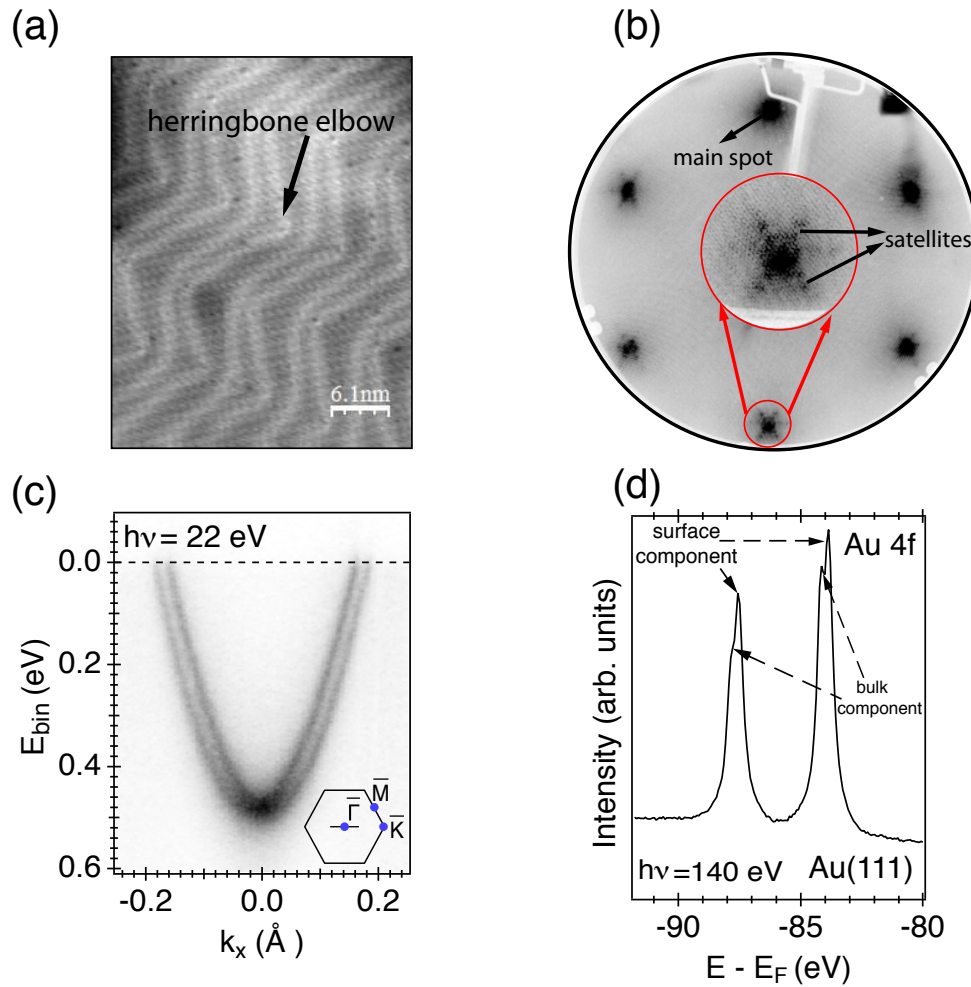


**Figure 4.1:** Features of clean Au(111). (a) STM images of clean Au(111) surface taken at room temperature. The cleanness of the sample is shown by the well visible herringbone reconstruction. Scanning parameters: (478.2 mV, 0.74 nA). (b) LEED image of clean Au(111) taken at 70 eV at room temperature. The herringbone reconstruction is also visible in this LEED image as satellites around the main spots. (c) The photoemission intensity of clean Au(111) taken at the normal emission. Dark color corresponds to high intensity. The splitting of the surface state is an indication of the clean sample. (d) Core level of Au(111) 4f presenting the surface and bulk components. The presence of the surface components on these 4f peaks is also an indication of the clean Au sample. The ARPES and XPS data were acquired at  $\approx 30$  K.

The previous growth process described above has been much more improved, which made a big contribution on the progress on this technique. The improvement consists of using a Ta filament instead of the Ta evaporator, and dosing H<sub>2</sub>S gas through the hot Ta filament located close ( $\approx 1$  cm) to the surface of the hot substrate ( $\approx 550^\circ$  C) during many cycles until the desired coverage is obtained. The coverage was checked by STM in between the cycles. The results from this method on the SL TaS<sub>2</sub>/Au(111) are domains of large size in

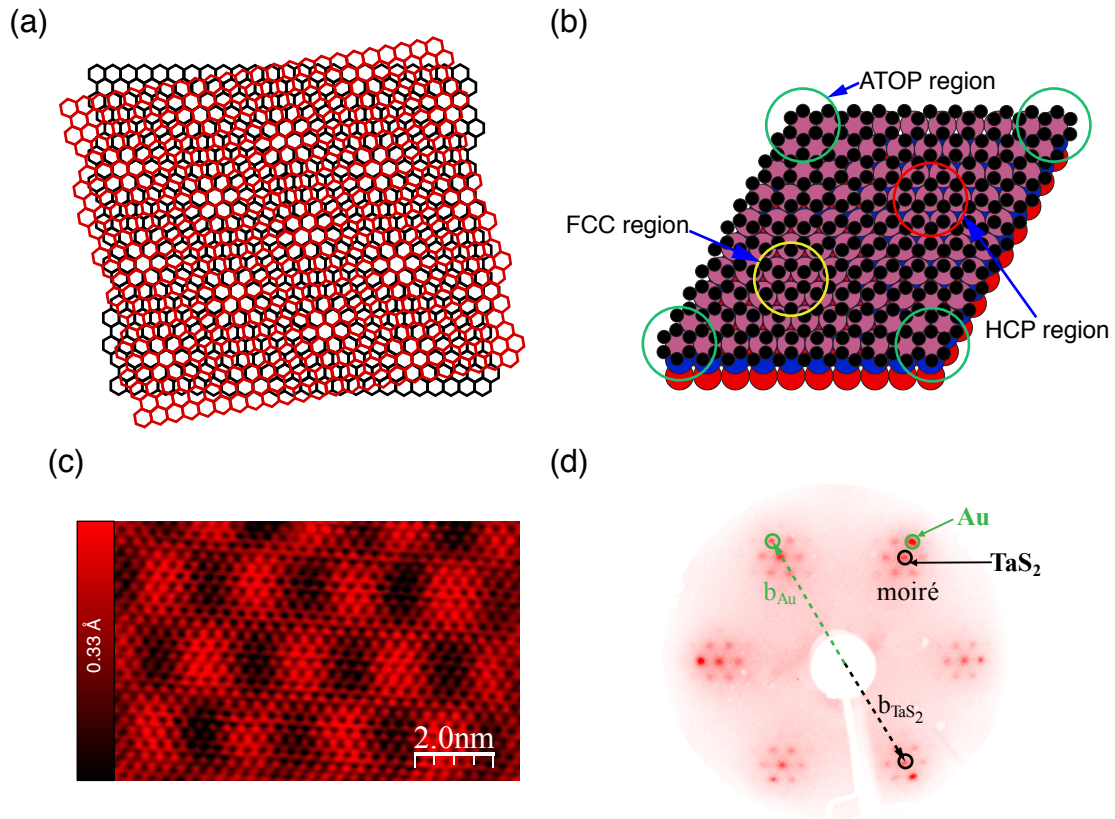


**Figure 4.2:** Explanation on the formation of the moiré pattern in solid. (a) Schematic representation of two periodic hexagonal lattices that differ in size and are overlaid at an angle of about  $10^\circ$ . The resulting atomic arrangement is periodic and forms a moiré pattern. The schematic is intended only for illustration of the general principle; the ratio of lattice constants and rotational alignment of the two lattices are different from those of the TaS<sub>2</sub>/Au(111) system. Figure modified from Ref. [173] (b) Formation of the superstructure from a bulk material showing three distinct regions namely FCC (yellow), ATOP (green) and HCP (red). Figure modified from Ref. [174]. (c) Atomically resolved STM image of TaS<sub>2</sub> acquired at room temperature, showing distinct moiré pattern. (d) LEED image of epitaxially grown TaS<sub>2</sub>/Au(111) acquired at  $E=95$  eV and  $T=94$  K. The moiré pattern is also visible in this image. The green and black arrows indicate the reciprocal unit cell vectors of Au(111) and TaS<sub>2</sub>. There is no rotation between the two lattices. The coverage of TaS<sub>2</sub> in figures c and d is  $\approx 0.9$  monolayer.

comparison with those obtained from the evaporator method. Our supposition is that, H<sub>2</sub>S volatilized TaS<sub>2</sub> species which are then precipitated on the substrate. This second growth method is referred as the “filament method”.

Due to the importance of understanding the features present in the STM and LEED images of the SL TaS<sub>2</sub>/Au(111), moiré structures will be here explained. By superimposing two regular lattices, a third one can be generated, the so-called moiré. Figure 4.2(a) presents an example of such a moiré, where two hexagonal lattices are overlaid. Figure 4.2(b) illustrates

a realistic example of a moiré where different adsorption sites such as the face centered cubic hollow, the hexagonal close packed hollow and atop (simply defined as an adsorbate on the top of) sites are identified. The moiré is a superstructure with greater periodicity than the two unit cells that form it. It can also be generated by a lattice mismatch or rotation between the adlayer and substrate.

Since TaS<sub>2</sub> and Au(111) have different lattice constants, their combination results in the moiré superstructure shown in Figures 4.2(c) and 4.2(d). The STM and LEED images of TaS<sub>2</sub>/Au(111) presented in Figures 4.2(c) and 4.2(d) were acquired at room temperature from a sample grown with the evaporator method. The LEED image of TaS<sub>2</sub>/Au(111) (see Figure 4.2(d)) confirms the sample's uniformity in crystallinity and orientation. From the LEED image, the measured length ratio between the reciprocal lattice vectors  $b_{\text{Au}}/b_{\text{TaS}_2} = 1.156(3)$  is in accordance with theoretical values (i.e., length ration between crystal unit cell vectors  $a_{\text{TaS}_2}/a_{\text{Au}}$ ) of 1.158(7) [33, 175]. As can be seen in Figure 4.2(d), there is no measurable rotation between the SL TaS<sub>2</sub> lattice and the Au(111) substrate (see green and black arrows in Figure 4.2(d)).

A study of the similar system MoS<sub>2</sub>/Au(111) [176] has found that the parts of the moiré that appear as minima (maxima) in the effective height, as measured by STM, are the parts of the moire structure in which S atoms sit on hollow sites of the underlying Au(111) surface (S atoms are placed on top of Au(111)). By following the same approach, we can now interpret the formation of the moiré pattern in TaS<sub>2</sub> as follows: the bright domains are connected with the case where the S atoms are placed above Au atoms. While the other colors are associated to the case where S atoms are placed in hollow sites (see Figure 4.2(c)).

## 4.2 SL of TaS<sub>2</sub> on Au(111)

The coverage of SL TaS<sub>2</sub> on Au(111) used during the ARPES, STM/STS, and LEED measurements presented in this section was chosen to be below a complete monolayer (ML) i.e.,  $\approx 0.7$  ML. The sample temperature during the ARPES and LEED measurements was 95 K. The energy and angular resolutions during ARPES measurements was better than 20 meV and 0.2°, respectively. The photon energy used during the ARPES measurements was 30 eV. The calculated electronic structure for free-standing 1H and 1T SL TaS<sub>2</sub> was done using DFT calculations and the computational details of these calculations can be found in Ref. [61]. The temperature during the STM and STS measurements was 4.7 K.

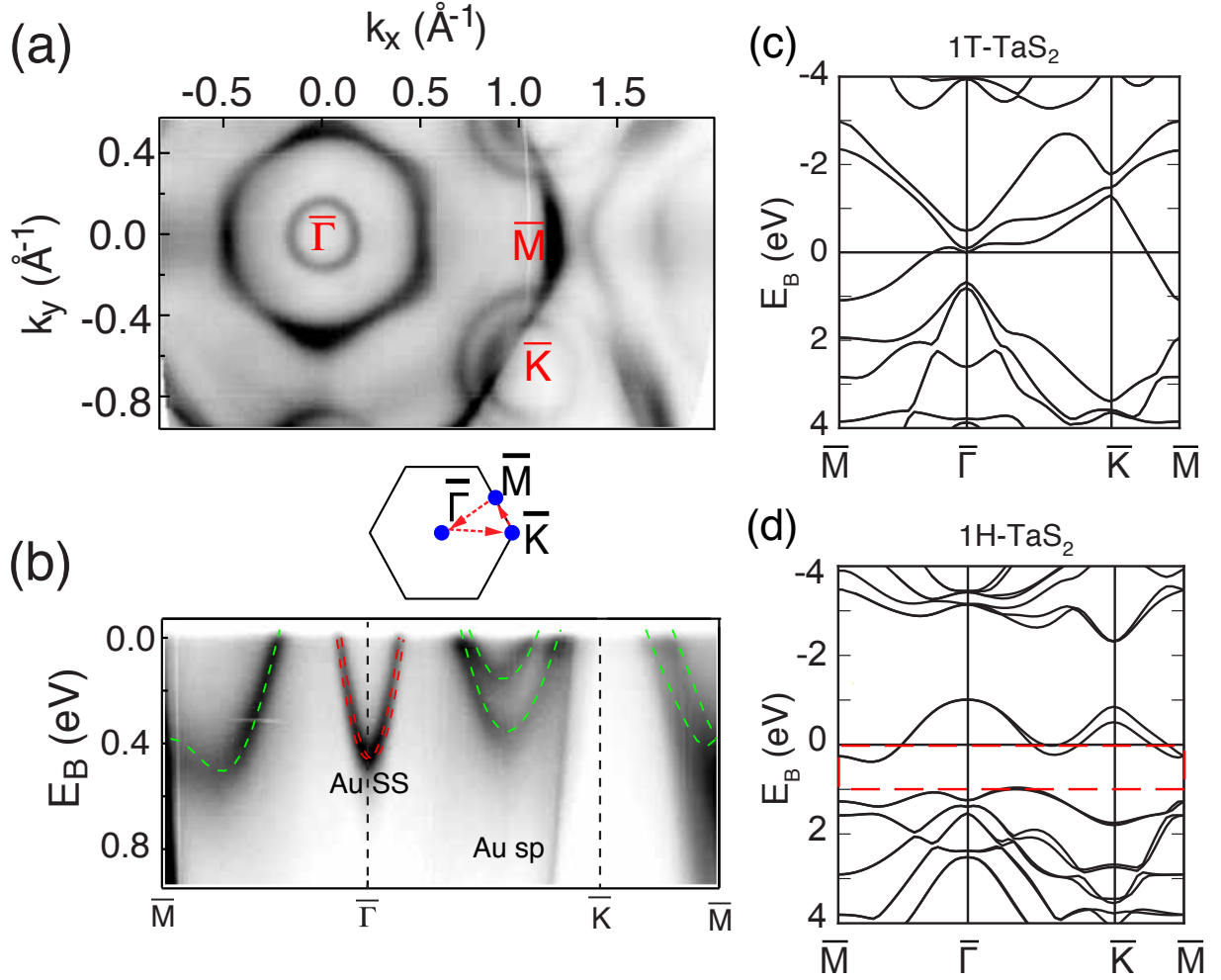


**Figure 4.3:** (a) Fermi surface map of SL TaS<sub>2</sub> on Au(111) taken at  $h\nu = 30$  eV and  $T = 95$  K. High symmetry points are indicated by  $\bar{\Gamma}$ ,  $\bar{M}$  and  $\bar{K}$ . The high photoemission intensity is represented by the dark color. This photoemission intensity at the Fermi energy exhibits three features, two centered at the  $\bar{K}$  point and one centered at the  $\bar{\Gamma}$  point. (b) Band dispersion of SL TaS<sub>2</sub> on Au(111) along high symmetry directions indicated by red dashed arrows in the 2D hexagonal Brillouin zone schematic located above the panel. In this ARPES spectrum, the contributions of the Au surface state (SS) and the sp bands are visible and are shown on the image. The theoretical dispersion for the free standing SL 1H-TaS<sub>2</sub> (green dashed curves) is overlaid on the data together with the results of SS fitting (red dashed curves) performed on clean Au(111). The theoretical dispersion (extracted from the calculation shown in (d)) of the free standing SL 1H-TaS<sub>2</sub> has been shifted by 0.12 eV to higher binding energy. (c), (d) Theoretical dispersions of the free-standing SL 1T- (c) and 1H- (d) of TaS<sub>2</sub>. In the 1H band dispersion, the calculated spin splitting at  $\bar{K}$  is 0.348 eV. The energy and momentum range measured by ARPES in (b) is indicated by the red dashed rectangle. Figures modified from Ref. [61].

### 4.2.1 ARPES Study of SL TaS<sub>2</sub> on Au(111)

The data presented in this section was obtained from a sample grown with the filament method. Qualitatively similar results were obtained from samples grown by the evaporator method, but in that case the bands were significantly broader, presumably due to the small domain size that results from that growth method.

The photoemission intensity of SL TaS<sub>2</sub>/Au(111) close to the Fermi level is presented in Figure 4.3. The Fermi surface of SL TaS<sub>2</sub>/Au(111), which consists of two distinct features is shown in Figure 4.3(a). The first feature is a contour centered around  $\bar{\Gamma}$  point with an apparently hexagonal shape, and the second are two concentric rings centered around the  $\bar{K}$  point. Furthermore, the Au surface state centered at  $\bar{\Gamma}$  point and the sp states close to the edge of the Brillouin zone (BZ) is also shown in this Fermi map. Figure 4.3(b) reveals the electronic band structure of SL TaS<sub>2</sub>/Au(111) along the high symmetry direction  $\bar{M}$ - $\bar{\Gamma}$ - $\bar{K}$ - $\bar{M}$ . The Au surface state as well as the sp bands are shown in this figure. Figure 4.3(c) and 4.3(d) are DFT calculated band structures of free standing SL 1T-TaS<sub>2</sub> and SL 1H-TaS<sub>2</sub>, respectively. These two figures differ significantly and, thus, this difference allows us immediately to identify the polymorph as 1H.

By looking at the uppermost band structure of Figures 4.3(b), 4.3(c) and 4.3(d) in the binding energy range of  $E_{bin} = 0$  to 1 eV, it is obvious that by shifting the band structure of 1H-TaS<sub>2</sub> a little bit down (i.e., toward the higher binding energy), there will be a good qualitative agreement with the experimental data. The quantitative agreement between Figures 4.3(b) and 4.3(d) is obtained when the calculated bands are shifted by 0.12(2) eV to higher binding energy (see green lines in Figure 4.3(b)) to account for electron doping. In addition, the experimental Fermi surface of TaS<sub>2</sub> (see Figure 4.3(a)) is in accordance with the calculated Fermi surface for doped free standing SL 1H-TaS<sub>2</sub> (see Figure 4.4(c)). Figure 4.4 shows calculated Fermi surfaces for doped and charge neutral SL, with panel 4.4(a) showing the dependence of the Fermi level position on doping level. Comparing these to the measured data in Figure 4.3, we can confirm a doping level of approximately 0.12(2) eV.

By exploring the band dispersion of SL 1H-TaS<sub>2</sub> along the high symmetry direction  $\bar{M}$ - $\bar{\Gamma}$ - $\bar{K}$ - $\bar{M}$  (see Figures 4.3(b) and 4.3(d)), one can notice that all the features of the Fermi contour around  $\bar{\Gamma}$  and  $\bar{K}$  points are hole pockets. By comparing the calculated Fermi contour of SL 1H-TaS<sub>2</sub> around the  $\bar{\Gamma}$  point (Figure 4.4(c)) with the experimental one presented in Figure 4.3(a), we see that a finite but unresolved splitting of the band around this point is

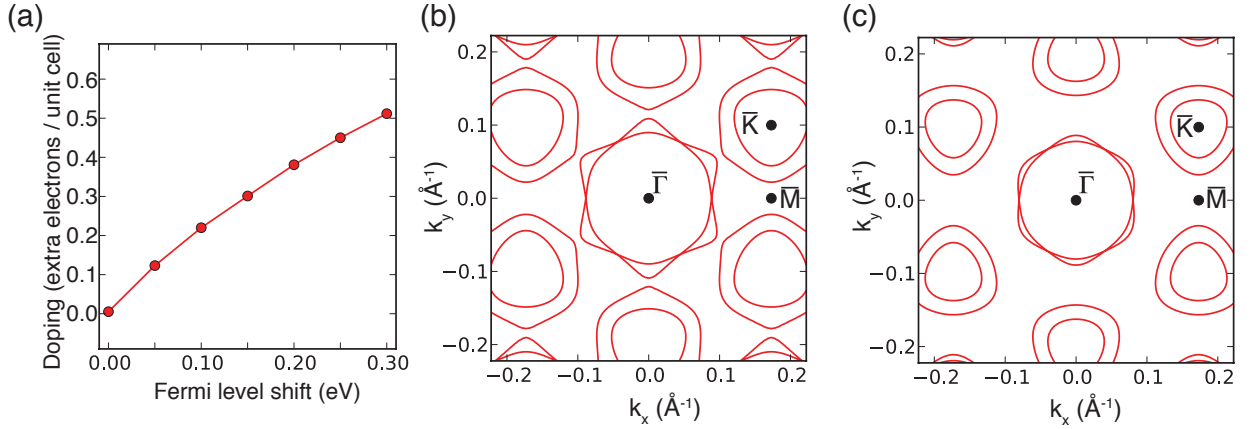


**Figure 4.4:** Relation between the most upper valence band occupation (1 electron per unit cell in the charge neutral case) and the doping (the change of Fermi level necessary to reach this occupation) for SL 1H-TaS<sub>2</sub>. (b, c) Fermi contours of SL 1H-TaS<sub>2</sub> calculated for the case of the charge neutral and a doping level of 0.15 eV, respectively.

accountable for the apparently hexagonal shape of this hole pocket, even if the individual bands do not have hexagonal Fermi contours.

#### 4.2.2 Absence of CDW in SL TaS<sub>2</sub> on Au(111)

After a careful analysis of the band dispersion of SL 1H-TaS<sub>2</sub>, we now consider whether the sample exhibits CDW or superconductivity. This is done by studying the STS/STM data taken at 4.7 K. From chapter 1, we already know that 2H-TaS<sub>2</sub> develops a CDW states at 75 K accompanied by a  $(3 \times 3)$  lattice distortion [44, 51], and its superconducting critical temperature is  $T_C = 0.6$  K [177]. This lattice distortion should be clearly visible, if it occurs, as a periodic superstructure in the STM data [31, 178]. Figure 4.5(a) shows a low temperature STM image with no indication of any additional periodicity except the lattice and moiré superstructure, as we have seen also in the STM image of the same compound taken at room temperature (Figure 4.2(c)). This is also confirmed by the Fourier transformation of the STM image presents in Figure 4.5(b) that shows the moiré pattern as discussed above and looks very similar to the LEED pattern of 1H-TaS<sub>2</sub> acquired at room temperature (Figure 4.2(d)). The LEED image (Figure 4.5(c)) acquired from the SL 1H-TaS<sub>2</sub> samples grown with the filament method, shows higher order moiré spots. Furthermore, additional spots can be clearly observed in Figure 4.5(c), which resemble 30° rotated first order TaS<sub>2</sub> spots. The presence of such structure was not observed with STM and might originate from the contribution of the rotated TaS<sub>2</sub>, or could be a moiré superstructure, or may be even just a

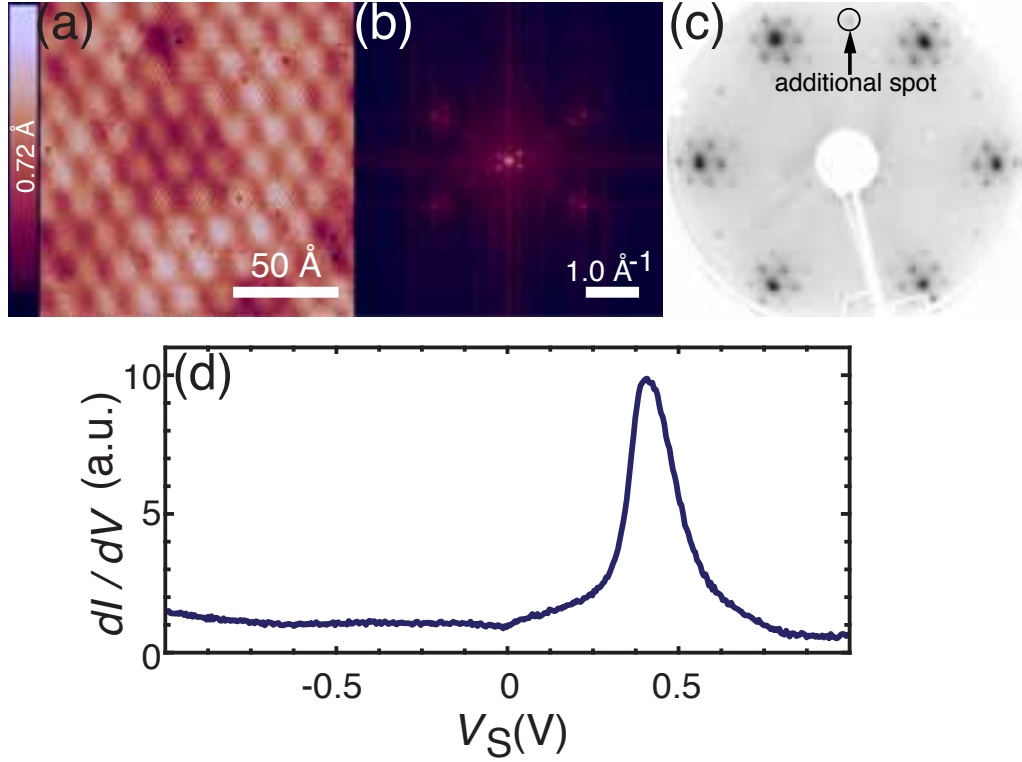


**Figure 4.5:** STM/STS data from SL TaS<sub>2</sub> acquired at 4.7 K indicating the absence of the CDW state in this system. (a) AtOMICALLY resolved STM image of SL TaS<sub>2</sub> showing the moiré superstructure and the atomic lattice. Scan parameters:  $I_{set} = 0.5$  nA and  $V_S = 4.3$  mV. (b) Fast Fourier transform data of (a). (c) LEED data of the submonolayer coverage of TaS<sub>2</sub> on Au(111) taken at  $E_{Kin} = 65.3$  eV. The diffraction patterns of Au and TaS<sub>2</sub> are both visible, as well as the moiré superstructure. Halfway between the integer order spots, the higher order moiré spots are visible. (d) Typical STS point spectrum of SL TaS<sub>2</sub>. Scanning parameters:  $I_{stab} = 0.5$  nA,  $V_S = 1$  V,  $V_{mod} = 5$  mV,  $f_{mod} = 4423$  kHz. Figures modified from Ref. [61].

higher order moiré.

Figure 4.5(d) presents STS measurements from SL 1H-TaS<sub>2</sub> taken at 4.7 K. This figure shows a strong feature at approximately 430 meV above the Fermi energy. This strong feature is consistent with the results obtained from NbSe<sub>2</sub>, where this has been linked with the top of the valence band at  $\bar{\Gamma}$  point [31]. One should note that this interpretation would not be consistent with the calculated band structure for 1H-TaS<sub>2</sub> in Figure 4.3(d). The spectrum does not present any indications of CDW gap opening or a superconductivity. With regard to superconductivity, this might be so because the measurement temperature (4.7 K) is greater than the critical temperature of the superconductivity in bulk 2H-TaS<sub>2</sub>:  $T_C = 0.6$  K. Some recent studies have proposed that the critical temperature in thin flakes

might be greater than the bulk value [179, 180]. If this is true, it is contrary to what was observed for the case of NbSe<sub>2</sub>, where  $T_C$  is suppressed in the SL limit [31, 169].

The absence of CDW in 1H-TaS<sub>2</sub> is however surprising. After all, the CDW instability observed in bulk 2H-TaS<sub>2</sub> at 75 K is significantly above the temperature used to acquire our STM and STS data. There have been contradictory findings for the CDW onset temperature in the SL with respect to the bulk in the similar material NbSe<sub>2</sub>. A slightly decreased  $T_{CDW}$  was noticed for the SL NbSe<sub>2</sub> in UHV on bilayer graphene [31], whereas a strongly increased value was observed in SL NbSe<sub>2</sub> on silicon oxide [169].

Another way to investigate the absence of CDW in the SL 1H-TaS<sub>2</sub> grown on Au(111) is to determine the doping, in terms of electrons per unit cell, by analyzing the photoemission intensity at the Fermi level. The analysis of the doping is important because a previous study actually showed that in these material systems the CDW can be suppressed by doping [10]. Specifically, we calculated the sizes of the three hole pockets centered around the high symmetry points  $\bar{\Gamma}$  and  $\bar{K}$  (see Figure 4.3(a)), as well as the size of the Brillouin zone and the value of the Fermi vector  $|2\mathbf{k}_F|$  measured across the hole pocket at  $\bar{\Gamma}$ . This Fermi vector will be compared with the nesting vector ( $0.73 \text{ \AA}^{-1}$ ) that would be required if a  $(3 \times 3)$  CDW states were present in this system and the CDW were driven by nesting. The areas of these 3 hole pockets were determined as well as the value of the Fermi vector  $|2\mathbf{k}_F|$  by using this following procedure:

- Consider for instance, the hole pocket centered around the high symmetry point  $\bar{\Gamma}$  as shown in the  $k_y k_x$  map in Figure 4.6(a). By extracting the band dispersion along the dark green line (see Figure 4.6(a)), we obtain the dispersion presented in Figure 4.6(b).
- By extracting for example, a momentum distribution curve (MDC) at a given binding energy i.e., for example from the location indicated by the dark green arrow in Figure 4.6(b), we get the photoemission spectrum shown in Figure 4.6(c). This MDC is then fitted with a Lorentzian profile with a linear background. This is done in order to have the precise corresponding  $k_y$  value for that peak position (see Figure 4.6(c)). The choice of a MDC rather than an energy distribution curve (EDC) was made because fitting an EDC would give problems in the peak finding due to the necessity of also fitting the Fermi edge in the EDC spectrum.
- The previous three steps were performed for MDCs extracted at several different binding energies. We only consider binding energies outside the energy window relevant

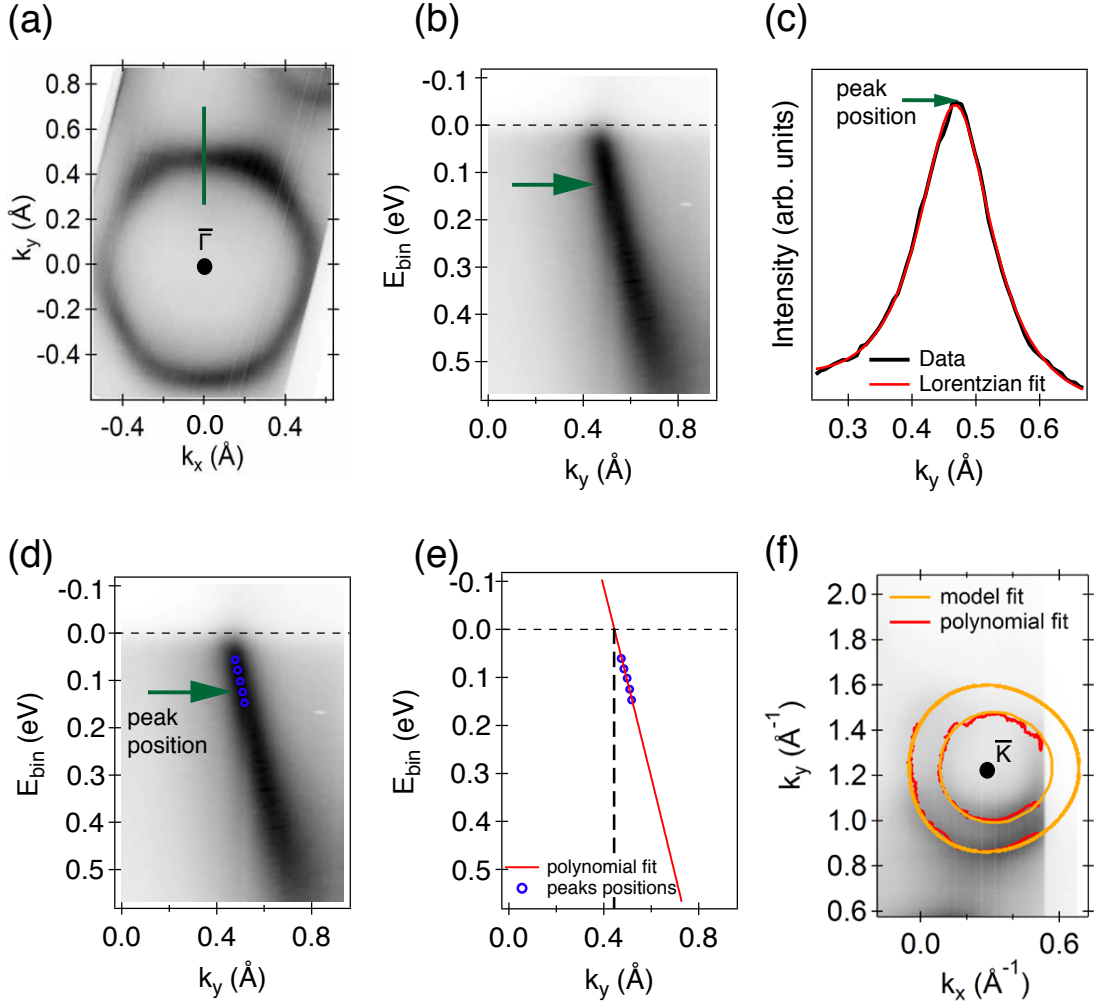


**Figure 4.6:** Method used to determine the areas of hole pockets centered around  $\bar{\Gamma}$  and  $\bar{K}$ . (a) Photoemission intensity of 1H-TaS<sub>2</sub> at the Fermi energy centered around  $\bar{\Gamma}$  point. (b) Band dispersion taken along the green line shows in (a). (c) MDC curve extracted from the position indicated by the green arrow in (b). This MDC was fitted with a Lorentzian curve (red curve) in order to extract the peak position. (d) This peak position obtained from the MDC fitting in (c) is then superimposed with the band dispersion (see green arrow), together with other peaks positions (blue open circles) obtained in the same way. (e) These peaks positions from the MDC fittings are then fitted with a polynomial function in order to get the value of momentum at zero binding energy (see black dashed line). (f) ARPES Fermi surface of 1H-TaS<sub>2</sub> centered around  $\bar{K}$  point. The red curves are coming from the polynomial fitting as states above and are overlaid with the experimental data together with curves coming from the interpolation with the trigonally warped parabolic state (see text for more details).

for electron-phonon coupling. The MDCs' maxima are plotted on top of the measured photoemission intensity in Figure 4.6(d) (see blue open circles).

- These peaks positions (from the Lorentzian fit) were extrapolated to the Fermi level

by fitting them with a polynomial function and so to obtain the  $k_y$  value at the Fermi level crossing. (see Figure 4.6(e)). This procedure was inspired by method 3 presented in Ref [181]. It should be noted that one crossing is determined for the hole pocket centered around  $\bar{\Gamma}$  in the high symmetry direction  $\bar{\Gamma}-\bar{M}$ , where the two spin split bands remain degenerate (see Figures 4.3(b) and 4.4(c)), while two crossings are determined along the  $\bar{\Gamma}-\bar{K}$  direction, deriving from the two well divided bands along the  $\bar{\Gamma}-\bar{K}$  direction (see Figures 4.3(b) and 4.4(c)).

- All these previous steps were repeated all over the whole hole pocket centered at  $\bar{\Gamma}$  (see Figure 4.6(a)), until the exact positions forming the apparent hexagonal contour were obtained. By using these contour positions, we were able to determine the area of the hole pocket centered at  $\bar{\Gamma}$  point. This was done by using different methods such as some built-in functions in Igor pro software (areaxy, polygonarea) and the area formula for a regular hexagon ( $A_h$ ). The value for this area from these methods was similar and the value obtained is  $0.74 \text{ \AA}^{-2}$ .
- Using the same method (see the red curves in Figure 4.6(f)), we were able to get some peak positions from the visible part of the bands centered around  $\bar{K}$  point (the intensity of the whole pocket centered at  $\bar{K}$  point is not visible due to matrix element effects. The shape of the two contours centered around  $\bar{K}$  (see the two orange contours in Figure 4.6(f)) was determined by using a more advanced interpolation method that considers a parabolic state with trigonal warping and spin split of the band presented in equation 1 in Ref. [38] (although fitting the contour as a simple ellipse gives nearly the same results). The two contours are plotted in orange in Figure 4.6(f).
- The value of the two areas were similar using these methods. The values of the areas were found to be: area of the outer ( $A_o$ ) hole pocket is  $0.39 \text{ \AA}^{-2}$  and that of the area of the inner ( $A_i$ ) hole pocket is  $0.18 \text{ \AA}^{-2}$ .

By using the method described above, the value of the Fermi vector  $|2\mathbf{k}_F|$  along the high symmetry direction  $\bar{\Gamma}-\bar{M}$  was found to be  $0.96 \text{ \AA}^{-1}$ . This value is then compared with the nesting vector  $|\mathbf{q}| = |2\mathbf{k}_F|$  would need to be  $0.73 \text{ \AA}^{-1}$ . The value of the Fermi vector that we found ( $0.96 \text{ \AA}^{-1}$ ) is very different from the value of the nesting vector  $0.73 \text{ \AA}^{-1}$ , this might be one of the reason why there is no sign of the CDW state in our system SL 1H-TaS<sub>2</sub>, but this is not sufficient to explain the absence of a CDW in this system, since nesting does not explain the CDW in the bulk parent materials either [58, 182, 183].

By considering the area formula of a regular hexagon, the area of the 2 dimensional Brillouin zone (BZ) was calculated, and it is  $4.18 \text{ \AA}^{-2}$ . Thus, knowing the value of the area of the surface BZ with those of the FS hole pockets centered around  $\bar{\Gamma}$  and  $\bar{K}$  points will allow us to estimate the doping or the number of electron per unit cell. The number of electrons per unit cell is then given by:

$$\text{number of electron per unit cell} = 2 - \frac{2A_h + 2(A_i + A_o)}{\text{Area of BZ}}. \quad (4.1)$$

By using the equation 4.1 together with the areas of the three hole pockets and the surface BZ, we obtain 1.37 electron per unit cells. This value of 1.37 shows that our system i.e., the SL 1H-TaS<sub>2</sub> grown on Au(111) is strongly electron doped since we would normally expect a half filled band i.e., 1 electron per unit cell. Our results on the number of electrons per unit cell (i.e., 0.37 extra electrons per unit cells) are consistent with the DFT calculations relating the band shift to extra electron occupation as shown in Figure 4.4(a). Earlier studies of alkali-intercalation compounds [10] have exhibited that the CDW state can already suppresses at a more modest electron doping, proposing that this plays a crucial role.

Recently, Wehling [184] has suggested a mechanism of “pseudodoping” in metallic SL TMDCs. He has demonstrated how apparently heavy doping of 2D materials manifesting itself as shifts of bands in ARPES experiments can be caused by a weak band hybridization of metallic 2D materials with their metallic substrates. He also shows that this “pseudodoping” can imply less electron transfer between the layer and its substrate than the modifications in the Fermi surface would suggest. The calculated band shift for the SL TaS<sub>2</sub> on Au(111) is in accordance with our observations. In addition, the proposed pseudodoping is expected to influence the formation of the CDW state [184].

One should note that the CDW transition might also be affected by other factors, e.g.: substrate interactions other than doping such as screening [36, 185], reduced dimensionality, chemical bonding or strain [186]. Nevertheless, the uncertainty in the measurement of the atomic lattice sets a higher limit of approximately 3% on the in-plane strain. Nevertheless, these factors mentioned above might still play a small role in suppressing CDW formation [187].

### 4.3 ARPES Study on BL of TaS<sub>2</sub> on Au(111)

The so-called BL TaS<sub>2</sub>/Au(111) was synthesized using the filament method described in section 4.1. Figures 4.7(a) and 4.7(b) show the Fermi surface and electronic band structure of BL TaS<sub>2</sub>/Au(111), acquired with the photon energy of 30 eV and temperature of  $\approx 30$  K. In addition to the features arising from the exposed Au substrate (i.e., the Au surface state centered around the  $\bar{\Gamma}$  point and the Au sp states located close to the edge of the BZ, the TaS<sub>2</sub> overlayer presents a Fermi contour (Figure 4.7(a)) that consists of two distinct features. The first consists of two apparently hexagonal shapes centered around  $\bar{\Gamma}$  point and the second is composed of two apparently concentric rings centered around the  $\bar{K}$  point. The stripe features observed in these two figures are just the dust streaks due to dust on the entrance slit of the analyzer. The Fermi surface maps of the areas around pockets centered at  $\bar{\Gamma}$  and  $\bar{K}$  points is presented in Figures 4.7(c) and 4.7(b), respectively. Figure 4.7(c) shows two complete apparently hexagonal contours centered around  $\bar{\Gamma}$  point. While Figure 4.7(d) shows instead of two concentric rings like seen in Figure 4.7(a), we rather observed three concentric rings. In order to increase the visibility of the rings centered around the  $\bar{K}$  point, an alternative representations of the photoemission intensity presented in Figure 4.7(d) is shown by Figure 4.7(e) as second derivative analysis explained by Ref. [163]. This method improves the visibility of additional bands that were not well resolve in the raw data. For instance, by comparing Figure 4.7(d) and Figure 4.7(e), we observe not only the three well resolved concentric rings but also a fourth one is barely seen. By comparing the band dispersion along the high symmetry direction  $\bar{M}$ - $\bar{\Gamma}$ - $\bar{K}$ - $\bar{M}$  in Figure 4.3(b) and 4.7(b), we can say that the Fermi contour features centered around  $\bar{\Gamma}$  and  $\bar{K}$  are hole pockets. The size of the visible hole pockets were calculated in order to compare with those of the SL TaS<sub>2</sub>/Au(111). By using the same principle for the determination of the area of the Fermi surface as presented in section 4.2.2, we found that the Fermi contour areas for the outermost and innermost apparently hexagonal shapes around the  $\bar{\Gamma}$  point are  $0.73 \text{ \AA}^{-2}$  and  $0.39 \text{ \AA}^{-2}$ , respectively. Those of the hole pockets centered around the  $\bar{K}$  point are  $0.079 \text{ \AA}^{-2}$  (small one),  $0.25 \text{ \AA}^{-2}$  (middle one) and  $0.41 \text{ \AA}^{-2}$  (big one). From these values we can notice that the areas of the outermost contour features around the  $\bar{\Gamma}$  and  $\bar{K}$  points in Figures 4.7(c) and 4.7(d) are similar to the areas found for the SL TaS<sub>2</sub>/Au(111).

Before comparing our data with the calculated band structures in the similar system i.e., BL MoS<sub>2</sub>, let us have a look at the theoretical results on the band structure of BL MoS<sub>2</sub> presented by Fan and co-workers [188].

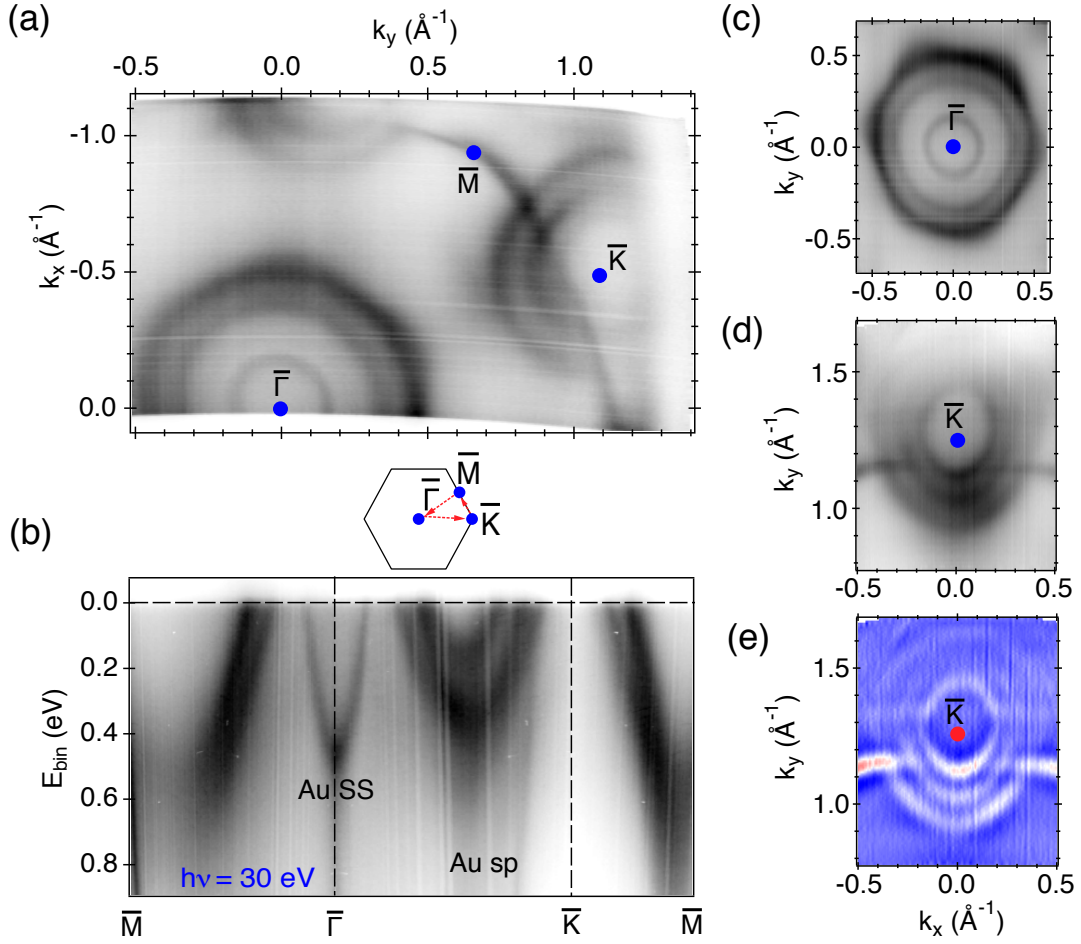


**Figure 4.7:** (a) ARPES Fermi contour of BL TaS<sub>2</sub>. (b) ARPES band dispersion along the  $\bar{M}$ - $\bar{\Gamma}$ - $\bar{K}$ - $\bar{M}$  directions. Photoemission intensity of the hole pockets centered around  $\bar{\Gamma}$  point (c) and around  $\bar{K}$  point (d). (e) Second derivative plots of the ARPES spectrum presented in (d) around the  $\bar{K}$ . This method of second derivative used comes from Ref. [163].

Many studies [188, 189] try to explain the electronic structure of one-layer, two-layer, three-layer, and bulk TMDCs. From chapter 1, we already know that the AB stacking sequence exists in the 2H phase of MoS<sub>2</sub>. The states of the valence band at  $\bar{\Gamma}$  are mostly composed of  $d_z^2$  orbitals, while the states at  $K$  point are composed of the  $d_{x^2-y^2}$  and  $d_{xy}$ . Furthermore, in the electronic structure of the bilayer, the extended nature of  $d_z^2$  orbitals results in a splitting of the bands at the  $\bar{\Gamma}$  point. Fan and co-workers [188] reveal the effect of the AB stacking order with spin-orbit coupling (SOC) in combination with layer coupling (LC) on the band structure of bilayer MoS<sub>2</sub> at the top of the valence band at the  $K$  point; by using first principle methods. The authors found that with the combination of the SOC and LC four bands exist around the  $K$  point. This is the result of the splitting between the two

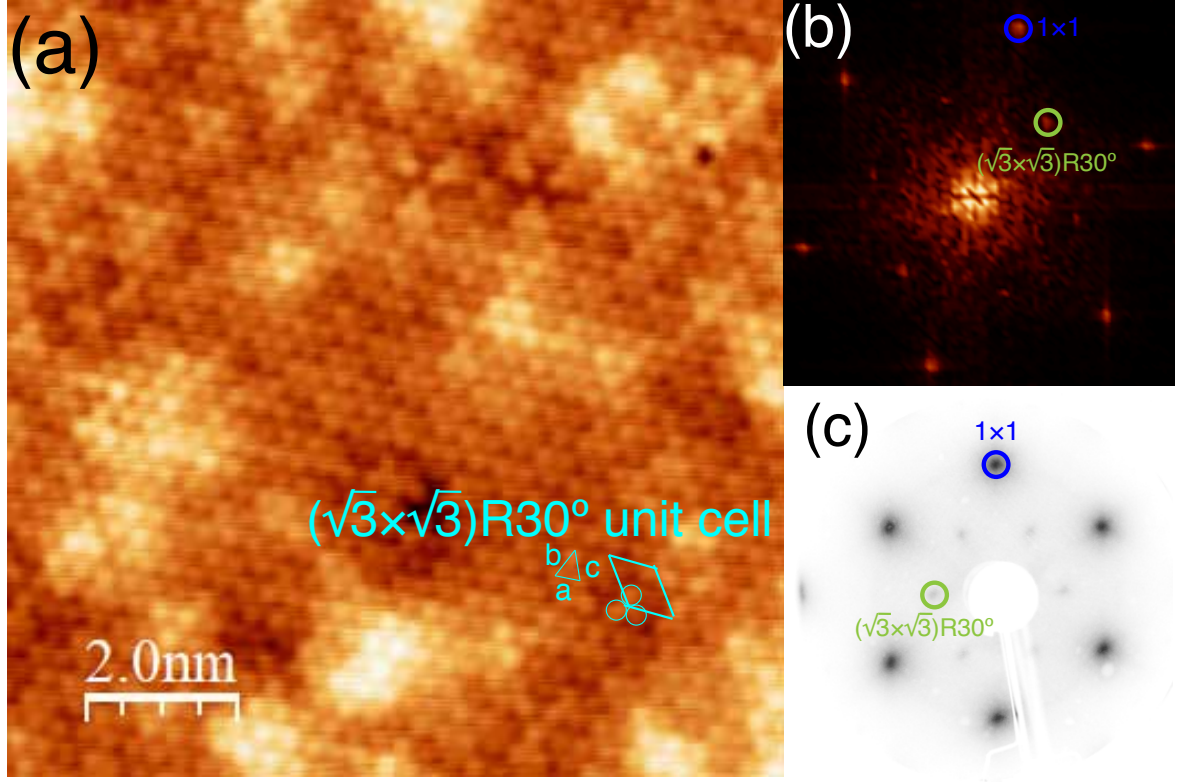


**Figure 4.8:** (a) Atomically resolved STM image for BL TaS<sub>2</sub> acquired at 4.7 K. Scan parameters:  $I_t = 500$  pA,  $V_S = 3$  mV. A cyan parallelogram indicates the  $(\sqrt{3} \times \sqrt{3})R30^\circ$  unit cell. The STM image shows blocks forming a triangular trimer structure as indicated by the cyan circles. These trimers are arranged according to the  $(\sqrt{3} \times \sqrt{3})R30^\circ$  periodicity and the distance within the block forming the trimer (see the size of the cyan triangle in the STM image labelled a, b and c) is  $\approx 2.855 \pm 0.328$  Å. (b) Fast Fourier transform data of (a). (c) LEED image of the BL TaS<sub>2</sub> on Au(111) taken at  $E_{Kin} = 95$  eV at room temperature. The green circles are the  $(\sqrt{3} \times \sqrt{3})R30^\circ$  reconstruction, and the blue circles are the TaS<sub>2</sub>  $1 \times 1$ . The signature of  $(\sqrt{3} \times \sqrt{3})R30^\circ$  surface reconstruction of TaS<sub>2</sub> is observed on the STM, FFT, LEED images

$d_{x^2-y^2}$  and  $d_{xy}$  orbitals due to the LC, together with the splitting between the spin down and spin up of each orbital due to the SOC. Because of the fundamental similarities between the band structures of MoS<sub>2</sub> and TaS<sub>2</sub>, it is likely that evolution of the band structure from one to two layers is similar in both cases.

Samples were synthesized in Aarhus and then transferred to the laboratories in Nijmegen under UHV conditions using a vacuum suitcase. The BL TaS<sub>2</sub>/Au(111) was measured at 4.7 K using the STM in Radboud University (Nijmegen-Netherlands) by our collaborators (group of Alexander Ako Khajetoorians). Figure 4.8(a) shows the high resolution STM image of BL TaS<sub>2</sub>/Au(111). This STM image exhibits blocks forming a triangular trimer structure as shown by cyan circles. These trimers are ordered according to a  $(\sqrt{3} \times \sqrt{3})R30^\circ$

periodicity. The distance within the block forming the trimer or the lengths of the sides of the trimer (see the size of the cyan triangle labelled a, b, c in the STM image) is  $\approx 2.855 \pm 0.328$  Å. The cyan parallelogram denotes the  $(\sqrt{3} \times \sqrt{3})R30^\circ$  unit cell. Figure 4.8(b) is the fast Fourier transform (FFT) of the STM image presented in Figure 4.8(a). Figure 4.8(c) is the LEED pattern of BL TaS<sub>2</sub>/Au(111) taken at kinetic energy of 95 eV and at room temperature. From the FFT and LEED images we can notice the  $(\sqrt{3} \times \sqrt{3})R30^\circ$  surface reconstruction of TaS<sub>2</sub> with respect to the TaS<sub>2</sub>  $1 \times 1$  atomic lattice.

In order to check if the reconstruction of the TaS<sub>2</sub> is due to a CDW state persisting even at room temperature, we annealed the sample while we were taking the LEED pattern up to  $\approx 400$  K, but the reconstruction was still visible (We do not show the data here). This reconstruction might be also due to the presence of some adsorbates on the surface of the sample, or the transition temperature for the CDW in this system might be very high. This reconstruction is not what we would expect for a CDW in this system, because the bulk 2H typically shows a  $3 \times 3$  reconstruction, instead. Furthermore, the STS measurements on this sample have not yet been conclusive. DFT calculations will be needed in order to help estimate the doping and to have more information about the band structure of this system.

---

# Electron-Phonon Coupling in Single-Layer TMDCs

---

Many-body effects and their interaction in materials are at the center of some of the most fascinating problems in current condensed matter physics. In complex materials, the presence of these various effects can happen very often at the same time. The three most influential of such effects are: electron-electron (e-e), electron-defect (e-df) and electron-phonon (e-ph) interactions. In this chapter, we are mainly interested in the latter interaction. E-ph coupling limits the lifetime of excited electrons (or holes) and can facilitate the understanding of several physical phenomena such as electrical resistivity [190], Peirls instability [191] and BCS-type superconductivity [192], to mention just a few.

The spin degeneracy of the spin-orbit splitted valence band in single layer  $\text{WS}_2$  and  $\text{MoS}_2$  is lifted due to lack of inversion symmetry in these systems. Therefore, this splitting allows us to directly compare the el-ph coupling strength in these two spin subbands. In this chapter, the e-ph coupling strength in the single layers  $\text{WS}_2$  and  $\text{MoS}_2$  is studied, together with that of SL 1H- $\text{TaS}_2$  both theoretically and experimentally; using first principles calculations, the Debye model, Einstein model and angle-resolved photoemission spectroscopy (ARPES) spectra.

This project was done in collaboration with groups from Aarhus University, Technical University of Denmark, University of Trieste and SuperESCA beamline located at Elettra Sincrotrone. The SL of  $\text{WS}_2$  and SL  $\text{MoS}_2$  were epitaxially grown on Au(111) at SuperESCA

beamline following the procedure described in Ref. [193]. An additional information about the growth of SL WS<sub>2</sub>/Au(111) and SL MoS<sub>2</sub>/Au(111) is presented in section B.1. ARPES data were acquired on the SGM3 beamline of ASTRID2 [113]. The angular and energy resolution were better than 0.2° and 30 meV, respectively.

The SL TaS<sub>2</sub>/Au(111) was synthesized *in situ*, at the SGM3 endstation of the ASTRID2 synchrotron radiation facility together with the ARPES measurements. The first principles calculations were done by Dr. Nicki Frank Hinsche, the ARPES experiments was done by me with the help of Sanjoy K. Mahatha, Kevin Guilloy, Antonija Grubišić Čabo and Maciej Dendzik. The ARPES data was analyzed by me.

Article of relevance for this chapter:

Nicki Frank Hinsche, Arlette S. Nganheu, Kevin Guilloy, Sanjoy K. Mahatha, Antonija Grubišić Čabo, Marco Bianchi, Maciej Dendzik, Charlotte E. Sanders, Jill A. Miwa, Harsh Bana, Elisabetta Travaglia, Paolo Lacovig, Luca Bignardi, Rosanna Larciprete, Alessandro Baraldi, Silvano Lizzit, Kristian Sommer Thygesen and Philip Hofmann: “*Electron-phonon Coupling in the Spin-split Valence Band of Single Layer WS<sub>2</sub>*”, Phys. Rev. B **96**, 121402(R), 2017 [194].

## 5.1 Electron-phonon Coupling

Before giving the determined values of the e-ph coupling strength in single layers WS<sub>2</sub>/Au(111), MoS<sub>2</sub>/Au(111) and TaS<sub>2</sub>/Au(111), let us first, have a look on the methods and theory used in order to obtain these values. The information presented in this section is mainly based on Refs. [96, 98].

The e-ph coupling can be defined as a measure of the probability that a given electron will be scattered by a certain lattice vibration, i.e., a phonon. This scattering processes modify the dispersion and the lifetime of the electronic states in a material. This modification of the dispersion consists of the renormalization of the band very close to the Fermi level, within the typical phonon energy  $\hbar\omega_D$ , in such a way that the dispersion is flat at the Fermi energy. Therefore, this leads to the increase of the density of states (DOS) and the effective mass of the electrons at the Fermi level. In this case the effective mass is given by  $m^* = m_0(1 + \lambda)$ , where  $\lambda$  denotes the mass enhancement parameter,  $m^*$  and  $m_0$  stand for the effective masses with and without e-ph interaction, respectively. The complex self energy

( $\Sigma$ ) whose expression is given by the equation 5.1, holds all information on the effect of the e-ph coupling on the dispersion and lifetime of the states

$$\Sigma(\epsilon_i, \mathbf{k}, T) = \Sigma'(\epsilon_i, \mathbf{k}, T) + i\Sigma''(\epsilon_i, \mathbf{k}, T). \quad (5.1)$$

The real part  $\Sigma'$  of the self energy gives rise to a renormalization of the dispersion by shifting the band, while the imaginary part  $\Sigma''$  takes into account the lifetime ( $\tau$ ) of the particle state and it is defined as follows:  $\Sigma'' = \hbar/2\tau$ . The expression of the inverse lifetime  $\Gamma$  is then given by  $\Gamma = \hbar/\tau$ . These parameters are frequently used and can be acquired from the spectral function  $A(\omega, \mathbf{k}, T)$ , which is proportional to the photoemission intensity as presented in section 2.4.2. The decay of the excited electrons (or holes) can be described by the lifetime ( $\tau$ ), the inverse lifetime ( $\Gamma$ ) or the imaginary part of the self energy ( $\Sigma''$ ), which are in fact the same quantity. Since we are primarily interested in the effect of the e-ph coupling in the material, let us briefly presents the effects of other interactions in the material (i.e., the e-e and e-df interactions) because they all contribute to the total function of the inverse lifetime as follows:

$$\Gamma = \hbar/\tau = \Gamma_{\text{e-df}} + \Gamma_{\text{e-e}} + \Gamma_{\text{e-ph}}. \quad (5.2)$$

The contribution of the inverse lifetime from the electron-defect scattering ( $\Gamma_{\text{e-df}}$ ) can be simply described as an offset to the total inverse lifetime ( $\Gamma$ ) since it is generally not strongly energy or temperature dependent. It should be noted that even though the defect scattering strength might not be temperature dependent, the number of defects can be thermally excited at higher temperatures resulting in the increase of  $\Gamma_{\text{e-ph}}$  [96]. The inelastic scattering of electrons is primarily due to the e-e interaction whose  $\Gamma_{\text{e-e}}$  is energy dependent. For higher binding energies,  $\Gamma_{\text{e-e}}$  can increase because of the extended phase space for inelastic e-e scattering [96]. On the other hand,  $\Gamma_{\text{e-e}}$  does not show a very important temperature dependence [96]. At sufficiently low temperatures, the most important process is the e-e scattering. While, at high temperature, the term  $\Gamma_{\text{e-ph}}$  increases because of the increased probability of phonon excitations [96]. The only strongly temperature dependence factor in equation 5.2 is the e-ph coupling term. Thus, this can be used for our advantage by isolating the e-ph part from other contributions experimentally [96].

### 5.1.1 Determination of the e-ph Coupling Strength

Let us now discuss how a mass enhancement parameter at the Fermi energy  $E_F$  ( $\lambda$ ) or a measure of the e-ph coupling strength at higher binding energies ( $\lambda$ ) can be determined

experimentally.

The scattering processes happen with a certain probability. Thus, the probability of scattering an electron from its initial state (i) with momentum  $\mathbf{k}$  to a final state (f) by a phonon (momentum  $\mathbf{q}$ , mode index  $\nu$ ) is presented by the e-ph matrix:

$$g^{i,f}(\mathbf{k}, \mathbf{q}, \nu) = \sqrt{\frac{1}{2M\omega_{\mathbf{q},\nu}}} \langle \Psi_{\mathbf{k}i} | \hat{\varepsilon}_{\mathbf{q},\nu} \cdot \delta V_{\mathbf{q},\nu}^{SCF} | \Psi_{\mathbf{k}+\mathbf{q}f} \rangle. \quad (5.3)$$

Where  $M$  represents the atomic mass,  $\Psi$  indicates the electronic wavefunctions for each corresponding state and the term  $\delta V_{\mathbf{q},\nu}^{SCF}$  denotes the derivation of the self-consistent potential with respect to the atomic displacements induced by the phonon mode ( $\mathbf{q}, \nu$ ) with frequency  $\omega_{\mathbf{q},\nu}$ , and phonon polarization vector  $\hat{\varepsilon}_{\mathbf{q},\nu}$  [96]. The expression of this potential and wavefunctions for instance, are not given because they are irrelevant for our study.

The probability of phonons to scatter electrons is given in terms of the Eliashberg coupling function  $\alpha^2 F(\omega)$ . The Eliashberg function is at the heart of the description of the e-ph coupling. By assuming fixed initial electron energy  $\epsilon_i$  and momentum  $\mathbf{k}$ , the Eliashberg coupling function between the initial state and all other final states ( $\epsilon_f$ ) (that differ in energy by  $\hbar\omega$ ) due to the phonon emission (E) or absorption processes(A)) is expressed as

$$\alpha^2 F^{E(A)}(\epsilon_i, \mathbf{k}; \omega) = \sum_{\mathbf{q},\nu,f} \delta(\epsilon_i - \epsilon_f \mp \omega_{\mathbf{q},\nu}) |g^{i,f}(\mathbf{k}, \mathbf{q}, \nu)|^2 \delta(\omega - \omega_{\mathbf{q},\nu}). \quad (5.4)$$

Where the signs ‘-’ and ‘+’ in the delta function denote the emission and absorption phonon, respectively,  $g$  is the probability matrix given in equation 5.3. In equation 5.4, the sum is performed over final states and all phonon mode ( $\mathbf{q}, \nu$ ). This Eliashberg function contains information about the phonon density of states (DOS) and their coupling with electrons, and the DOS has similar expression given by [195]:

$$D(\omega) = \sum_{\mathbf{q},\nu} \delta(\omega - \omega_{\mathbf{q},\nu}).$$

Since we already known that the DOS give information on how many phonons are available to scatter and how often they are scattered by the probability matrix, let us now relate these expressions to the mass enhancement parameter  $\lambda$  at  $E_F$  or to a measure of the e-ph coupling strength at higher binding energies ( $\lambda$ ).  $\lambda$  can be defined as a dimensionless parameter which measures the coupling strength of a hole of given energy ( $\epsilon_i$ ) and momentum  $\mathbf{k}$  to a lattice vibration mode or phonon of frequency  $\omega$ .

The variation of the energy of the scattered electron is due to the absorption or emission of the phonon. This energy variation can be neglected because the electronic energy scale

(range of eV) are much bigger than the phonon energies (range of meV). Therefore, the e-ph scattering modifies principally the direction of the electron motion i.e., momentum. Since the energy variation can be neglected, one can assume that the initial and final electron energies coincide. By taking into account this assumption, the delta function presents in equation 5.4 can be written as:

$$\delta(\epsilon_i - \epsilon_f \mp \omega_{\mathbf{q},\nu}) \approx \delta(\epsilon_i - \epsilon_f).$$

By applying this approximation or the so-called quasielastic assumption, the Eliashberg function for both emission and absorption processes are equivalent. Let us now relate the Eliashberg function with the parameter  $\lambda$  by using this assumption. The parameter  $\lambda$  can be written as the integral over the coupling function weighted by the phonon frequencies as follows:

$$\lambda(\epsilon_i, \mathbf{k}; \omega) = 2 \int_0^{\omega_{max}} \frac{\alpha^2 F(\epsilon_i, \mathbf{k}; \omega)}{\omega} d\omega, \quad (5.5)$$

where  $\omega_{max}$  represents the maximum phonon frequency and  $\omega_{max} = \omega_D$ , which represents the Debye frequency. This frequency ( $\omega_D$ ) indicates the highest frequency that a phonon can reach. The factor ‘2’ in front of the integral symbol in equation 5.5 comes from the equal contribution of the absorption and emission of phonons.

The influence of the e-ph interaction in the ARPES spectrum can be manifested by the shift in the dispersion of electronic states and by the changes in their lifetime. The imaginary part of the self energy ( $\Sigma''$ ) holds the information about the phonon-induced lifetime broadening of a hole (electron) state. Whereas, the real part ( $\Sigma'$ ) enables to evaluate the shift in electronic energies. Both parts of the complex e-ph self-energy can be fully described by the Eliashberg function. But in this thesis we will focus only in the relation between the e-ph Eliashberg function and the imaginary part of the e-ph self energy ( $\Sigma''$ ).

The inverse lifetime from the e-ph scattering can be expressed in terms of the imaginary part of the e-ph self-energy ( $\Sigma''$ ) as follows:

$$\Gamma_{e-ph}(\epsilon_i, \mathbf{k}, T) = 2\Sigma''(\epsilon_i, \mathbf{k}, T). \quad (5.6)$$

According to Ref. [96], the imaginary part of the e-ph self energy ( $\Sigma''$ ) is related to the Eliashberg function through the integral over all the possible phonon scattering events that conserve energy and momentum. By taking into account the quasielastic approximation, the imaginary part of the e-ph self energy ( $\Sigma''$ ) can be written as:

$$|\Sigma''(\epsilon_i, \mathbf{k}, T)| = \pi \int_0^{\omega_{max}} \alpha^2 F(\omega) [1 - f(\epsilon_i - \omega) + f(\epsilon_i + \omega) + 2\eta(\omega)] d\omega, \quad (5.7)$$

where  $f$  and  $n$  stand for the Fermi and Bose distribution function, respectively whereas,  $\epsilon_i$  is the initial energy of the electron. We can notice from equation 5.7 that temperature dependence of  $\Sigma''$  is introduced by the Fermi and Bose distribution function. At high temperatures i.e., when  $k_B T \gg \hbar\omega$ , the temperature dependence of  $\Gamma_{e-ph}(\epsilon_i, \mathbf{k}, T)$  and  $\Sigma''(\epsilon_i, \mathbf{k}, T)$  becomes linear and their slopes determine the parameter  $\lambda$ . In this case the expressions of  $\Gamma_{e-ph}(\epsilon_i, \mathbf{k}, T)$  and  $\Sigma''(\epsilon_i, \mathbf{k}, T)$  are then given by:

$$\Gamma_{e-ph}(\epsilon_i, \mathbf{k}, T) = 2\pi k_B \lambda(\epsilon_i, \mathbf{k}) T \quad (5.8)$$

$$\rightarrow \Sigma''(\epsilon_i, \mathbf{k}, T) = \pi k_B \lambda(\epsilon_i, \mathbf{k}) T. \quad (5.9)$$

One should note that equations 5.8 and 5.9 hold as long as the binding energy and momentum are kept constant.  $\lambda$  can be obtained from measurements of the lifetime broadening as a function of temperature [96].

By looking at equation 5.7, the question that arises immediately is the choice of an appropriate analytical expression for the Eliashberg coupling function in order to determine the parameter  $\lambda$ . The samples studied in this chapter are quasi two-dimensional and one could expect the use of the two-dimensional models in the description of the Eliashberg coupling function. Since there are no reasons why the phonons on the surface should not couple to phonons in the bulk (substrate), the use of the three dimensional (3D) model will be exploited. The choice of using the Debye and Einstein models comes from the fact that these models are used for estimating the phonon contribution to the specific heat or heat capacity in a solid. In the case of the Einstein model, each atom is treated as an independent harmonic oscillator, and the phonon frequencies are replaced by an average frequency for all phonons, called the Einstein frequency  $\omega_E$ . The Einstein model is generally poorly described at low temperatures especially for the heat capacity. This model was also chosen because it is a very easy model and just required one parameter to be fit that is the the Einstein frequency  $\omega_E$ . In the contrary, the Debye model is the improvement of the Einstein model because it treats the vibrations of the atomic lattice (heat) as phonons in a box and it correctly predicts the low temperature dependence of the heat capacity. Furthermore, a 3D debye model and Einstein model will be also used as Eliashberg coupling functions to describe the complex self energy. Although Einstein's model may have less physical meaning than the Debye model, we choose to include it because some information can still be obtained from it. Generally, one uses a simple models for the Eliashberg coupling function  $\alpha^2 F$ , such as:

the 3D Debye model given by the following analytical expression:

$$\alpha^2 F(\omega) = \lambda \left( \frac{\omega}{\omega_D} \right)^2, \quad \omega < \omega_D$$

and

$$\alpha^2 F(\omega) = 0, \quad \omega > \omega_D;$$
(5.10)

and the Einstein model given by

$$\alpha^2 F(\omega) = \frac{\lambda \omega_E}{2} \delta(\omega - \omega_E).$$
(5.11)

By looking at equation 5.10, one can view  $\alpha^2$  as the strength of the coupling linked to the DOS of the phonons  $F(\omega)$ . In Debye's model, the phonons disperse quadratically, making the DOS a parabola up to the Debye frequency. Whereas, in Einstein model (see equation 5.11) the dispersion is constant, making the DOS a single value. The two models gives almost the same results as long as the temperature is not very low [98].

We discussed in chapter 2 that it is possible to determine the real and imaginary part of the self-energy from the spectral function measured from ARPES experiment. Here, our main task now it is to find out how to extract the e-ph interaction parameter from ARPES spectra. From the above paragraphs, one can already notice that the most important quantity for describing the e-ph interaction is the Eliashberg function  $\alpha^2 F(\omega)$ , which cannot be extracted directly from the experiment. The main issue now is that the Eliashberg function is not a temperature-dependence function, while the self-energy ( $\Sigma$ ) is. In the subsequent paragraphs, we will illustrate the approaches that we used in order to obtain the e-ph coupling strength ( $\lambda$ ) from ARPES measurements.

The first approach consisted of using a computational function (or a type of programming in Igor pro software) of Einstein and Debye models in which the following expression (equation 5.12):

$$\Gamma = 2\pi \int_0^{\omega_{max}} \alpha^2 F(\omega) [1 - f(\epsilon_i - \omega) + f(\epsilon_i + \omega) + 2n(\omega)] d\omega + \Gamma_0,$$
(5.12)

together with equations 5.10 and 5.11, were considered, in order to fit the experimental data which are the temperature-dependence EDCs (MDCs) linewidths (But, section 5.2 gives more information on how these experimental data were obtained from ARPES spectra.). Thus, the value of  $\lambda$  was then obtained from the fitting. The equation 5.12 was obtained by using equations 5.6 and 5.7 and then by adding the term  $\Gamma_0$ . This term  $\Gamma_0$  denotes a temperature-independent offset, and it is supposed to be the contribution from the e-e

and e-df scatterings to the total inverse lifetime  $\Gamma$ . These two terms  $\Gamma_{e-e}$  and  $\Gamma_{e-df}$  were mentioned at the beginning of this section to be independent of the temperature.

The second approach that we used consisted to measure the temperature-dependence EDCs linewidth of the state far away from the Fermi level  $E_F$  in the ARPES spectra. By using this approach the linewidth is given by  $FWHM = 2|\Sigma''(T)| = \Gamma(T)$  [96, 98]. The expression of  $\Gamma(T)$  is given by equation 5.8, which shows the linearity of the curve. We then fitted our experimental data with a line above the Debye (Einstein) temperature to find the slope of the line and compared to equation 5.8 to extract the experimental value of  $\lambda$ .

For the metallic SL TaS<sub>2</sub>, the third approach that we used consisted of measuring the temperature-dependence MDCs linewidth of the state close to  $E_F$  in the ARPES spectra. From Refs. [96, 98], by using this approach the linewidth is given by  $FWHM = 2|\Sigma''(\omega)/v|$ , where by considering only one direction in  $\mathbf{k}$  space,  $v$  is defined as  $\epsilon(k) = vk$  such that the origin of the coordinates is at the Fermi level crossing. Here  $\epsilon$  corresponds to the energy. By using equation 5.8 and the expression of the  $FWHM$  in this case, together with the similar way explained in the second approach we were also able to extract the value of  $\lambda$ .

## 5.2 Analysis of temperature-dependent EDCs/MDCs

In this section, we will explain how the experiments were performed as well as, how we have obtained our experimental data or temperature-dependence linewidth that we mentioned in the previous section. One should note that we basically performed a similar experiment on the three TMDCs studied in this chapter, the only difference was the temperature range. Thus, we will take the case of WS<sub>2</sub>/Au(111) during the explanation. Furthermore, the temperature was measured by heating the sample with a filament mounted behind the sample holder.

An angular scan within a small momentum windows ( $\pm 0.15 \text{ \AA}^{-1}$ ) around the  $\bar{K}$  point were taken at each temperature, in order to obtain the temperature-dependent linewidth of states at  $\bar{K}$  point. This was taken in ascending (increasing temperature) and descending (decreasing temperature) series. The sample was annealed at 600 K for 1 min, after each descending temperature series to clean the sample surface. Afterwards, the sample was remeasured at the minimum temperature in order to verify the cleanliness of the sample and the consistency of the measurements. In total, two ascending and two descending series were

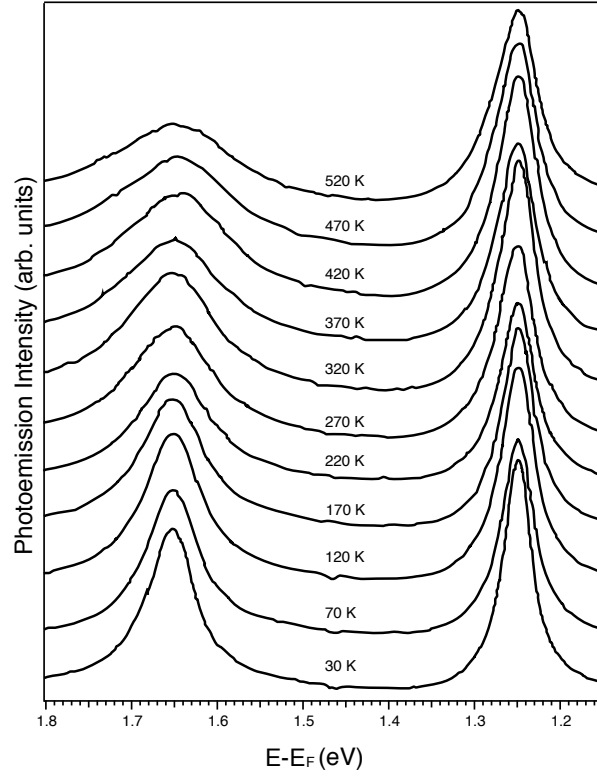


**Figure 5.1:** Temperature dependence energy distribution curves of SL WS<sub>2</sub>/Au(111) passing through the high symmetry  $\bar{K}$  point. The curves are displaced vertically.

performed. Figure 5.1 presents an example of a complete set of temperature-dependent EDCs (single series) passing through the  $\bar{K}$  point from SL WS<sub>2</sub>/Au(111) sample. For the case of the single layers WS<sub>2</sub>/Au(111) and MoS<sub>2</sub>/Au(111), each individual EDCs was fitted with a polynomial background and two Lorentzian peaks in order to obtain the value of the full width half maximum (FWHM) for each peaks. While, in the case of the SL TaS<sub>2</sub>/Au(111), the MDCs were fitted instead.

### 5.3 Tungsten and Molybdenum Dichalcogenides

The information presented in this section is mostly taken from Ref. [194]. The electronic structure of the semiconductors WS<sub>2</sub> and MoS<sub>2</sub> with trigonal prismatic structure have a sizable band gap compare to graphene [20, 21]. One should note that the lifting of the spin-degeneracy in the band structure of WS<sub>2</sub> and MoS<sub>2</sub> is due to the lack of inversion symmetry combined with the presence of heavy atoms in these materials. This can actually be observed near the valence band (VB) maximum at K point showing the splitting of the band (see Figure

5.2). The k-space spin splitting along with its spin-valley-locked band structure in lightly p-doped monolayer TMDCs are theoretically predicted to exhibit topological superconductivity which still needs to be confirmed experimentally [197].

The strong spin-splitting observed in the band structure of SL WS<sub>2</sub> and SL MoS<sub>2</sub> offers a particular opportunity to study electron-phonon (e-ph) coupling in system of states that simply differ by their spin [198]. In this section, we present theoretical and experimental results of e-ph coupling in SL WS<sub>2</sub> and SL MoS<sub>2</sub>. We have found that the coupling ( $\lambda$ ) is strongly branch-dependent of the spin-split band structure. These results can be clarified by spin-protected scattering and mostly by phase space restrictions [194].

Figure 5.2 presents the e-ph scattering contributions for the VB maximum of the SL WS<sub>2</sub>, in a diagram representing the band structure of this system. Figure 5.2 is also relevant for the case of SL MoS<sub>2</sub>. The relevant features in the band structure of SL WS<sub>2</sub> (SL MoS<sub>2</sub>) are the two spin-split VB maxima located at the high symmetry point K and K'. The spin structure is inverted at these two points due to the time-reversal symmetry. In the subsequent lines the spin-split band at K point will be assigned as the “upper” and “lower” bands. The “upper” band denotes the absolute VB maximum. The local VB maximum located at the high symmetry point  $\Gamma$ , which is spin-degenerate, is also shown in Figure 5.2.

Let us now described how a hole can be filled by an electron using the crystal momentum and energy of a phonon. A hole close to the top of the upper band located a K point (see Figure 5.2), can only be filled by an electron located at higher binding energy. This scenario necessitates the absorption of a thermally excited phonon. In process #1 (see Figure 5.2), the electron must come from the same band at higher binding energy. While, in process #2 (see Figure 5.2) the electron has to come from the upper VB located at K'. The process #2 is highly unlikely because a spin flip would be require or at least a considerable change in the value of the spin-expectation value in order to fill the hole located at the upper VB located at K [199]. It is important to note that due to the energy difference between the lower VB (or the band located at  $\Gamma$  point) and the upper VB which is  $\approx 0.43$  eV ( $\approx 0.22$  eV) and that exceed far from the maximum phonon energy  $\approx 52$  meV, no e-ph scattering processes from these bands are possible [194, 200]. On the other hand, various additional scattering processes are possible in the lower VB, thus, this can be seen for example from the VB at  $\Gamma$  point (see process #4 in Figure 5.2); or, from a state in the upper branch away from K point (see process #3 in Figure 5.2), for which the spin polarization is inferior than it is exactly at K; or from the lower VB near K' (this situation is not shown in Figure 5.2) [194].

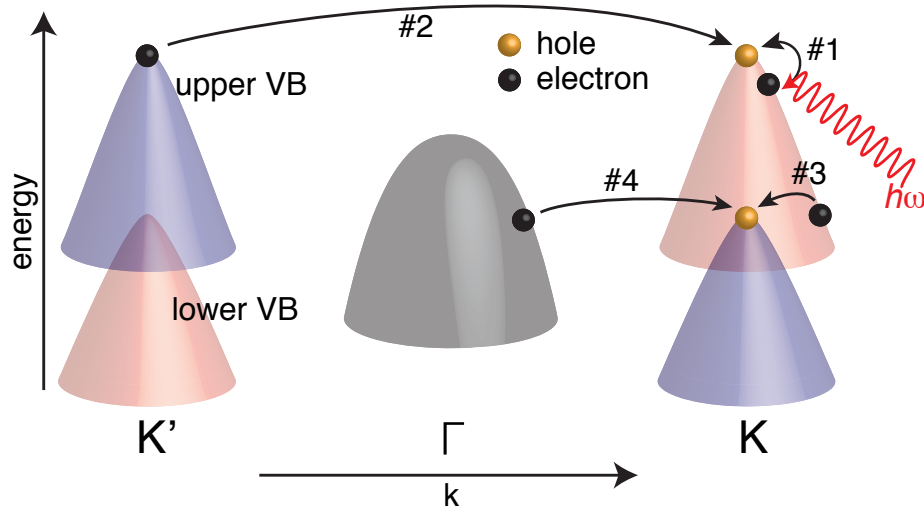


**Figure 5.2:** Schematic diagram of the valence band (VB) of SL WS<sub>2</sub> showing the valence bands maxima at K and K' together with the local maximum at  $\Gamma$  point. The VB at K and K' are spin split and the purple and pink colors indicate the direction of the spin. Whereas, the band at  $\Gamma$  point is spin degenerate. The e-ph scatterings processes to fill holes at the upper VB at K point are presented. The red curve shows the first process, where an electron is scattered into the hole by absorbing a phonon. The other scattering processes are not presented in this figure for the sake of clarity. This figure has been taken from Ref. [194]

Furthermore, all these processes can also proceed by phonon emission at low temperatures. On the basis of this simple image (Figure 5.2), one would expect a considerably lower el-ph coupling in the upper band than in the lower band, which will be also confirmed by our results. Even though the upper and lower valence bands differ only by the spin part of their wave function, one of the partly direct consequence of the state's spin texture is the difference of the value of the e-ph coupling strength between the two bands. It is also important to consider the restriction of scatterings number of available final states which can be a dominant factor for the el-ph coupling strength in this system.

### 5.3.1 Extraction of $\lambda$ from the Spin-Split Valence Bands of SL WS<sub>2</sub>/Au(111)

Many methods were used in order to extract the e-ph coupling strength from the spin-split VB of the SL WS<sub>2</sub>/Au(111) located at K point, and all of them gave approximately the same value. In the following paragraphs those different methods will be elucidated.

The first method consisted of using a very sophisticated calculations in order to compare

our experimental results with the theory. These calculations were done by Dr. Nicki Frank Hinsche from the department of Physics in the Technical University of Denmark. Here, I am only going to briefly introduce the method that he used, therefore, the readers can consult Ref. [194] and the supplementary material of the same article, where the complete computational details and calculations are available. Nicki has calculated the electronic structure and vibrational properties of SL WS<sub>2</sub>/Au(111) using the first principles calculations within density functional theory, as implemented in the Quantum-Espresso code [194]. In all his calculations, the relativistic effects such as the spin-orbit coupling were treated self consistently. He obtained the el-ph coupling strength of the free-standing SL WS<sub>2</sub> and that of the SL WS<sub>2</sub>/Au(111) within a modified version of the EPW code, based on the electronic and vibrational properties. He also calculated the linewidth  $\Gamma_{nk}$  from the hole mobility since the electrical conductivity tensor is inversely proportional to the linewidth  $\Gamma_{nk}$ , this can be seen in the supplemental material of Ref. [194].

The ARPES band structure for the high-quality SL WS<sub>2</sub>/Au(111) near the high symmetry K point is shown in Figure 5.3(a), presenting the two well separated spin-split branches of the VB. There is no direct hybridization between the SL WS<sub>2</sub> and the Au(111) substrate bands, since the area of the band structure very close to K point is located in a projected bulk band gap of the Au(111) [201], and the states are very narrow. The high quality of the sample reveals some undetected details until now on the band structure of the SL WS<sub>2</sub>/Au(111). Below the top of the upper and lower VB branches, a kink-like deviation from the almost parabolic dispersion is visible at energies of  $174 \pm 14$  meV and  $124 \pm 18$  meV, respectively (see Figure 5.3(a)). A magnification of the area enclosed by the black circle shows the kink-like deviation observed on the band dispersion of the upper VB in Figure 5.3(b). When such type of kinks occur on the bands dispersion of materials located close to the Fermi energy, they are frequently an indication of the strong e-ph coupling in such system [202]. Such kinks can also be found at higher binding energy on some band dispersion of some materials, for instance, the top of the sigma band of graphene presents such kink [97, 203]. Here, the e-ph coupling can be excluded as the cause of the kink, since its separation from the top of the valence band exceeds far the highest phonon energy ( $\approx 52$  meV). Furthermore, the situation is very different from that of the graphene [97, 203], since the calculated e-ph coupling is small and one would not expect any observable kinks [194]. We rather assign the observable kink on the bands dispersion of SL WS<sub>2</sub>/Au(111) to a minigap opening at the new Brillouin zone boundary caused by the moiré superstructure formed between the SL WS<sub>2</sub> and Au(111). One should note that the minigaps do not influence the band structure

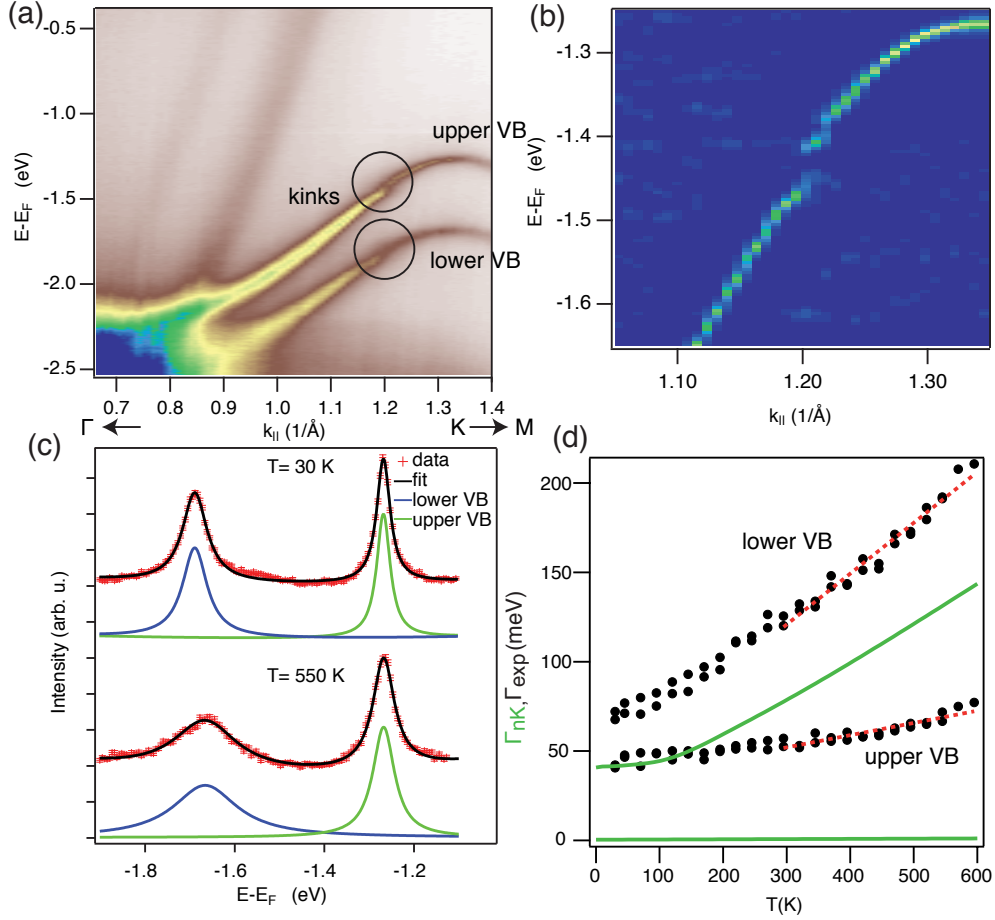


**Figure 5.3:** ARPES spectra on SL WS<sub>2</sub>/Au(111): (a) Band dispersion of SL WS<sub>2</sub>/Au(111) along the high symmetry direction  $\Gamma$ - $K$  acquired at 30 K. The black circles indicate the positions of the kinks in the dispersion. (b) Curvature [163] of the data presented in (a), exhibiting the kink in the dispersion of the upper valence band. (c) EDCs passing through the symmetry point  $K$  at low and high temperatures. The data are represented by markers. The black curves that are superimposed on top of the experimental data are the resulting fit with a polynomial background and two Lorentzian peaks (see the blue and green curves). (d) The back full circles are the temperature dependence Lorentzian linewidth of the upper and lower bands in an energy distribution curve passing through  $K$  point. The dashed red lines are fits of the experimental data at high temperature ( $T > 300$  K). The green curves are from the calculation of the temperature-dependent linewidth of the spin-split valence band at  $K$  point from the free-standing layer. These figures have been taken from Ref. [194].

exactly at the  $K$  point (see Appendix B).

The e-ph coupling strength of the two spin-split branches of SL WS<sub>2</sub>/Au(111) can be determined by analyzing several energy distribution curves (EDCs) passing through  $K$  point from data acquired at different temperatures. A comparison of two EDCs taken at 30 K and 550 K is presented in Figure 5.3(c). From this figure, it is obvious that the temperature-induced

broadening of the lower branch is significantly stronger than that of the upper branch, in qualitative agreement with the theoretical results. For more quantitative analysis, several EDCs acquired within a large temperatures range (i.e., here from 30 K to 550 K) are then fitted with two Lorentzian peaks and polynomial background (see the example of peaks fitting in Figure 5.3(c)) [96]. Figure 5.3(d) shows the resulting linewidth ( $\Gamma(T)$ ) plotted together with the theoretical result for the free-standing layer of WS<sub>2</sub>. Since the theoretical model used in order to obtain the theoretical curves (see green curves in Figure 5.3(d)), does not contain the contributions of e-e and e-df scattering, we do not expect the experimental linewidth to be similar to the theoretically calculated values (see Figure 5.3(d)). These can be important, but remember that these two contributions are generally independent of the temperature as mentioned in section 5.1. One should allow for a temperature independent offset, while comparing the calculation and the experiment as this was done for instance in equation 5.12.

The calculated linewidth (solid green lines) for the upper and lower VB at K point for the free-standing SL WS<sub>2</sub> as a function of temperature is shown in Figure 5.3(d). These calculated curves indicate the much strong e-ph coupling for the lower band, confirming the simple picture discussed in Figure 5.2. One can see in Figure 5.3(d) that the linear high-temperature regime starts above  $\approx 300$  K, and a linear fit to the linewidth between 300 K and 600 K gives  $\lambda_K = 0.0021$  and  $\lambda_K = 0.40$  for the upper and lower VB, respectively. Due to the high energy phonons not being equally occupied in this temperature range, the dependence of these curves are not linear. Thus, a fit for even higher temperatures range (550 K - 750 K) gives  $\lambda_K = 0.0025$  and  $\lambda_K = 0.42$  for the upper and lower VB, respectively, which are slightly higher. The very small el-ph coupling of the upper VB branch is also indicated in a theoretically estimated large hole mobility of  $988 \text{ cm}^2/V_s$  at hole carrier concentration of  $1 \times 10^{13} \text{ cm}^{-2}$  and  $T = 300 \text{ K}$  which is discussed in the supplemental material of Ref. [194].

One should note that a signature of the e-ph interaction is the linear temperature-dependence of  $\Gamma_{\text{exp}}$  or  $\Gamma_{\text{nk}}$  at high temperatures ( $T$ ). The coupling constant  $\lambda$  can be estimated from the data presented in Figure 5.3(d) in the same way as previously used in the precedent paragraph for the theoretical data. A linear fit of the data for elevated temperatures (i.e., at  $T > 300 \text{ K}$ , see red dashed lines in the Figure 5.3(d)) gives coupling constants of  $\lambda_K \approx 0.13$  and  $0.52$  for the upper and lower VB, respectively. From Figure 5.3(d), one can see that the experimental data above  $T > 300 \text{ K}$  is not truly linear and therefore, the resulting  $\lambda$  depends on the chosen temperature range for the fit.

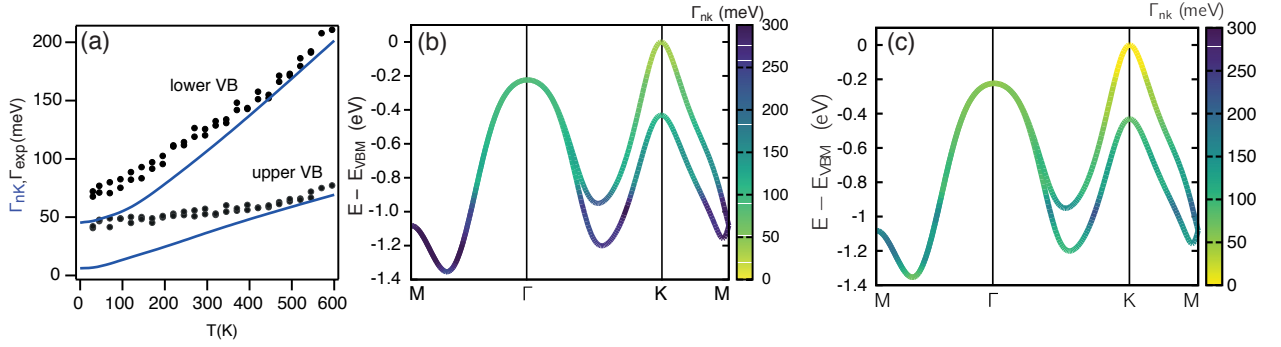


**Figure 5.4:** (a) Temperature-dependence of the linewidth of the two valence bands centered at K point (see Figure 5.3(a)), exhibiting the experimental data as well as the calculation, containing the contributions of the scattering from the Au(111) substrate. Calculated band structure of SL WS<sub>2</sub> with encoded linewidths holding the effects of the Au(111) substrate (b) and for free-standing layer (c). Figures have been taken from Ref. [194].

From Figure 5.3(d), by allowing a temperature independent offset between the curves, we can notice a good agreement between the experimental and calculated linewidths for the lower band. Moreover, the calculated slope at high temperature is similar to the experimental result. Unlike in the case of the lower band, the agreement between the experimental and calculated linewidths for the upper band is less satisfactory. Moreover, the experimental linewidth for the upper band has a noticeable slope (reflected by  $\approx 0.13$ ) compared to the calculated one which is the nearly flat ( $\approx 0.0021$ ), therefore, even by adding a constant offset to the calculated linewidth, there will always a disagreement between the two curves.

One should note that, a possible implication of the Au(111) substrate states on the resulting calculated linewidths has not yet been considered so far. The presence of the substrate allows new decay channels via e-e, e-df and e-ph scatterings [194]. Note that the scattering into the substrate is known to be an important process for the decay of excited carriers in the conduction band [36]. It is straight forward to include the substrate states in the calculation of the imaginary part of the e-ph self energy ( $\Sigma''$ ) and  $\lambda$ , since it simply requires that the sums in equations 1 and 2 in Ref. [194] are extended over the Au(111) electron and phonon states (see supplemental material of Ref. [194]). Note that in this approach, the effects of band hybridization between SL WS<sub>2</sub> and the Au substrate are still neglected, together with the impact of the Au(111) surface state, at the expense of computational feasibility [194]. Here, the good news is that none of the latter effects have a significant impact on the final results at K point, since band hybridization effects were mostly found to occur near the  $\Gamma$  point at high binding energies. The Au(111) surface state should not play a role here, because it is located at energies well above the VB maximum [204]. Note that the

quantitative results can still be affected by the hybridization in the possible final states for scattering processes.

By taking into account the substrate's contribution to the e-ph coupling, a linear fit to the calculated linewidth between 300 K and 600 K was performed, and the e-ph coupling strength is found to be  $\lambda_K = 0.58$  and  $\lambda_K = 0.20$  for lower and upper VB, respectively. Figure 5.4(a) shows the experimental data plotted together with the calculated temperature-dependence linewidth where the substrate's contribution was taken into account. From this figure, there is an improved agreement between the experimental and calculated linewidths for the upper band, leading to a closer value of  $\lambda$ , while, the theoretical coupling strength is now exceeds a little bit the experimental value. The calculated VB structures for free-standing SL WS<sub>2</sub> and for the SL WS<sub>2</sub>/Au(111) with color coding of the linewidth are presented in Figures 5.4(c) and 5.4(b), respectively [194]. The comparison of Figures 5.4(b) and 5.4(c) shows that the Au substrate leads to a broadening of the states, particularly at high binding energies. Even by taking into account the Au(111) substrate, the strong branch dependence of the el-ph coupling strength is still present in both calculations. Figure 5.4(a) shows that even by allowing a temperature independent offset between the experimental and calculated linewidth curves, there is no good agreement between the two curves for the lower band, as well as for the upper band. The most probably explanation might lie in the simplicity of the model used, which needs a small unit cell to be manageable and does not describe sufficiently the hybridization between the SL WS<sub>2</sub> and Au(111) bands.

The second method consisted of using the first approach presented at the end of subsection 5.1.1, i.e., by fitting our data with the Einstein and Debye models in order to determine the e-ph coupling strength  $\lambda$ . Figure 5.5(a) shows the temperature-dependent Lorentzian linewidth of SL WS<sub>2</sub>/Au(111) at K point as well as the calculations for the expected  $\Gamma_{\text{e-ph}}$  from the Einstein and Debye models, which all have a similar trend. The values of the e-ph coupling strength for the lower VB was found to be  $\lambda = 0.47 \pm 0.01$  from both the Debye and Einstein models. While that of the upper VB are  $\lambda = 0.12 \pm 0.01$  from both Debye and Einstein models. Note that the Debye temperature used here was 213.6 K from Ref. [205] and the Einstein temperature was 181.03 K. This value was obtained by leaving the Einstein temperature as a free parameter during the fitting. By comparing these  $\lambda$  values with those obtained from the first principles calculations ( $\lambda = 0.20$  for the upper VB and  $\lambda = 0.58$  for the lower VB), we can notice a significant difference. This difference might be linked for example to the value of the Debye temperature that we used, because it was for a free-standing SL of WS<sub>2</sub>. However, in the case of SL WS<sub>2</sub>/Au(111), one can consider that some

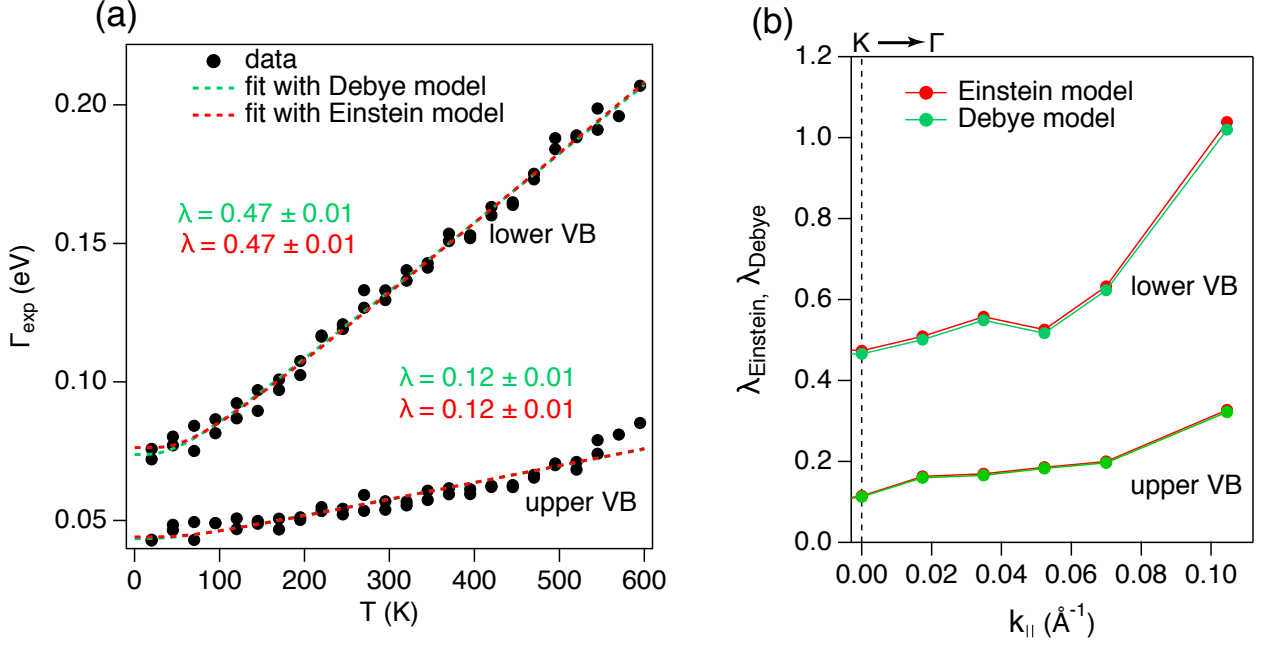


**Figure 5.5:** (a) Temperature-dependence linewidth of the SL WS<sub>2</sub>/Au(111) taken at K point. The red and green dashed lines are the e-ph contributions to the linewidth calculated within the Einstein and 3D Debye models, respectively. It should be note that the e-e and e-df scatterings have been taken into account in these two models. The values of e-ph coupling strengths obtained from these two models are written on the picture. (b) E-ph coupling strength  $\lambda$  as a function of momentum from the Einstein and Debye model acquired along the  $\Gamma$ -K direction. Note that the position of the high symmetry point K has been set to zero just to show how far from the K point the  $\lambda$  values were determined.

vibration is also coupled to the underlying Au(111) substrate through the bindings between the WS<sub>2</sub> layer and the substrate. Therefore, the mixture of many parameters present in the system can modify the value of the Debye temperature. Figure 5.5(b) shows  $\lambda$  as a function of momentum when moving away from K point towards  $\Gamma$  point, with the expected trend. The increase of  $\lambda$  value while moving far away from K point can be explained by the fact that electrons will have more and more chances to scatter to  $\Gamma$  or to another K/K' valley by phonon coupled momenta. Furthermore, the momentum dependence of  $\lambda$  for the upper VB is not very strong within the momentum range presented in Figure 5.5(b), it changes from 0.2 to 0.32 in a momentum range of 0.035. While, the momentum dependence of  $\lambda$  for the lower VB is most stronger, it changes from 0.62 to 1.06 within the same momentum range and the relative increase is very similar. From Figures 5.5(a) and 5.5(b), we can notice that the values of lambda obtained from the Debye and Einstein models are the same, this is due to the fact that much of the data was taken at elevated temperatures relative to Debye's temperature, where the precise nature of the phonon spectrum becomes negligible.

Furthermore, at high temperature the Debye and Einstein models are both correct.

In summary, by using multiple methods to determine the e-ph coupling strength  $\lambda$  in SL WS<sub>2</sub> we obtained similar values. Most importantly, our results show significant difference between the e-ph coupling strength in the spin-split VB states at K.

### 5.3.2 Extraction of $\lambda$ from the Spin-Split Valence Band of SL MoS<sub>2</sub>/Au(111)

The same methods, mentioned in the previous section, were used to determine the e-ph coupling strength in a similar system i.e., in a SL MoS<sub>2</sub>/Au(111). Figure 5.6(a) presents a band structure of SL MoS<sub>2</sub>/Au(111) taken along the  $\Gamma$ -K direction, where the two spin-split branches are well visible. Figures 5.6(b) and 5.6(c) show a comparison of two EDCs taken at 30 K and 530 K. These two figures also show how the temperature-induced broadening of the lower branch is stronger than that of the upper branch. Several EDCs acquired within a wide temperatures range (i.e., from 30 K to 580 K) were fitted with two Lorentzian peaks with a polynomial background in order to extract the value of the temperature-dependent linewidth presented by the black filled circles in Figure 5.6(d). Note that to acquire the data for this study, a total of two ascending and one descending temperature series were performed. These temperature-dependent linewidths for the upper and lower VB were then fitted with Debye and Einstein models in order to obtain the value of the e-ph coupling strength  $\lambda$  for this system. For the lower band, the  $\lambda$  found are  $\lambda = 0.32$  (Debye) and  $\lambda = 0.33$  (Einstein). For the upper band  $\lambda = 0.05$  (Debye) and  $\lambda = 0.05$  (Einstein). The values found from fitting linear relation equation 5.8 (see the blue dashed lines in Figure 5.6(d)) to the data are  $\lambda = 0.40$  and  $\lambda = 0.09$  for the lower and upper VB, respectively. Since we do not have the calculated  $\lambda$  value for this system from the first principles calculations, we will rather compare our results between the three methods used (from Debye and Einstein models and from the fitting of a linear relation). The values of  $\lambda$  from the three methods used are more or less the same. Thus, we can also compare the results here with those found in the previous section. These values are not so similar to those found in SL WS<sub>2</sub>/Au(111) ( $\lambda = 0.20$  for the upper VB and  $\lambda = 0.58$  for the lower VB) determined by using the first principles calculations. This might also due to the choice of the Debye temperature which was 262.3 K for the free-standing SL of MoS<sub>2</sub> from Ref.[205], which is not taking into account the presence of the Au(111) substrate. The Einstein temperature in this case was found to be

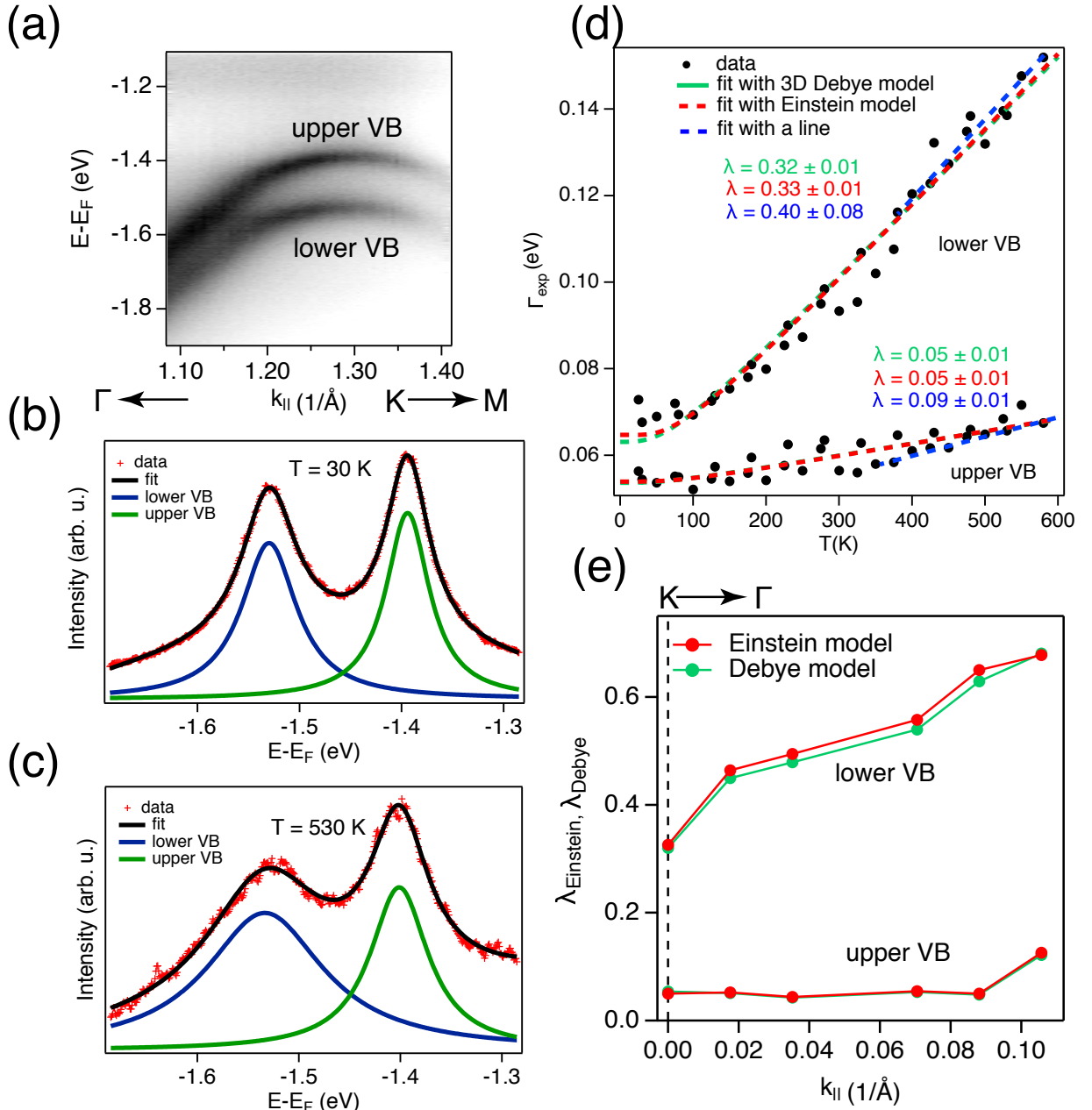


**Figure 5.6:** (a) Photoemission intensity of SL MoS<sub>2</sub>/Au(111) along the  $\Gamma$ -K direction acquired at 30 K. The upper and lower bands are indicated on the picture. (b, c) The EDCs cuts passing through K point at low (30 K) and high (530 K) temperatures fitted with two Lorentzian peaks together with a polynomial background are also shown. (d) The filled black circles are the temperature-dependence Lorentzian linewidths of the lower and upper valence bands. The e-ph contributions to the linewidth calculated within the Einstein and 3D Debye model are shown by the red and green dashed lines, respectively. Here, the e-e and e-df scatterings have been taken into account in the two models. The values of the e-ph mass-enhancement parameter  $\lambda$  are written on the figure. The blue dashed lines are just the fit along the linear parts of the curves in order to determine the value of  $\lambda$  (this method was described as second approach at the end of section 5.1.1.). (e) E-ph mass-enhancement parameter  $\lambda$  as a function of the momentum from the Einstein and Debye model taken along the  $\Gamma$ -K direction. Note that the K point here has been set to zero just to show how far from K point the  $\lambda$  values were determined.

215.8 K, this value was also obtained by leaving the Einstein temperature as a free parameter during the fitting.

A significant difference between the e-ph coupling strength in the spin-split VB states at K in the SL MoS<sub>2</sub> was not expected since the calculated band structure of the free standing SL MoS<sub>2</sub> using the first-principles calculations based on DFT [206] and in the case of the calculation that include many-body effects [207], shows that the upper VB maxima at K and  $\Gamma$  have nearly the same binding energy. But in the case of the SL MoS<sub>2</sub>/Au(111) the situation is different due to the fact that the upper VB near  $\Gamma$  has an out-of-plane character that favor the hybridization between the SL MoS<sub>2</sub> and the Au(111) substrate orbitals leading to the distortion of the upper VB near  $\Gamma$ , this situation is explained in Ref. [208]. Thus, in the case of our present study the situation becomes similar to what we saw in Figure 5.2 where there is an energy difference between the lower VB (or the band located at  $\Gamma$  point) and the upper VB of  $\approx 145$  meV (of  $\approx 0.31$  eV) that exceed the maximum phonon energy of  $\approx 22.60$  meV (this value was calculated using the Debye temperature that we used for the case of MoS<sub>2</sub>/Au(111) i.e., 262.3 K) or 48 meV from Ref. [209]. Therefore, one would expect a considerably lower el-ph coupling strength in the upper band than in the lower band.

The e-ph coupling strength  $\lambda$  as a function of momentum when moving from K towards  $\Gamma$  is presented in Figure 5.6(e), with the expected trend. Furthermore, one can see that in SL MoS<sub>2</sub>/Au(111), the momentum dependence of the upper VB is less stronger than, the one for the lower VB. The same situation was observed in the case of SL WS<sub>2</sub>/Au(111) (see Figure 5.5(b).)

## 5.4 Extraction of $\lambda$ from the Spin-Split Valence Band of SL 1H-TaS<sub>2</sub>/Au(111)

In this section, we present how we determine the e-ph coupling strength on the SL 1H-TaS<sub>2</sub>/Au(111) using some preliminary data. Only a total of one ascending and one descending series were performed because it was really challenging to obtain the data since the sample was getting dirty very quickly. Figure 5.7(a) shows the two hole pockets of SL 1H-TaS<sub>2</sub>/Au(111) centered around K point. A cut taken along the dashed line shown in Figure 5.7(a) is presented in 5.7(b), where the two dispersion observed in this figure are labeled peak 1 and peak 2. In order to extract the value of the temperature-dependent linewidth presented

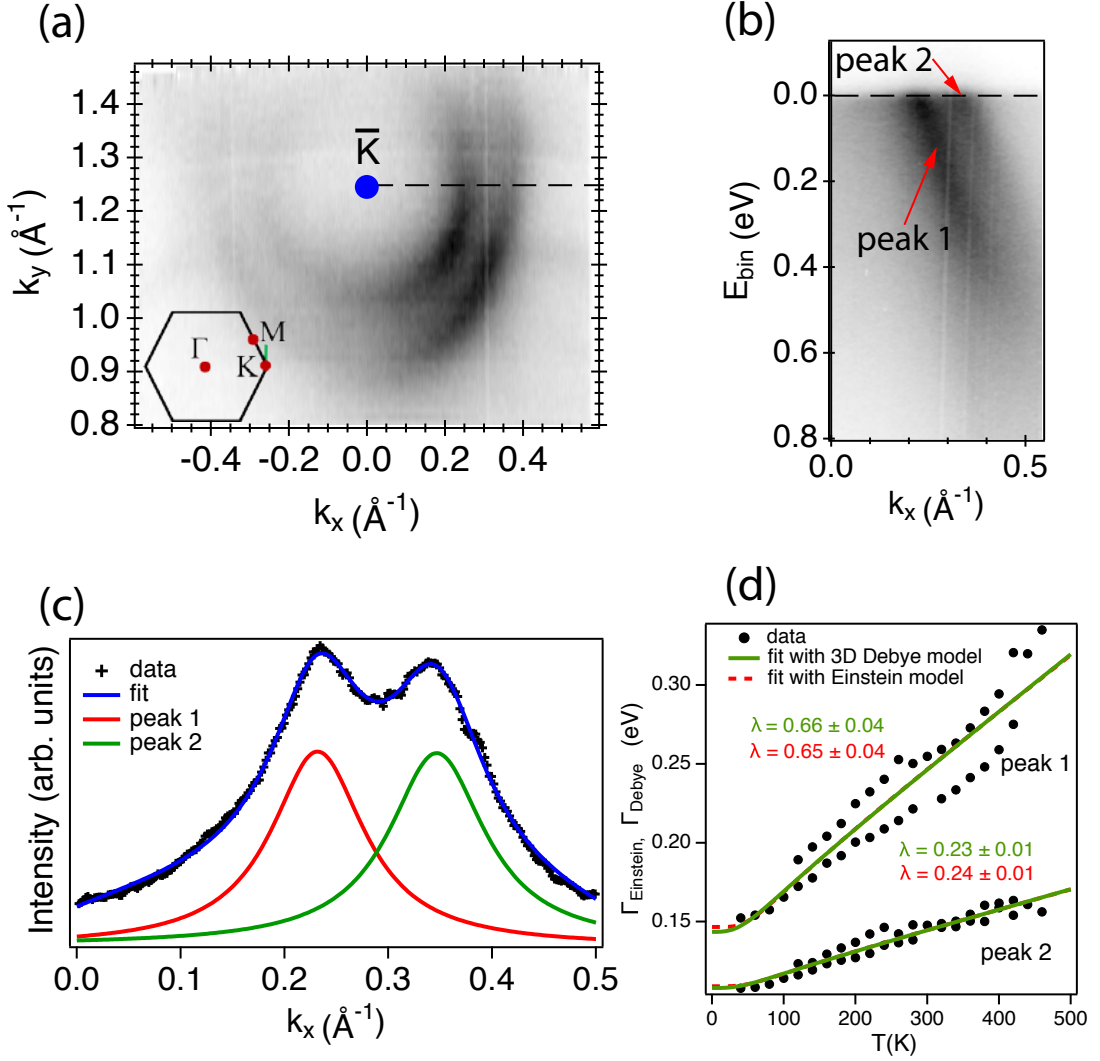


**Figure 5.7:** (a) ARPES measured Fermi surface of SL 1H-TaS<sub>2</sub>/Au(111) around the high symmetry point K. The measurement was taken with the photon energy and temperature of 30 eV and 30 K, respectively. (b) ARPES spectrum extracted along the direction indicated by the black dashed line in (a) (or simply along the green solid line on the BZ). The spectrum presents two bands dispersion, that are labeled peak 1 and peak 2. (c) Example of an momentum distribution curve (MDC) taken at the Fermi level in b (see black dashed line at the Fermi level). This MDC cut (data) is fitted with two Lorentzian peaks together with a polynomial background. (d) The markers are the temperature-dependent Lorentzian linewidths of peak 1 and peak 2, respectively. The lines are e-ph contributions to the linewidth calculated within the Einstein (red) and 3D Debye (green) models. Note that in the two models, the e-e and e-df scatterings have been taken into account. The values of the e-ph coupling strength are written on the figure.

by the black filled circles in Figure 5.7(d), several MDCs at the Fermi level acquired within a large temperature range (i.e., from 30 K to 480 K) and fitted with two Lorentzian peaks with a polynomial background and then multiplied with  $v = \epsilon(k)/k$ . The unrenormalized

dispersion ( $\epsilon(k)$ ) was obtained from a measurement of the dispersion at high temperature where the renormalization due to the e-ph coupling is insignificant [96]. Figure 5.7(c) shows an example of such type of fit. These temperature-dependent linewidths for the peak 1 and peak 2 were then fitted with Debye and Einstein models in order to obtain the value of the mass enhancement parameter for this system. For the peak 2, the  $\lambda$  found is 0.23 for Debye and 0.24 for Einstein models, respectively. For peak 1, the  $\lambda$  found are 0.66 from Debye model and 0.65 from Einstein model. The Debye temperature that we used here was that of the free-standing SL WS<sub>2</sub> i.e., 213.6 K [205]. The reason for choosing this value of the Debye temperature is due to the fact that Ta and W are neighbor elements in the periodic table and therefore have more or less similar effective masses. The Einstein temperature was found to be 174.07 K. This value was obtained by leaving the Einstein temperature as a free parameter during the fitting. We also observe in this case a significant difference between the e-ph coupling strength in the spin-split VB states located near the K point in the SL 1H-TaS<sub>2</sub>/Au(111). There is no e-ph coupling strength calculation in 1H-TaS<sub>2</sub>/Au(111) in the literature so far that we can use to compare our results. In the most recent paper of Nicki and his colleague [210], the value of the  $\lambda$  given in this paper was averaged over the whole Fermi surface. Therefore, we cannot compare our result with this because we rather focus on a specific point on the Fermi surface.

---

# Conclusion and Outlook

---

The aim of this thesis was, first, to study the 3D band structures of the highly correlated material 1T-TaS<sub>2</sub> in all its known different CDW phases at different temperatures; secondly, to find a suitable method to synthesize TaS<sub>2</sub> from few monolayers down to the single layer limit, in order to investigate the presence or absence of the CDW states in these systems; and, finally, to study the electron-phonon coupling in the 2D TMDCs SL WS<sub>2</sub>, SL MoS<sub>2</sub> and SL 1H-TaS<sub>2</sub>. These studies were done by analysis data from ARPES, STM/STS and LEED experiments. This chapter summarizes all the chapters and results presented in this thesis. An outlook based on the theoretical calculations and experiments planned in the future is presented, as well.

## 6.1 Conclusion

Chapter 1 of this thesis presents a general description of TMDCs, together with some physical and electronic properties of WS<sub>2</sub>, MoS<sub>2</sub> and TaS<sub>2</sub> in particular, since they are the compounds that are the main topic of this thesis.

Chapter 2 gives an overview of the experimental techniques (LEED, STM and ARPES) used in order to acquire the data presented in this thesis. This chapter also describes the SGM3 beamlines where the majority of the experiments took place.

Chapter 3 is dedicated to the study of the bulk 1T-TaS<sub>2</sub> in all its known CDW phases at

different temperatures. This was done based on the study of the temperature-dependence of the in-plane/out-of-plane electronic structures of bulk 1T-TaS<sub>2</sub>, using ARPES and XPS experiments. It has been predicted by recent band calculations that the CDW in the C-CDW phase coexists with a nearly one-dimensional metallic dispersion perpendicular to the crystal planes in this compound. By means of ARPES, we have shown that this metallic band indeed exists. Furthermore, it not only exists in the C-CDW phase but also in the NC-CDW phase as well. Since the CDW can be also studied via the core levels of Ta [103], we have presented in this work XPS measurements on the Ta 4f spectra for 1T-TaS<sub>2</sub> at temperatures ranging from  $\approx 30$  K to above  $\approx 600$  K. Moreover, we have presented the first experimental data on the band dispersion of 1T-TaS<sub>2</sub> taken at the normal phase, which is in agreement with the theoretical predictions.

Chapter 4 presents the methods used to synthesize 1H-TaS<sub>2</sub> in single-layer and bilayer thicknesses. The growth method was successfully modified to create large single-domains. This can be seen in the STM images of SL TaS<sub>2</sub>/Au(111) grown by the filament method, which produces large size domains in comparison with those obtained from the evaporator method (More details can be found in Ref. [110]). The geometric and electronic structure of these compounds were analyzed as well. Moreover, the STM/STS measurements taken at 4.7 K show no sign of the CDW state in SL 1H-TaS<sub>2</sub>, and no sign of superconductivity, either. The absence of CDW in this system is explained by the strong electron doping originating from the substrate. Recent theoretical studies on the suppression of the CDW in this system have suggested that the origin of the doping seen in the SL 1H-TaS<sub>2</sub> derives from band hybridization rather than from actual charge transfer between the Au(111) and TaS<sub>2</sub> [184]. Furthermore, the study of the BL TaS<sub>2</sub> in its H form reveals a reconstruction of  $(\sqrt{3} \times \sqrt{3})R30^\circ$  TaS<sub>2</sub>. This might be a sign of a CDW in this system that exists even above room temperature; or, it might be some other type of surface reconstruction of TaS<sub>2</sub>. This study is still an ongoing project so it is difficult to draw any conclusions so far.

Chapter 5 describes different methods used for determining the electron-phonon coupling strength in single layer WS<sub>2</sub>, MoS<sub>2</sub> and 1H-TaS<sub>2</sub>. Our results show a significantly different electron-phonon coupling strength between the two spin-split VB states at the K point, due to phase-space restrictions. Furthermore, we have also shown that the strong difference in the electron-phonon coupling strength in the two spin-split branches of SL WS<sub>2</sub> persists in the presence of a highly interactive substrate. Finally, the high quality of the sample reveals kinks in the spin-split VB of SL WS<sub>2</sub>. Such kinks are assigned to the minigaps opening at the Brillouin zone boundaries caused by the moiré superstructure formed by the Au(111)

substrate and the SL WS<sub>2</sub>.

## 6.2 Outlook

We do not know yet the range of temperature in which the normal phase of the bulk 1T-TaS<sub>2</sub> can survive. It has been predicted by Ref. [157] that at high temperature (from the normal phase) the bulk 1T-TaS<sub>2</sub> slowly transforms into the bulk 2H-TaS<sub>2</sub>, resulting also in the change of the shape of the core level peaks of the materials. Therefore, a careful temperature-dependent study based on XPS measurements of the Ta 4f core levels is needed. The choice of this experiment is due to the fact that it is faster to perform than ARPES.

A careful temperature-dependent LEED study of this system is also needed since we might come across some new phases due to the richness of the physical and electronic properties that this system contains. The choice of the LEED experiment is due to the fact that it will be faster to perform it than ARPES and the determination of a change of the surface structure or symmetry of the compound will be very easily noticeable.

Given that there is a strong  $(\sqrt{3} \times \sqrt{3})R30^\circ$  reconstruction of TaS<sub>2</sub> in the BL TaS<sub>2</sub> that we do not fully understand so far, if this might be the possible adsorbates on the surface or of intercalates between the 1st and 2nd layer, or simply a sign of the CDW in this system, therefore, theoretical studies of the BL TaS<sub>2</sub> is needed. Furthermore, maybe a different growth method could be used to prevent this. Since during the LEED measurement that we have performed in this sample, we did not heat the sample to a very high temperature, we could also do some temperature-dependent LEED study up to 600 K to check if we could try to melt the reconstruction and then cooling it again down to see if the reconstruction reforms. After understanding the origin of this reconstruction, we can also extend our study of TaS<sub>2</sub>/Au(111) to few-and higher-numbers of layers to investigate if there anything interesting such as superconductivity, CDW. We can also grow a BL TaS<sub>2</sub> on different substrates to see if there is a sign of  $(\sqrt{3} \times \sqrt{3})R30^\circ$  reconstruction of TaS<sub>2</sub>.

Since there are no calculated electron-phonon coupling strengths from the SL MoS<sub>2</sub> and 1H-TaS<sub>2</sub>, some theoretical studies on this might be needed with which to compare our results. The determination of the electron-phonon coupling strength was only done on a specific position of the band structure of single layer WS<sub>2</sub>, MoS<sub>2</sub> and 1H-TaS<sub>2</sub> and a bit far away for K point (SL WS<sub>2</sub> and MoS<sub>2</sub>), an additional studied are needed to fully study the influence

---

of the electron-phonon coupling in the entire band structure of these 2D systems, since the study of the electron-phonon coupling is still a viable route to achieve superconductivity.

# Appendix A

---

## Free-Electron Final States

---

The information presented in this appendix has been taken from the supplementary material of Ref. [131]. As mentioned in chapter 3, the photon energies axis for the whole photon energy dependence scans acquired at different temperatures were converted to  $k_{\perp}$  by assuming a free-electron final state model [84, 144]. In this model, the expressions of the kinetic energy ( $E_k$ ) and the momentum ( $k_{\perp}$ ) of the free-electron are given by equations 2.3 and 2.6, respectively. In these equations,  $m_e$  is the mass of the electron,  $\theta$  is the polar angle,  $V_0$  indicates the inner potential,  $h\nu$  the photon energy,  $\Phi$  the work function and finally  $E_B$  the electron binding energy.

In the case where the data are acquired at the normal emission (as in Figures 3.4(a), 3.4(b), 3.4(c), 3.7(a), 3.7(b), 3.7(c), 3.9 and 3.12 in chapter 3), the momentum  $k_{\perp}$  becomes:

$$\mathbf{k}_{\perp} = \frac{1}{\hbar} \sqrt{2m_e(h\nu - \Phi - E_B + V_0)}. \quad (\text{A.1})$$

By using  $V_0 = 20$  eV,  $\Phi = 4.5$  eV and  $E_B = 0$  eV (at the Fermi level), we can predict the photon energies at which  $\bar{\Gamma}$  corresponds to  $\Gamma$  or  $A$ . These energies are the following: 24, 54, 94, 142, and 199 eV (resp. 12, 38, 73, 117 and 170 eV) for  $\Gamma$  (resp.  $A$ ).

To be precise, an angular scan taken with photon energy of  $h\nu = 94$  eV or 73 eV will attain the high symmetry point only for  $k_{\parallel} = 0$  and only approximately when the angular scan will be taken a little away from the center of the first Brillouin zone (BZ). The estimate values on the error of  $k_{\perp}$  when  $k_{\parallel} \neq 0$  is presented in table A.1. An angular scan acquired at a constant photon energy provides an appropriate estimate for the points inside the first BZ, but fails to correctly pass through the second  $\Gamma_1$  point.

---

$h\nu$	$\Delta k_{\perp}$ at $\bar{\Gamma}_0$	$\Delta k_{\perp}$ at $\bar{M}$	$\Delta k_{\perp}$ at $\bar{K}$	$\Delta k_{\perp}$ at $\bar{\Gamma}_1$
94 eV	0	-0.10	-0.14	-0.43
73 eV	0	-0.12	-0.15	-0.48

---

**Table A.1:** Calculated deviation on  $k_{\perp}$  in units of  $2\pi/c$  for an angular scan taken at constant photon energy (94 or 73 eV) at different high symmetry points. One should note that here  $\bar{\Gamma}_0$  corresponds to the 3D  $\Gamma$  (94 eV) or  $A$  (73 eV),  $\bar{M}$  corresponds to the 3D  $M$  (94 eV) or  $L$  (73 eV),  $\bar{K}$  corresponds to the 3D  $K$  (94 eV) or  $H$  (73 eV) and finally  $\bar{\Gamma}_1$  corresponds to the second 3D  $\Gamma_1$  point of the second BZ, that corresponds to 3D  $\Gamma$  (94 eV) or  $A$  (73 eV) of the second BZ.

## Appendix B

---

# Origin of Kinks in the Measured Band Dispersion

---

The information presented in this appendix have been taken from the supplementary material of Ref. [194]. Figure B.1(a) shows the experimental LEED image of SL WS<sub>2</sub>/Au(111) taken at the kinetic energy of 114 eV. From this figure we can see that the SL WS<sub>2</sub> generally grows well aligned with the Au(111) substrate [204], but the small lattice mismatch between them results in a moiré superstructure. Figures B.1(b-c) exhibit the additional periodicity  $\mathbf{b}_{\text{moiré}} = \mathbf{b}_{\text{Au}} - \mathbf{b}_{\text{WS}_2}$  that leads to the formation of an additional moiré induced reciprocal lattice points [211, 212]. A mini-surface Brillouin zone (BZ) corresponding to the moiré periodicity can be constructed in order to predict the regions in k-space where dodged band crossings (mini gaps) will occur, by analogy to the Kronig-Penney model [213]. Figure B.1(c) presents how the mini gap openings can be observed for both bands at  $k = b_{\text{moiré}}/\sqrt{3} = 0.13 \text{ \AA}$  from the K point in the high symmetry direction  $\Gamma$ - $K$ - $M$ . The position of the kink-like structure in Figures 5.3(a) and 5.3(b) is consistent with the predicted position of a moiré induced mini gap.

In addition to the mini gaps opening, the moiré pattern might affect the measured spectral function by producing band replica either in the initial or in the final state. Thus, the determined width of the EDC might be influenced by such replicas. We did not observe any replicas in our band dispersion presented in Figure 5.3(a), even in the curvature shown in Figure 5.3(b). Despite the absence of such replica in our data, we will describe how

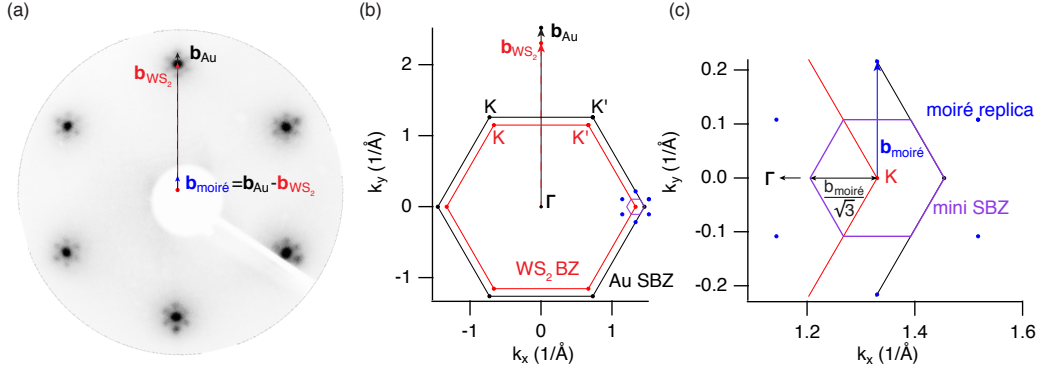


**Figure B.1:** (a) Experimental LEED patterns of SL WS<sub>2</sub>/Au(111) recorded at kinetic energy of  $E_{kin} = 114$  eV. The blue, red and black arrows indicate the reciprocal lattice vectors for the moiré, adlayer and substrate, respectively. (b) The black and red hexagons correspond to the surface Brillouin zone (SBZ) of Au(111) and WS<sub>2</sub>, respectively. The tiny purple hexagon is a mini SBZ corresponding to the moiré periodicity. (c) Magnification of (b) around the mini SBZ showing the positions of the moiré replica and  $\mathbf{b}_{\text{moiré}}$ .

to determine the position of such replica bands. Figure B.2 illustrates the formation of the replicas from a simulated spectral function generated by fitting ARPES spectra with a simple  $\mathbf{k} \cdot \mathbf{p}$  dispersion [38] given by:

$$E(\mathbf{q}) = \frac{\hbar^2 \mathbf{q}^2}{2m_{eff}} + C|\mathbf{q}|^3 \cos 3\Phi; \quad (\text{B.1})$$

where the wavevector  $\mathbf{q}$  can be measured from the high symmetry K point,  $m_{eff}$  denotes the effective mass,  $\Phi = \arctan \frac{q_y}{q_x}$  and  $C$  indicates the parameter describing the trigonal warping. The replica bands are then created from this spectral function by translating it through the reciprocal lattice vectors of the moiré pattern. In Figure B.2, the black simulated bands dispersion represent the original spectral function whereas the replica bands are shown in grey. Figure B.2(a) presents the constant energy contour taken just below the maximum of the upper band. This figure shows that the top of the upper band remains well separated from the moiré-induced BZ boundaries. However, one can see that the top of the lower band might coincide with the moiré-induced replica bands from the cuts along the high symmetry directions  $\Gamma$ -K-M and A-K-A presented in Figures B.2(b-c). Since the signal from replicas is too low to be observed in the performed experiment, one can expect this to have a minor effect on the measured FWHM. This situation is rather different in the case of graphene/Ir(111) since in that system can be clearly observed [211]. The orbital character of the band around the K point in graphene is different from that of SL WS<sub>2</sub>. Because in graphene the band around K point stem from the out-of-plane  $\pi$  electrons in contrast to the SL WS<sub>2</sub> where the bands around K point are from the in-plane d-orbitals.

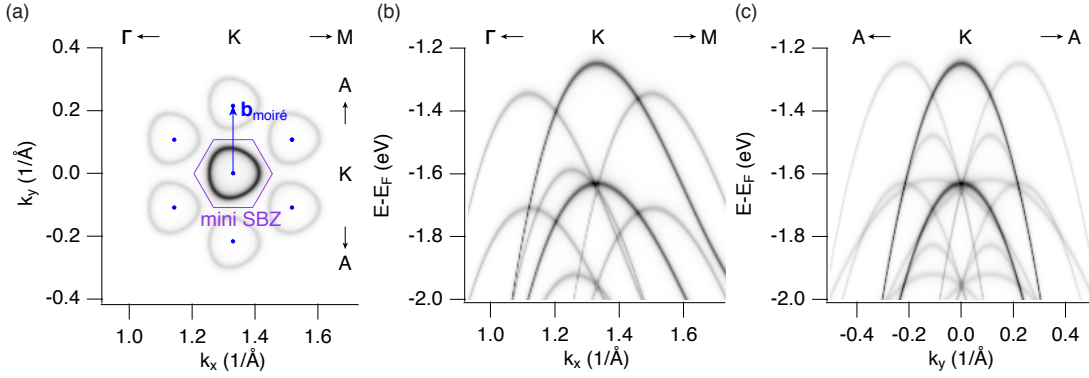


**Figure B.2:** The simulated spectral function obtained by fitting ARPES spectra with a simple  $\mathbf{k} \cdot \mathbf{p}$  dispersion [38]. (a) The black and gray color indicate the main dispersion and the moiré replica, respectively. This image shows a simulated constant energy contour at  $E - E_F = -1.3$  eV. The purple hexagon is a mini SBZ whereas the blue arrow denotes the vector  $\mathbf{b}_{\text{moiré}}$ . (b-c) Simulated cuts along the high symmetry directions  $\Gamma$ -K-M and A-K-A, respectively.

Therefore, the influence of moiré in the band dispersion is greatly decreased by the in-plane character of the bands.

## B.1 Additional Information about the Sample Growth

The growth of SL  $\text{WS}_2/\text{Au}(111)$  and  $\text{MoS}_2/\text{Au}(111)$  presented in this section were achieved in a similar way as illustrated in section 4.1 i.e., by evaporating tungsten W or Mo onto the clean  $\text{Au}(111)$  surface in a background pressure of  $\text{H}_2\text{S}$ , following the procedure described in Refs. [204, 214, 215]. Additionally to this growth procedure, a careful optimization of the growth conditions, oriented by the minimization of the linewidth of the core level spectra, led to a higher crystal quality than in Ref. [204], as also evidenced in the narrower VB features in this current study. Indeed, the small kinks observed in the band dispersion in Figures 5.3(a) and 5.3(b) were not previously detected because they had been masked by the broad bands. For more detailed information on this way of synthesizing the very high quality samples, the reader can consult Ref. [193]. The two samples were synthesized at the SuperESCA beamline at ELETTRA [216] and then transferred in air to the SGM3 beamline at ASTRID2 in Aarhus [113] for ARPES and LEED measurements. The samples were cleaned by a brief annealing to  $550^\circ\text{C}$  after re-inserting them into the ultra high vacuum recipient.

---

# References

---

- [1] B. S. Yizhi Ge. *First-Principles Study of Charge Density Waves, Electron-Phonon Coupling, and Superconductivity in Transition-Metal Dichalcogenides*. PhD thesis, (2013).
- [2] K. S. Novoselov, D. Jiang, F. Schedin, T. J. Booth, V. V. Khotkevich, S. V. Morozov and A. K. Geim. *Proc. Natl. Acad. Sci.* **102** 10451, (2005).
- [3] <http://sciencenotes.org/printable-periodic-table-chart-2015>.
- [4] Visualisation for Electronic and STructural Analysis (VESTA) Software. Downloaded from. <http://jp-minerals.org/vesta/en/>.
- [5] M. K. Momma and F. Izumi. *J. Appl. Cryst.* **44** 1272, (2011).
- [6] <http://www.povray.org/>.
- [7] G. V. Subba Rao and M. W. Shager. *Phys. and Chem. of Mater. with Layered Structure* **6** 99, (1979).
- [8] J. Huang Y. Kim and C. M. Lieber. *Appl. Phys. Lett.* **59** 23, (1991).
- [9] A. R. Beal and W. Y. Liang. *Philos. Mag.* **27** 1397, (1973).
- [10] R. H. Friend and A. D. Yoffe. *Adv. Phys.* **36** 1, (1987).
- [11] M. Chhowalla, H. S. Shin, G. Eda, L. J. Li, K. P. Loh and H. Zhang. *Nat. Chem.* **5** 263, (2013).
- [12] Z. Wang, D. Gresch, A. A. Soluyanov, W. Xie, S. Kushwaha, X. Dai, M. Troyer, R. J. Cava and B. A. Bernevig. *Phys. Rev. Lett.* **117** 056805, (2016).

- 
- [13] A. A. Soluyanov, D. Gresch, Z. Wang, Q. Wu, M. Troyer, X. Dai and B. A. Bernevig. *Nat.* **527** 495, (2015).
- [14] S. Nagata, T. Aochi, T. Abe, S. Ebisu, T. Hagino, Y. Seki and K. Tsutsumi. *J. Phys. Chem. Solids* **53** 1259, (1992).
- [15] I. Guillaumon, H. Suderow, S. Vieira, L. Cario, P. Diener and P. Rodière. *Phys. Rev. Lett.* **101** 166407, (2008).
- [16] T. W. Scharf, S. V. Prasad, M. T. Dugger, P. G. Kotula, R. S. Goeke and R.K. Grubbs. *Acta Mater.* **54** 4731, (2006).
- [17] A. Ennaoui, S. Fiechter, W. Jaegermann and H. Tributsch. *J. Electrochem. Soc.* **133** 97, (1986).
- [18] S. E. Skrabalak and K. S. Suslick. *J. Am. Chem. Soc.* **127** 9990, (2005).
- [19] K. S. Novoselov, A. K. Geim, S. V. Morozov, D. Jiang, Y. Zhang, S. V. Dubonos, I. V. Grigorieva and A. A. Firsov. *Science* **306** 666, (2004).
- [20] K. F. Mak, C. Lee, J. Hone, J. Shan and T. F. Heinz. *Phys. Rev. Lett.* **105** 136805, (2010).
- [21] A. Splendiani, L. Sun, Y. Zhang, T. Li, J. Kim, C. Y. Chim, G. Galli and F. Wang. *Nano Lett.* **10** 1271, (2010).
- [22] R. S. Sundaram, M. Engel, A. Lombardo, R. Krupke, A. C. Ferrari, P. Avouris and M. Steiner. *Nano Lett.* **13** 1416, (2013).
- [23] Y. C. Lin, R. K. Ghosh, R. Addou, N. Lu, S. M. Eichfeld, H. Zhu, M. Y. Li, X. Peng, M. J. Kim, L. J. Li, R. M. Wallace, S. Datta and J. A. Robinson. *Nat. Commun.* **6** 7311, (2015).
- [24] M. Bernardi, M. Palumbo and J. C. Grossman. *Nano Lett.* **13** 3664, (2013).
- [25] V. K. Sangwan, D. Jariwala, I. S. Kim, K. S. Chen, T. J. Marks, L. J. Lauhon and M. C. Hersam. *Nat. Nanotechnol.* **10** 403, (2015).
- [26] D. Krasnozhon, D. Lembke, C. Nyffeler, Y. Leblebici and A. Kis. *Nano Lett.* **14** 5905, (2014).

- [27] B. Radisavljevic, A. Radenovic, J. Brivio, V. Giacometti and A. Kis. *Nat. Nanotechnol.* **6** 147, (2011).
- [28] Z. Y. Zhu, Y. C. Cheng and U. Schwingenschlögl. *Phys. Rev. B* **84** 153402, (2011).
- [29] P. C. Yeh, W. Jin, N. Zaki, D. Zhang, J. T. Liou, J. T. Sadowski, A. Al-Mahboob, J. I. Dadap, I. P. Herman, P. Sutter and R. M. Osgood. *Phys. Rev. B* **91** 041407, (2015).
- [30] D. W. Latzke, W. Zhang, A. Suslu, T.-R. Chang, H. Lin, H.-T. Jeng, S. Tongay, J. Wu, A. Bansil and A. Lanzara. *Phys. Rev. B* **91** 235202, (2015).
- [31] M. M. Ugeda, A. J. Bradley, Y. Zhang, S. Onishi, Y. Chen, W. Ruan, C. Ojeda-Aristizabal, H. Ryu, M. T. Edmonds, H.-Z. Tsai, A. Riss, S.-K. Mo, D. Lee, A. Zett, Z. Hussain, Z.-X. Shen and M. F. Crommie. *Nat. Phys.* **12** 92, (2016).
- [32] D. Y. Qiu, F. H. da Jornada and S. G. Louie. *Phys. Rev. Lett.* **111** 216805, (2013).
- [33] J. A. Wilson and A.D. Yoffe. *Adv. Phys.* **18** 193, (1969).
- [34] Q. H. Wang, K. Kalantar Zadeh, A. Kis, J. N. Coleman and M. S. Strano. *Nat. Nano.* **7** 699, (2012).
- [35] T. Cheiwchanchamnangij and W. R. L. Lambrecht. *Phys. Rev. B* **85** 205302, (2012).
- [36] A. G. Čabo, J. A. Miwa, S. S. Grønberg, J. M. Riley, J. C. Johannsen, C. Cacho, O. Alexander, R. T. Chapman, E. Springate, M. Grioni, J. V. Lauritsen, P. D. C. King, P. Hofmann and S. Ulstrup. *Nano Lett.* **15** 5883, (2015).
- [37] C. Mai, A. Barrette, Y. Yu, Y. G. Semenov, K. W. Kim, L. Cao and K. Gun-dogdu. *Nano. Lett.* **14** 202, (2014).
- [38] A. Kormányos, G. Burkard, M. Gmitra, J. Fabian, V. Zólyomi, N. D. Drummond and V. Fal'ko. *2D Mater.* **2** 022001, (2015).
- [39] A. Spijkerman, J. L. de Boer, A. Meetsma and G. A. Wiegers. *Phys. Rev. B* **56** 13757, (1997).
- [40] D. E. Moncton, J. D. Axe and F. J. DiSalvo. *Phys. Rev. Lett.* **34** 734, (1975).
- [41] J. Kim, C. Park and H. Olin. *J. of the Korean Phys. Society* **31** 713, (1997).
- [42] G. Grüner. *Rev. Mod. Phys.* **60** 1129, (1988).

- [43] A. Thompson, F. R. Gamble and J. F. Revelli. *Solid State Commun.* **9** 981, (1971).
- [44] J. P. Tidman, O. Singh, A. E. Curzon and R. F. Frindt. *Philos. Mag.* **30** 1191, (1974).
- [45] J. A. Wilson, F. J. Di Salvo and S. Mahajan. *Phys. Rev. Lett.* **32** 882, (1974).
- [46] R. E. Thomson, B. Burk, A. Zettl and J. Clarke. *Phys. Rev. B* **49** 16899, (1994).
- [47] T. R. T. Han, F. Zhou, C. D. Malliakas, P. M. Duxbury, S. D. Mahanti, M. G. Kanatzidis and C. Y. Ruan. *Sci. Adv.* **1** e1400173, (2015).
- [48] J. J. Kim, W. Yamaguchi, T. Hasegawa and K. Kitazawa. *Phys. Rev. Lett.* **73** 2103, (1994).
- [49] F. Zwick, H. Berger, I. Vobornik, G. Margaritondo, L. Forró, C. Beeli, M. Onellion, G. Panaccione, A. Taleb-Ibrahimi and M. Grioni. *Phys. Rev. Lett.* **81** 1058, (1998).
- [50] T. Pillo, J. Hayoz, H. Berger, M. Grioni, L. Schlapbach and P. Aebi. *Phys. Rev. Lett.* **83** 3494, (1999).
- [51] M. Naito and S. Tanaka. *J. Phys. Soc. Jpn.* **51** 219, (1982).
- [52] S. Sugai, K. Murase, S. Uchida and S. Tanaka. *Solid State Commun.* **40** 399, (1981).
- [53] G. A. Scholz, O. Singh, R. F. Frindt and A. E. Curzon. *Solid State Commun.* **44** 1455, (1982).
- [54] K. E. Wagner, E. Morosan, Y. S. Hor, J. Tao, Y. Zhu, T. Sanders, T. M. McQueen, H. W. Zandbergen, A. J. Williams, D. V. West and R. J. Cava. *Phys. Rev. B* **78** 104520, (2008).
- [55] S. A. Raj and N. Lawrence. *J. Applied Sci.* **14** 2738, (2014).
- [56] R. Peierls. *Quantum Theory of Solids*. Oxford University Press, (1955).
- [57] M. D. Johannes, I. I. Mazin and C. A. Howells. *Phys. Rev. B* **73** 205102, (2006).
- [58] M. Calandra, I. I. Mazin and F. Mauri. *Phys. Rev. B* **80** 241108, (2009).
- [59] B. Sipos, A. F. Kusmartseva, A. Akrap, H. Berger, L. Forró and E. Tutiš. *Nat. Mater.* **7** 960, (2008).
- [60] F. Weber, S. Rosenkranz, R. Heid and A. H. Said. *Phys. Rev. B* **94** 140504(R), (2016).

- [61] C. E. Sanders, M. Dendzik, A. S. Ngankeu, A. Eich, A. Bruix, M. Bianchi, J. A. Miwa, B. Hammer, A. A. Khajetoorians and P. Hofmann. *Phys. Rev. B* **94** 081404(R), (2016).
- [62] K. Rossnagel. *J. Phys.: Condens. Matter* **23** 213001, (2011).
- [63] T. Ritschel, J. Trinckauf, K. Koepernik, B. Buchner, M. v. Zimmermann, H. Berger, Y. I. Joe, P. Abbamonte and J. Geck. *Nat. Phys.* **11** 328, (2015).
- [64] F Clerc, C Battaglia, H Cercellier, C Monney, H Berger, L Despont, M G Garnier and P Aebi. *J. Phys.: Condens. Matter* **19** 355002, (2007).
- [65] X.-L. Yu, D.-Y. Liu, Y.-M. Quan, J. Wu, H.-Q. Lin, K. Chang and L.-J. Zou. *Phys. Rev. B* **96** 125138, (2017).
- [66] P. Darancet, A. J. Milli and C. A. Marianetti. *Phys. Rev. B* **90** 045134, (2014).
- [67] Philip Hofmann. *Surface Physics: An Introduction*. (2013).
- [68] D. R. Penn. *Phys. Rev. B* **35** 482, (1987).
- [69] M. A. Van Hove, W. H. Weinberg and C. M. Chan. *Springer Series in Surface Science*. Springer, (1986).
- [70] H. L. Tierney and E. C. H. Sykes. *Scanning Tunneling Microscopy in Surface Science*. Nanoscience and Catalysis. Wiley-VCH, (2010).
- [71] G. Binnig and H. Rohrer. *Scanning Tunneling Microscopy*. *Helv. Phys. Acta* **55** 726, (1982).
- [72] Anders Tuxen. *Atomic-Scale Investigations of MoS<sub>2</sub> Based Hydrotreating Model Catalysts*. PhD thesis, (2011).
- [73] C. Julian Chen. *Introduction to Scanning Tunneling Microscopy*. Oxford University Press, (2008).
- [74] G. Binnig and H. Rohrer. *Surface Science* **126** 236, (1983).
- [75] P. Sutter. *Science of Microscopy, Volume Scanning Tunneling Microscopy in Surface Science*. John Wiley Sons, (2007).
- [76] J. C. Chen. *Introduction to Scanning Tunneling Microscopy*. Oxford University Press, (2007).

- [77] A. Bruix, J. A. Miwa, N. Hauptmann, D. Wegner, S. Ulstrup, S. S. Grønberg, C. E. Sanders, M. Dendzik, A. G. Čabo, M. Bianchi, J. V. Lauritsen, A. A. Khajetoorians, B. Hammer and P. Hofmann. *Phys. Rev. B* **93** 165422, (2016).
- [78] J. V. Lauritsen. *Atomic-scale Study of a Hydrodesulfurization Model Catalyst*. PhD thesis, (2002).
- [79] S. Wendt and L. Lammich. *Scanning Tunneling Microscopy Users Course*. Users manual, (2016).
- [80] F. Besenbacher, E. Lægsgaard, K. Mortensen, U. Nielsen and I. Stensgaard. *Rev. Sci. Instrum.* **59** 7, (1988).
- [81] E. Laegsgaard, F. Besenbacher, K. Mortensen and Stensgaard. *J. Microsc.* **152** 663, (1988).
- [82] Phys.au.dk homepage. <http://phys.au.dk/forskning/forskningsomraader/condensed-matter-physics/spm/the-aarhus-stm/>.
- [83] Prof. dr. Alexander Khajetoorians homepage. <http://www.ru.nl/spm/group-members/prof-dr-alexander/>.
- [84] A. Damascelli. *Physica Scripta* **T109** 61, (2004).
- [85] A. Damascelli, Z. Hussain and Z. X. Shen. *Rev. Mod. Phys.* **75** 473, (2003).
- [86] A. Damascelli, D. H. Lu and Z. X. Shen. *J. Electron. Spectrosc. Relat. Phenom.* **165** 117, (2001).
- [87] L. Ma, C. Ye, Y. Yu, X. F. Lu, X. Niu, S. Kim, D. Feng, D. Tománek, Y. W. Son, X. H. Chen and Y. Zhang. *Nat. Commun.* **7** 10956, (2016).
- [88] D. Cho, S. Cheon, K. S. Kim, S. H. Lee, Y. H. Cho, S. W. Cheong and H. W. Yeom. *Nat. Commun.* **7** 10453, (2016).
- [89] H. Hertz. *Ann. Phys.* **267** 983, (1887).
- [90] A. Einstein. *Ann. Phys.* **17** 132, (1905).
- [91] P. Hofmann. *Synchrotron-Radiation Studies of Topological Insulators*. In: E. Beaurepaire, H. Bulou, L. Joly, F. Scheurer (eds) *Magnetism and Synchrotron Radiation:*

- 
- Towards the Fourth Generation Light Sources*. Springer Proceedings in Physics **151**. Springer, Cham, (2013).
- [92] M. Wöhlecke, A. Baalmann and M. Neumann. *Solid State Commun.* **49** 217, (1984).
- [93] S. Hüfner. *Photoelectron Spectroscopy*. Springer, (2003).
- [94] Madhab Neupane. *Angle Resolved Photoemission Studies on Ruthenates and Iron-Based Superconductors*. PhD thesis, (2010).
- [95] A. A. Kordyuk, S. V. Borisenko, A. Koitzsch, J. Fink, M. Knupfer and H. Berger. *Phys. Rev. B* **71** 214513, (2005).
- [96] P. Hofmann, I. Y. Sklyadneva, E. D. L. Rienks and E. V. Chulkov. *New J. Phys.* **11** 125005, (2009).
- [97] F. Mazzola, J. W. Wells, R. Yakimova, S. Ulstrup, J. A. Miwa, R. Balog, M. Bianchi, M. Leandersson, J. Adell, P. Hofmann and T. Balasubramanian. *Phys. Rev. Lett.* **111** 216806, (2013).
- [98] C. Kirkegaard, T. K. Kim and P. Hofmann. *New J. Phys.* **7** 99, (2005).
- [99] A. Bostwick, T. Ohta, T. Seyller, K. Horn and E. Rotenberg. *Nat Phys.* **3** 36, (2007).
- [100] Matteo Michiardi. *Study of Electronic States in Novel Materials: Topological Insulators and Rare Earth Diantimonides*. PhD thesis, (2015).
- [101] Z. Sun, Y. D. Chuang, A. V. Fedorov, J. F. Douglas, D. Reznik, F. Weber, N. Aliouane, D. N. Argyriou, H. Zheng, J. F. Mitchell, T. Kimura, Y. Tokura, A. Revcolevschi and D. S. Dessau. *Phys. Rev. Lett.* **97** 056401, (2006).
- [102] J. Fink, S. Borisenko, A. Kordyuk, A. Koitzsch, J. Geck, V. Zabalotnyy, M. Knupfer, B. Buechner and H. Berger. Dressing of the Charge Carriers in High- $T_c$  Superconductors. In: Hüfner S. (eds) *Very High Resolution Photoelectron Spectroscopy*. Lecture Notes in Physics, **715** (2007). Springer, Berlin, Heidelberg.
- [103] G. Wertheim, F. Disalvo, and S. Chiang. *Phys. Lett.* **54A** 304, (1975).
- [104] S. Hofmann. *Auger and X-ray Photoelectron Spectroscopy in Materials Science*. (2013).
- [105] S. Tougaard. *Surf. Sci. Lett.* **139** A125, (1984).

- [106] D. A. Shirley. *Phys. Rev. B* **5** 4709, (1972).
- [107] H. P. Hughes and J. A. Scarfe. *Phys. Rev. Lett.* **74** 3069, (1995).
- [108] S. Doniach and M. Šunjić. *J. Phys. C: Solid State Phys.* **3** 285, (1970).
- [109] S. Hüfner. *Very High Resolution Photoelectron Spectroscopy*. Springer, (2007).
- [110] Maciej Dendzik. *Growth and Electronic Structure of Single-Layered Transition Metal Dichalcogenides*. PhD thesis, (2016).
- [111] Centre for Storage Ring Facilities ISA. Aarhus, Denmark. On the web.: <http://isa.au.dk>.
- [112] S. Møller. *IPAC12 Proceedings*. 1605 (2012).
- [113] S. V. Hoffmann, C. Søndergaard, C. Schultz, Z. Li and P. Hofmann. *Nucl. Instr. Meth. Phys. Res. A* **523** 441, (2004).
- [114] W. Eberhardt. *J. Electron. Spectrosc. Relat. Phenom.* **200** 31, (2015).
- [115] H. Kjeldsen. *Cross Sections for Photoionisation of Positive Atomic Ions: Absolute Measurements using Synchrotron Radiation*. PhD thesis, (1999).
- [116] J. Wilson, F. Di Salvo and S. Mahajan. *Adv. Phys.* **24** 117, (1975).
- [117] P. Fazekas and E. Tosatti. *Phil. Mag. B* **39** 229, (1979).
- [118] F. J. Di Salvo, J. A. Wilson, B. G. Bagley and J. V. Waszczak. *Phys. Rev. B* **12** 2220, (1975).
- [119] D. F. Shao, R. C. Xiao, W. J. Lu, H. Y. Lv, J. Y. Li, X. B. Zhu and Y. P. Sun. *Phys. Rev. B* **94** 125126, (2016).
- [120] M. J. Hollander, W.-J. Liu, Y. Lu, L.-J. Li, Y.-P. Sun, J. A. Robinson and S. Datta. *Nano Lett.* **15** 1861, (2015).
- [121] A. W. Tsen, R. Hovden, D. Wang, Y. D. Kim, J. Okamoto, K. A. Spoth, Y. Liu, W. Lu, Y. Sun, J. C. Hone, L. F. Kourkoutis, P. Kim and A. N. Pasupathy. *Proc. Nat. Acad. Sci.* **112** 15054, (2015).

- [122] Y. Yu, F. Yang, X. F. Lu, Y. J. Yan, Y.-H. Cho, L. Ma, X. Niu, S. Kim, Y.-W. Son, D. Feng, S. Li, S.-W. Cheong, X. H. Chen and Y. Zhang. *Nat. Nanotechnol.* **10** 270, (2015).
- [123] P. Fazekas and E. Tosatti. *Physica B+C* **99** 183, (1980).
- [124] L. Perfetti, P. A. Loukakos, M. Lisowski, U. Bovensiepen, H. Berger, S. Biermann, P. S. Cornaglia, A. Georges and M. Wolf. *Phys. Rev. Lett.* **97** 067402, (2006).
- [125] L. Stojchevska, I. Vaskivskiy, T. Mertelj, P. Kusar, D. Svetin, S. Brazovskii and D. Mihailovic. *Science* **344** 177, (2014).
- [126] K. T. Law and P. A. Lee. *Proc. Natl. Acad. Sci.* **114** 6996, (2017).
- [127] M. Bovet, S. van Smaalen, H. Berger, R. Gaal, L. Forró, L. Schlapbach and P. Aebi. *Phys. Rev. B* **67** 125105, (2003).
- [128] P. Lazar, J. Martincová and M. Otyepka. *Phys. Rev. B* **92** 224104, (2015).
- [129] K. Haupt, M. Eichberger, N. Erasmus, A. Rohwer, J. Demsar, K. Rossnagel and H. Schwoerer. *Phys. Rev. Lett.* **116** 016402, (2016).
- [130] P. Hambourger and F. di Salvo. *Physica B+C* **99** 173, (1980).
- [131] Arlette S. Ngankeu, Sanjoy K. Mahatha, Kevin Guilloy, Marco Bianchi, Charlotte E. Sanders, Kerstin Hanff, Kai Rossnagel, Jill A. Miwa, Christina Breth Nielsen, Martin Bremholm and Philip Hofmann. *Phys. Rev. B* **96** 195147, (2017).
- [132] M. Bovet, D. Popović, F. Clerc, C. Koitzsch, U. Probst, E. Bucher, H. Berger, D. Naumović and P. Aebi. *Phys. Rev. B* **69** 125117, (2004).
- [133] K. Rossnagel, E. Rotenberg, H. Koh, N. V. Smith and L. Kipp. *Phys. Rev. Lett.* **95** 126403, (2005).
- [134] M. Arita, H. Negishi, K. Shimada, F. Xu, A. Ino, Y. Takeda, K. Yamazaki, A. Kimura, S. Qiao, S. Negishi, *et al.* *Physica B: Condens. Matter* **351** 265, (2004).
- [135] L. Perfetti, T. A. Gloor, F. Mila, H. Berger and M. Grioni. *Phys. Rev. B* **71** 153101, (2005).
- [136] F. Clerc, C. Battaglia, M. Bovet, L. Despont, C. Monney, H. Cercellier, M. G. Garnier, P. Aebi, H. Berger and L. Forró. *Phys. Rev. B* **74** 155114, (2006).

- 
- [137] L. F. Mattheiss. *Phys. Rev. B* **8** 3719, (1973).
- [138] R. Manzke, O. Anderson and M. Skibowski. *J. Phys. C: Solid State Physics* **21** 2399, (1988).
- [139] W. Shen, Y. Ge, A. Y. Liu, H. R. Krishnamurthy, T. P. Devereaux and J. K. Freericks. *Phys. Rev. Lett.* **112** 176404, (2014).
- [140] R. A. Pollak, D. E. Eastman, F.J. Himpsel, P. Heimann and B. Reihl. *Phys. Rev. B.* **24** 7435, (1981).
- [141] S. Hellmann, C. Sohr, M. Beye, T. Rohwer, F. Sorgenfrei, M. Marczyński-Bühlow, M. Kalläne, H. Redlin, F. Hennies, M. Bauer, A. Föhlisch, L. Kipp, W. Wurth and K. Rossnagel. *New J. Phys.* **14** 013062, (2012).
- [142] H. P. Hughes and R. Pollak. *Phil. Mag.* **34** 1025, (1976).
- [143] R. Ang, Y. Miyata, E. Ieki, K. Nakayama, T. Sato, Y. Liu, W. J. Lu, Y. P. Sun and T. Takahashi. *Phys. Rev. B* **88** 115145, (2013).
- [144] E. W. Plummer and W. Eberhardt. *Adv. Chem. Phys.* **49** 533, (1982).
- [145] J. K. Freericks, H. R. Krishnamurthy, Y. Ge, A. Y. Liu and T. Pruschke. *Phys. Status Solidi (b)* **246** 948, (2009).
- [146] S. Tanda, T. Sambongi, T. Tani and S. Tanaka. *J. Phys. Soc. Jpn.* **53** 476, (1984).
- [147] T. Ishiguro and H. Sato. *Phys. Rev. B* **44** 2046, (1991).
- [148] K. Rossnagel and N. V. Smith. *Phys. Rev. B* **73** 073106, (2006).
- [149] F. Di Salvo and J. Graebner. *Solid State Commun.* **23** 825, (1977).
- [150] H. Sato, M. Arita, Y. Utsumi, Y. Mukaegawa, M. Sasaki, A. Ohnishi, M. Kitaura, H. Namatame and M. Taniguchi. *Phys. Rev. B.* **89** 155137, (2014).
- [151] Y. Yu, F. Yang, X. F. Lu, Y. J. Yan, Y. H. Cho, L. Ma, X. Niu, S. Kim, Y.-W. Son, D. Feng, S. Li, S.-W. Cheong, X. H. Chen and Y. Zhang. *Nat. Nanotechnol.* **10** 270, (2015).

- [152] K. Ishizaka, T. Kiss, T. Yamamoto, Y. Ishida, T. Saitoh, M. Matsunami, R. Eguchi, T. Ohtsuki, A. Kosuge, T. Kanai, M. Nohara, H. Takagi, S. Watanabe and S. Shin. *Phys. Rev. B.* **83** 081104(R), (2011).
- [153] E. Tosatti. *Surface States, Surface Metal-Insulator, and Surface Insulator-Metal Transitions*. “Electronic Surface and Interface States on Metallic Systems”, Proceedings of the 134th We-Heraeus Seminar, ed E. Bertel and M. Donath (World Scientific, Singapore), (1995).
- [154] N. V. Smith and M. M. Traum. *Phys. Rev. B.* **11** 2087, (1975).
- [155] L. F. Mattheis. *Phys. Rev. B.* **8** 3719, (1973).
- [156] A. M. Woolley and G. Wexlers. *Phys. Rev. B.* **10** 2601, (1977).
- [157] S. C. Bayliss, A. Clarke and W. Y. Liang. *J. Phys. C: Solid State Phys.* **16** L831, (1983).
- [158] S. V. Borisenko, A. A. Kordyuk, A. N. Yaresko, V. B. Zabolotnyy, D. S. Inosov, R. Schuster, B. Büchner, R. Weber, R. Follath, L. Patthey and H. Berger. *Phys. Rev. Lett.* **100** 196402, (2008).
- [159] K. Rossnagel, Eli Rotenberg, H. Koh, N. V. Smith and L. Kipp. *Phys. Rev. B* **72** 121103R, (2005).
- [160] J. Renteria, R. Samnakay, C. Jiang, T. R. Pope, P. Goli, Z. Yan, D. Wickramaratne, T. T. Salguero, A. G. Khitun, R. K. Lake and A. A. Balandin. *J. Appl. Phys.* **115** 034305, (2014).
- [161] H. J. Crawack and C. Pettenkofer. *Solid State Commun.* **118** 325, (2001).
- [162] K. F. Mak, K. L. McGill, J. Park and P. L. McEuen. *Science* **344** 1489, (2014).
- [163] P. Zhang, P. Richard, T. Qian, Y.-M. Xu, X. Dai and H. Ding. *Rev. Sci. Instrum.* **82** 043712, (2011).
- [164] O. L. Sanchez Y.-C. Kung D. Krasnozhon M.-W. Chen S. Bertolazzi P. Gillet, A. Fontcuberta i Morral, A. Radenovic D. Dumcenco, D. Ovchinnikov, K. Marinov, P. Lazić, M. Gibertini, N. Marzari and A. Kis. *ACS Nano* **9** 4611, (2015).
- [165] P. R. Wallace. *Phys. Rev.* **71** 622, (1947).

- [166] S. Hagstrom, H. B. Lyon and G. A. Somorjai. *Phys. Rev. Lett.* **15** 491, (1965).
- [167] P. Chen, Y. H. Chan, X. Y. Fang, Y. Zhang, M. Y. Chou, S. K. Mo, Z. Hussain, A. V. Fedorov and T. C. Chiang. *Nat. Commun.* **6** 8943, (2015).
- [168] K. Sugawara, Y. Nakata, R. Shimizu, P. Han, T. Hitosugi, T. Sato and T. Takahashi. *ACS Nano* **10** 1341, (2016).
- [169] X. Xi, L. Zhao, Z. Wang, H. Berger, L. Forró, J. Shan and K. F. Mak. *Nat. Nanotechnol.* **10** 765, (2015).
- [170] J. Barth, H. Brune, G. Ertl and R. J. Behm. *Phys. Rev. B* **42** 15, (1990).
- [171] M. E. Dávila and G. L. Lay. *Sci. Rep.* **6** 20714, (2016).
- [172] S. Helveg, J. V. Lauritsen, E. Lægsgaard, I. Stensgaard, J. K. Nørskov, B. S. Clausen, H. Topsøe and F. Besenbacher. *Phys. Rev. Lett.* **84** 951, (2000).
- [173] Antonija Grubišić Čabo. *Two-Dimensional Materials: From Basic Research in Transition Metal Dichalcogenides to Technique Development for Graphene Applications*. PhD thesis, (2017).
- [174] A. T. N'Diaye, J. Coraux, T. N. Plasa, C. Busse and T. Michely. *New J. Phys.* **10** 043033, (2008).
- [175] S. Nie, N. C. Bartelt, J. M. Wofford, O. D. Dubon, K. F. McCarty and K. Thürmer. *Phys. Rev. B* **85** 205406, (2012).
- [176] S. G. Sørensen, H. G. Füchtbauer, A. K. Tuxen, A. S. Walton and J. V. Lauritsen. *ACS Nano* **8** 6788, (2014).
- [177] P. Garoche, P. Manuel, J. J. Veyssié, and P. Molinié. *J. Low Temp. Phys.* **30** 323, (1978).
- [178] I. Guillamón, H. Suderow, J. G. Rodrigo, S. Vieira, P. Rodière, L. Cario, E. Navarro-Moratalla, C. Martí-Gastaldo and E. Coronado. *New J. Phys.* **13** 103020, (2011).
- [179] J. A. Galvis, L. Chirolli, I. Guillamón, S. Vieira, E. Navarro-Moratalla, E. Coronado, H. Suderow and F. Guinea. *Phys. Rev. B* **89** 224512, (2014).

- [180] E. Navarro-Moratalla, J. O. Island, S. Mañas-Valero, E. Pinilla-Cienfuegos, A. Castellanos-Gomez, J. Quereda, G. Rubio-Bollinger, L. Chirolli, J. A. Silva-Guillén, N. Agrait, G. A. Steele, F. Guinea, H. S. J. van der Zant and E. Coronado. *Nat. Commun.* **7** 11043, (2016).
- [181] L. Kipp, K. Rossnagel, C. Solterbeck, T. Strasser, W. Schattke and M. Skibowski. *Phys. Rev. Lett.* **83** 5551, (1999).
- [182] A. H. Castro Neto. *Phys. Rev. Lett.* **86** 4382, (2001).
- [183] K. Rossnagel, O. Seifarth, L. Kipp, M. Skibowski, D. Voß, P. Krüger, A. Mazur and J. Pollmann. *Phys. Rev. B* **64** 235119, (2001).
- [184] T. O. Wehling. *arXiv:1609.00220*, (2016).
- [185] M. M. Ugeda, A. J. Bradley, S.-F. Shi, F. H. da Jornada, Y. Zhang, D. Y. Qiu, W. Ruan, S.-K. Mo, Z. Hussain, Z.-X. Shen, F. Wang, S. G. Louie and M. F. Crommie. *Nat. Mater.* **13** 1091, (2014).
- [186] A. Soumyanarayanan, M. M. Yee, Y. He, J. van Wezel, D. J. Rahn, K. Rossnagel, E. W. Hudson, M. R. Norman and J. E. Hoffman. *Proc. Natl. Acad. Sci.* **110** 1623, (2013).
- [187] Y. Ge and A. Y. Liu. *Phys. Rev. B* **86** 104101, (2012).
- [188] X. Fan, W. T. Zheng, J.-L. Kuo, D. J. Singh, C. Q. Sun and W. Zhu. *Sci. Rep.* **6** 24140, (2016).
- [189] J.-A. Yan, M. A. D. Cruz, B. Cook and K. Varga. *Sci. Rep.* **5** 16646, (2015).
- [190] N. F. Mott. *Proc. Phys. Soc. London* **46**, (1934).
- [191] R. E. Peierls. *Quantum Theory of Solids*. Clarendon, Oxford, (1964).
- [192] J. Bardeen. *Science* **181** 1209, (1973).
- [193] H. Bana, E. Travaglia, L. Bignardi, P. Lacovig, C. E. Sanders, M. Dendzik, M. Michiardi, M. Bianchi, D. Lizzit, F. Presel, D. D. Angelis, N. Apostol, P. K. Das, J. Fujii, I. Vobornik, R. Larciprete, A. Baraldi, P. Hofmann and S. Lizzit. *Synthesis of Single-Orientation High-Quality MoS<sub>2</sub> Monolayers with Complete Spin Polarization*. Submitted, (2017).

- [194] N. F. Hinsche, A. S. Ngankeu, K. Guilloy, S. K. Mahatha, A. G. Čabo, M. Bianchi, M. Dendzik, C. E. Sanders, J. A. Miwa, H. Bana, E. Travaglia, P. Lacovig, L. Bignardi, R. Larciprete, A. Barald, S. Lizzit, K. S. Thygesen and P. Hofmann. *Phys. Rev. B* **96** 121402(R), (2017).
- [195] Giuseppe Grosso and Giuseppe Pastori Parravicini. *Solid State Physics. 2nd. Ed. Primarily chapters 9 and 18*. Elsevier, (2014).
- [196] X. Xu, W. Yao, D. Xiao and T. F. Heinz. *Nat. Phys.* **10** 343, (2014).
- [197] Y.-T. Hsu, A. Vaezi, M. H. Fischer and E.-A. Kim. *Nat. Commun.* **8** 14985, (2017).
- [198] D. Xiao, G.-B. Liu, W. Feng, X. Xu and W. Yao. *Phys. Rev. Lett.* **108** 196802, (2012).
- [199] J. Fabian and S. Das Sarma. *Phys. Rev. Lett.* **83** 1211, (1999).
- [200] A. M.-Sánchez and L. Wirtz. *Phys. Rev. B* **84** 155413, (2011).
- [201] N. Takeuchi, C. T. Chan and K. M. Ho. *Phys. Rev. B* **43** 13899, (1991).
- [202] A. Lanzara, P. V. Bogdanov, X. J. Zhou, S. A. Kellar, D. L. Feng, E. D. Lu, T. Yoshida, H. Eisaki, A. Fujimori, K. Kishio, J.-I. Shimoyama, T. Noda, S. Uchida, Z. Hussain and Z.-X. Shen. *Nat.* **412** 510, (2001).
- [203] F. Mazzola, T. Frederiksen, T. Balasubramanian, P. Hofmann, B. Hellsing and J. W. Wells. *Phys. Rev. B* **95** 075430, (2017).
- [204] M. Dendzik, M. Michiardi, C. Sanders, M. Bianchi, J. A. Miwa, S. S. Grønberg, J. V. Lauritsen, A. Bruix, B. Hammer and P. Hofmann. *Phys. Rev. B* **92** 245442, (2015).
- [205] B. Peng, H. Zhang, H. Shao, Y. Xu, X. Zhang and H. Zhu. *RSC Adv.* **6** 5767, (2016).
- [206] Z. Y. Zhu, Y. C. Cheng and U. Schwingenschlögl. *Phys. Rev. B* **84** 153402, (2011).
- [207] T. Cheiwchanchamnangij and W. R. L. Lambrecht. *Phys. Rev. B* **85** 205302, (2012).
- [208] J. A. Miwa, S. Ulstrup, S. G. Sørensen, M. Dendzik, A. G. Čabo, M. Bianchi, J. V. Lauritsen and P. Hofmann. *Phys. Rev. Lett.* **114** 046802, (2015).
- [209] K. Kaasbjerg, K. S. Thygesen, and K. W. Jacobsen. *Phys. Rev. B* **85** 115317, (2012).
- [210] N. F. Hinsche and K. S. Thygesen. *2D Materials* **5** 1, (2017).

- 
- [211] I. Pletikosić, M. Kralj, P. Pervan, R. Brako, J. Coraux, A. T. N'Diaye, C. Busse and T. Michely. *Phys. Rev. Lett.* **102** 056808, (2009).
- [212] M. Kralj, I. Pletikosić, M. Petrović, P. Pervan, M. Milun, A. T. N'Diaye, C. Busse, T. Michely, J. Fujii and I. Vobornik. *Phys. Rev. B* **84** 075427, (2011).
- [213] R. de L. Kronig and W. G. Penney. *Proc. Roy. Soc. London Ser. A: Math. Phys. Eng. Sci.* **130** 499, (1931).
- [214] J. V. Lauritsen, J. Kibsgaard, S. Helveg, H. Topsoe, B. S. Clausen, E. Laegsgaard and F. Besenbacher. *Nat. Nanotechnol.* **2** 53, (2007).
- [215] J. A. Miwa, S. Ulstrup, S. G. Sørensen, M. Dendzik, A. G. Čabo, M. Bianchi, J. V. Lauritsen and P. Hofmann. *Phys. Rev. Lett.* **114** 046802, (2015).
- [216] A. Baraldi, G. Comelli, S. Lizzit, M. Kiskinova and G. Paolucci. *Surf. Sci. Rep. (Netherlands)* **49** 169, (2003).